

LA-5656-PR
Progress Report

UC-20
Issued: July 1974

c.3

CIC-14 REPORT COLLECTION
**REPRODUCTION
COPY**

Progress Report

LASL

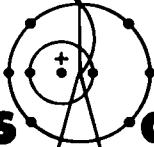
Controlled Thermonuclear Research Program

for a 12-Month Period Ending December 1973



Compiled by

Maurice J. Katz



los alamos
scientific laboratory
of the University of California
LOS ALAMOS, NEW MEXICO 87544

This report was prepared as an account of work sponsored by the United States Government. Neither the United States nor the United States Atomic Energy Commission, nor any of their employees, nor any of their contractors, subcontractors, or their employees, makes any warranty, express or implied, or assumes any legal liability or responsibility for the accuracy, completeness or usefulness of any information, apparatus, product or process disclosed, or represents that its use would not infringe privately owned rights.

This report presents the status of the LASL Controlled Thermonuclear Research program. Previous annual progress reports in this series, all unclassified, are:

LA-4351-MS, LA-4585-MS, LA-4888-PR, and LA-5250-PR.

In the interest of prompt distribution, this progress report was not edited by the Technical Information staff.

This work supported by the U.S. Atomic Energy Commission's Division of Controlled Thermonuclear Research.

Printed in the United States of America. Available from
National Technical Information Service
U.S. Department of Commerce
5285 Port Royal Road
Springfield, Virginia 22151
Price: Printed Copy \$7.60 Microfiche \$1.45

. ABSTRACT

This report presents the status of the Controlled Thermonuclear Research Program at the Los Alamos Scientific Laboratory for calendar year 1973.

CONTENTS

I.	INTRODUCTION	1
II.	THETA-PINCH PROGRAM	5
	A. Summary of θ -Pinch Activities	5
	B. Scyllac 8-Meter Toroidal Sector Experiment	5
	C. Feedback Stabilization Experiments on the 8-m Toroidal Sector	18
	D. Scyllac Torus	26
	E. Staged Theta Pinch	30
	F. Scylla IV-3	33
	G. Scylla I-B	39
	H. Diagnostics	45
	I. High-Density Linear Theta-Pinch Studies	52
	J. Automatic Data Processing	53
	References	54
III.	IMPLOSION HEATING EXPERIMENT	57
	A. Summary	57
	B. Development of the Current Source	59
	C. Preionization	67
	D. Computer Modeling of the Heating In A Fast Piston Implosion of an Unmagnetized Plasma	68
	References	70
IV.	Z-PINCH PROGRAM	71
	A. Summary	71
	B. Electron Temperature by Thomson Scattering	72
	C. Electron Temperatures from Time-Resolved Spectroscopy	73
	D. Ion Temperature from Doppler Broadening Measurements	75
	E. Plasma Density Measurements with Laser Interferometer	76
	F. Derating of the ZT-1 Experiment	77
	G. MHD-Stability Analysis	80
	H. Symmetric Suydam Modes	80
	I. Crowbar Spark Gaps	81
	References	81

V.	THEORETICAL PHYSICS PROGRAM	83
	A. General Summary	83
	B. Scyllac Summary	84
	C. Highlights of the Numerical Simulation and Computer Applications Program	91
	D. Highlights of Toroidal Z-Pinch Theory	96
	References	102
VI.	EXPERIMENTAL PLASMA PHYSICS RESEARCH PROGRAM	105
	A. Summary	105
	B. Absorption of Electromagnetic Waves Near the Electron Plasma Frequency	106
	C. Weak Field Electrical Resistivity	111
	D. Experimental Evidence for Nonlinear Inverse Bremsstrahlung Absorption	112
	References	115
VII.	CTR ENGINEERING	117
	A. Scyllac Engineering	117
	B. Component Development	119
	C. Engineering Analysis	120
	References	123
VIII.	FUSION TECHNOLOGY	125
	A. Introduction	125
	B. Reactor Design Studies	125
	C. Theta-Pinch Reactor Neutronic Studies	132
	D. Nuclear Data Program	140
	E. Electrical Insulator Research	141
	F. Alloy Research	148
	G. Environmental Studies	150
	H. Numerical Studies of RTPR Burn and Plasma Cooling Processes	154
	References	155
IX.	MAGNETIC ENERGY TRANSFER AND STORAGE (METS)	159
	A. Summary of METS Effort	159
	B. New METS Facility	159
	C. 300-kJ Energy Transfer Experiment	159
	D. Low Energy Tests and Transfer Experiments	161
	E. Switch Development	162
	F. Alternatives to Cryogenic Switches	162
	G. Parametric Analysis of Energy Transfer Systems	163
	H. Industrial Coil Development	163
	I. High Critical Current Test Facility	164
	J. Low-Loss Superconductor	164
	References	166

X.	DEVELOPMENT AND ENGINEERING OF THE SFX/FTR	167
A.	General Description of the SFX/FTR	167
B.	METS and EETS Development	168
C.	Transfer Capacitor Development	169
D.	SFX/FTR Staging Technology	169
E.	SFX/FTR Implosion Heating Technology	170
F.	Design of SFX/FTR Plasma Chamber	172
G.	SFX/FTR First-Wall Design and Fabrication	176
	References	177
	PUBLICATIONS	179

I. INTRODUCTION

(F. L. Ribe)

During this year most of the Scyllac activity has been concerned with conversion to the full torus. As part of this program the plasma behavior in an 8-meter toroidal sector ($R = 4.0$ m) was analyzed and compared with that in the 5-meter sector ($R = 2.4$ m). This stable period of toroidal equilibrium scales with sector length. This is indicative that the terminating $m = 1$ motion may be an end effect. However, other explanations, e.g., effects of axial pressure equilibration over the different $\ell = 0$ half-periods for $R = 2.4$ m and $R = 4.0$ m, are possible. Construction of the full torus was complete in March 1974, and plasma experiments began in April.

Some feedback experiments on the 8-m sector were performed. They showed a perturbation of the equilibrium fields by the $\ell = 0$ feedback coils. Eddy currents in the feedback coils reduce the periodic mirroring amplitude δ_0 and caused an upward shift of the $\ell = 0$ magnetic axis. Corrections will be made in the full-torus feedback system to eliminate this effect. Excitation of the feedback system on the 8-m sector was observed to correct the downward plasma motion induced by the shift of the magnetic axis.

The Scylla IV-3 system, before its being dismantled to make way for the staged θ -pinch, was used to make more careful measurements of the $m = 1$ instability driven by $\ell = 1$ and $\ell = 0$ fields and to observe its correction by externally driving $\ell = 0$ feedback coils. An important effect on the onset of the $m = 1$ instability was found to be displacement of the $\ell = 1$ or $\ell = 0$ magnetic axis from the center of the discharge tube, to which the plasma implodes.

An exciting new diagnostic development has been the successful application to Scyllac of side-on laser Thomson scattering through the quartz discharge-tube wall without benefit of the usual elaborate collimators and beam dumps. The major component is a new, highly rejective, 3-grating spectrometer which eliminates stray light. Side-on holography using a HF laser is also being developed. Considerable progress has been made toward fully automated computerized data taking and control of the Scyllac device.

The Scylla I-B experiment has produced good data on implosion dynamics, indicating satisfactory agreement with the elastic or bounce-model theory.

The important, new, staged θ -pinch experiment has reached the point of staging bank completion and initial operation of a 0.9-m section of shock heating on a 20-m-diameter discharge tube. Two new spark gaps must be developed to run the 4.5-m staged device. The first, a pulse-forming-network gap, has been developed and is being delivered. The second, a "staging" gap, which is a multi-arc-channel rail device, to isolate and then switch on the 800-kJ, 50-keV staging bank after the pulse-forming-network pulse, is still under development.

The 40-cm-diameter one-meter-long implosion heating θ -pinch experiment is driven at four feed slots by four 125-kV pulse-forming networks. Unlike previous, collisionless-shock experiments at low plasma density at other laboratories, the present device operates at $n = 10^{21}/\text{m}^3$ and has correspondingly lower impedance. This has involved much new high-voltage component development. The apparatus is now complete. The preionization method has been worked out and the first plasma experiments are beginning.

Considerable progress has been made on the ZT-1 toroidal-pinch experiment. Thomson scattering and doppler broadening measurements establish that the electron temperature is much lower than the ion temperature, and the non-Gaussian nature of the scattered light spectrum strongly suggests turbulence involving electron plasma waves. In order to study the conditions of reverse-field stability more carefully the discharge was derated from the "fuse" mode ($\dot{I} = 1.3 \times 10^{12}$ A/s, $I = 200$ kA, $T_e \simeq 25$ eV, $T_i \simeq 800$ eV) by inserting 0.5- Ω series resistors to give $\dot{I} = 0.4$ to 2×10^{11} A/s, $I = 80$ kA. Under these conditions T_e is about 4 eV and T_i is typically about 60 eV. Good correlation of plasma stability with B_z field reversal is observed, and stable times of ~ 10 μ s occur as long as the total flux does not reverse.

There are separate and well-defined programs in the CTR theory group on MHD-Vlasov macrostability theory of Scyllac, Z-pinch, and Tokamak configurations and also on plasma simulation of microinstabilities. In Scyllac theory the MHD calculations are proceeding toward more and more realistic stability estimates for diffuse profiles. The Vlasov-fluid theory has provided estimates of finite-Larmor-radius effects, which seem to account for the absence of modes with azimuthal numbers greater than unity -- as is observed experimentally. A simple model of $\ell = 1$ wall stabilization has been made. In Z-pinch theory, generalized estimates by Baker and Phillips show the important fact that poloidal field diffusion in the initial stages of high-beta Z-pinch and Tokamaks leads to

loss of confinement which must be alleviated by energy and particle loss to the wall. Two-dimensional computer simulation of θ -pinch implosion-sheath microinstabilities is being pursued, coupled with examination of the analytic theories of candidate microinstabilities for ad hoc transport coefficients in hybrid simulation codes, which suppress the electron-wave time scale. On a more general level, alternative means to particle simulation for solving the Vlasov equation are being explored.

In the experimental plasma physics research program the measurements on A-C resistivity and plasma heating have been extended to include nonlinear departures from Ohm's law below the density threshold of parametric instabilities and to measurements of electron energy distributions in the region of strong parametric instabilities.

On the engineering side the main achievement has been the conversion of Scyllac to its full-torus configuration (25-m circumference). The feedback stabilization system is still under test and construction. Component development for the staging and transfer-capacitor portion of the θ -pinch Fusion Test Reactor system is under way. Improved switching components for the ZT-1 toroidal pinch have also been developed.

A systematic group design effort for the θ -pinch Fusion Test Reactor has been initiated. Of primary importance is the careful design and definition of the shock-heating and staging waveforms and circuits to be compatible with the slowly rising (~ 1 -ms) compression field. The geometry and electrical decoupling of the (end-fed) shock-heating and compression coils has also been considered. The development of metal-ceramic discharge tubes to withstand plasma and radiation loads over times of tens of ms is being undertaken. The design group effort also includes tritium handling and estimates of D-T burn dynamics.

In the superconducting magnetic energy transfer and storage research area, the main achievement has been the bringing on line of the first 300-kJ storage coil which has shown stable operation above its rated value. Development contracts for 300-kJ storage coils capable of low-loss discharge in 1 ms have been initiated with three industrial firms. A systems cost study of the θ -pinch FTR with superconducting METS has been carried out. Vacuum-breakers as alternatives to the superconducting switch are being developed. A research contract has been let to the Westinghouse Corporation to determine the feasibility of various inertial energy-transfer schemes for the Reference Theta-Pinch Reactor.

In the fusion technology area, the main accomplishment has been completion of the joint ANL-LASL design of the Reference Theta-Pinch Reactor power plant. A report:

LA-5336/ANL-8019 has been issued. This involved close cooperation by the LASL neutron-transport-computational and nuclear cross-section groups. Materials research on insulators has been extensive, a major result being the demonstration of greatly enhanced dielectric strength of alumina under θ -pinch pulse conditions at elevated temperatures appropriate to reactors. In the area of pulsed metallurgy, cyclic stressing of molybdenum at 1150 K has shown that failure occurs by creep -- not fatigue, as might have been expected. In the important area of reactor plasma heat removal by a neutral-gas blanket, the previous calculations have been refined to take realistic account of finite mean-free-path transport in the neutral gas.

II. THETA-PINCH PROGRAM

A. SUMMARY OF θ -PINCH ACTIVITIES

(G. A. Sawyer)

Conversion of Scyllac to its full-torus configuration has been a major activity during 1973. The conversion is nearly completed and plasma experiments will begin in early 1974 (Sec. D). During conversion, the Scyllac radius was increased from 2.4 to 4.0 meters; interim experiments were performed in an 8-m sector at the new radius. These experiments showed an $m = 1$ sideways motion to the wall, as in the previous 5-m sector, but the onset time for the motion was later in the 8-m experiments, scaling from the 5-m experiments directly as the coil length. This result suggests that the $m = 1$ sideways motion is caused by end effects (Sec. B).

Feedback experiments on the 8-m sector demonstrated the performance of the system, and revealed the need for an improved design of the $\ell = 0$ feedback coils. Limited experiments with a closed feedback loop showed that the system responded correctly to unbalance signals but did not have sufficient power to overcome the strong sideways motion that prevailed in the toroidal sector (Sec. C).

A Staged Theta-Pinch program was started in FY-74. The initial implosion heating and subsequent adiabatic compression will be separated and operated from different power supplies. Construction of a 4.5-m-long linear-staged θ -pinch has been started (Sec. E).

A series of experiments on Scylla IV-3 studied the scaling of instability growth rates with $\ell = 0$ and $\ell = 1$ parameters. The scaling of experimental growth

rates agrees best with the sharp-boundary theory with old ordering (Sec. F).

The implosion phase of a conventional θ -pinch has been investigated in Scylla 1-B. Magnetic probing shows a 2-cm-thick current sheath imploding at a maximum velocity of $\sim 2 \times 10^7$ cm/sec. Holographic interferograms show some plasma traveling ahead of the sheath and also show flute structure on the trailing edge of the plasma (Sec. G).

Development of plasma diagnostics and computer systems has been continuing during the past year as an important activity in the θ -pinch group.

B. SCYLLAC 8-METER TOROIDAL SECTOR

EXPERIMENT (W. R. Ellis, C. R. Harder, R. Kristal, W. E. Quinn, G. A. Sawyer, and R. E. Siemon)

1. Introduction

The experiments on the 5-m toroidal sector^{1,2} were terminated at the end of 1972 to allow the conversion to the full torus to begin. Experiments on the 5-m sector, feedback stabilization experiments on the Scylla IV-3 device, and studies of the effects of the major radius of curvature on the plasma equilibrium and stability and the feedback stabilization requirements suggested an increase in the Scyllac major radius from 2.4 to 4.0 m (cf. Sec. D). The initial conversion work concentrated on the sector to increase its major radius of curvature. The conversion of the 5-m, 120° sector to the 8-m long 4.0-m radius was completed in May and plasma experiments began on the larger 8-m sector in June, while the conversion work continued on the remainder of the torus. The objective of these experiments was to

study the plasma equilibrium and stability in the larger radius of curvature as well as the scaling of the toroidal experiment from the 2.4-m to the 4.0-m radius.

The plasma experiments in the previous 5-m sector demonstrated the existence of high- β , $\ell = 1,0$ toroidal equilibrium. The plasma remained in a helical toroidal equilibrium for 4 to 7 μsec , followed by an $m = 1$ sideward motion of the plasma column, which was nearly the same all along the sector. The $m = 1$ motions, which occurred predominantly in the horizontal plane of the torus, suggest either an imbalance between the equilibrium $F_{1,0}$ and toroidal forces at later times due to end effects or the occurrence of the long wavelength $m = 1$ instability possibly triggered by the same effects. It has not been possible to discriminate between these phenomena. Measurements of the plasma parameters and the applied magnetic fields show that the product of the $\ell = 1$ and $\ell = 0$ fields for plasma equilibrium agree with sharp-boundary MHD theory. In these experiments, with the 5-m sector operating at one-half the capacity of the energy storage bank, the plasma had an ion temperature of ~ 1 keV, an electron temperature of ~ 350 eV, a peak plasma density of $\sim 2 \times 10^{16}$ cm^{-3} , and a plasma β on axis of ~ 0.8 .

During the past year plasma experiments were performed on the $\ell = 1,0$ helical equilibria and stability in the larger 8-m toroidal sector. These initial experiments were completed in August. A feedback stabilization system was installed on the sector during August and September. Plasma experiments with the feedback system began in late September and were terminated in November to allow the conversion to the full torus to be completed.

2. Summary of $\ell = 1,0$, Sharp-Boundary, Toroidal Equilibrium Theory

When a straight theta pinch is bent into a torus the combination of plasma pressure and the gradient of the toroidal compression field B_0 forces the plasma

toward the outside of the torus. In the Scyllac sector, with a major radius R and plasma radius a , the toroidal drift force,

$$F_R = \beta B_0^2 a^2 / 4R, \quad (1)$$

is compensated by a combination of $\ell = 1$ helical and $\ell = 0$ bumpy fields. (β is the ratio of plasma pressure to the external magnetic field pressure.) The superposition of the $\ell = 1$ and $\ell = 0$ equilibrium fields^{3,4,5} on the main toroidal field B_0 produces first-order plasma distortions about the plasma radius of the form

$$r = a [1 + \delta_1 \cos(\theta - hz) + \delta_0 \cos hz], \quad (2)$$

where $h = 2\pi/\lambda$ is the $\ell = 1,0$ wave number, z is the toroidal coordinate, and θ is the azimuthal polar coordinate. The plasma column distortions, δ_1 and δ_0 , are related to the applied fields by

$$\delta_1 = \frac{B_{\ell=1}/B_0}{\epsilon^2 I_1'(\epsilon) K_1(\epsilon) [1 - (1-\beta) I_1(\epsilon) K_1'(\epsilon) / I_1'(\epsilon) K_1(\epsilon)]} \quad (3)$$

$$= \frac{1}{\epsilon(1-\beta/2)} \frac{B_{\ell=1}}{B_0}, \quad (\epsilon = ha \ll 1) \quad (4)$$

and

$$\delta_0 = \frac{I_0(\epsilon) K_0'(\epsilon) [1 - I_0'(\epsilon) K_0(\epsilon) / I_0(\epsilon) K_0'(\epsilon)]}{\epsilon K_0(\epsilon) [1 - (1-\beta) I_0(\epsilon) K_0'(\epsilon) / I_0'(\epsilon) K_0(\epsilon)]} \frac{B_{\ell=0}}{B_0} \quad (5)$$

$$= \frac{1}{2(1-\beta)} \frac{B_{\ell=0}}{B_0}, \quad (\epsilon = ha \ll 1) \quad (6)$$

The I_ℓ and K_ℓ are the modified Bessel functions and $\epsilon = ha$ is the product of the $\ell = 1,0$ wave number and the plasma radius.

The $\ell = 0$ bumpy fields produce the asymmetry in the sum of the plasma excursions δ_1 and δ_0 , which is needed to produce

the equilibrating force

$$F_{1,0} = h^2 a^3 \beta B_0^2 [1 + (1-\beta) I_0(\epsilon) / I_1'(\epsilon)] \frac{\delta_1 \delta_0}{4} \quad (7)$$

$$= \beta(3-2\beta) B_0^2 h^2 a^3 \delta_1 \delta_0 / 8, \quad (ha \ll 1). \quad (8)$$

Equating the outward toroidal force to the $F_{1,0}$ force gives the equilibrium condition

$$\delta_1 \delta_0 = 2/h^2 a R [1 + (1-\beta) I_0(\epsilon) / I_1'(\epsilon)] \quad (9)$$

$$= 2/(3-2\beta) h^2 a R, \quad (ha \ll 1). \quad (10)$$

It should be noted that the singular behavior in the approximate relations, Eqs. (6) and (8), as β approaches unity does not occur in the exact expressions. With $B_{\ell=1}$ and $B_{\ell=0}$ fields of equal magnitudes, Eqs. (4) and (6) show that δ_1 is appreciably larger than δ_0 for β values which are not too close to unity. Typical values for the Scyllac experiment are: $B_{\ell=0}/B_0 = B_{\ell=1}/B_0 \approx 0.07$; $\epsilon \sim 0.2$; $\delta_1 \sim 0.9$; $\delta_0 \sim 0.1$; and $\beta \sim 0.8$. Figure II-1 shows graphs of the $F_{1,0}/F_R$ force ratio, from Eqs. (7) and (1), as a function of the plasma β .

The choice of the $\ell = 1,0$ equilibrium for Scyllac was the result of both theoretical and experimental studies. Experiments with high- β , high-temperature θ -pinches have shown that, in general, only long wavelength ($k \gg 0$) $m = 1$ modes are observed experimentally. Based on this empirical result, the $m = 1$ stability of high- β helical systems was investigated using sharp-boundary MHD theory.^{5,6,7} The theoretical

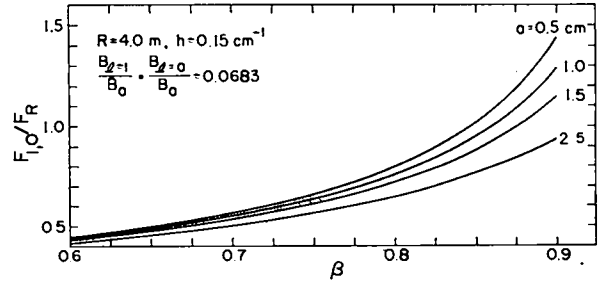


Figure II-1

Ratio of the $F_{1,0}$ equilibrium force to the outward toroidal force as a function of β for the indicated plasma radii a .

results showed that to leading order in ϵ , the $\ell = 1$ configuration is stable. Further theoretical studies⁸ with diffuse profiles indicate that the vanishing of the leading order destabilizing term for $\ell = 1$ is not just characteristic of sharp-boundary profiles, but occurs for a wide class of profiles satisfying the very weak condition, $\frac{1}{B(r)} \frac{dB(r)}{dr} > 0$, where $B(r)$ is the main θ -pinch field.

When the higher order terms in the $m = 1$ dispersion relation are calculated and the harmonic content of the $\ell = 1$ fields optimized, the dispersion relation for the $m = 1$ mode is given by^{4,9,10}

$$\gamma_1^2 \approx h^2 v_A^2 \left[-\beta^2 \left(\frac{a}{b}\right)^4 + \frac{(4-3\beta)(2-\beta)}{8(1-\beta)} \epsilon^2 \right] \delta_1^2, \quad (11)$$

where a/b is the ratio of plasma to wall radius and v_A is the Alfvén velocity. The first term in Eq. (11) is a wall stabilization term which is negligible in conventional θ -pinches as a result of the small a/b values, but which could be made to dominate with increased implosion heating such as in a staged θ -pinch.¹¹ The second term in Eq. (11) is a weak destabilizing term arising from unfavorable curvature of

the $\ell = 1$ field. The apparent singularity as β approaches unity is a result of the approximations used, $\delta_1 \ll \epsilon < 1$.

Weitzner¹⁰ has devised a new expansion with $\epsilon \ll \delta_1 \lesssim 1$, which gives an $m = 1$ growth rate,

$$\gamma_1^2 = h^2 \frac{v^2}{A} \left[-\beta^2 \left(\frac{a}{b}\right)^4 + \frac{\beta^5}{32(2-\beta)} \delta_1^2 \right] \delta_1^2. \quad (12)$$

For the Scyllac parameters the destabilizing term of Eq. (12) is approximately one-fourth that of Eq. (11). Weitzner¹⁰ has also extended the analysis with the new ordering to the more general case of slightly elliptical plasma cross section. This analysis shows that the plasma can be $m = 1$ stable by conducting walls located at any finite location.

3. Experimental Arrangement of 8-m Sector

a. Sector Parameters. The 8-m sector, which will comprise one-third of the Scyllac torus, had a larger major radius of 4.0 m and a coil arc length of 8.4 m. The compression coil, whose inner surface was shaped to generate the $\ell = 1,0$ equilibrium fields, had a mean bore of 16.0 cm to accommodate feedback coils. The inside diameter of the quartz discharge tube was 8.8 cm. The 8.4-m coil was driven by a 3.5-MJ capacitor bank of 1,050 1.85- μ F, 60-kV capacitors. The experiments were performed with the bank charged to 40 and 45 kV to produce peak magnetic compression fields of 40 and 45 kG with risetimes of ~ 4.1 μ sec. A 50-kV, 9-kJ θ -preionization bank, which produced a 400-kHz oscillating field, was used to preionize the initial deuterium gas fillings of 10 to 20 mTorr.

b. $\ell = 1,0$ Shaped Compression Coil.

The product of the helical $\ell = 1$ and bumpy $\ell = 0$ fields designed into the shaped toroidal coils was determined through the sharp-boundary equilibrium relations, Eqs. (3), (5), and (9), to give

$$\frac{B_{\ell=1} B_{\ell=0}}{B_0^2} = -\frac{2ha^2}{R} \frac{I_1'(\epsilon) K_0(\epsilon)}{I_0(\epsilon)} \times \frac{[1 - (1-\beta) I_1(\epsilon) K_1'(\epsilon)/I_1'(\epsilon) K_1(\epsilon)]}{[1 + (1-\beta) I_0(\epsilon)/I_1'(\epsilon)]}. \quad (13)$$

A graph of the equilibrium field-product, for β in the range of 0.6 to 0.9, is given in Figure II-2 for plasma radii in the range of 0.6 to 1.0 cm. The equilibrium field product is nearly a linear function of β in this range and is not a sensitive function of the plasma radius. Equal magnitudes of $B_{\ell=1}$ and $B_{\ell=0}$ were chosen ($B_{\ell=1}/B_0 = B_{\ell=0}/B_0 = 0.0683$); this produces a bumpiness δ_0 of the plasma column, which is small compared with the helical displacements δ_1 .

The designs of the shaped coils were determined by calculating the shape of the magnetic flux surfaces for the required vacuum fields from

$$\bar{B}/B_0 = \hat{e}_z (1 - \frac{r}{R} \cos \theta) + \nabla \phi, \quad (14)$$

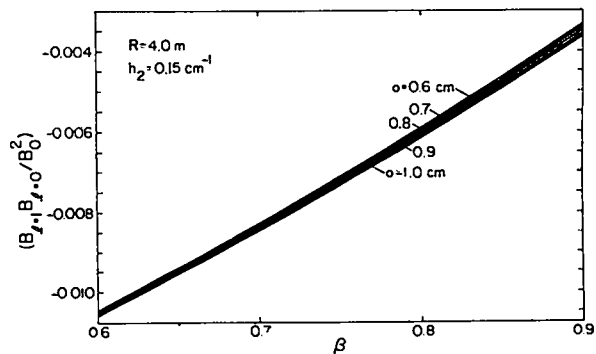


Figure II-2

Values of the equilibrium field product, $B_{\ell=1} B_{\ell=0} / B_0^2$, predicted by sharp-boundary theory for equilibrium in the 8-m toroidal sector.

where

$$\begin{aligned} \phi = & (B_{\ell=1}/B_0) [2 I_1(\text{hr})/h] \sin(\theta - hz) \\ & + (B_{\ell=0}/B_0) [I_0(\text{hr})/h] \sin hz \\ & + (B_V/B_0) r \sin \theta \\ & + B_{1,2}/B_0 [I_1(2\text{hr})/h] \sin(\theta - 2hz). \end{aligned} \quad (15)$$

The small vertical field B_V and $B_{1,2}$ field are required for equilibrium according to the sharp-boundary theory.¹² The amplitude of these fields is given by

$$\frac{B_V}{B_0} = \frac{B_{1,2}}{B_0} = \frac{B_{\ell=1} B_{\ell=0}}{4B_0^2}. \quad (16)$$

The $B_{1,2}$ field varies in space as $\sin(\theta - 2hz)$, and produces a small ellipticity in the plasma cross section, in contrast to the $\ell = 1$ field which varies as $\sin(\theta - hz)$.

Each wavelength, $\lambda_{1,0} = 41.9$ cm (cf. Sec. D), of the 8-m sector was divided into 330 steps, with 1.25 mm/step, and flux surfaces calculated for each step. Figure II-3 shows plots of the flux surfaces at 4 z positions: $hz = 0$, center of a land region; $hz = \pi/2$, between a land and groove region; $hz = \pi$, center of a groove region; and $hz = 3\pi/2$, between a groove and land region. The annular cross-hatched areas of Figure II-3 represent the region between the ID of the discharge tube and the OD of the $\ell = 0$ feedback stabilization coils. The flux surfaces with the dashed lines were computed with $B_V/B_0 = 0.001166$, which is the prescribed theoretical value [Eq. (16)]. We note that the outer flux surface has an elliptical shape. A vertical field amplitude of $B_V/B_0 = 0.00168$, 44% larger than the theoretical value, was used to give flux surfaces (solid lines, Figure II-3) at the coil wall which have circular cross sections for simplicity of machining. This larger value of vertical field shifts the

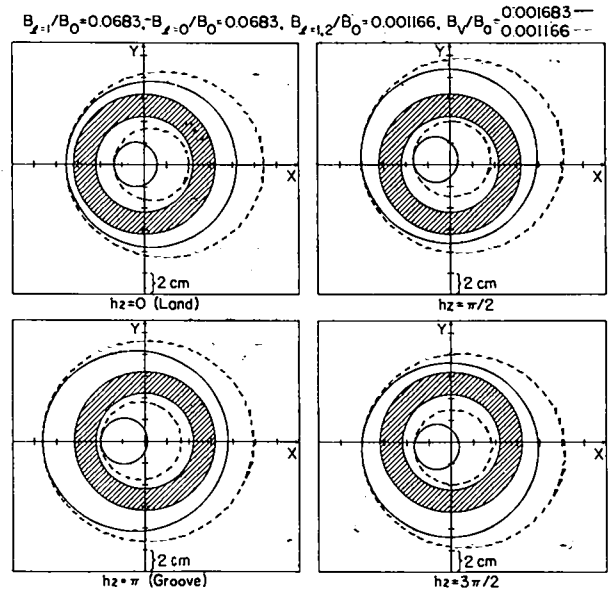


Figure II-3

Magnetic flux surfaces at four z locations, with the theoretical value of the vertical field ($B_V/B_0 = 0.001166$, dashed lines), and the actual value used ($B_V/B_0 = 0.001683$, solid lines). The cross-hatched area contains the discharge tube and $\ell = 0$ feedback coils. The radial plane where B_z is maximum on axis due to the $\ell = 0$ field is referred to as the land ($hz=0$), and where B_z is minimum on axis as a groove ($hz=\pi$).

inner flux surfaces inward in the horizontal plane and decreases their area. With this design the vacuum flux surfaces can be centered in the discharge tube by the addition of a vertical field from driven windings.

c. Discharge Tube. The quartz discharge tubes were purchased in 45° toroidal sections because of shipping problems and compatibility of the toroidal bending fixture with the requirements of the full torus. Three 45° sections were aligned in a plane and to the sector major radius of 4.0 m. The sections were fused together into a single tube with an arc length of 9.4 m. The tube had an inside diameter of 88 mm with a 3-mm wall thickness.



Figure II-4
Photograph of the 8-m toroidal sector device.

d. Comparison of 8- and 5-m Sector Parameters. The parameters of the 8- and 5-meter toroidal sectors are compared in Table II-1. Figure II-4 is a photograph of the front end of the 8-m sector with the compression coil and discharge tube installed. The feedback modules are shown

in the upper portion of the photo above the compression coil.

e. Plasma Diagnostic Apparatus. The following measurements were made of the plasma properties: (1) three high-speed streak cameras, viewing the plasma column side-on, were used to record the transverse,

TABLE II-1

SCYLLAC TOROIDAL SECTOR PARAMETERS

Parameter	5-m Sector (Half Bank)	8-m Sector (Full Bank)
R (m)	2.375	4.0
Coil Length (m)	5.0	8.38
Coil Bore (cm)	14-20	16.0
C (μ F)	971	1,942
Bank transfer efficiency	0.71-0.80	0.86
$\tau/4$ (μ sec)	3.6 - 4.3	4.1
V_{Bank} (kV)	50	50
B_0 (kG)	48 - 36	50
E_0 (V/cm)	510 - 280	470
h (cm^{-1})	0.19	0.15
$\lambda_{1,0}$ (cm)	33.15	41.89
No. of λ 's in sector	15	20
$B_{\ell=1}/B_0$		0.0683
$B_{\ell=0}/B_0$		0.0683
B_V/B_0		0.00168
$B_{1,2}/B_0$		0.001166

motions of the plasma column; (2) a coupled-cavity He-Ne laser interferometer was used to measure the time history of plasma electron density integrated along a chord of the plasma cross section; (3) a magnetic loop and probe arrangement was used to measure the magnetic flux excluded by the plasma. Combined with density profiles from the luminosity, the excluded flux can be expressed in terms of the plasma β ; (4) a ten-channel, side-on luminosity experiment was used to obtain the intensity profiles of the plasma column. These luminosity profiles, in conjunction with the coupled-cavity interferometer data, give absolute density profiles; (5) scintillation and silver-foil activation counters were used to measure the neutron emission; and (6) Thomson scattering was used to determine the plasma electron temperature with a unique three-grating polychrometer.

4. Plasma Equilibrium and Stability

In the experiments on the 8-m sector with fixed $\ell = 1$ and $\ell = 0$ fields generated by the $\ell = 1,0$ shaped inner surface of the compression coil, the plasma equilibrium was achieved by adjusting the initial deuterium filling pressure to give a balance between the $F_{1,0}$ and toroidal forces

through their β dependence (cf. Figure II-1). With the bank operating at 40 kV, $B_0 = 40$ kG, the plasma equilibrium was achieved with a deuterium filling pressure of 16-19 mTorr compared with a pressure of 19-21 mTorr at a bank voltage of 45 kV ($B_0 = 45$ kG). The ratio $F_{1,0}/F_R$ decreases with increasing pressure in the range of 8 to 45 mTorr. Since the ratio increases with β this implies that β is decreasing with pressure in this range. The equilibrium pressure value of 16 to 21 mTorr is higher than the preferred operating pressure of 10 to 15 mTorr. This means that the magnitudes of the $\ell = 1$ and $\ell = 0$ fields generated by the shaped coil are slightly too large.

a. Transverse Plasma Motions. The streak photographs of Figure II-5 show typical transverse plasma motions observed in the 8-m sector. Figure II-5A shows the plasma column in the helical equilibrium position until approximately 6 μ sec when it moves slightly inward in the horizontal plane in both land and groove regions followed by a reversal at 8.5 μ sec with an outward motion that terminates the confinement at 12 μ sec. The motion in the vertical plane, which is inverted in the photograph, is shown in the center frame. The vertical field windings shadow a portion of this view at the top and bottom.

Figure II-5B shows no motion in the vertical plane, but an outward motion at later times in the horizontal plane of the torus in both land and groove regions.

Figure II-5C shows a slow downward motion in the vertical plane with an outward motion occurring at later times in the horizontal plane. In the experiments with driven $\ell = 1$ windings,¹ a small change in the magnitude of the $\ell = 1$ fields moved the plasma from its equilibrium position. Likewise, in the shaped coil with fixed $\ell = 1,0$ field ratios, a few percent change in the deuterium filling pressure, with a corresponding change in plasma β , produced the same results.

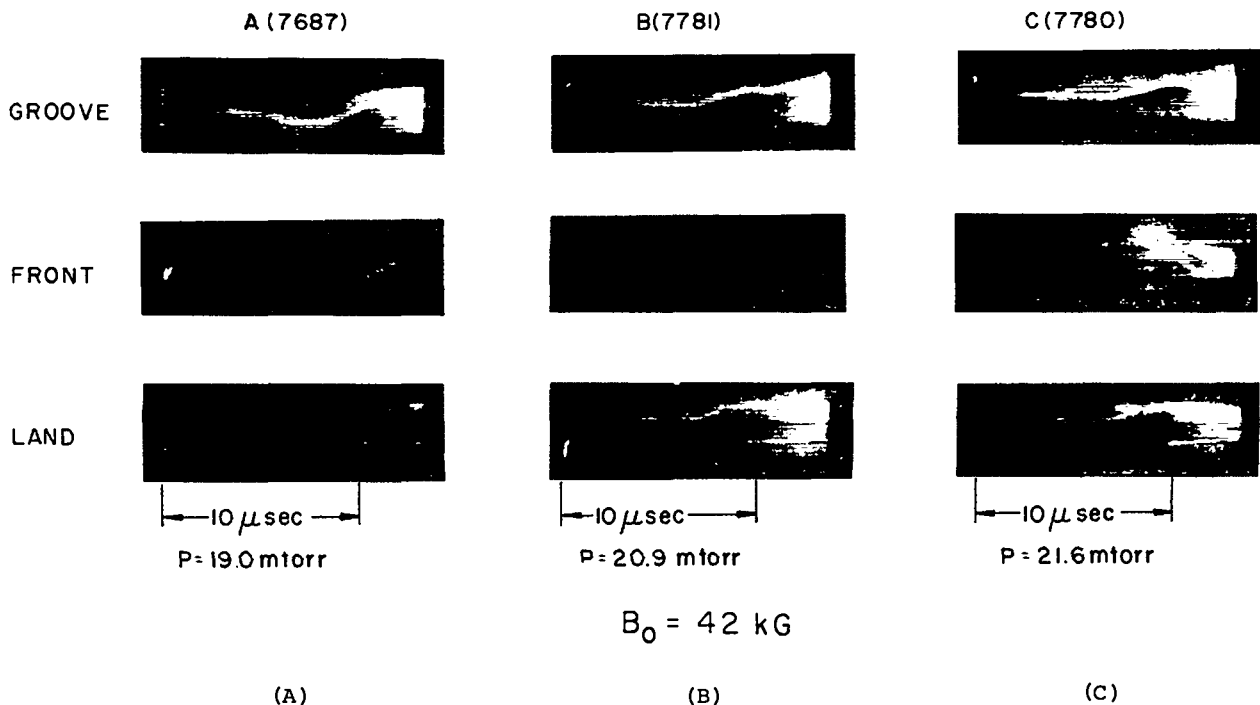


Figure II-5
Streak photographs showing the transverse plasma motions in the horizontal plane of adjacent land and groove regions and in the vertical plane midway between these regions.

The observed transverse motions of the plasma at various positions around the sector show the following: (1) the plasma column takes up an initial helical shift and comes into an equilibrium position which lasts 7 to 10 μsec in contrast to a complete absence of equilibrium without $\ell = 1, 0$ fields; and (2) as the plasma moves away from the equilibrium position, the motion in the land and groove regions is similar around the sector, i.e., a long wavelength $m = 1$ motion.

The streak photographs of Figure II-6 compare the plasma transverse motions in the 5- and 8-m sectors having shaped compression coils. The general characteristics of the plasma motions are similar except that in the 8-m sector the confinement is increased. The transverse motions are also similar to those observed with the $\ell = 1$ driven windings, except that the

long wavelength $m = 1$ motion tends occasionally to occur in planes other than that of the torus.

Vertical magnetic fields of 25 to 100 G were applied by two pairs of toroidal windings to the discharge tube region. These fields were superimposed in opposition to the vertical field generated by the shaped compression coil to produce the theoretical value of the vertical field (cf. Table II-1). However, this additional vertical field did not have an observable effect on the plasma column. This result is similar to that observed previously in the 5-m sector experiments.¹

b. Scaling of the $m = 1$ Onset Times.
The examination of many streak photographs shows that the plasma column remains in stable equilibrium for 7 to 10 μsec in the 8-m sector, compared with 4 to 7 μsec in the 5-m experiment, at which times the

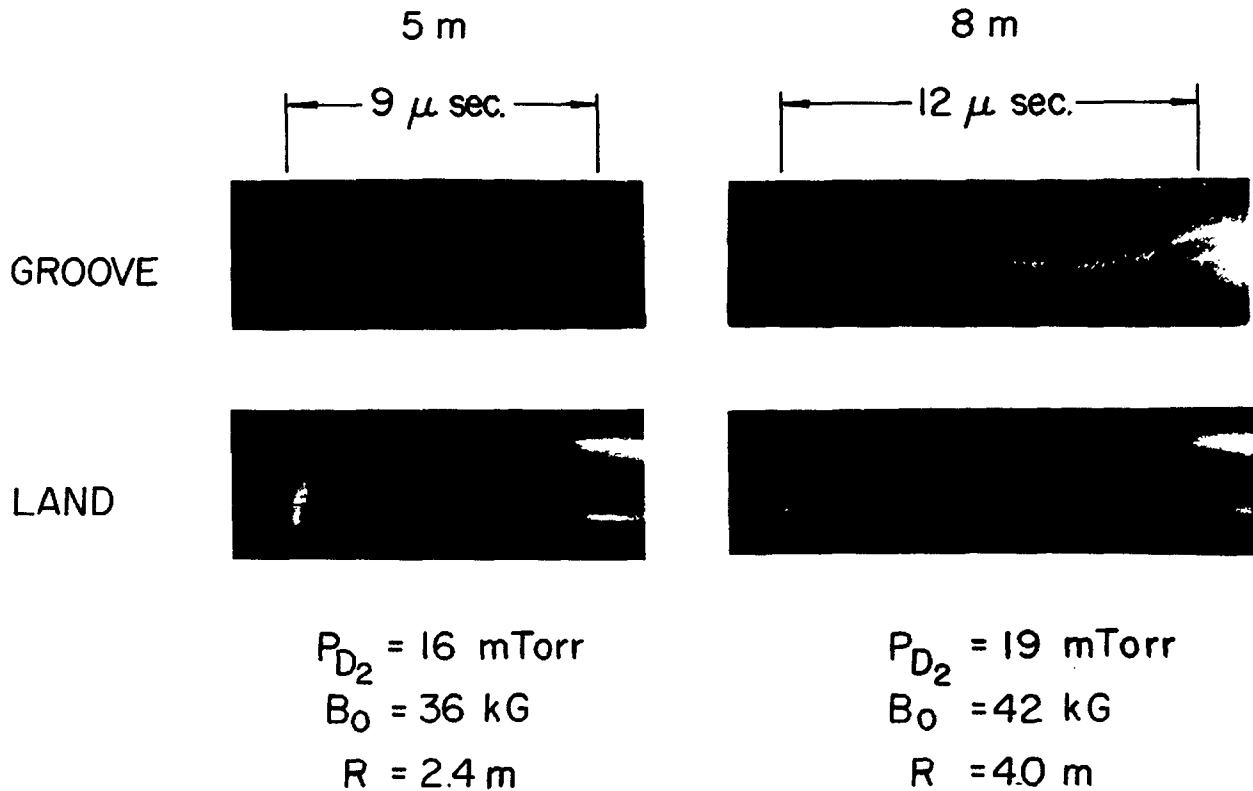


Figure II-6
Streak photographs comparing plasma behavior
in the 5-m and 8-m toroidal sector experiments.

onset of the terminating $m = 1$ sideward motion occurs. The ratio of the onset times,

$$\frac{\tau_{os}(8-m)}{\tau_{os}(5-m)} = \frac{7 \text{ to } 10 \text{ } \mu\text{sec}}{4 \text{ to } 7 \text{ } \mu\text{sec}} = 1.5, \quad (17)$$

can be compared with the Alfvén times,

$$\frac{\tau_A(8-m)}{\tau_A(5-m)} = \frac{11.8 \text{ } \mu\text{sec}}{7.1 \text{ } \mu\text{sec}} = 1.7, \quad (18)$$

and with the scaled plasma end-loss times,

$$\frac{\tau_p(8-m)}{\tau_p(5-m)} = \frac{26.9 \text{ } \mu\text{sec}}{16.8 \text{ } \mu\text{sec}} = 1.6 \quad (19)$$

Thus, the onset-time scaling is in agreement with the assumption that it is produced by end-effects. The plasma is

apparently stable until end-effects propagate to the center of the sector.

Assuming that the motion which terminates the stable period is the instability predicted by theory, its measured growth rates are $\gamma_1(5-m) \approx 1.1 \text{ MHz}$ and $\gamma_1(8-m) \approx 0.6 \text{ MHz}$. The growth rates calculated from

$$\begin{aligned} \gamma_1^2 &= \frac{\beta(4-3\beta)(2-\beta)}{8(1-\beta)} v_A^2 h^4 a^2 \delta_1^2 \\ &= \frac{\beta(4-3\beta)}{2(1-\beta)(2-\beta)} v_A^2 h^2 \left(\frac{B_{\ell=1}}{B_0}\right)^2 \end{aligned} \quad (20)$$

are 1.0 MHz and 0.6 MHz for the 5- and 8-m experiments, respectively. Thus the terminating growth rates are in good agreement with theory and scale between the 5- and 8-m experiments according to the theory.

c. Scaling of the $\ell = 1,0$ Equilibrium Fields. The product of the $\ell = 1$ and $\ell = 0$ fields designed into the 8-m sector coils was scaled by sharp-boundary theory from the previous 5-m experiments through the equilibrium relations, Eqs. (9), (3), and (5) by

$$\left(\frac{B_{\ell=1} B_{\ell=0}}{B_0^2} \right)_{8m} = \frac{f_{8m}[\beta, I_i(\text{ha}), K_j(\text{ha})]}{f_{5m}[\beta, I_i(\text{ha}), K_j(\text{ha})]} \times \left[\frac{h_{8m} a_{8m}^2 R_{5m}}{h_{5m} a_{5m}^2 R_{8m}} \right] \times \left(\frac{B_{\ell=1} B_{\ell=0}}{B_0^2} \right)_{5m} \quad (21)$$

Graphs of this relationship are shown in Figure II-7, where the curves represent the 8-m equilibrium-field-product ratio scaled theoretically from its value at 5 meters. The equilibrium-field-product ratio used in the 8-m experiment is shown by the horizontal dashed line; and the solid point gives the averaged observed β value (cf. Sec. B5a below) with an indication of the upper limit of β by the circle. The average value of the plasma radius is 0.9

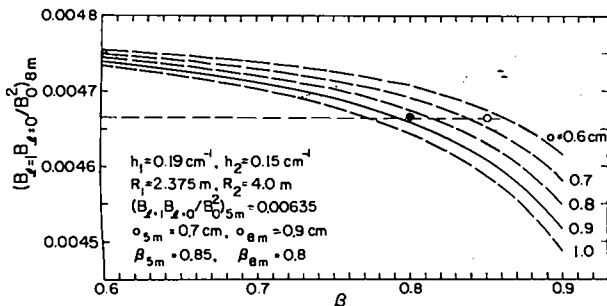


Figure II-7

Values of the equilibrium field product ($B_{\ell=1} B_{\ell=0} / B_0^2$) predicted for plasma equilibrium in the 8-m toroidal sector, scaled from the 5-m sector equilibrium. The measured 8-m ratio is shown by the horizontal dashed line, and the two points give the limits of the measured values of β .

cm (cf. Sec. B5a below) represented by the solid curve. Thus the scaling of the equilibrium field product is confirmed by experiment.

5. Measurements of Plasma Parameters

a. 8-m Sector Results. Measurements have been made of the plasma radius as a function of time, determined by luminosity profiles, and plasma diamagnetism as a function of time, determined by the balanced probe method. These measurements have been made in positions of minimum and maximum plasma radius [land (L) and groove (G), respectively] in order to study the approach of the plasma column to theoretically predicted axial and radial force equilibrium (see Sec. B6).

b. Comparison of 8-m and 5-m Sectors.

The differences between the 8-m data (Experiment K) and 5-m data (Experiment J) are indicated in Figures II-8 and II-9, which show plots of the plasma radius a , excluded flux $\Delta\phi$, and beta on axis β_A vs time for these two experiments in the land and groove locations (45 kV in both experiments). Each curve represents an average of 4 or more nominally identical shots, and the error bars represent rms (standard) deviations from the average value.

These figures illustrate some important differences between the 5-m and 8-m data. These differences are most pronounced for the groove location, Figure II-9. The plasma radius in a groove is $\sim 50\%$ larger in the 8-m experiment after peak field and confinement of the plasma column is $\sim 50\%$ longer. The final value of β is near unity in both experiments, but with larger variations in the 8-m case. The low starting value of beta in each case is thought to be associated with the presence of $\ell = 1$ fields during the implosion phase. Similar behavior has been observed in the 3-m linear Scylla IV-3 experiment, during growth rate studies employing an $\ell = 1$ grooved coil (see Sec. F). The pronounced oscillations in radius and beta which occurred in the 5-m

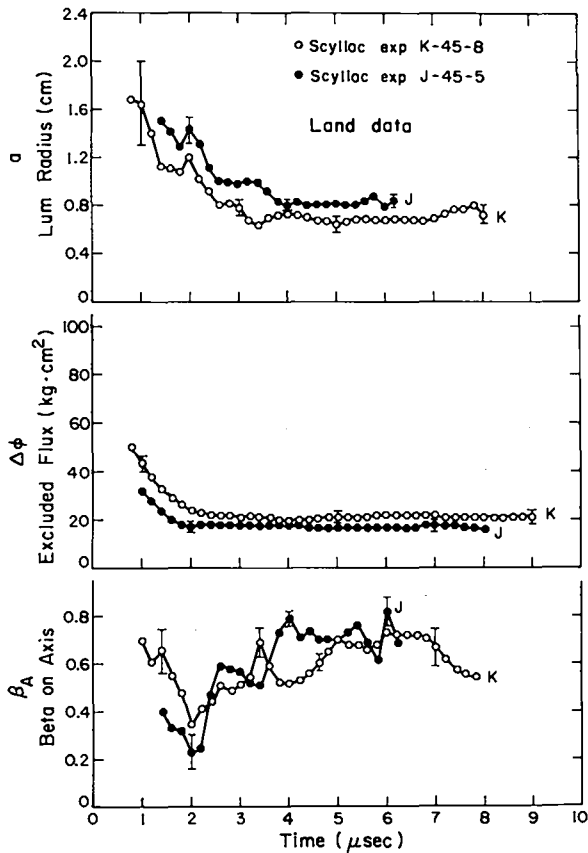


Figure II-8

Comparison of the observed time variations of plasma radius, excluded flux, and computed β on axis in a land region in the 5-m (J) and 8-m (K) sector experiments.

experiments are nearly absent in the 8-m case. The excluded flux in a groove is much larger in the 8-m case, as it should be for the observed larger radius and same β . The time behavior is different in the two cases, there being a clear tendency in the 8-m case for the excluded flux to level out in time. In the 5-m experiments, $\Delta\phi$ was a monotonically decreasing function of time in the grooves, without exception.

In the land location, Figure II-8, the data in the two experiments are more similar than in the groove location, but some differences are still worth noting. In particular, the plasma radius is smaller and the excluded flux larger in the 8-m

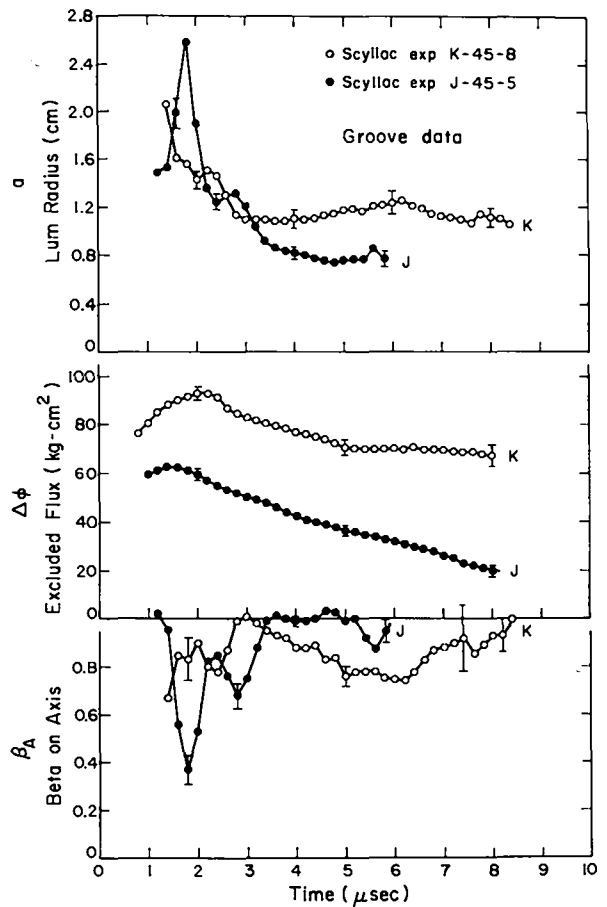


Figure II-9

Comparison of the observed time variations of plasma radius, excluded flux, and computed β on axis in a groove region in the 5-m (J) and 8-m (K) sector experiments.

experiment, while the computed β remains about the same. This can only be possible if the B field is larger in the 8-m experiment, as is, in fact, the case. In the 5-m experiment, we measured $(B_L)_{\max} = 36.0$ kG at $4.6 \mu\text{s}$. In the 8-m experiment, $(B_L)_{\max} = 46.0$ kG at $4.0 \mu\text{s}$, an increase of about 28%. The corresponding groove data were: $(B_G)_{\max} = 30.0$ kG (5 m) and $(B_G)_{\max} = 38.8$ kG (8 m) (peak fields reached at the same time as in a land).

c. Scyllac Density Measurement. Measurements have been made of electron density in a groove region using a new modified coupled-cavity interferometer: Typical results are shown in Figure II-10.

SHOT 7696



a- GROOVE STREAK PHOTOS



b- INTEGRATED DENSITY, THREE WAVELENGTHS AWAY

Figure II-10

Integrated plasma electron density along a chord from the laser coupled-cavity in a groove region taken simultaneously with a streak photograph in a nearby groove region.

The laser beam was positioned 2 mm forward of the coil center. However, its position with respect to the plasma column is known only at one or two times in a discharge: shortly after implosion or during a swing through the beam due to drift or instability. Density is therefore obtained only at these times using radii derived from luminance measurements. In the optimum pressure range (18-20 mTorr) the average density at early times ($< 7 \mu\text{sec}$) is about $3.4 \times 10^{16} \text{ cm}^{-3}$.

d. Electron Temperature. The electron temperature was measured by Thomson scattering using a special polychromator to reject stray light (cf. Sec. H3). A 10-Joule, 30-ns Q-switched ruby laser beam passed side-on through the 88-mm-diameter quartz discharge tube. Although focussed at the center of the tube, the beam was expanded at the wall to cover an elliptical area $10 \times 20 \text{ mm}$. Thus the energy density on the wall (about 0.02 J/mm^2) was held below the level found to cause spalling on similar quartz tubes (about 0.1 J/mm^2).

Data were taken in the 8-m sector (main bank voltage 45 kV and filling pressure $\sim 20 \text{ mTorr}$). Signals of typically 0.5 volts from seven channels were recorded with oscilloscopes. The plasma luminosity was comparable in intensity to the scattered

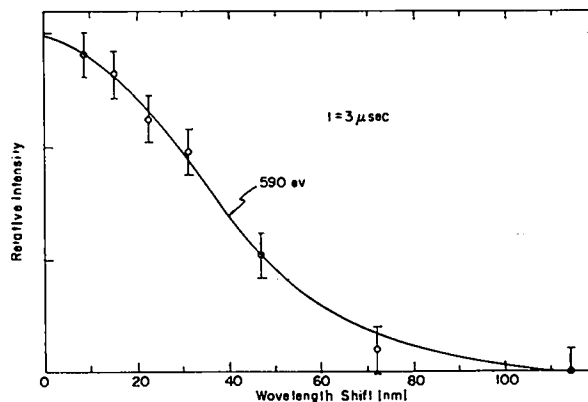


Figure II-11

Relative intensity of the Thomson scattered laser light from the sector plasma (experimental points) compared with the theoretical curve (solid line) for $T_e = 590 \text{ eV}$

signal and fluctuations in the luminosity were the limiting noise source in the experiment. Typical data are shown in Figure II-11. Each point represents the scattered intensity for a channel centered on the indicated wavelength. The spectral width of each channel was made progressively wider as the separation from the incident wavelength increased. The indicated curve for $T_e = 590 \text{ eV}$ represents a least-squares fit of a theoretical curve which 1) assumes the spectrum is Gaussian and 2) accounts for the varying spectral widths of the detector channels. The theoretical curve does not include relativistic effects, which are nonnegligible at these temperatures according to Gondhalekar and Kronast.¹³ Corrections for this effect are being made and may drop the temperature to about $T_e = 500 \text{ eV}$.

6. Time-Dependent Scyllac Equilibrium

a. Toroidal Equilibrium. As shown in Figure II-1, for each value of the plasma radius a , there is a corresponding value of β predicted by MHD theory for toroidal equilibrium. The sharp-boundary equivalent radius for the bumpy plasma in Scyllac is taken to be the average of the radii measured in lands and grooves, viz:

$$a_{SB} = \frac{a_L + a_G}{2} \quad (22)$$

With this assumption, the experimental radius values shown in Figures II-8 and II-9 have been used to compute a theoretical sharp-boundary equivalent beta,

$$\beta_{SB} = \frac{\beta_L + \beta_G}{2} \quad (23)$$

which can be split into its land and groove components using the axial pressure equilibrium condition

$$\frac{\beta_L}{\beta_G} = \left(\frac{B_G}{B_L} \right)^2 = \left(\frac{1 - \frac{B_{\ell=0}}{B_0}}{1 + \frac{B_{\ell=0}}{B_0}} \right)^2 \quad (24)$$

where $B_G = B_0 - B_{\ell=0}$ and $B_L = B_0 + B_{\ell=0}$. The results, expressed in terms of the applied field ratio, are

$$\beta_L = \beta_{SB} \left[\frac{\left(1 - \frac{B_{\ell=0}}{B_0} \right)^2}{1 + \left(\frac{B_{\ell=0}}{B_0} \right)^2} \right] \quad (25)$$

and

$$\beta_G = \beta_{SB} \left[\frac{\left(1 + \frac{B_{\ell=0}}{B_0} \right)^2}{1 + \left(\frac{B_{\ell=0}}{B_0} \right)^2} \right] \quad (26)$$

for the theoretical land and groove equilibrium beta values.

Figure II-12 shows the time behavior of the experimental and theoretically predicted beta values in land and groove positions for both the 5-m sector (J) and the 8-m sector (K) experiments. In both of these experiments doubly grooved coils were used, with applied field ratios of $B_{\ell=1}/B_0 = B_{\ell=0}/B_0 = 0.080$ (J) and $B_{\ell=1}/B_0 = B_{\ell=0}/B_0 = 0.068$ (K), respectively.

The agreement between theory and experiment is good after an initial time delay of 4-6 μ sec, corresponding to the period required for the plasma to come into axial pressure equilibrium (see below). The explanation for an increasing $\beta(t)$ is not known at this time, but may be related to dissipative processes associated with axial pressure pulses or shock waves accompanying pressure equilibration. Adiabatic compression also occurs during this period.

b. Axial Equilibrium. The approach to axial pressure equilibrium is illustrated in Figure II-13 for the 5-m and 8-m experiments. Here we plot the experimental beta ratio against the theoretical equilibrium value [Eq. (24)] as a function of time. The experimentally measured magnetic field ratio is also shown, and is in generally good agreement with the grooved-coil design value.

The direction of equilibration is the same in the two experiments and corresponds to a transfer of energy density from grooves to lands. This is consistent with "overloading" the grooves initially with plasma, as a result of the curved magnetic piston from the $\ell = 0$ field which is present during the implosion phase. The relaxation time is longer in the 8-m experiment (42-cm wavelength for $\ell_{1,0}$) than in the 5-m experiment (33-cm wavelength for $\ell_{1,0}$) by approximately the ratio of wavelengths.

These studies confirm in detail that a toroidal equilibrium is achieved in Scyllac in both the 5-m and the 8-m sector configurations, in agreement with the streak photographs. The lack of axial equilibrium during the early stages of the discharge does not appear to affect the toroidal equilibrium in a significant way. The fact that the plasma appears to obtain a toroidal equilibrium without axial equilibrium initially, and to maintain it during substantial shifts in β and nkT , indicates an unexpectedly stable behavior for the Scyllac plasma.

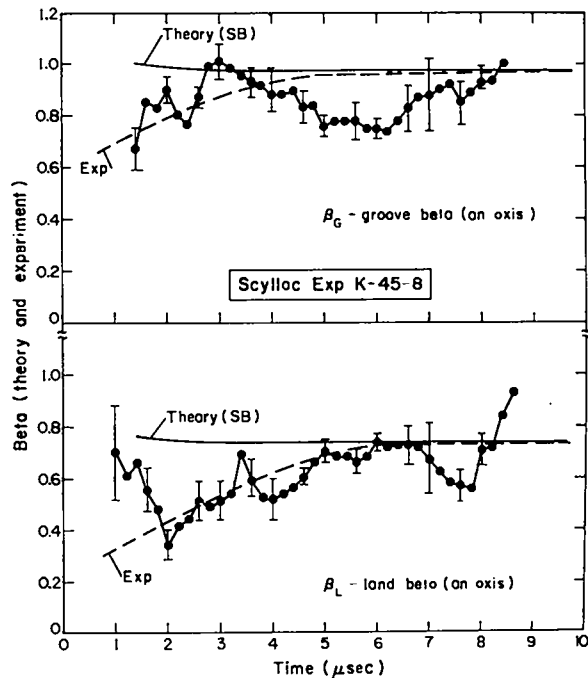
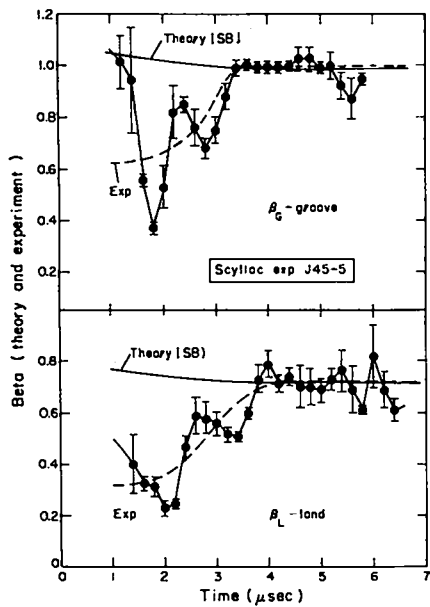


Figure II-12
 Comparison of experimental values of β in land and groove regions with theoretical values corresponding to toroidal equilibrium in the 5-m (left) and 8-m (right) toroidal sector experiments.

7. Summary

The plasma experiments on the 5-m and 8-m toroidal sectors show the following: (1) the plasma column takes up a helical shift, comes into an equilibrium position, and remains stable for 5 to 10 μsec , which is approximately the time for end effects to propagate to the center of the sectors; (2) the period of stable plasma confinement is terminated by a long wavelength ($k \approx 0$), $m = 1$ sideward motion of the plasma column from its equilibrium position which usually develops in the plane of the torus; (3) the onset-time scaling of the $m = 1$ motion from the 5-m to the 8-m experiments is in good agreement with the assumption that the terminating motion is produced by end effects; (4) the experiments confirm the equilibrium scaling in Scyllac by sharp-boundary theory from the 5-m to the 8-m device; and (5) measurements of the magnetic field, the plasma beta,

radius, and relative density profile confirm in detail that a toroidal equilibrium is achieved in Scyllac.

C. FEEDBACK STABILIZATION EXPERIMENTS ON THE 8-m TOROIDAL SECTOR (R. F. Gribble, C. R. Harder, K. Kutac, W. E. Quinn, G. A. Sawyer, and E. L. Zimmermann)

1. Introduction

The feedback stabilization system for Scyllac was developed by Gribble to control the long wavelength $m = 1$ motion and was described in the 1971 annual report.^{14,15} Initial plasma experiments with the feedback system were performed on the Scylla IV 3-m linear θ -pinch with superimposed $\ell = 1$ helical fields driving the $m = 1$ motion (Sec. F). The feedback stabilization system was installed on the 8-m sector and checked out by Kutac during the summer. Plasma experiments with the feedback system began in September and were terminated in

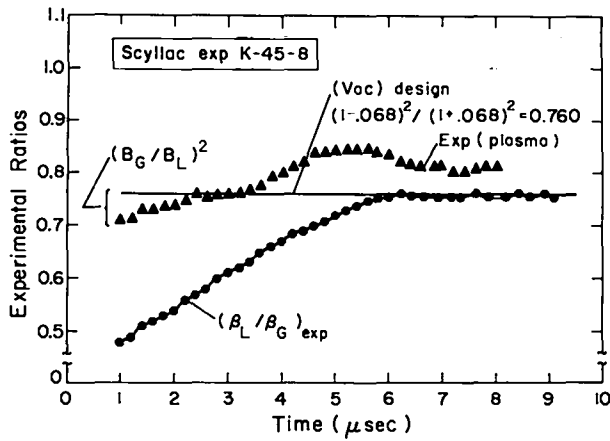
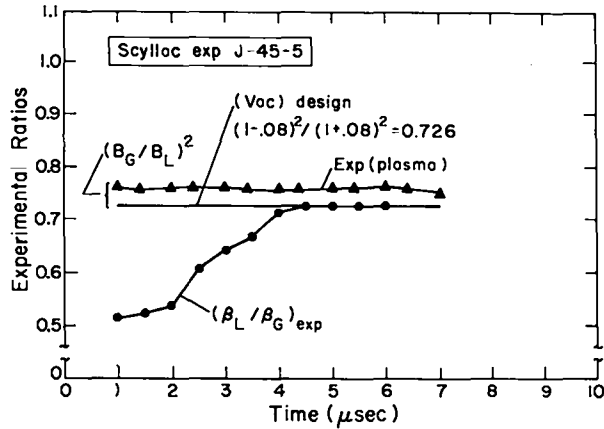


Figure II-13

Comparison of the measured ratio of beta's in the land and groove regions with experimental and design ratios of the magnetic field corresponding to axial pressure equilibrium. The upper curves are for the 5-m and the lower curves for the 8-m experiment.

November to allow the conversion to the full torus to be completed.

2. Feedback Considerations

In the $\ell = 0$ MHD feedback stabilization system for Scyllac, the feedback control is implemented through the generation of small controllable $\ell = 0$ fields which interfere with the $\ell = 1$ equilibrium field to produce a perturbation $F_{1,0}^{FB}$ feedback force. This is the same type of transverse body force that provides the toroidal equilibrium in the curved geometry and has been previously shown to exert the predicted force on a deliberately induced

$m = 1$ instability in the linear Scylla IV-3 experiment.¹⁶ Its magnitude per unit length is given by sharp-boundary theory as

$$F_{1,0}^{FB} = [\beta(3-2\beta)/8] B_0^2 h^2 a^3 \delta_1 \delta_0^{FB}, \quad (27)$$

where

$$\delta_0^{FB} \approx - B_{\ell=0}^{FB} / 2 B_0 (1-\beta) \quad (28)$$

is the plasma bumpiness produced by the $\ell = 0$ feedback fields and δ_1 is the helical plasma excursion produced by the $\ell = 1$ equilibrium field (Eq. (4)). The destabilizing force per unit length due to the $\ell = 1$ fields is

$$F_1 = \pi a^2 \rho \gamma_1^2 \xi, \quad (29)$$

where ρ is the plasma mass density on axis, ξ is the displacement from equilibrium, and γ_1 is the growth rate of the $m = 1$ instability given by,

$$\gamma_1^2 = [\beta(4-3\beta)/2 (1-\beta) (2-\beta)] h^2 (B_0^2/4\pi\rho)$$

$$(B_{\ell=1}/B_0)^2. \quad (30)$$

Equating the destabilizing force, Eq. (29), to the feedback force, Eq. (27), and utilizing the relations for δ_0 , δ_1 , and γ_1^2 gives the $\ell = 0$ field required for stabilization of the $m = 1$ instability,

$$\frac{B_{\ell=0}^{FB}}{B_0} = \frac{4-3\beta}{3-2\beta} h \xi B_{\ell=1}/B_0. \quad (31)$$

The $\ell = 0$ field produced by the single-turn feedback coils is given by

$$B_{\ell=0}^{FB} = 0.4 \pi I_{\ell=0}^{FB} / [L^2 + 4b^2]^{1/2}$$

$$= 0.2 h I_{\ell=0}^{FB} / f, \quad (32)$$

where L is the coil length, b is the coil radius, and f is a geometrical parameter of the $\ell = 0$ feedback coil defined by

$$f = h(L^2 + 4b^2)^{1/2} / 2\pi. \quad (33)$$

Using Eqs. (31) and (32), the feedback current required in each $\ell = 0$ feedback coil is given by

$$I_{\ell=0}^{FB} = \frac{5(4-3\beta)}{3-2\beta} f \xi B_0 \frac{B_{\ell=1}}{B_0}. \quad (34)$$

The feedback system produces a peak current of 4.0 kA in each $\ell = 0$ coil with a risetime of 0.9 μ sec. This produces a field, $B_{\ell=0} = 235$ G. From Eq. (34), these feedback parameters should be able to control plasma displacements of up to 6 mm with a plasma β of 0.8, $B_{\ell=1}/B_0 = 0.068$, $B_0 = 45$ kG, and $f = 0.35$. Computer modeling indicates the additional constraint that the current risetime τ should be less than the reciprocal of the growth rate ($\tau < 1/\gamma_1 \approx 1.6 \mu$ sec).

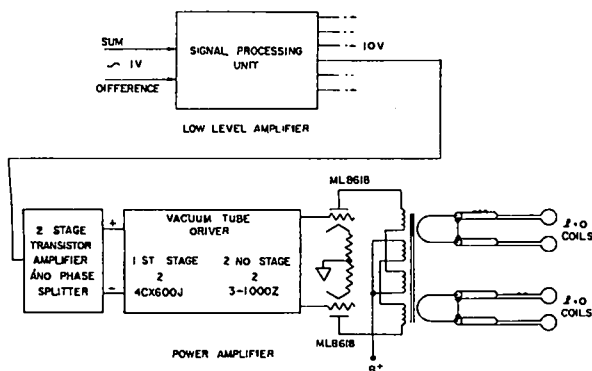


Figure II-14
Feedback stabilization system.

The ratio of the feedback force, Eq. (27), to the outward toroidal drift force,

$$F_R = \beta B_0^2 a^2 / 4R, \quad (35)$$

is given by

$$\frac{F_{1,0}^{FB}}{F_R} = \frac{(3-2\beta)}{4(1-\beta)(1-\beta/2)} hR \frac{B_{\ell=1}}{B_0} \frac{B_{\ell=0}^{FB}}{B_0}, \quad (36)$$

where use has been made of the approximate relations for δ_0^{FB} and δ_1 . Using the parameters given above, $F_{1,0}^{FB}/F_R = 0.065$.

3. Experimental Arrangement

The feedback stabilization system, shown schematically in Figure II-14, consists of four basic components: (1) the plasma position detectors consist of quad-cell optical detectors capable of detecting plasma motion of 1 to 10 mm away from the equilibrium position with an approximate linear response; (2) signal processing units, which act as intermediate amplifiers while adding damping and filtering to the position detector signal, gate the position detectors off during the initial period when the plasma forms and electronically select the plasma position at the time when the gates open as the null position for feedback; (3) power amplifier modules, each of which consists of 3 separate stages of amplification ending in push-pull operation of two ML-8618 power vacuum tubes operating at 35-kV plate voltage; and (4) $\ell = 0$ feedback coils driven by the power module output transformer.

Figure II-15 shows the front end of the sector with the feedback stabilization system installed. The feedback power modules are shown on the upper platform above the compression coil. The module output cables connect to the primaries of the transformers located above and to the rear of the coil. The $\ell = 0$ feedback coil junction boxes are located on top of the compression coil and connect the feed tabs



Figure II-15
 Photograph of the 8-m toroidal sector with
 the feedback stabilization system installed.

of each coil to cables from the transformer secondaries.

a. $\ell = 0$ Feedback Coils. In Scyllac both the $\ell = 1$ and $\ell = 0$ equilibrium fields are generated by the shaped inner surface of the main toroidal coil, while the $\ell = 0$ feedback fields are produced by single-turn coils inside the main coil as illustrated in Figure II-16. The slots in the $\ell = 0$ coils allow the penetration of the $\ell = 1$ helical field. The feedback coils are of brass construction and vacuum encapsulated with epoxy. The two coils in the groove region, which has a minimum in the toroidal field, have a diameter of 12.4 cm compared

with a diameter of 11.8 cm in the land region, which has a maximum in the toroidal field. This choice of diameters results in the same toroidal magnetic flux threading all the feedback coils. Four feedback coils are used for each of the twenty $\ell = 1,0$ wavelengths in the sector with its 8.4-m arc length. Appropriate phasing of the currents in these coils provides a feedback force in the desired transverse direction. The output transformer drives alternate $\ell = 0$ coils in series as indicated in Figure II-14. This arrangement nulls the induced voltage from the main compression field. Each feedback module

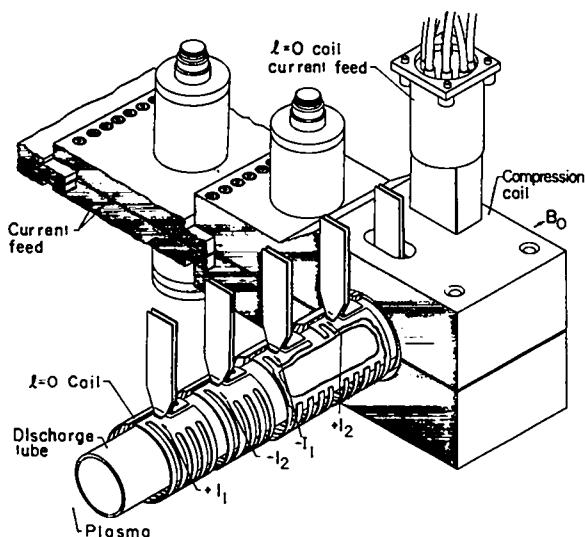


Figure II-16
Perspective view of the $\ell=0$ feedback coils installed over the discharge tube in the sector coil.

drives two pairs of feedback coils in series (Figure II-14) through a 5 to 1 step-down transformer.

b. Position Detectors. The feedback plasma position detectors consist of silicon quad-cell optical detectors, which are capable of detecting plasma motions of 1 to 10 mm away from the equilibrium position with an approximate linear response. These detectors have a risetime of about 25 nsec. Two position detectors sense the plasma motion in orthogonal directions, 45° above and below the horizontal plane of the torus. The sum and difference signals from each position detector are fed to an immediate amplifier to provide the control signal for equilibrium compensation of one degree of freedom of the transverse plasma motion. Three pairs of position detectors and corresponding intermediate amplifiers were used for the Scyllac sector.

4. Transverse Plasma Motions with $\ell = 0$ Feedback Coils Installed in the Sector Coil

The initial experiments investigated the toroidal plasma equilibrium with the $\ell = 0$ feedback coils installed in the

toroidal compression coil. With the bank operating at 40 kV ($B_0 \sim 40$ kG), the side-on streak photographs showed two dominant features: (1) Plasma equilibrium in the $\ell = 1,0$ shaped compression coil required an initial deuterium filling pressure of ~ 6 to 8 mTorr compared with 16 to 19 mTorr in the absence of the $\ell = 0$ feedback coils; and (2) a downward vertical motion of the plasma column developed at 2 to 3 μ sec after the initiation of the discharge and carried the plasma to the discharge tube wall in approximately 2 to 3 μ sec. The downward plasma motion was essentially the same all around the 8.4-m sector.

a. Plasma Equilibrium. In these experiments with fixed $\ell = 1$ and $\ell = 0$ equilibrium fields generated by the shaped inner surface of the toroidal coils, the plasma equilibrium was achieved by adjusting the initial deuterium filling pressure to give a balance between the $F_{1,0}$ and toroidal forces through their β dependence (Figure II-1). With the $\ell = 0$ feedback coils installed and the bank operating at 40 kV, the approximate plasma equilibrium occurred with a deuterium filling pressure of 6 to 8 mTorr compared with 16 to 19 mTorr in the previous experiments without feedback coils. With the filling pressure greater than 8 mTorr, the plasma column moved outward ($F_{1,0} < F_R$). This result indicated that a larger plasma β was required to produce the equilibrium force balance than previously without the feedback coils (Figure II-1). Since the $F_{1,0}$ force is proportional to the equilibrium field product, $B_{\ell=1} B_{\ell=0} / B_0^2$, these results imply that the $\ell = 0$ feedback coils were decreasing the equilibrium fields.

With the filling pressures of 6 to 8 mTorr required for approximate equilibrium, the streak photographs were underexposed and not suitable for reproduction.

Previous magnetic probing with feedback coils in a straight coil grooved to generate $\ell = 1$ helical fields showed that a small decrease and a slight phase shift

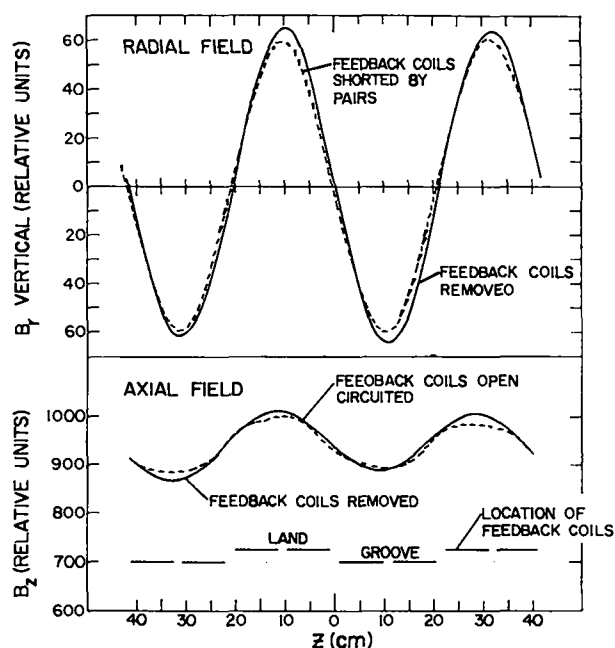


Figure II-17
Magnetic field plots of the vertical radial component of the $\ell=1$ field (upper graph) and the axial field taken on the axis of the shaped compression coil, with and without the $\ell=0$ feedback coils in place.

occurred in the B_r component of the $\ell = 1$ field. However, the effect of the feedback coils on a groove-generated $\ell = 0$ field was not explored. In order to determine the effects of the feedback coils on the toroidal equilibrium fields an additional meter of coils was grooved identical to those used in the sector. The magnetic probing results showed that the presence of feedback coils produced an appreciable distortion of the $\ell = 0$ field and had a lesser effect on the $\ell = 1$ field. The B_r and B_z components on axis are shown in Figure II-17. Although the presence of the coils distorted the fields, it made very little difference whether the coils were shorted by pairs or open-circuited. For clarity on the figures, therefore, only one of the cases is shown for each field component (open-circuited for B_z and shorted by pairs for B_r).

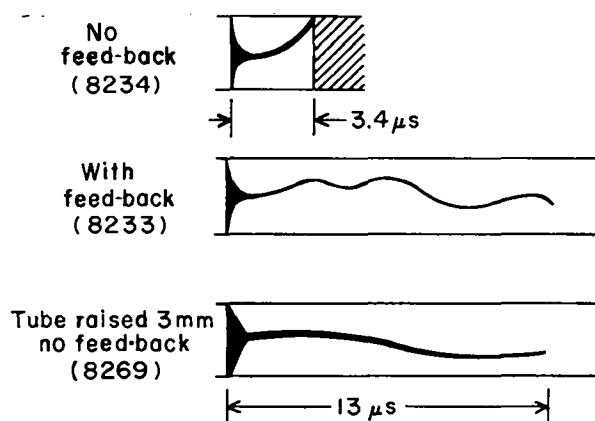


Figure II-18
Tracings of underexposed streak photographs showing the transverse plasma motions in the vertical plane of the torus.

The feedback coils were, of course, designed to minimize interference with the grooved-in $\ell = 0$ and $\ell = 1$ fields. Figure II-16 shows the slotted construction used to reduce eddy currents. The probing shows, however, that the fields were somewhat distorted and attenuated by eddy currents flowing on the surface of the feedback coils. The $B_{\ell=1}/B_0$ ratio was reduced only about 7%, but the $B_{\ell=0}/B_0$ ratio was affected to a considerably greater extent and the waveform was distorted so that it was flat-topped. The reduction in peak amplitude was 21%, and Fourier analysis shows that the sine wave fundamental was reduced about 15%.

The probing results gave the following values for the equilibrium fields:

	Design Value	Without Feedback Coils	With Feedback Coils
$B_{\ell=1}/B_0$	0.0683	0.068	0.063
$B_{\ell=0}/B_0$	0.0683	0.065	0.051 (0.054)

The equilibrium field product was reduced by 27.3% (23.0%) with the feedback coils, which reduces the $F_{1,0}$ force a corresponding amount. The quantity in parentheses results from the use of the fundamental component of the measured $B_{\ell=0}$ waveform.

It is this component that is important to the plasma equilibrium.

The reduction of the $B_{\ell=0}/B_0$ field by the feedback coils can be overcome by either increasing this field through deeper $\ell = 0$ grooves or by shaping the feedback coils to conform to the spatial variation of the $\ell = 0$ equilibrium field.

b. Vertical Plasma Motion. The downward vertical motion of the plasma column, which developed at 2 to 3 μsec after the initiation of the discharge, carried the plasma to the wall in 2 to 3 μsec . The upper tracing of the underexposed streak photographs shows the vertical plasma motion in Figure II-18. (The direction of the motion is inverted in Figure II-18.) This behavior is to be contrasted with the absence of vertical motion with the same operating conditions without feedback coils (Figure II-5).

It is likely that the dominant vertical motion resulted from a shift of the magnetic axis in the vertical plane of the torus. The vertical feed tabs of the $\ell = 0$ feedback coils (Figure II-16) may produce a perturbation in the $\ell = 1$ field which shifts the helical axis upward. The plasma implodes to the center of the discharge tube and finds that it is not in its equilibrium position about the helical magnetic axis. Consequently, the plasma column begins to move farther off the axis in a long wavelength $m = 1$ instability motion. This type of plasma behavior was observed in the Scylla IV-3 $\ell = 1$ experiments (Sec. F) with the $\ell = 1$ helical fields generated by grooves in the compression coil. It was found that the direction of the $m = 1$ instability motion of the plasma column could be controlled by varying the position of the discharge tube within the compression coil. A few mm displacement of the tube off the magnetic axis was sufficient to induce the instability in a predicted transverse direction.

The vertical position of the discharge tube in the toroidal compression coil was

measured and was found on the average to be 0.5 mm below the minor axis. It should be noted that the axis of the discharge tube lies in a plane to within ± 1.5 mm. In order to check the above prediction on the cause of the vertical plasma motion, the discharge tube was raised 1.1 mm by shimming it up inside the $\ell = 0$ feedback coils. This reduced the rate at which the vertical motion carried the plasma column downward to the discharge tube wall. Although this result is not completely definitive, it does suggest that the above explanation may be correct.

5. Application of Feedback Fields

In the initial experiments the feedback system was energized in a fixed configuration to produce an upward force on the plasma column. With the feedback current applied between 0.3 and 0.7 μsec after the initiation of the main discharge, the $m = 1$ downward vertical motion of the plasma was overcome and the column remained in the horizontal plane of the torus as shown in the center tracing of the streak photographs of Figure II-18. Although the streak photographs were quite underexposed due to the low filling pressures required for toroidal equilibrium, the estimated growth rate of the vertical motion was of the order of 1 MHz or greater. With the feedback filaments operating at 9.0 V, the plate voltage at 30 kV, and the feedback current applied later than 0.7 μsec after the beginning of the discharge, the feedback force was unable to overcome the $m = 1$ vertical motion.

With the feedback applied to produce a force in the horizontal plane of the torus, a perceptible push of the plasma column is observed on both the streak photographs and the position detector signals. However, this result is overshadowed by the vertical motion of the column.

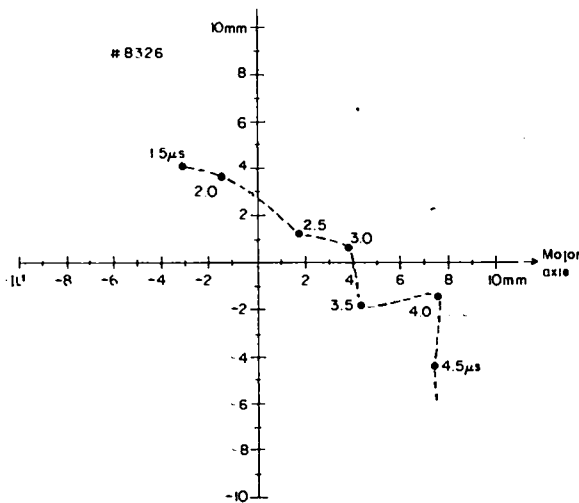


Figure II-19
Position of the plasma column in a radial plane as a function of time without feedback, as observed by the position detector.

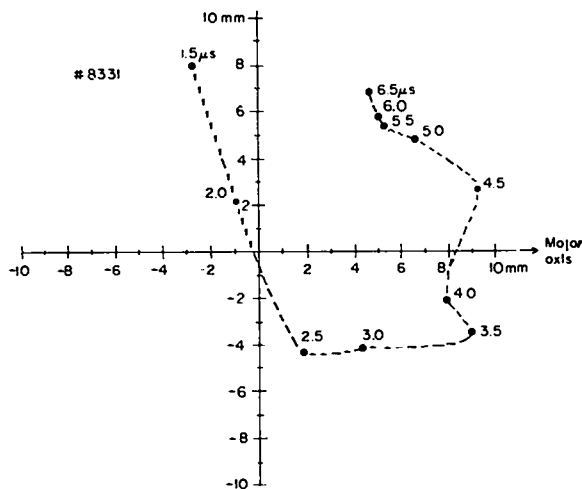


Figure II-20
Trajectory of the plasma column in a radial plane with the feedback stabilization system energized.

6. Results with the Discharge Tube Raised 3 mm

a. Plasma Motion without Feedback.

The discharge tube was raised 3 mm by machining insulation from the tops of the feedback coils and shimming these coils up

in the main compression coil. The bottom tracing of streak photographs in Figure II-18 shows the plasma motion in the vertical plane with the raised tube and without the feedback coils energized. This motion, which is comparable to that without feedback coils (Figure II-5), is to be contrasted with that of the upper streak (Figure II-18) before the tube was raised. This result verifies the hypothesis above (Sec. C4b) that the vertical motion resulted from a shift of the magnetic axis in the vertical plane of the torus due to asymmetries introduced by the presence of the feedback coils. Although the position of the magnetic axis cannot be determined by the magnetic probing, the feedback coil geometry is likely to produce such a shift.

b. Results with Feedback. Only fifteen discharges were taken with the feedback loop closed prior to an electrical fault in an $l = 0$ feedback coil which broke the discharge tube. Unfortunately, this fault occurred 3 days before the sector experiments were to be terminated to allow the torus conversion work to continue. Much of the time during this period was spent adjusting the gain and damping controls of the feedback system. However,

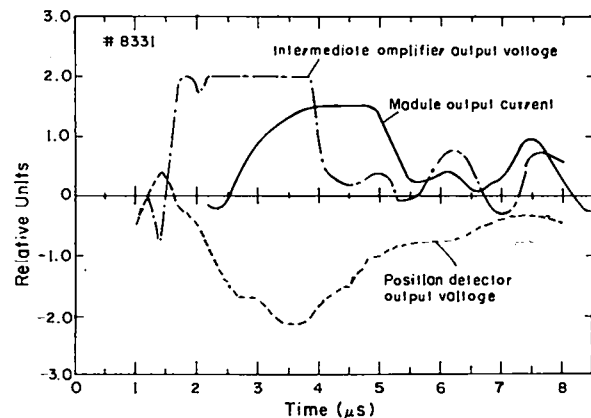


Figure II-21
Plots of the output voltage from the position detector, the intermediate amplifier voltage, and the corresponding output current of the feedback system.

the feedback system appeared to be responding to the plasma motions and applying appropriate corrections.

Transverse plasma motions without and with feedback are compared in Figures II-19 and II-20, respectively. The position of the center of the plasma column, which was observed with the position detector, is plotted as a function of time in Figures II-19 and II-20. The feedback system appears to reverse the plasma motion in Figure II-20. Figure II-21 shows a plot of the output voltage from the position detector, which drives the feedback system, and the corresponding output current of the feedback system on the same discharge from which Figure II-20 was obtained. This shows that the feedback system was responding properly to the input signal from the position detectors.

D. SCYLLAC TORUS (J.J. Banta, W.H. Borkenhagen, K.W. Hanks, C.R. Harder, H.W. Harris, E.L. Kemp, W.E. Quinn, A.S. Rawcliffe, and B.A. Sawyer)

1. Introduction

The conversion to the full Scyllac torus began on January 2, 1973. The 5-m Scyllac toroidal sector was closed down on December 29, 1972, to allow the conversion work to begin. The experiments on the 5-m linear Scyllac device with strong magnetic mirrors were terminated on March 1, 1973, to allow the conversion work to continue. The conversion work was a cooperative effort between Q-4, Q-3, and Zia with Ward Harris of Q-4 directing the overall effort. The construction work involved in the conversion to the full torus was completed in late December 1973.

Considerations concerning the effects of the major radius of curvature on the plasma equilibrium and stability and the feedback stabilization requirements necessitated an increase in the Scyllac major radius from 2.4 to 4.0 m. This increase in radius was implemented during the conversion.

2. Scyllac Major Radius of Curvature

Equilibrium, stability, and feedback stabilization considerations show that the probability of successful high- β plasma confinement in toroidal geometry is considerably increased as the major radius of curvature increases. Studies¹⁷ show that the initially proposed Scyllac major radius of 2.4 m places more stringent requirements on the plasma equilibrium and stability than will be encountered, for example, in a high- β toroidal feasibility experiment. The $m = 1$ instability growth rate and the requirements of the feedback stabilization system decrease approximately in a linear manner with increasing major radius.

The plasma experiments in the 5-m toroidal sector, which produced a plasma with an ion temperature of ~ 1 keV, were performed with the capacitor bank operating with one-half of its capacity. Therefore, with the full bank, the capability exists for producing a plasma with identical properties to those in the 2.4-m radius sector in a device with twice the major radius of curvature. An 8-m-diameter torus is the largest practical major diameter which can be accommodated in the Scyllac facility under the criterion that a hot collisionless plasma be produced with the existing Scyllac energy storage system. The increased major radius of 4.0 m was implemented during the conversion to the full torus with minimum cost.

3. Experimental Arrangement

The Scyllac torus has a major radius of 4.0 m and a circumference of 25.13 m. The initial compression coil, whose inner surface is shaped to generate the $\ell = 1$ helical and $\ell = 0$ bumpy equilibrium fields, has an average bore of 14.2 cm. The toroidal quartz discharge tube has an inside diameter of 88 mm. The primary energy storage consists of a 10.5-MJ capacitor bank of 3,150 1.85- μ F, 60-kV capacitors. The primary energy storage system and the compression coil are divided into 15

independent sections. Each 1.67-m arc-length section of the compression coil is energized by a 700-kJ rack.

a. Arrangement of the Energy Storage Racks. The five pairs of energy storage and machine racks of the 5-m sector were moved outward approximately one meter to accommodate the increased major radius of 4 m. The seven racks of the former linear machine and three new racks were moved to complete the toroidal configuration. A new platform structure fills the central core of the torus. This structure consists of three different levels above the basement floor with the upper or diagnostic level situated 6.7 m above the basement floor and 1.3 m below the horizontal plane of the torus.

b. "Front End" Arrangement of Collector Plates and Compression Coils. The original Scyllac collector plates have been disassembled and the rear current-contact surfaces modified and reassembled. In the original design with a 4.8-m diameter, the collector plates had a large, constant width for the rear half of the assembly and a tapered decreasing width in the front half toward the coil feedpoints. The collector plates have been reversed such that the original rear portions with the greater widths now form the front end, in the 8-m-diameter arrangement, to which the transition and compression coil sections are attached. The upper levels of the machine racks have been modified to accept the new orientation of the collector plates and to allow the plates to be positioned farther to the rear of the rack. New transition sections, which join the compression coils to the collector plates, are shorter and have an increased width of 1.67 m. Each rack of the Scyllac energy storage system feeds a single collector plate assembly which in turn drives a 1.67-m arc-length of the toroidal compression coil. Each of the fifteen collector plates has been cabled with 1,260 coaxial load cables from the 210 capacitor-spark gap units of the

main bank and with 24 cables from the two 0.7- μ F capacitors of the preionization bank.

c. Scyllac Control System. The Scyllac control system, which formerly performed a dual function in the operation of the toroidal sector and the linear machine, has been unified for the operation of a single device. It is planned to increase the monitoring functions of the Scyllac computer in the operation of the full torus. In particular, the detailed monitoring of the various bank voltages during the charge and pretrigger phases will be done in such a manner that the computer has an abort control of the over-all system.

d. Spark Gap Firing Monitor System. The original spark gap monitor system, which has been used to monitor the main bank start gaps and crowbar gaps, is being extended to include the monitoring of the crowbar trigger spark gaps. This extension will facilitate the maintenance and trouble shooting on the 24 crowbar trigger spark gaps per energy storage rack.

e. Parameters of the Scyllac Torus. The parameters of the full Scyllac torus are listed in Table II-2.

4. $\ell = 1, 0$ Toroidal Equilibrium Fields

The experiments on the 5-m toroidal sector and the dependence of the instability growth rates on the equilibrium plasma column excursions, δ_1 and δ_0 , indicated that δ_1 and δ_0 should not be appreciably increased. This consideration, $\delta_1 \delta_0 = \text{constant}$, places an upper limit on the $\ell = 1, 0$ wavelength through the equilibrium condition of Eq. (9). For technical reasons it is undesirable to make the $\ell = 1, 0$ wavelength shorter than in the 5-m sector ($\gamma_{1,0} = 33.15$ cm). Scaling studies¹⁷ for the equilibrium, stability, and feedback parameters resulted in a choice of 41.9 cm for the $\ell = 1, 0$ wavelength.

A new compression coil, whose inner surface is shaped to generate the $\ell = 1$ and $\ell = 0$ equilibrium fields, has been

designed and fabricated for the 8-m-diameter torus. The values of the helical $\ell = 1$ and bumpy $\ell = 0$ equilibrium fields designed into the shaped coil were determined through the theoretical sharp-boundary relations Eqs. (9), (3), and (5) for the plasma distortions δ_1 and δ_0 required for equilibrium with $R = 4.0$ m. The equilibrium field values are $B_{\ell=1}/B_0 = B_{\ell=0}/B_0 = 0.064$ and $B_v/B_0 = B_{1,2}/B_0 = 0.001024$. The coil was designed by calculating the shape of the magnetic flux surfaces as described in Sec. B3. Figure II-22 shows plots of the flux surfaces at four z positions: $hz = 0$, center of a land region; $hz = \pi/2$, between a land and groove region; $hz = \pi$, center of a groove region; and $hz = 3\pi/2$, between a groove and land region. The annular cross-hatched areas of Figure II-22 indicate the quartz discharge tube. The outer flux surfaces give the coil bore cross sections at the indicated z position.

This initial coil for the full torus has a smaller tangent bore (11.2 cm) than that used in the 8-m sector experiments (14.2 cm), which was designed to accommodate the $\ell = 0$ feedback stabilization coils. With the smaller tangent bore and the choice of the $B_{\ell=1}$ and $B_{\ell=0}$ fields, the theoretical value of the vertical field, Eq. (16), gave flux surfaces which were very nearly circular. This is in contrast to the shaped coil used in the 8-m sector, which required a vertical field 44% larger than the theoretical field to yield circular flux surfaces. This difference in flux surfaces results from the dependence of the modified Bessel functions on the coil radius, Eq. (15).

Figure II-22 also shows that the inner flux surfaces are circular in cross section and as a set are centered about the minor axis of the torus. The helical shift of the flux surfaces about the minor axis is produced by the $\ell = 1$ field.

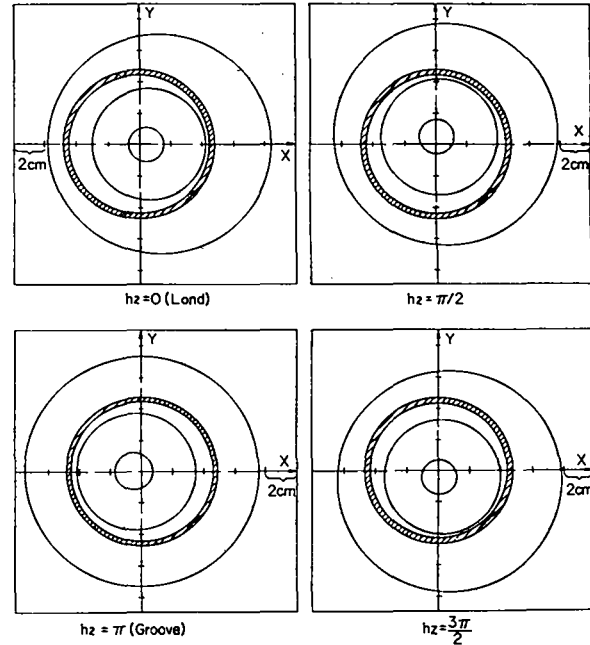


Figure II-22
Magnetic flux surfaces at four z locations relative to the minor axes with $B_{\ell=1}/B_0 = B_{\ell=0}/B_0 = 0.064$ and $B_v/B_0 = B_{1,2}/B_0 = 0.001024$. The inner surface of the compression coil was machined to the outer flux surface in these radial planes. The annular cross-hatched area represents the discharge tube.

5. Toroidal Discharge Tube and Pump-Out Ports

The discharge tube for the 8-m torus consists of 10 quartz tube sections, each with an arc length of 2.5 m. The quartz sections are joined by O-ring seals to short (5-cm length) ceramic sections of 99% alumina. The ceramic sections have an oval-shaped pump-out stub (1.5-cm x 4.0-cm) extending downward from the plane of the torus. In addition the wall of the cylindrical portion of the ceramic section is semicontinuous over the region of the pump-out stub with 10, 5-mm apertures opening into the stub. The series arrangement of apertures and stub has a conductance of 12 ℓ /sec compared with a discharge tube volume of 15 ℓ to be pumped

TABLE II-2
SCYLLAC PARAMETERS

Parameter	Full Torus	
	Preionization Bank	
Bank capacitance	21	μF
Bank operating voltage	50	kV
Bank energy storage	26	kJ
Ring frequency	400	kHz
Peak current	2.4	MA
Maximum magnetic field	1.2	kG
	Primary Bank	
Bank capacitance	5,828	μF
Bank voltage	60	kV
Bank energy storage	10.5	MJ
Normal operating voltage range	40 - 55	kV
Major radius	4	m
Torus circumference	25.13	m
Average coil bore radius	7.1	cm
Discharge tube wall radius	4.4	cm
Source inductance	0.17	nH
Coil inductance	0.80	nH
Transfer efficiency	0.82	
Risetime	3.7	μsec
L/R decay time	250	μsec
Peak current (@ 50 kV)	110	MA
Maximum magnetic field (@ 50 kV)	55	kG
Aximuthal electric field (@ 4.4 cm and 50 kV)	0.57	kV/cm
$\lambda = 1,0$ wavelength	41.89	cm
$\lambda = 1,0$ wave number	0.15	cm^{-1}
No. of $\lambda = 1,0$ wavelengths	60	
$B_{\lambda=1}/B_0$	0.064	
$B_{\lambda=0}/B_0$	0.064	
B_v/B_0	0.001024	
$B_{1,2}/B_0$	0.001024	

by each port. The objective in the design of the pump-out ports was to achieve sufficient pumping speed while minimizing the perturbation in the magnetic field due to the pump-out slot in the main compression coil.

The ceramic pump-out stubs terminate into a 9-cm-diameter ceramic tube after partial penetration through the compression

coil wall. The cylindrical ceramic tubes, which have a metal valve near the center of their 1-m length, provide appropriate voltage insulation. These tubes connect into a common toroidal manifold below the torus.

6. Status of the Full Torus

The construction work on the Scyllac torus, which involved the Zia crafts, was completed in late December 1973. The three new capacitor racks, i.e., the racks which were not previously used on the toroidal sector and linear devices, have been checked out electrically and operated for a number of shots at 50 kV. In addition, the primary and crowbar master trigger systems have been tested on five of the seven former linear energy-storage racks.

Two of the vacuum pump-out ports have been installed in the previous toroidal sector device and have been tested in normal operation with plasma discharges. Some minor difficulties were encountered and corrected relative to vacuum seals. The voltage insulation of the plasma column from the main compression coil via the vacuum system has been evaluated and found to be satisfactory.

The delivery of the main compression coils by the fabricator has been delayed as a result of material procurement problems. An outside fabricator provides finished coil sections with a toroidal "tangent" bore. The Scyllac machine shop bores the final $\lambda = 1,0$ shaped surfaces and adds the diagnostic and pump-out slots. The machining of the coils should be completed on March 1, 1974. The assembly of the compression coils with the discharge tube should be completed on March 22, 1974. Plasma operation with the full torus should occur by the first of April 1974.

E. STAGED THETA PINCH

1. Introduction (K. Thomas, Q-7)

The Staged Theta Pinch is a new experiment which was begun in 1973. Previous theta pinches have performed initial implosion heating of the ions and subsequent adiabatic compression with a single capacitor bank power supply. Projected theta-pinch feasibility experiments and fusion reactors, however, will require separation of the two functions to achieve greater implosion heating and less adiabatic compression. The Staged Theta Pinch is a 4.5-m-long linear theta pinch designed to study the technological and physics problems associated with separating the two functions. It will use a relatively low-energy, high-voltage capacitor bank to produce the theta-pinch plasma. A lower voltage, higher energy capacitor bank will be used to contain the plasma and provide a variable amount of adiabatic compression. The experiment will be capable of producing high-temperature plasmas with a much larger ratio of plasma radius to discharge tube radius than is possible in conventional theta pinches. Plasma experiments will include studies of the effect of magnetic field amplitude and time history on plasma formation, the properties of the plasma formed, and later, studies of the effect of helical magnetic fields on plasma stability. If the ratio of plasma radius to coil radius can be made large enough, the effect of plasma stabilization by image currents in the coil walls will be observable.

2. Theory of Operation

The implosion heating phase of a theta pinch is illustrated in Figure II-23. A fast rising magnetic field drives the previously ionized plasma inward. In this bounce model the ions are projected forward with twice the velocity of the magnetic sheath. They cross the discharge tube axis and again make the contact with the magnetic sheath. The plasma is compressed until the plasma pressure is

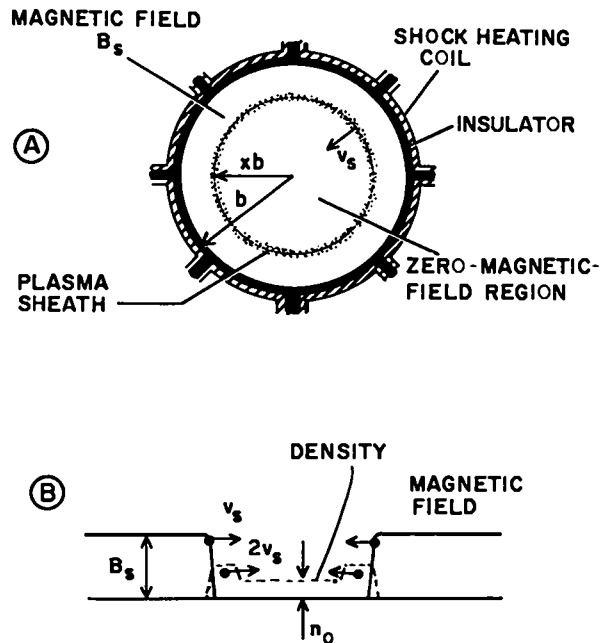


Figure II-23
Illustration of the processes involved in ideal implosion heating.

sufficient to stop inward motion of the magnetic sheath. The plasma then expands and thermalizes until it comes into equilibrium with the external magnetic field. These processes are illustrated in the results of the Scylla 1-B experiment (described elsewhere in this report) and the theory is treated in detail in the report LA-5026-P (Rev).

In order to obtain the maximum heating and largest possible plasma diameter the implosion magnetic field should rise rapidly to its maximum. In the idealized case of a step function rise in magnetic field, the plasma comes to equilibrium with a radius which is 0.63 times the discharge tube radius. Computer simulations show that little change in radius occurs if the magnetic field reaches its maximum before the magnetic sheath propagates one-third of the way to the discharge tube axis.

Additional heating and even larger diameter plasmas may be obtained using the

"free expansion" method of programming the magnetic field. The plasma does work on the magnetic field as it expands after the initial implosion. If the external magnetic field is reduced at the time when the ions which have crossed the discharge tube axis contact the magnetic sheath and then raised again just before the plasma contacts the discharge tube wall, this work is reduced and more energy remains in the plasma, resulting in higher plasma temperatures and larger diameter plasmas.

To aid in the design of the experiment the NET-II computer code was used. This code is available on all the large computers at Los Alamos and allows the treatment of electrical circuits with varying values of the electrical circuit parameters. R. F. Gribble used this code to model the plasma in two ways. The first calculations modeled the varying inductance in the coil region by means of an analytical expression which could treat either the bounce model, mentioned previously, or the snowplow model, where all the plasma is trapped in the magnetic sheath. This method could treat the plasma up to the time at which the magnetic sheath had advanced 2/3 of the way to the discharge tube axis. The plasma was then allowed to thermalize to find out the relative effectiveness of different circuit designs. In later modeling, a simple plasma simulation (up to 25 particles) was made by treating the plasma particles as analog circuits. This allowed the following of plasma behavior through the compression phase and showed the effects of magnetic field programming. This simulation technique was compared in the case of idealized magnetic waveforms with more complex plasma simulations performed by personnel in Q-6 and the results agreed to three significant figures, giving considerable confidence in the method. To test the effectiveness of the model in predicting experimental results, the Scylla 1-B experiment was modeled and the code gave

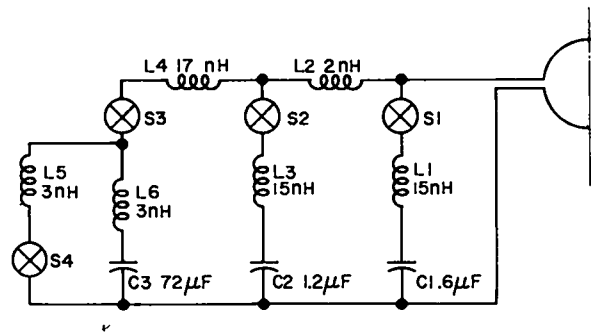


Figure II-24
Circuit diagram of 0.9-m section of Staged Theta Pinch.

good agreement with the experimental results when the bounce model for plasma-magnetic sheath interaction was used.

3. Experiment Design (R. F. Gribble, R. K. Linford, E. M. Little, Q-7; W. H. Borkenhagen, R. S. Dike, and C. F. Hammer, Q-4)

The Staged Theta-Pinch experiment was originally designed to use the same high-voltage circuit as the implosion heating experiment. Since the rail switch used in that experiment is not capable of handling the large amounts of energy required for staging, it would have been necessary to feed in the staging current between the rail switch and the compression coil. Upon investigation it was determined that this arrangement would add an unacceptably large source inductance to the circuit. Therefore, in order to allow the staging current to be supplied at the end of the collector plates away from the coil it was decided to mount an individual spark gap on each high-voltage capacitor. In addition, by building a new spark gap which does not prefire when the other high-voltage gaps in the circuit are fired, it is possible, with this arrangement, to vary the time history of the magnetic field in the compression coil (field programming) by changing the time at which different parts of the circuit are activated.

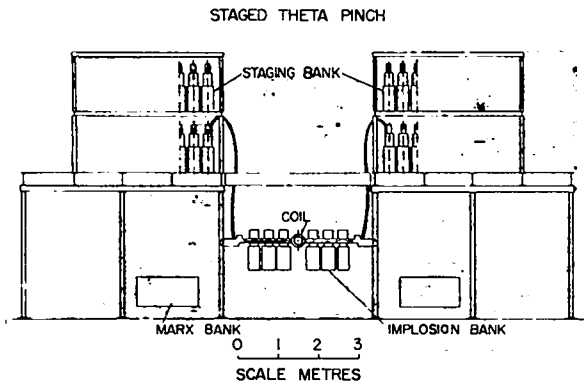


Figure II-25
Layout of Staged Theta Pinch.

The final circuit design is shown in Figure II-24. The 22.5-cm-i.d. compression coil is fed from both sides and Figure II-24 represents a 0.9-m-long section. There will be five such sections on each side of the machine. The opposite sides will operate at different electrical polarities, necessitating the insulating of the electrical components from ground potential. The high-voltage (125-kV) part of the circuit is divided into two parts with independent trigger systems.

The layout of the experiment in the old Scylla IV experimental area is shown in Figure II-25. The staging bank, which is the Scylla IV 50-kV main bank, is located on a platform above the high-voltage implosion circuit. The start switches for the staging bank have been moved down to the collector plate in order to isolate the load cables from the high-voltage circuit. This necessitated the replacement of the start switch in the Scylla IV capacitor gaps with a shorting column. The crowbar system was left intact. The high-voltage gaps are connected directly into the collector plates.

In addition to the high-voltage technology developed for the implosion heating experiment, the Staged Theta-Pinch design required the development of two new spark gap designs. The switch for the implosion circuit, designed by R. F.

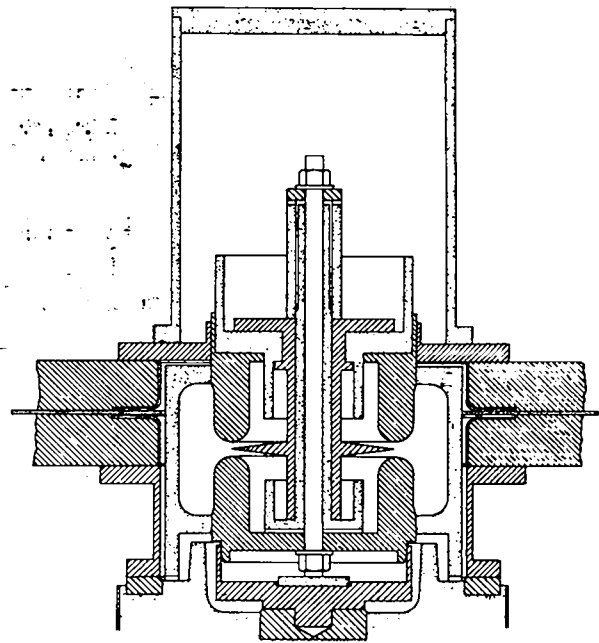


Figure II-26
Implosion circuit spark gap.

Gribble, is shown in Figure II-26. This switch has the high-voltage hold-off and fast trigger-electrode biasing characteristics required for field programming. It also has lower inductance than the present Scyllac design. The second gap, used to switch-in the staging bank, must also have these characteristics and also be able to carry larger currents for a longer time. Two designs are under investigation, one linear and the other coaxial like the implosion circuit gap.

In order to trigger these gaps reliably a higher voltage trigger system than the one used on Scyllac is under development.

4. Experiment Status

During 1973, the following progress on the Staged Theta-Pinch Experiment was made:

- a. The Scylla IV experiment was disassembled and removed from the experimental area.
- b. The start gaps on the Scylla IV main bank capacitors were replaced by shorting columns and the crowbar gaps were

rebuilt.

c. A new platform and capacitor racks for the staging bank were designed, built, and installed.

d. The electrical circuit for the experiment was designed.

e. A 0.9-m-long prototype of one section of the experiment was designed and construction started. It will be operated originally with modified Scyllac spark gaps and later be fitted with the new implosion circuit spark gaps. It will allow evaluation of electrical components in the final geometry and provide preliminary physics results.

f. A new high-voltage implosion circuit spark gap was designed and tested.

g. Two versions of a staging circuit gap were designed and one version was constructed.

h. Preliminary development of a new higher voltage trigger system was carried out.

F. SCYLLA IV-3 (W. R. Ellis, R. F. Gribble, C. R. Harder, and R. Kristal)

Scylla IV-3 is a 3-m linear theta pinch which was terminated as an active experiment on June 28, 1973, to make way for the new staged theta-pinch facility (Q-7). The experimental activity on Scylla IV-3 during the six months of 1973 in which it was in operation covered two areas: feedback stabilization of deliberately induced $\ell = 1$, $m = 1$ instabilities, and quantitative $m = 1$ growth rate measurements for $\ell = 0$ and $\ell = 1$ fields of various wavelengths (usually called "variable- ϵ " experiments).

1. Feedback Stabilization

The $\ell = 0$ MHD feedback stabilization system developed for Scyllac to control long wavelength ($k \approx 0$), $m = 1$ sideward motions of the plasma column was installed on Scylla IV-3 for checkout and preliminary evaluation. A plasma instability was deliberately induced by adding an $\ell = 1$ field to the main theta-pinch field B_0 .

The $\ell = 1$ field was produced by internally grooving the compression coil to coincide with a computer generated $\ell = 1$ flux surface. The $\ell = 1$ wavelength was 30 cm, and the $\ell = 1$ field strength was $B_{\ell=1}/B_0 = 0.04$.

The feedback system was tested to see if it could handle the resulting growth rate of $\sim 0.9 \times 10^6 \text{ sec}^{-1}$. There were four feedback coils per 30-cm wavelength positioned between the discharge tube and the compression coil wall, with a resulting gap of 9 mm to accommodate the return flux. When the feedback system was switched on at sufficiently early times ($\leq 0.5 \mu\text{sec}$ after main bank time), the feedback force was sufficient to stop the plasma motion to the wall and drive the column in the opposite direction (Figure II-27).

The feedback force was fairly small in these experiments ($B_{\ell=0}/B_0 = 0.004$), and the feedback loop was not "closed" to incorporate position-detector activation. These deficiencies were remedied to some extent in subsequent Scyllac sector experiments (see Sec. II-C).

A paper summarizing these feedback experiments on Scylla IV-3 has been submitted to Physics of Fluids for publication.

2. Variable- ϵ Experiments

The name "variable- ϵ experiment" ($\epsilon = ha = 2\pi a/\lambda$) has been given to scaling experiments concerned with measuring experimental growth rates relevant to the Scyllac configuration. Experimentally, it is not yet clear whether plasma confinement in the 5-m and 8-m Scyllac sector experiments is terminated due to a loss of stability or a loss of equilibrium or both. Theoretically, however, $m = 1$ instabilities are predicted when either $\ell = 1$ or $\ell = 0$ fields are added to a straight theta pinch, and such instabilities have been observed on Scylla IV-3. Preliminary determinations of the growth-rate scaling with wavelength were completed before Scylla IV-3 was decommissioned in June 1973. We intend to continue these studies on the new Scylla IV-P 5-m linear

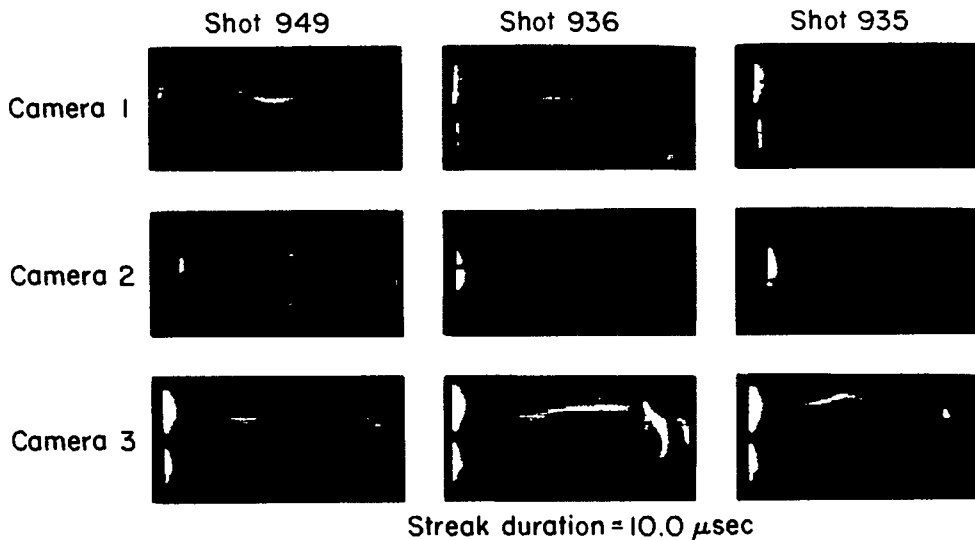


Figure II-27
 Demonstration of feedback force on Scylla IV-3. Shot 949 is a control shot showing $k \approx 0$ motion toward the feed slot. Shots 936 and 935 show the effects of applying $l = 0$ fields from the feedback modules with polarities to aid and oppose the instability, respectively. Streak camera orientation: Cameras 1 and 3 show stereoscopic views of the plasma at locations 90 cm from the east and west ends of the machine, respectively. The top picture of the pair shows motion in the horizontal plane with motion away from the feed slot appearing as an upward motion in the photograph. The bottom picture of the pair shows motion in the vertical plane (downward for a down-going image). Camera 2, located 135 cm from the east end of the machine, shows horizontal motion only.

theta-pinch machine as soon as that facility is available.

a. Sensitivity to Discharge Tube Position. It was observed that the $m = 1$ sideward motion of the plasma column in the presence of $l = 1$ or $l = 0$ fields was very sensitive to the position of the quartz discharge tube within the compression coil. This is especially true in the case of $l = 1$ fields. This effect is shown in Figure II-28, where the plasma trajectory, $\xi(t)$, is seen in the streak photographs to be a strong function of the tube position. The off-axis displacement indicated in the figure is measured from the empirically located equilibrium position for the plasma, which was ~ 1 mm from the coil center in a direction away from the feed slot. By appropriately "tilting" the discharge tube, the plasma $m = 1$ motion could be made essentially $k = 0$ along the entire column length.

The explanation for this effect is thought to be that the plasma implodes to the center of the discharge tube, regardless of the tube placement relative to the magnetic axis (i.e., equilibrium position). If we assume that the unstable plasma motion obeys the simple equation

$$\xi(t) = \xi_0 e^{\gamma t} \quad (37)$$

where ξ_0 is the initial displacement away from equilibrium and γ is the growth rate, then the tube displacement in this case can be identified with ξ_0 .

Figure II-29 shows a semilog plot of the plasma trajectory $\xi(t)$ vs time for the shots in Figure II-28, obtained by digitizing side-on luminosity profiles of the plasma. According to Eq. (37) these should produce parallel lines of constant slope γ , and this is seen to be the case. The growth

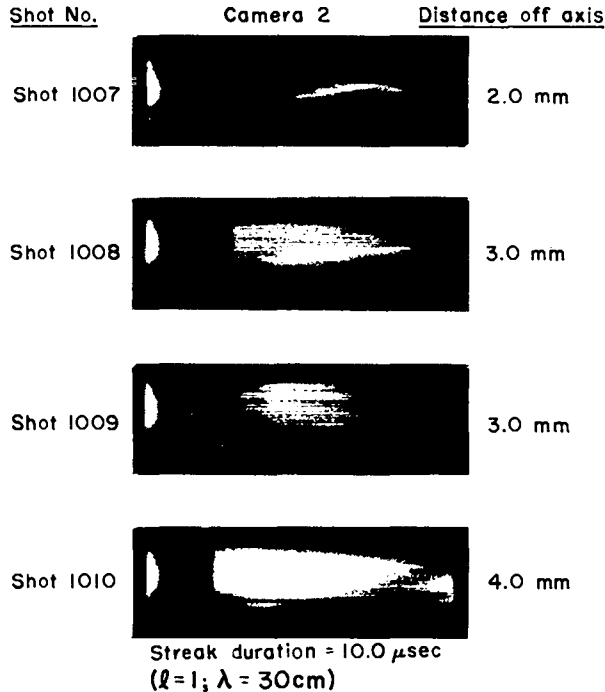


Figure II-28
Streak photographs showing the effect of discharge tube position on the $m=1$ instability motion in Scylla IV-3.

rate indicated by this graph is $\gamma_1 = 0.95 \times 10^6 \text{ sec}^{-1}$. In this manner we have verified the theoretical prediction that the growth rate γ has the same value for all shots shown in Figure II-28, although the appearance of the streak photographs does not immediately suggest this fact.

The discovery of the tube-displacement phenomenon gave rise to immediate concern over its implication for the Scyllac experiment, and the effect was subsequently verified there (cf. Sec. II-C). In the case of the Scylla IV-3 growth rate measurements, however, the tube displacement effect was used to advantage to control the plasma trajectory and to confirm Eq. (37) quantitatively over a wide range of experimental conditions. In order to measure widely different growth rates, which were a consequence of using different wavelengths and magnetic field strengths, B_ℓ/B_0 , in the various experiments, it was necessary that the column move at least 1-2 column diameters in the short time (4-5 μ sec) available before end effects influenced the

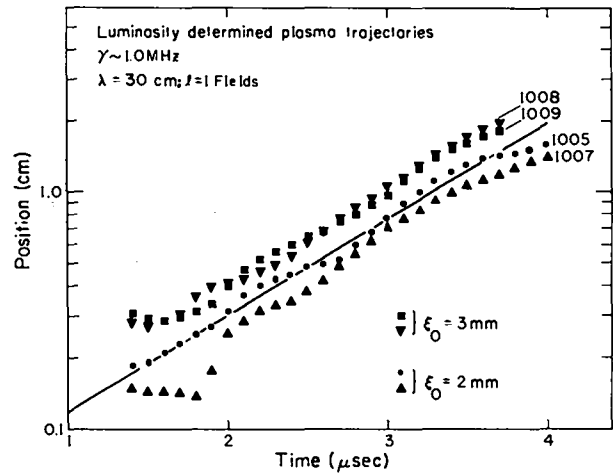


Figure II-29
Plasma displacement $\xi(t)$ vs time for the 30-cm wavelength $\ell=1$ experiment on Scylla IV-3 (same shots as in Figure II-30).

central plasma. In cases where this failed, accurate growth rate measurements could not be made.

b. $\ell=1$ Growth Rate Measurements.

Growth rates were measured for two $\ell=1$ wavelengths, $\lambda=15$ and 30 cm, using the computer-designed, helically grooved coils shown in Figure II-30, B and C. These coils produced essentially "pure" $\ell=1$ perturbation fields of magnitude $B_{\ell=1}/B_0 = 0.03$ and 0.06, respectively.

(1). Old Ordering. According to sharp-boundary theory for the "old ordering" ($\delta_1 \ll \epsilon \leq 1$), the $\ell=1$, $m=1$ growth rate is given by

$$\gamma_1^2 = h^2 v_A^2 \left[\frac{\beta(4-3\beta)(2-\beta)}{8(1-\beta)} \right] \epsilon^2 \delta_1^2 \quad (38)$$

where $\epsilon = ha$, $h = 2\pi/\lambda$ is the $\ell=1$ wave number, $v_A = B_0/(4\pi\rho_0)^{1/2}$ is the Alfvén speed, and δ_1 is the (normalized) helical distortion,

$$\delta_1 = \frac{1}{\epsilon(1-\beta/2)} \left(\frac{B_{\ell=1}}{B_0} \right). \quad (39)$$



A

B

C

Figure II-30
Three of the coils used in variable epsilon scaling experiments on Scylla IV-3.

- A. $\ell = 0; \lambda = 30 \text{ cm}, B_{\ell=0}/B_0 = 0.157$
 B. $\ell = 1; \lambda = 15 \text{ cm}, B_{\ell=1}/B_0 = 0.030$
 C. $\ell = 1; \lambda = 30 \text{ cm}, B_{\ell=1}/B_0 = 0.060$

If we assume that the plasma density is equal to the filling density multiplied by the compression ratio (an assumption verified by the interferograms), the growth rate can be written as

$$\gamma_1 = \frac{4.09 \times 10^7}{\sqrt{P}} \frac{B_0 a}{\lambda R_t} \left[\frac{\beta(4-3\beta)(2-\beta)}{(1-\beta)(1-\beta/2)^2} \right]^{1/2} \times \left(\frac{B_{\ell=1}}{B_0} \right) \quad (40)$$

in terms of experimental quantities. Here γ_1 is in sec^{-1} for B_0 in kG, a , λ , and R_t (the tube radius) in cm, and P (the filling pressure) in mTorr.

Simultaneous luminosity measurements were made one-half wavelength apart (7.5 cm and 15 cm, respectively) to measure δ_1 , the plasma radius a , and the column trajectory $\xi(t)$. The luminosity measurements were combined with the excluded flux measurements to yield $\beta(t)$ and $B_0(t)$ and with end-on hologram data to yield an independent

measurement of $\delta_1(t)$. Streak photographs were taken at three axial positions, the center one of which coincided with the luminosity viewing slot. Typical streak photographs from this center camera are shown in Figure II-31. Note the apparent $m = 2$ rotation.

Experimental growth rates derived from digitized streak and luminosity data generally agreed well, and also were reproducible from shot to shot (e.g., Figure II-29). The measured value of γ_1 for the conditions studied (45 kV, 10 mTorr) was $1.0 \times 10^6 \text{ sec}^{-1}$ for $\lambda = 30 \text{ cm}$, and $1.1 \times 10^6 \text{ sec}^{-1}$ for $\lambda = 15 \text{ cm}$, which is equivalent to agreement within experimental error. This confirms the predicted

$$\frac{1}{\lambda} \left(\frac{B_{\ell=1}}{B_0} \right)$$

scaling of Eq. (40). The measured value of $1.0\text{--}1.1 \times 10^6 \text{ sec}^{-1}$, however, is numerically in disagreement with Eq. (40) by roughly a factor of two. For our experiment typical

Streak photographs (2)
 Duration = 4.50 μ sec
 $\ell = 1$ fields ; $\lambda = 15$ cm

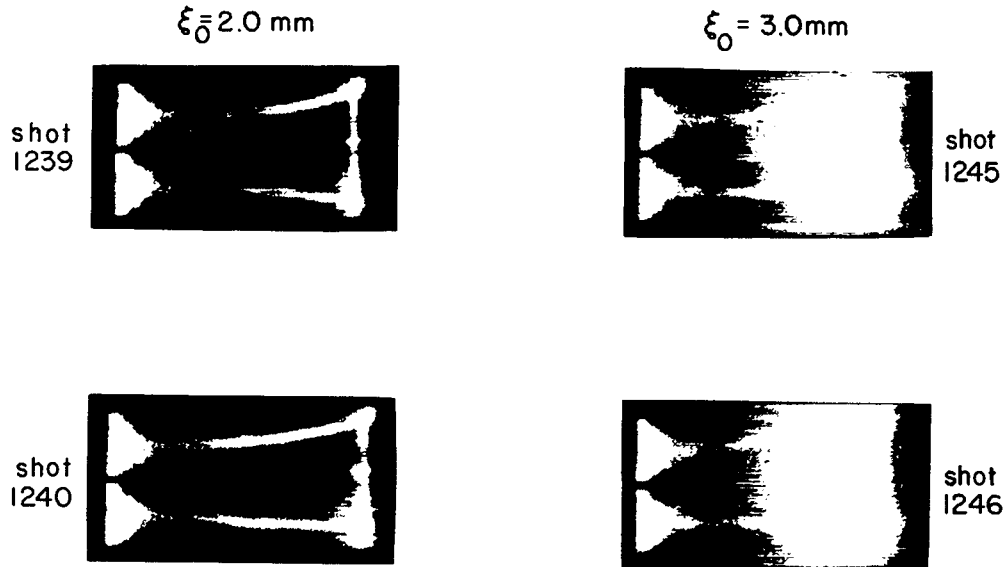


Figure II-31
 Stereoscopic streak photographs showing predominantly $m = 1$, $k \approx 0$
 plasma motion in the 15-cm wavelength $\ell = 1$ experiment on Scylla IV-3.

data values were $\beta = 0.57$, $a = 0.70$ cm, $B_0 = 40$ kG, $R_t = 4.2$ cm, $\lambda = 30$ cm, $B_{\ell=1}/B_0 = 0.06$, and $P = 10$ mTorr (for example, shot 1005 at $t = 4$ μ sec), in which case Eq. (40) predicts $\gamma_1 = 0.5 \times 10^6$ sec $^{-1}$.

(2). New Ordering. According to sharp-boundary theory with the "new ordering" ($\epsilon_1 \ll \delta_1 \leq 1$), the $\ell = 1$, $m = 1$ growth rate is given by

$$\gamma_1^2 = h^2 v_A^2 \left[\frac{\beta^5}{32(2-\beta)} \right] \delta_1^4 \quad (41)$$

which, following the above procedure, can be written in terms of experimental quantities as:

$$\gamma_1 = \frac{5.18 \times 10^5}{\sqrt{P}} \frac{B_0 \lambda}{a R_t} \left[\frac{\beta^5}{(2-\beta)(1-\beta/2)^4} \right]^{1/2} \times \left(\frac{B_{\ell=1}}{B_0} \right)^2 \quad (42)$$

[same units as Eq. (40)]. Since this equation predicts that γ_1 scales as

$$\lambda \left(\frac{B_{\ell=1}}{B_0} \right)^2,$$

the difference between the predicted and observed changes is a factor of 8 in the present experiment, which seems to be very strong evidence for the old ordering.

Furthermore, the calculated new-ordering value of γ_1 is much smaller than observed: $\sim 1.2 \times 10^4 \text{ sec}^{-1}$ for $\lambda = 15 \text{ cm}$, and $\sim 9.5 \times 10^5 \text{ sec}^{-1}$ for $\lambda = 30 \text{ cm}$.

We can calculate the relative ϵ , δ_1 ordering in our experiments. From the data values above we find $\epsilon = 0.30$, $\delta_1 = 0.15$ for $\lambda = 15 \text{ cm}$, and $\epsilon = 0.15$, $\delta_1 = 0.60$ for $\lambda = 30 \text{ cm}$. Thus the new ordering is theoretically applicable to the $\lambda = 30\text{-cm}$ experiment, and the old ordering to the $\lambda = 15\text{-cm}$ experiment. The old ordering gives the best agreement in both cases to the experimental data, however.

c. $\ell = 0$ Growth Rate Measurements.

Growth rates for the $m = 1$ mode were measured for two $\ell = 0$ wavelengths, $\lambda = 30 \text{ cm}$ and $\lambda = 90 \text{ cm}$, using the square-annular grooved coil shown in Figure II-30. The $\ell = 0$ field strength was $B_{\ell=0}/B_0 = 0.157$ for both wavelengths and the calculated harmonic content was about 15% of the periodic field on axis. At 45-kV bank voltage the field in a land was $B_L = 54 \text{ kG}$, and in a groove $B_G = 39 \text{ kG}$.

The procedure used to measure $\ell = 0$ growth rates was similar to that described above for the $\ell = 1$ experiments, with a few exceptions. End-on holography was of limited value in the $\ell = 0$ experiments because of the plasma bumps, and growth rates were measured separately in land and groove regions to check against the possibility of ballooning modes. In analogy to the $\ell = 1$ case, the sharp-boundary theoretical growth rate (for either old or new ordering) can be written in terms of directly measureable quantities as [same units as Eq. (40)]:

$$\gamma_0 = \frac{5.79 \times 10^7}{\sqrt{P}} \frac{B_0 a}{\lambda R_t} \left[\frac{\beta(3-2\beta)}{(2-\beta)(1-\beta)} \right]^{1/2} \times \left(\frac{B_{\ell=0}}{B_0} \right). \quad (43)$$

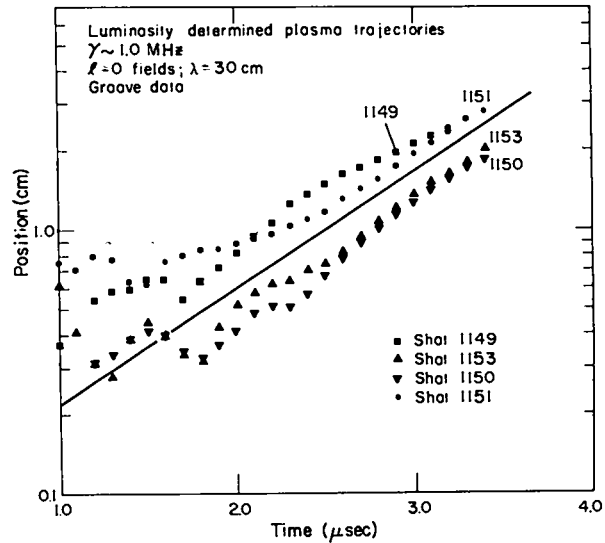


Figure II-32
Plasma displacement $\xi(t)$ vs time for the 30-cm wavelength $\ell = 0$ experiment on Scylla IV-3.

Typical results for the $\lambda = 30\text{-cm}$ case are shown in Figure II-32. These data were taken in a groove location and indicate a growth rate $\gamma_0 = 1.0 \times 10^6 \text{ sec}^{-1}$. Similar data taken in a land indicate $\gamma_0 \approx 1.1 \times 10^6 \text{ sec}^{-1}$, which is equivalent to agreement within experimental error. Typical plasma parameters (the averages of many shots at time $t = 2.3 \mu\text{sec}$, when one of the two holograms was exposed) were $\beta_L = 0.57$, $\beta_G = 0.93$, $B_L = 54 \text{ kG}$, $B_G = 39 \text{ kG}$, $a_L = 0.70 \text{ cm}$, $a_G = 1.40 \text{ cm}$, $\lambda = 30 \text{ cm}$, $R_t = 4.2 \text{ cm}$, and $P = 10 \text{ mTorr}$. Forming land-groove averages in the usual way gives $B_0 = 46.5 \text{ kG}$, $\bar{\beta} = 0.73$, and $\bar{a} = 1.05 \text{ cm}$, and hence a theoretical value of $\gamma_0 = 1.8 \times 10^6 \text{ sec}^{-1}$. Thus the measured $\ell = 0$ growth rate is about 0.5 - 0.6 times the sharp-boundary theoretical prediction, which is in disagreement in the opposite direction from that found in the $\ell = 1$ case.

A further check on these results was provided by the diffuse boundary $\ell = 0$ code, written by B. Marder (Q-6). When the experimental values quoted above were used as input parameters to this code, the γ_0 growth rate was computed numerically. The result

Streak photographs
 $\ell = 0$ fields ; $\lambda = 90$ cm

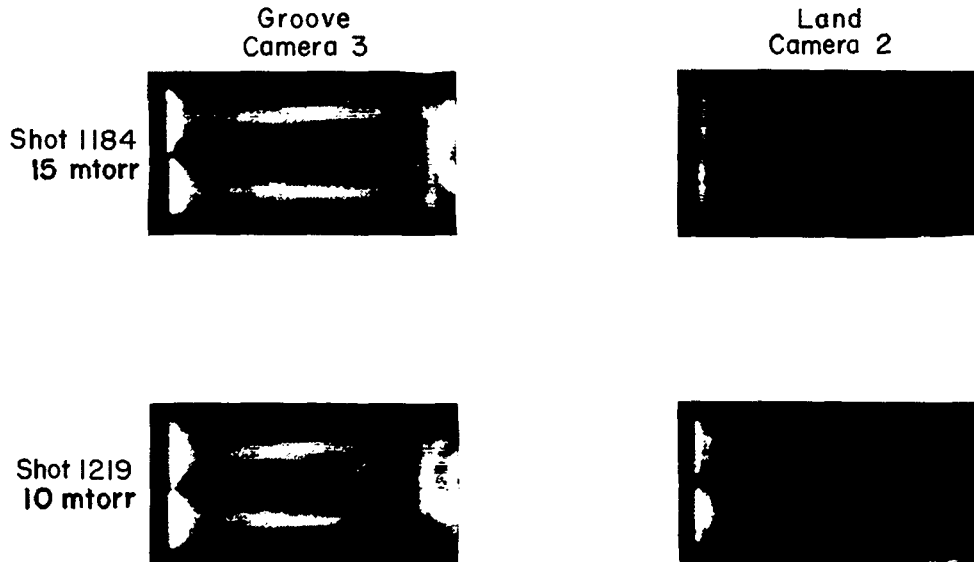


Figure II-33
 Stereoscopic streak photographs of $m = 1$ and $m = 2$ plasma motions for the 90-cm wavelength $\ell = 0$ experiment on Scylla IV-3.

was $\gamma_0 = 1.25 \times 10^6 \text{ sec}^{-1}$, which is intermediate in value between the sharp-boundary theoretical and experimentally measured results.

In the $\lambda = 90$ -cm case the growth rate was too slow to be measured accurately before end effects set in, as shown in Figure II-33. This result was not totally unexpected since γ_0 scales as $1/\lambda$. Because of the long equilibration time, commensurate with the longer wavelength, there was also some doubt whether axial pressure equilibrium was established in the available 4-5 μsec . Figure II-33 also shows the unusually well-developed $m = 2$ distortions of the plasma column which were apparent in both land and groove regions in this experiment. These distortions have not been analyzed in detail, but show generally damped behavior in time.

These scaling results will be reported in more detail in a planned journal article.

G. SCYLLA 1-B. (K. F. McKenna, R. Kristal, F. C. Jahoda, R. F. Gribble, K. S. Thomas, E. L. Zimmermann, F. T. Seibel)

1. Introduction

The transient interaction between the imploding plasma and driving magnetic piston field in low-density ($10^{12} \text{ cm}^{-3} \leq n_0 \leq 6 \times 10^{13} \text{ cm}^{-3}$) fast magnetic compression θ -pinch devices has received considerable investigation.¹⁸⁻²⁰ In these experiments the implosion behavior can generally be described, depending on the density range, by either snowplow or free particle models. However, in Scyllac-type devices which operate at higher fill densities ($n_0 \sim 10^{15} \text{ cm}^{-3}$) the plasma-piston field interaction has not been studied and, accordingly, the processes involved in the implosion event are not well understood. A basic knowledge of these processes is fundamental to the proposed staged θ -pinch concept and is required for a better understanding of existing θ -pinch devices.

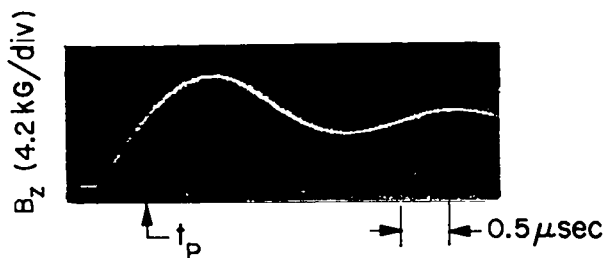
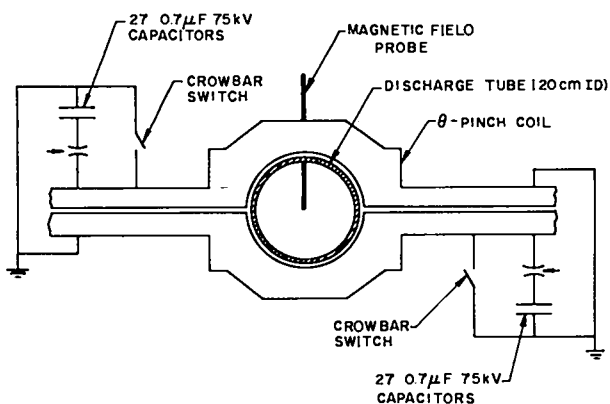


Figure II-34

Schematic of the Scylla 1-B θ -pinch apparatus. t_p indicates time of plasma arrival on axis.

The Scylla 1-B linear θ -pinch has been constructed in order to investigate the implosion phase at filling densities and E_θ 's characteristic of conventional θ -pinches and to explore the diagnostic problems inherent in the study of transient nanosecond time scale events. Operation with plasma began in June 1973 and experiments are currently being conducted.

2. Apparatus

A schematic of the Scylla 1-B linear θ -pinch apparatus, together with a vacuum magnetic field waveform taken at 40-kV main bank voltage, is presented in Figure II-34. The apparatus is shown in Figure II-35. Scylla 1-B has a maximum capacitor energy storage of 106 kJ at 75 kV, and a two-feed-point compression coil 100 cm long and 22 cm in diameter. The discharge tube has a

20-cm i.d. Experiments with 10-mTorr D_2 filling pressure have been completed at a main bank voltage of 40 kV. The initial azimuthal electric field at the inside wall of the discharge tube was 0.7 kV/cm and a peak crowbarred compression field of 9.5 kG was obtained 1.25 μ sec after main discharge initiation.

3. Preionization Studies

Preionization of the 10-mTorr D_2 fill gas was accomplished with a 500-kHz capacitor discharge through the compression coil. The 0.7- μ F preionization capacitor was charged to 55 kV. Time-resolved measurements of the preionization discharge plasma radial electron density distribution were carried out with an end-on He-Ne coupled-cavity interferometer; data were collected in 1-cm radial increments. Integration of the resulting density profiles over the tube diameter indicated that 15% of the initial fill deuterium atoms were ionized at the time of main bank discharge (14.5 μ sec after preionization discharge). At that time, a spatially uniform -60 G trapped preionization field (B_z opposite to direction of main compression field) was detected within the preionized plasma by internal magnetic field probes.

The magnetic field probe contained three identical ten-turn B_z coils with a 2-cm separation between coils. The 0.16-cm-diameter coils were mounted within a sealed 0.65-cm-diameter alumina tube and inserted radially through the discharge tube at an axial position 17 cm from the tube center. Radial surveys of the preionization discharge were made in 1-cm increments from the discharge tube axis ($r = 0$ cm) to the tube wall ($r = 10$ cm). Perturbations of the plasma by the probe were investigated and found to be negligible.

4. Main Discharge Magnetic Field Profiles

Profiles of the transient magnetic field distribution during the main discharge implosion phase were obtained from the internal field probe data. Measurements

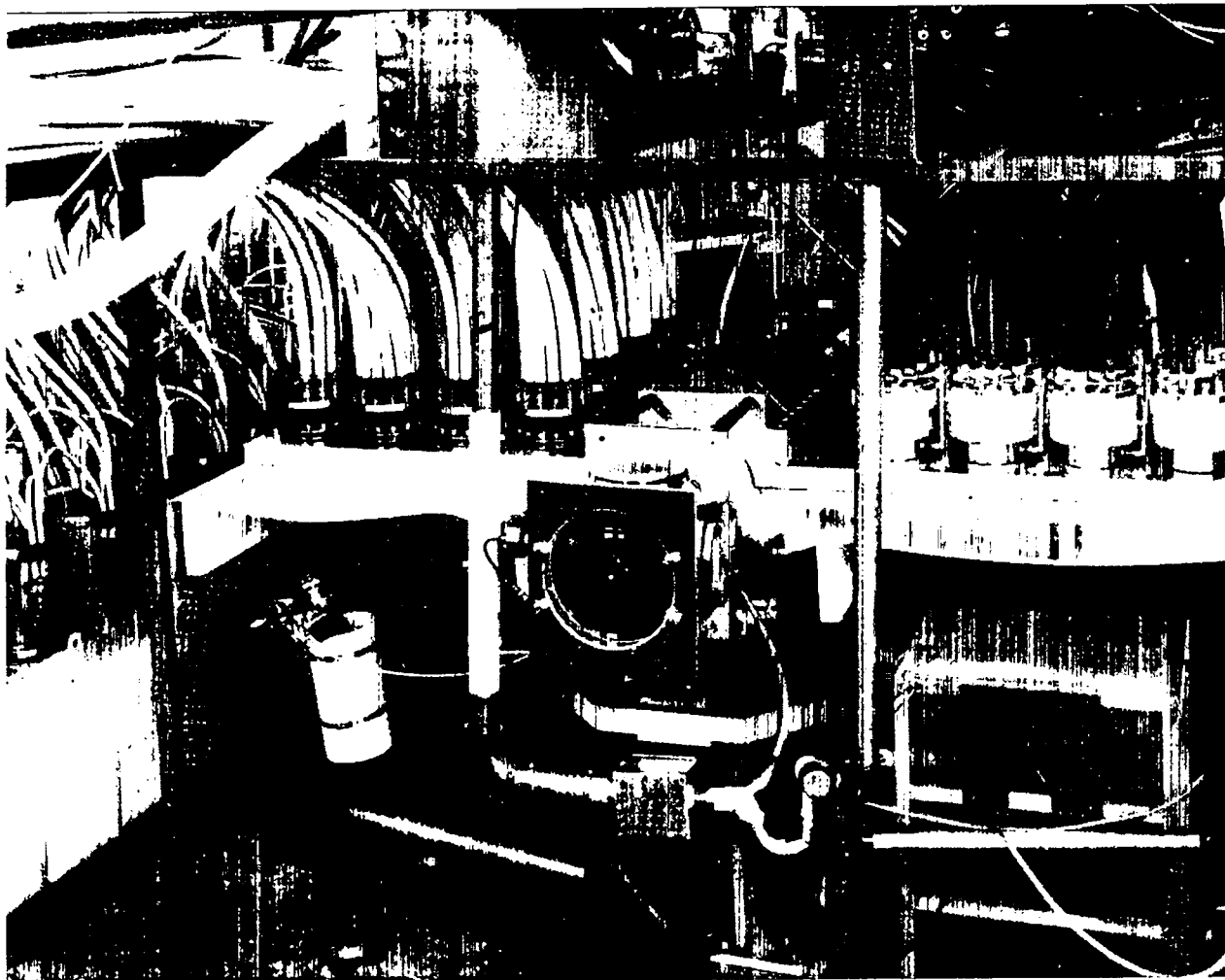


Figure II-35
Scylla 1-B Linear θ -Pinch Experiment.

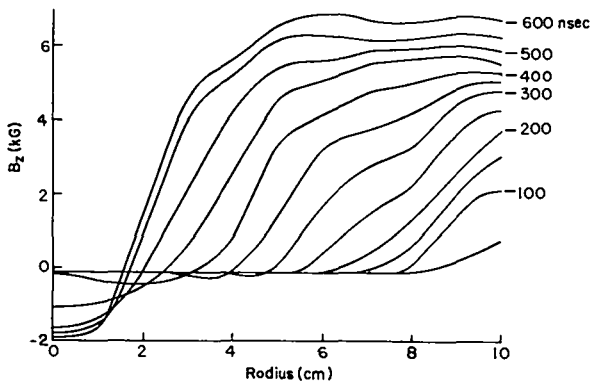


Figure II-36

Magnetic field profiles during radial plasma implosion, reconstructed from magnetic probe data. The profiles are shown in 50-nsec time increments.

were made in 1-cm increments from $r = 0$ to $r = 10$ cm. The time development of the magnetic-piston field, reconstructed from the magnetic probe data, is presented in Figure II-36. The profiles are shown for 50-nsec time increments. The magnetic-piston sheath accelerates to a maximum velocity U_s of 1.9×10^7 cm/sec at about 400 nsec. The piston sheath thickness halfway through the implosion ($r = 5$ cm, $t = 350$ nsec) is about 2 cm. The sheath thickness was determined from the tangent slope intercept technique. Rapid deceleration of the imploding field occurs during the initial formation of the plasma column; the piston field is finally stopped by the kinetic pressure of the compressed plasma at about 600 nsec. At this time, a compression ratio η (ratio of tube radius to plasma radius) of about 3.8 is indicated from the field profiles. The nearly complete exclusion of main field from the compressed plasma column indicates a $\beta \sim 1$ plasma. A similar observation was made by Keilhacker et al.¹⁹ at initial densities $n_0 \geq 10^{13}$ cm⁻³. The formation of a field-free, $\beta \sim 1$, plasma column was interpreted as resulting from the separation of plasma ions and magnetic field by elastic ion

reflections from the imploding magnetic piston (free-particle model).

It is of interest to note that the observed magnetic field penetration rate during the implosion requires plasma resistivities several hundred times higher than classical. However, at the end of the implosion phase the compressed trapped pre-ionization field (Figure II-36) is not annihilated and remains within the plasma column for the duration of the experiment. Such behavior implies a sharp drop in resistivity within the compressed plasma. Accordingly, if microinstabilities are responsible for the anomalous resistivity during the implosion,²¹ then such instabilities are apparently not supported in the plasma column.

5. Excluded Flux Measurements

The effective radius at which magnetic flux is excluded from the imploding plasma can be determined from standard differential magnetic loop probe measurements which are obtained totally external to the plasma. The same measurement can be made using the reduced internal magnetic field profiles discussed above. Defining the excluded flux, $\Delta\phi$, by

$$\Delta\phi = \int_0^{R_w} \left[B_{R_w}(t) - B_i(r,t) \right] 2\pi r dr \quad (44)$$

where B_{R_w} is the magnetic field measured at the $r = 10$ -cm radial position which coincides with the inner radius of the discharge tube, and B_i is the internal field determined from the internal magnetic field probe data, the effective excluded flux radius, R_ϕ , is then calculated from the expression

$$R_\phi = \sqrt{\frac{\Delta\phi}{B_{R_w}(t) \pi}} \quad (45)$$

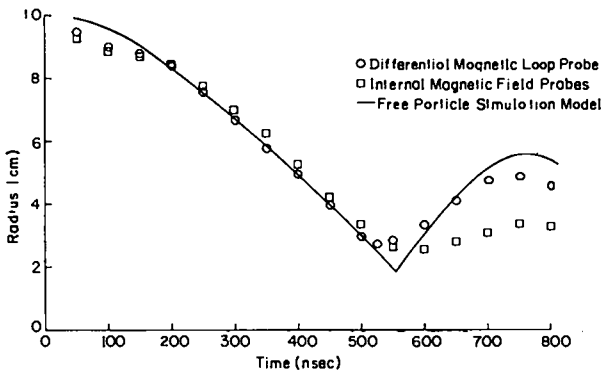


Figure II-37
Experimental and calculated plasma excluded flux radius.

The excluded flux radius calculated from the differential magnetic loop probe data and from integration over the internal field profiles, as discussed above, is presented in Figure II-37. The imploding current sheath dynamics are clearly identified by both diagnostics, each indicating the development of a nearly constant sheath velocity of 1.9×10^7 cm/sec.

The time-to-maximum-plasma-compression and the minimum-excluded-flux radius, indicated by each diagnostic, also display satisfactory agreement. A significant divergence in the two excluded flux radius measurements after completion of the implosion phase is noted. Nevertheless, the relatively good agreement between these two completely different techniques during the implosion phase serves as an effective check on the consistency and validity of the experimental data and diagnostics. Furthermore it increases confidence in the excluded flux measurements on the Scyllac sector, where no cross-checks against internal probes have been made.

6. Holographic Interferometry

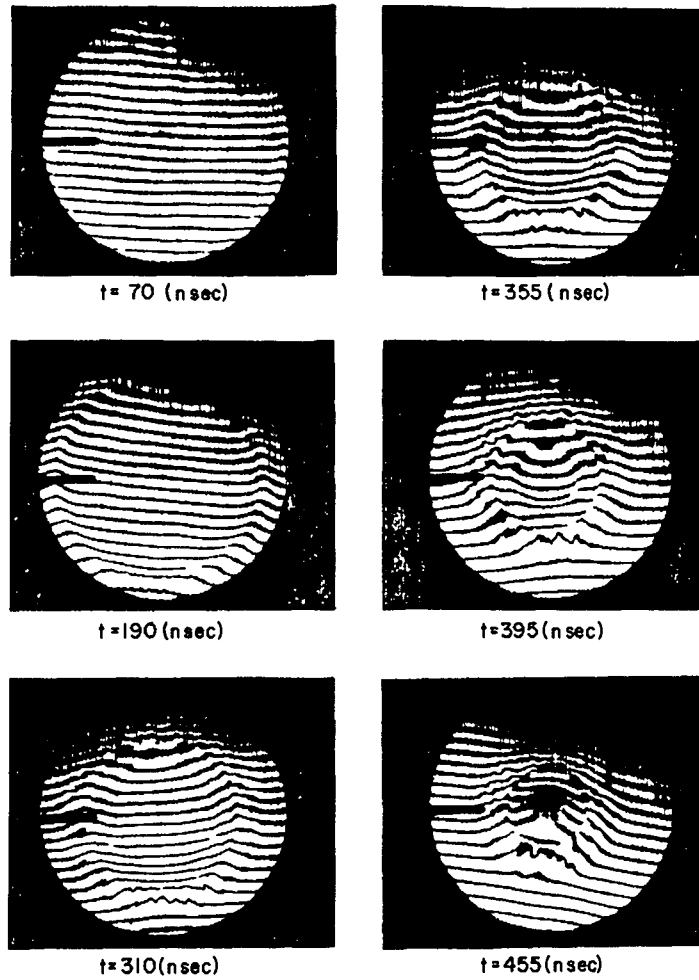
The imploding-plasma electron density distribution was measured by means of a 30-nsec pulsed holographic ruby laser interferometer. A double-pass, modified Michelson end-on system was used to double the interferometer sensitivity. This

technique has a 1/10 fringe shift resolution which corresponds to $n_e \approx 1.6 \times 10^{14}$ cm⁻³ for a 1 m length of plasma. Figure II-38 shows interferograms taken at various times during the radial plasma implosion. The data were collected with a filling pressure of 10 mTorr D₂ and 40-kV main bank voltage. Each interferogram was obtained from a separate plasma discharge. The entire 20-cm diameter of the discharge tube was illuminated by the laser light. The tip of the magnetic field probe, seen in the interferograms, was located 5 cm from the discharge tube axis. At early times during the implosion ($t \lesssim 190$ nsec) a relatively smooth density distribution is observed. At later times a definite structure develops (Figure II-38). Large-scale flute-like instabilities can be seen on the trailing edge of the density distribution.

Interferograms of the compressed plasma column are shown in Figure II-39. Spatial integration of the reduced plasma column density profiles, $n_e(r)$, indicated that all of the initial fill gas was swept up by the magnetic piston field. Although only 15% of the fill gas was ionized at the time of main bank discharge, the remaining neutral particles were ionized and swept up during the implosion process. At the termination of the plasma implosion ($t \approx 600$ nsec), a peak density on axis, $n_e(0)$, of 7×10^{15} cm⁻³ was obtained. A compression ratio $n = 3.8$ was indicated from the half-width of the approximately Gaussian $n_e(r)$ profile, in good agreement with that derived from the magnetic field profiles. After a few radial oscillations the plasma column settled to a mean radius of about 3.8 cm ($\eta = 2.6$). Over this period ($t \geq 1.2$ usec) an average compressed plasma kinetic temperature ($T_e + T_i$) of 500 eV was determined from pressure balance.

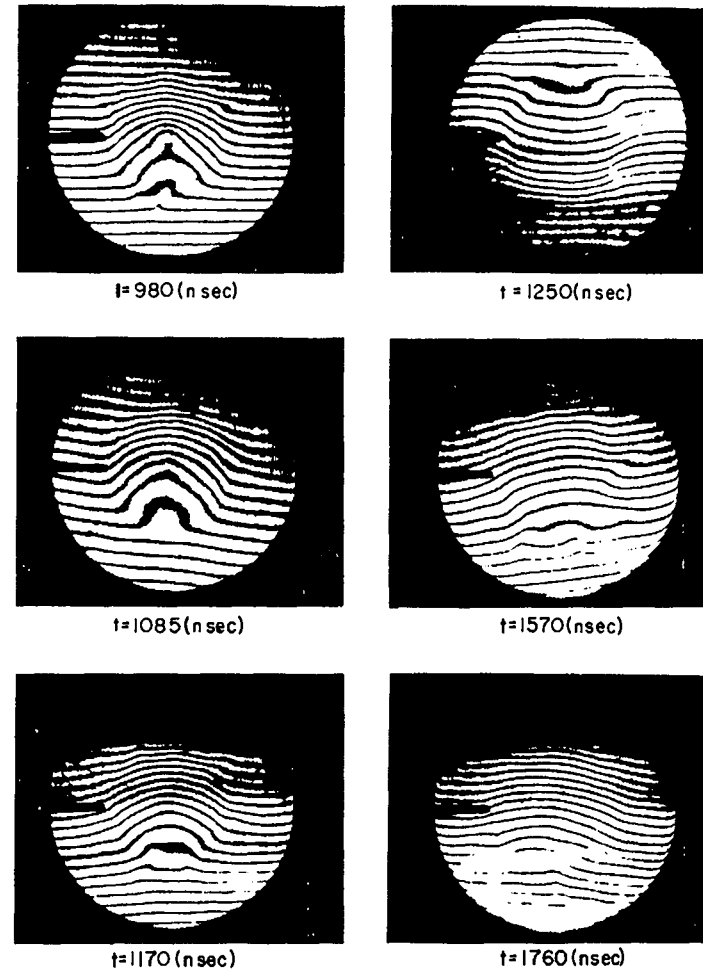
7. Plasma-Magnetic Field Interaction During the Implosion Phase

Profiles of $n_e(r)$ and $B_z(r)$ at fixed times during the implosion, derived from



Plasma Radial Implosion

Figure II-38
Time sequence of interferograms taken during the plasma implosion phase.



Confined Plasma Column

Figure II-39
Time sequence of interferograms taken during the quiescent plasma column phase.

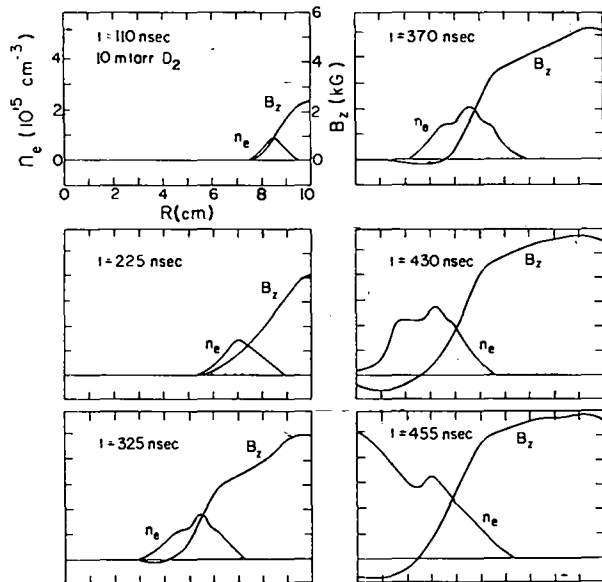


Figure II-40
 Implosion profiles of $n_e(r)$ and $B_z(r)$ at fixed times, reduced from interferograms and magnetic field probe data.

the interferograms and magnetic field probe data, are presented in Figure II-40. At 110 nsec the density and magnetic field profiles coincide, a behavior indicative of snowplow dynamics. With increasing time, the density front accelerates away from the piston field, attaining a velocity $U_p = 1.5 U_s$ immediately prior to plasma arrival at the discharge tube axis. This indicates that a fraction of the particles incident on the magnetic piston is reflected, generating a density distribution ahead of the piston field. For total elastic particle reflection, $U_p = 2 U_s$. The difference between the observed velocity of the plasma leading the magnetic piston and that predicted from the free-particle model may be a result of the current sheath acceleration during the implosion. In addition, the reflection properties of the piston could be altered by instabilities within the current sheath.¹⁸

A numerical circuit code was used to simulate the Scylla 1-B plasma and driving electrical circuit.²² In the simulation the current sheath dynamics and plasma density

distribution were calculated during the radial implosion; electron heating and thermal conduction were not included. Both free particle and snowplow models of the plasma implosion were simulated. The excluded flux radius predicted by the simulation code using the free-particle model is shown in Figure II-37. Comparison of the experimental data with these preliminary calculations indicates that the plasma-magnetic field interaction is most nearly described by the free-particle model.

H. DIAGNOSTICS

1. Excluded Flux Measurements (W. R. Ellis)

Excluded flux measurements in the Scyllac sector have proceeded in the past without the benefit of a direct, in-place calibration on the experiment. The lack of an experimental calibration point was recognized early as a potentially serious matter for the beta measurements on Scyllac, since a calibration point is absolutely essential for quantitative beta measurements. The problem arose primarily from a desire not to risk discharge-tube breakage or contamination by introducing a section of copper pipe or other conductor through the ends of the discharge tube into the central regions of the curved sector where the loop-probe diagnostics were located. A secondary reason was the knowledge that the traditional copper-pipe method would probably have to be abandoned on the full torus anyway, so a reliable alternative was a high priority item.

The alternative method which has been developed and successfully used on Scyllac involves a bench-top calibration of various electrical components of the loop-probe system (e.g., difference-circuit losses, RC integrator time constants, loop area, voltage divider ratio, cable losses, etc.) and a subsequent theoretical calculation of the desired calibration point. The method was described briefly in the last annual report (LA-5250-PR, pp. 38-40).

Recently, a series of $\ell = 1$ and $\ell = 0$ experiments on the 3-m linear theta-pinch Scylla IV-3 presented the opportunity to test our new calibration method against the older copper-pipe technique. The results of this test were very favorable. The two methods showed a difference of less than 3% in the determination of the plasma beta. Furthermore the indicated value of $r_{\text{eff}}(t)$ for the copper pipe was within 4% of the measured radius of the pipe and constant in time for the first 7 μsec (before skin effects become significant) to within 1.5%.

An LA report describing the Scyllac beta measurement in more detail is planned for the near future.

2. Helmholtz Coil (W.R. Ellis, E.M. Little)

A small Helmholtz coil has been built to serve as a magnetic field standard for calibrating small search coils for use in probing and in excluded flux measurements.

A Helmholtz coil is made by placing two identical current-carrying circular hoops a distance apart equal to their radius. If a multiturn coil is desired it can be built as shown in Figure II-41, where each pair of turns meets this requirement. Such a coil produces a field uniform to within 1% over a relatively large cylindrical volume near its center.

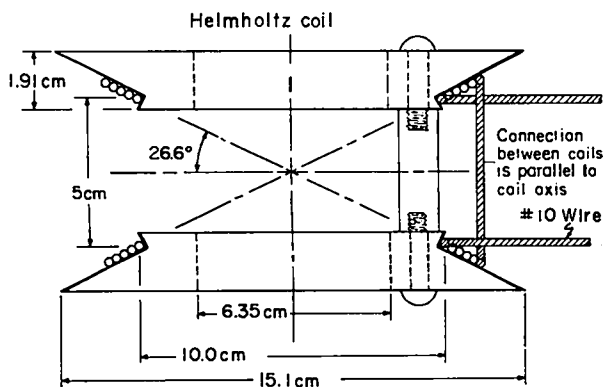


Figure II-41

Coil wound with No. 10 magnet wire. All other material phenolic stock except nylon screws.

The Helmholtz coil shown in Figure II-41 was constructed and probed with an uncalibrated search coil to obtain relative plots of $B_z(r, \theta, z)$. These plots were then compared to predictions from a computer code provided by D. Baker (Q-6). The cylindrical volume defined by the Helmholtz coil is roughly 50 mm long by 100 mm in diameter. According to the code, the B_z magnetic field is uniform to within 1% within a smaller volume roughly 30 mm long by 25 mm in diameter. The probing results confirmed the code predictions.

The Helmholtz coil was designed to accommodate a variable frequency oscillator current source supplied by R. Gribble (Q-7). This oscillator is limited to ~ 2 amp max at a frequency of 50 kHz for the Helmholtz coil inductance of 13 μH , and is very steady. For higher currents (and hence larger B_z), a series resonant circuit was formed by adding capacitors in series with the coil. For example, with $C = 0.91 \mu\text{F}$ the resonant frequency was 50.6 kHz and I_{max} was 51 amp. At this current level the coil and capacitors become very hot to the touch in a minute or two, and the current must be dropped to ~ 10 amp if steady-state operation is desired. At 10 amp the magnetic field on axis is ~ 8 gauss, and dB_z/dt is $\sim 2 \times 10^6$ gauss/sec at 50 kHz.

3. A Polychrometer for Thomson Scattering on Scyllac (R. E. Siemon)

A three-grating polychrometer has been designed to transmit efficiently a broad passband of light ($\Delta\lambda = 1200 \text{ \AA}$) while rejecting a particular wavelength ($\lambda = 6943 \text{ \AA}$). Transmission efficiencies of about 20% have been obtained coupled with rejection ratios of 10^{-10} to 10^{-12} . This instrument has permitted temperature measurements in Scyllac despite the quartz discharge tube surrounding the plasma which precludes the use of an entrance port, an exit-port, a beam dump, or a viewing dump.

Thomson scattering, by which plasma electrons redirect and doppler shift a portion of an incident laser beam, is an

exceedingly useful plasma diagnostic technique.^{23,24} One of the practical obstacles to its use, however, is the small Thomson cross section which makes the scattered light intensity, I_s , many orders of magnitude weaker than the incident laser beam intensity I_0 . Typically, for a portion of the scattered spectrum, one has

$$I_s = 10^{-29} n_e I_0 \quad (46)$$

where n_e is the plasma electron density (cm^{-3}). For example, in Scyllac $n_e \sim 10^{16} \text{cm}^{-3}$ so that $I_s \sim 10^{-13} I_0$. This small fraction is made acceptable in most experiments by elaborate procedures which permit almost none (i.e., less than 10^{-13} or so) of the incident laser light to reach the detector. However, in the geometry required by our experiment, the quartz tube surrounding the plasma directs a large fraction of the incident beam ($\sim 10^{-3}$) toward the detector. We have therefore chosen to rely entirely on the spectral shift of the scattered light to distinguish it from the incident light and thus we require an instrument with far greater rejection of an unwanted wavelength than the typical $10^{-3} - 10^{-5}$ found for single filters or gratings.

Our basic approach is to use gratings in series to permit the consecutive rejection of ruby laser light ($\lambda_0 = 6943 \text{ \AA}$) while transmitting the desired spectrum. The Thomson spectrum, for 90° scattering from the Scyllac plasma (electron temperature about 1.0 keV), is a Gaussian spectrum centered on λ_0 with $1/e$ half-width of about 600 \AA . To record this broad spectrum for a single laser pulse we need a polychromator with a broad passband which rejects the stray light at λ_0 . Double monochromators that have been used in Thomson scattering experiments heretofore transmit a narrow passband and thus require many pulses of the plasma device and laser to scan the spectrum.^{25,26} Our attempts to

meet these requirements led to the rediscovery of the varioilluminator principle first described by van Cittert²⁷ in 1923 and recently discussed by Lipsett et al.²⁸ The basic idea for a series of gratings is to alternate the direction of dispersion for each grating. Arranged in this manner, three gratings will reject stray light at each stage, transmit a wavelength passband of arbitrary width, and provide a final dispersion equivalent to a single grating. The advantage for stray light rejection is illustrated in Figure II-42 where we compare the result of 1) reversing the dispersion of the first two gratings and 2) adding the dispersion of the first two gratings. We imagine in this figure that λ_0 is to be rejected while preserving λ_1 and λ_2 . After one grating we have λ_0 , λ_1 , and λ_2 separated according to the dispersion of the grating. We can eliminate most

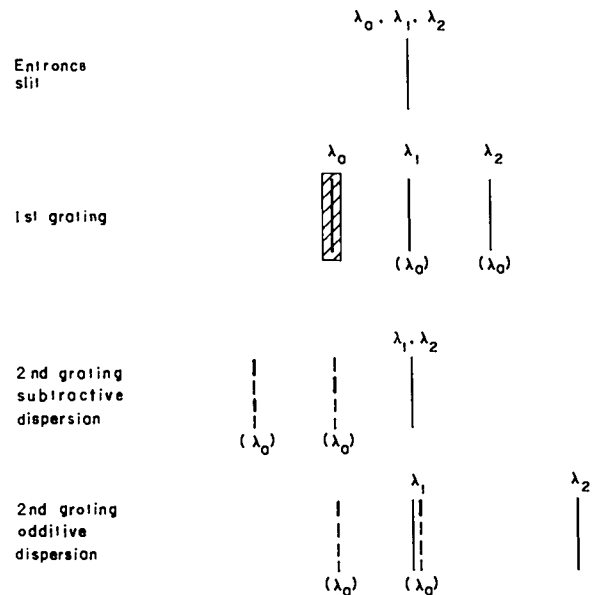


Figure II-42

The behavior of three discrete wavelengths is displayed at 1) the entrance slit assumed to be very narrow, 2) at the exit plane of the first grating stage which is also the entrance plane of the second grating stage, and 3) at the exit plane of the second grating stage for both additive and subtractive dispersion. Stray light indicated by (λ_0) is best rejected by subtractive dispersion.

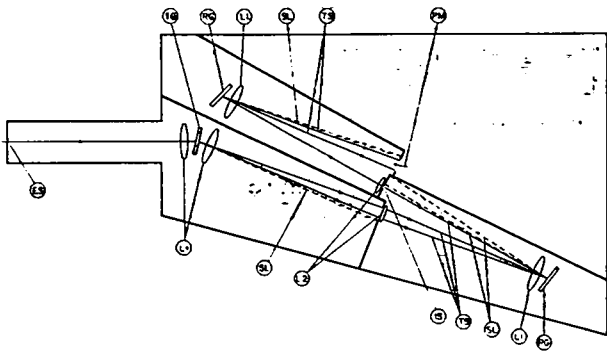


Figure II-43

Diagram of the three-grating polychrometer. ES, entrance slit; L1, collimating lens; TG, transmission grating; SL, stray light; L2, relay lens; TS, transmitted spectrum; RG, reflection grating; IS, intermediate slit; PM, photomultiplier array.

of λ_0 with a mask but a small amount of λ_0 is still mixed with λ_1 and λ_2 due to instrumental stray light from the first grating. If the second grating is reversed in dispersion, λ_1 and λ_2 superimpose in the focal plane while their stray light component λ_0 is diffracted to the side where it can again be eliminated with a mask. On the other hand, if the dispersion of the second grating is the same or additive, the separation of λ_1 and λ_2 doubles but the stray light mixed with λ_2 from the first grating falls on λ_1 . It becomes clear that if we are interested in only one wavelength we can use the two gratings in either configuration, but if we wish to observe λ_1 and λ_2 we must reverse the dispersion of the second grating and use a third grating for the final dispersion. We have considered the case where

$$\lambda_2 - \lambda_0 = 2(\lambda_1 - \lambda_0) \quad (47)$$

but except for this constraint λ_2 and λ_1 are arbitrary so the problem exists for half of the desired spectrum.

Figure II-43 shows a ray diagram for our three-grating polychrometer constructed according to the above principle. Gratings

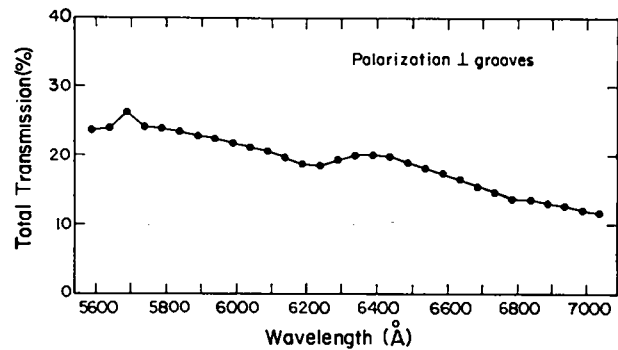


Figure II-44

Optical transmission efficiency vs λ for the three-grating polychrometer with no masks to reject λ_0 .

are used in the Littrow manner. A single incident ray at the entrance slit, ES, is diffracted by the first (transmission) grating, TG, permitting stray light, SL, to be separated from the transmitted spectrum, TS. The behavior of stray light at each stage is indicated with dashed lines. Lens L2 relays light to the second (reflection) grating, RG, where due to the grating's orientation it recombines the transmitted spectrum into a single ray (subtractive dispersion). The transmission grating mixes a relatively small (but large in absolute magnitude) component of λ_0 light with the transmitted spectrum. This component, being of a different wavelength, is diffracted by the reflection grating as shown by the dashed lines and is stopped by a mask at the intermediate slit, IS. Beyond the intermediate slit, which is the same width as the entrance slit, the light is dispersed by the third grating and detected by an array of photomultipliers, PM, illuminated through acrylic plastic light pipes. The last stage, consisting of a grating used as in a conventional polychrometer, provides the final rejection of λ_0 as shown with the dashed line. Only a ray on axis has been considered in this discussion, but because of the collimation lenses, L1, the

argument can be extended to include all rays which illuminate the gratings.

The machine-ruled (replica) gratings obtained from Bausch and Lomb (102 mm x 102 mm with 600 g/mm) were selected for high efficiency and freedom from ghosts. In Figure II-44 the transmission efficiency vs wavelength is displayed for the combined three-grating system using light with the same polarization as the Thomson spectrum (E perpendicular to grooves). The efficiency is less for the other polarization. The total transmission of stray light is very small and thus difficult to determine experimentally. Furthermore it varies with wavelength, becoming smallest for wavelengths furthest from 6943 Å. We found approximately 10^{-10} at 6850 Å and 10^{-12} at 5500 Å. This could probably be further improved by the use of holographic gratings. For the most part stray light is relayed by the gratings themselves although specular reflections from the collimation lenses of the last two stages form a comparable source.

The lenses L1 (focal length 629 mm and diameter 128 mm) are telescope objectives available from A. Jaegers Optical Corporation, as are the lenses L2 having one-half the focal length and the same numerical aperture. The entrance slit width (1.1 mm) determines the minimum resolvable pass-band and the diameter of lens L2 determines the total passband transmitted. The linear dispersion of the instrument is 27 Å/mm and the numerical aperture is 1:5.7.

In summary we have developed a method for making Thomson scattering measurements in the presence of an extraordinary stray light level. It should be mentioned that such a high stray light level prevents density calibrations with spectrally unshifted Rayleigh scattering and if such calibrations are essential one has to prevent the stray light with conventional methods. On the other hand, this approach is appealing in that the usual tedious alignment procedures attendant to a Thomson

scattering experiment are circumvented. The incident laser beam needs no complicated apertures and is thus more accessible for ease in alignment. The resulting ease of installation and time saved thereby is of particular significance to a large experiment such as Scyllac.

4. Side-on Holographic Interferometry System (R. Kristal)

We have developed a system for making holographic interferometric measurements of the Scyllac plasma density profile. The plasma is probed side-on through the quartz discharge tube using HF laser emission at 2.8 μm as the source. The system is ready for installation on Scyllac.

The optical layout is shown in Figure II-45. The source is an HF oscillator-amplifier combination emitting up to ~ 2 joules in single mode pulses 100 nsec long. Output pulse waveform is shown in Figure II-46. A photograph of a typical laser module, suspended above its insulating oil tank, is shown in Figure II-46. Line

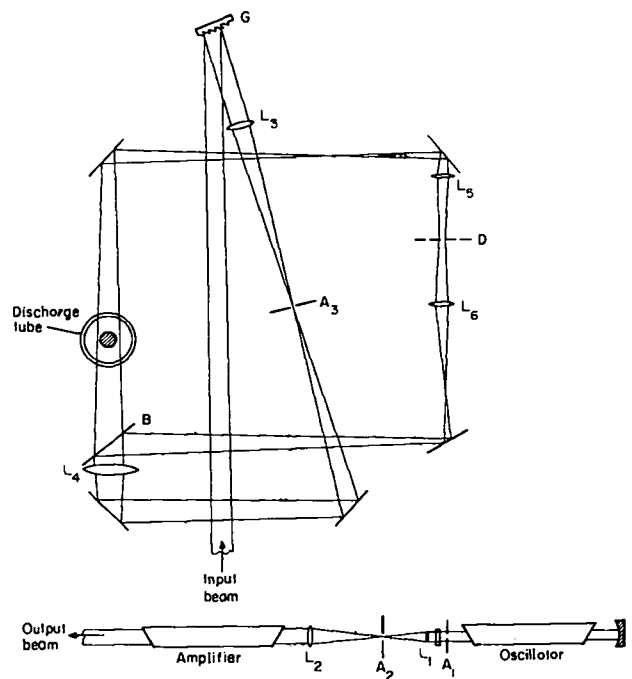
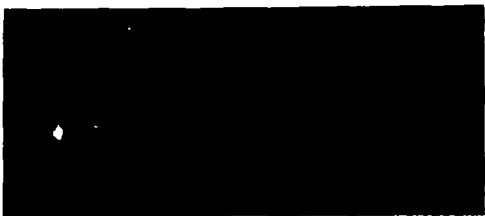


Figure II-45
HF laser side-on holographic interferometry layout.



A



B

Figure II-46

- A. HF laser module.
- B. Output pulse waveform, 100 nsec/div.

selection is accomplished externally by a plane reflectance grating setup. The beam is then allowed to expand to ~ 5 cm before entering the discharge tube to cover the region of interest. Lens L_4 provides a convergent beam into the tube to compensate for the negative lens effect of the tube on a collimated beam. The detector plate, D, is a thin bismuth film (200 \AA), exposed by local evaporation. To provide enough energy to expose the film, the beam size is reduced by about 5:1 by imaging lenses L_5 and L_6 in the scene and reference beams. Since the detector plate is not optically thick, scene and reference beams can be incident from opposite sides. This method is more flexible than the conventional

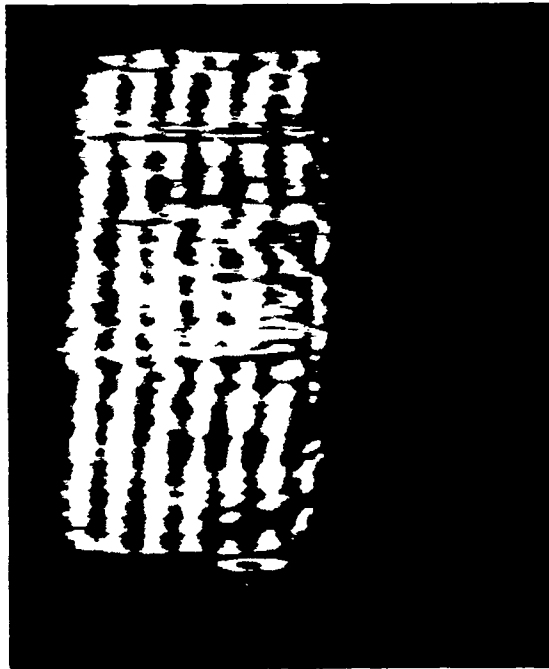


Figure II-47

Double exposure holographic interferogram through quartz discharge tube.

method in terms of fringe spacing and direction. Coarse background fringes are introduced by tilting the plate between exposures.

Figure II-47 shows a double exposure interferogram taken through the quartz tube. This was done at an interim stage in the development. The coarse fringes run perpendicular to the tube axis. Image size is about 1.3 by 2.7 cm and the fine fringe spacing is in the range of several hundred lines/mm. Playback photography was done in diffracted white light. Resolution at present is limited to about 1/4 fringe, even without the discharge tube. This is to be compared with the expected maximum fringe shift of ~ 1 fringe due to plasma in the groove of the Scyllac coil. The net error can be reduced, however, by averaging the results for as many fringes as are desired within the field, provided the fringe spacing is greater than the error correlation distance.

Because of the narrow dynamic range (essentially that allowed by the interference pattern) we are also experimenting with other detector types. So far, however, we have not found any material with sensitivity or resolution comparable to that of the bismuth film.

Numerous problem areas were uncovered during the development, frequently requiring redesign of components. The details will be more fully discussed elsewhere.

5. Collective Light Scattering Experiment (R. Kristal)

We are evaluating the feasibility of a side-on, forward light scattering measurement on Scyllac. Such a measurement would yield information on either ion temperature, microturbulence levels, or both. Data on these quantities become increasingly important as thermonuclear conditions are approached.

The experimental basis for end-on forward scattering in a θ -pinch was provided years ago.²⁹⁻³² However, a scattering experiment on the Scyllac toroidal plasma must be done side-on through the quartz discharge tube since there are no ports or windows. This feature introduces high stray scattered light levels into the receiver. The severity of the problem depends on the forward scattering angle, and the largest scattering angles are usable at the longest wavelengths. Therefore we propose the HF laser as a light source. In the optical domain it is the longest high-energy wavelength available, at present, that penetrates the quartz discharge tube.

Detailed design has not yet been considered, but the following estimates seem to hold good promise for the technique. HF output energies available from transversely excited lasers are about 1 joule, single line, in a 100-nsec-long pulse. (Electron beam excited systems can presumably increase this substantially.) With this incident power, total scattered power in the ion feature into a 10^{-2} str solid angle is estimated to be 2.5 μ W. Optical

efficiency of 10% is assumed with a 4-mm field of view and density of 2.5×10^{16} cm^{-3} . The solid angle is defined by a 1-cm-wide slit in a groove of the Scyllac compression coil at a 6-cm radius, with a scattering angle range from 17° to 13° . This corresponds to $1.5 \leq \alpha \leq 2$, where α is the scattering parameter. The scattering angle advantage over the ruby laser wavelength is a factor of 4. This also permits an increase in the receiver solid angle by a factor of 4 for a given range in α .

For reception, highest detectivities of $\sim 2 \times 10^{11} \frac{\text{cm}^2/\text{Hz}}{\text{W}}$ are obtained with indium arsenide detectors cooled to 77°K. (This is an order-of-magnitude detectivity advantage over CO₂ scattering experiments at 10.6 μ m.) With a detector diameter of 1 mm and half-width of 30 MHz, then about 0.03 μ W is needed for an S/N ratio of 10. Since the scattered light provides an average of 0.25 μ W per channel (for 10 channels), there is more than enough signal available to see even purely thermal scattering.

Both plasma background light and the noise due to plasma background light are estimated to be negligible. This is based on the bremsstrahlung continuum at 2.8 μ m and $T_e = 500$ eV. This amounts to about 6×10^{-4} μ W into a 2 \AA -wide channel, compared to a signal of ~ 0.3 μ W.

Signal statistics also look good. Assuming a 10% quantum efficiency, about 4×10^5 scattered photons per channel give an S/N of 200.

The major problem to be addressed is rejection of the high stray scattered light levels with moderately high resolution (~ 2 \AA for 1.5-keV ion temperature). We are studying several possibilities, including both grating systems based on the varioilluminator principle³³ and etalon systems.

6. Laser Heating (K. F. McKenna, G. A. Sawyer, F. C. Jahoda, W. R. Ellis, T. Stratton, L-1, G. Stark, L-1)

Experiments on laser heating of a theta-pinch plasma are planned for Scylla 1-B in 1974 in cooperation with the CO₂ laser group, L-1. A 5-cm bore, 1-m-long coil on Scylla 1-B will provide a peak magnetic field of 58 kG. The laser adapted from the A-3 amplifier provided by L-1 will produce about 100 J of energy in 100 ns. Studies of anomalous backscatter, laser beam channeling, and plasma heating will begin in mid-1974.

I. HIGH-DENSITY LINEAR THETA-PINCH STUDIES (W. R. Ellis, G. A. Sawyer)

Summary

During this report period several versions³⁴ of the high-density linear theta pinch have been studied which might find possible application in the CTR program.

In the confinement program, the straight, open-ended theta pinch remains of interest as a possible back-up candidate to toroidal Scyllac. A question of considerable importance is how the linear system will scale up to a reactor. The answer turns out to be sensitive to the choice of magnetic field strength used, with higher field strengths being favored. Such a design concept would probably necessitate locating the magnet coil inside the lithium breeding blanket, from strength of materials and energy storage considerations. A neutronics analysis³⁵ has consequently been started to look into the problem of radiation damage effects on a high-field inside coil, employing various conceptual blanket structures.

Another important question involves the maximum magnetic field that can be used, and whether one should apply magnetic mirrors. It turns out that the maximum $n\tau$ is produced, all else being equal, when the applied mirror ratio is unity and consequently $B = B_{\max}$ along the entire plasma column. A survey³⁶ of the literature on

high magnetic field technology indicates that the largest magnetic fields obtained so far have been in single term solenoids. The limits for coils that last many shots are about 600 kG for coils of 1-cm bore and 300 kG for coils of 10-cm bore.³⁷ The LASL high-density theta-pinch studies have treated magnetic fields in the range 200-400 kG, although fields up to 500 kG have been proposed elsewhere in connection with the laser-heated solenoid concept.³⁸

Scaling studies^{36,39,40} have been made of the length, confinement time, ion density, cycle time, etc., for a linear reactor as functions of the magnetic field strength B , for two assumed methods of plasma heating. In the first method, conventional theta-pinch (staged magnetic) heating was assumed (i.e., shock heating followed by adiabatic compression). In the second method, long wavelength (direct) laser heating was assumed (i.e., classical inverse bremsstrahlung absorption of 10.6- μ m CO₂ laser radiation, incident from the ends). For both methods, plasma confinement was assumed to be limited by particle flow out of the open ends at essentially the ion thermal velocity. In order to have a conceptual reactor with reasonably low values of circulating power (10% - 20%), a minimum plasma radius requirement must be met.^{39,40} This minimum plasma radius turns out to be a few cm for magnetic fields of a few hundred kG, and the concomitant minimum laser energy, assuming the laser does all the heating, turns out to be a few GJ. This laser energy requirement is so enormous by present standards that laser heating can probably be practical only if it is one of several stages. For example, one can imagine replacing the shock-heating stage in a conventional theta pinch with a laser stage.

To illustrate the sort of reactor parameters one can calculate for the high-density linear theta pinch, we consider the following example. For the plasma, assume

a sharp-boundary MHD model with $\beta = 1$, $kT = 10$ keV, and $n\tau = 10^{15}$ cm⁻³ sec for the burn. For the reactor, assume an overall thermal conversion efficiency of 40%, an overall circulating power fraction of 20%, and an average first-wall loading of 3.5 MW/m², due to 14-MeV (primary) neutrons. The compression coil is assumed to be 10-cm-thick Be-Cu at 500°C (electrical resistivity 5×10^{-6} Ω -cm). The coil bore is derived from plasma heating requirements.

With these assumptions, together with the end loss criterion⁴¹ mentioned above, the reactor size and power output are found to be sensitive functions of B, but not very sensitive functions of the shock-heating electric field E_0 .⁴⁰ At 2 kV/cm (the current RTPR design value⁴²) and 400 kG, for instance, the magnetically heated reactor has a length of 1.2 km, an ion density of 2×10^{17} cm⁻³, a plasma radius of 2.3 cm, a coil radius of 12 cm, a magnetic energy storage requirement of 58 GJ, and a plant electrical output of 1.8 GW(e) on the line. Such a reactor compares favorably with current toroidal (RTPR) theta-pinch reactor designs.⁴² The major uncertainty is with the high-field coil design and coil lifetime. Experiments with high-field coils 5 m long (250 kG) are scheduled to be undertaken next year on the new linear facility Scylla IV-P,⁴³ and neutronics studies³⁵ are under way.

Other potential applications of the high-density linear theta pinch which have been studied include fusion/fission reactor systems,⁴⁴ and a FERF facility for materials testing.⁴⁵ These studies will be continued during the coming year.

J. AUTOMATIC DATA PROCESSING (J. W. Lillberg and F. T. Seibel)

The computer-based system for acquiring and processing Scyllac data has been expanded considerably during the past year.

The new gap monitor systems necessary for the rest of the toroidal Scyllac, which were built by E-2, are currently being

tested and installed. The new gap monitor system was in use during checkout of the new Scyllac capacitor racks.

The gap monitor display program has been modified to present a histogram display of the start-gap and crowbar-gap firing times. This display presents all the pertinent data from fifteen gap monitors on the four TV screens available at the operator's console. In addition, 15 push-buttons have been installed which give the operator random access to a numerical readout of any desired rack.

The arrival of an order for 24 Biomation transient recorders will bring the total number on-line to 64. All of the 610's have been modified to allow computer readout at 50 kHz instead of the 2 kHz originally available. These Biomations will be used mainly for monitoring the feedback control system. The Scyllac program now has the capability of reading and displaying the Biomations independently on an actual shot, allowing a quick test of the feedback system just prior to a shot. The capacity of the Biomations for performing routine monitoring functions has been doubled with an add-on chopping pre-amplifier which allows two signals to be multiplexed into a single Biomation. In this mode, a Biomation can operate with a 500-ns sample interval which gives a 1-MHz sample rate and a range of 128 μ s.

In addition to feedback monitoring, the Biomations have been shown to be an effective means of recording physics data. "Real-time" reduction of the data has been shown to be feasible. Specifically the luminosity data from ten photomultipliers which view ten chords through the discharge tube were recorded at a 10-MHz rate using the Biomations. Following the shot, density profiles were generated as a function of time; from these data, plots of plasma position and radius as functions of time were produced and displayed for the experimenter.

In a similar vein, data from the position detectors utilized in the feedback system have been recorded with Biomations and polar plots of plasma position vs time have been generated. This feature is currently being incorporated into the Scyllac monitor program.

At the present time some real-time control of the firing of the Scyllac capacitor bank is being implemented. A set of critical power supply voltages is being monitored using the Fifth Dimension A/D convertor. A histogram of these voltages is displayed at the operator's console. If any of these voltages drops below a preset amount the charging cycle is stopped by the computer and the capacitor bank is discharged.

The Graf-Pen digitizer continues to be very useful as a means of reducing photographic data. The addition of a plotter to one of the computers has greatly increased the usefulness of this technique of interactive data reduction.

A second scan-convertor controller was tested and installed. There are now two racks of scan convertors working although the reliability of the scan-convertor tubes is still a problem.

In addition a Vidicon-based digitization system was built and tested and appears to be a feasible method of automatically digitizing oscilloscope traces.

REFERENCES

- Los Alamos Scientific Laboratory reports, LA-4888-PR, p. 4 and LA-5250-PR, p. 4.
- W. E. Quinn, W. R. Ellis, R. F. Gribble, C. R. Harder, R. Kristal, F. L. Ribe, G. A. Sawyer, R. E. Siemon and K. S. Thomas, "Review of Scyllac Theta-Pinch Experiments," Proc. Sixth European Conference on Plasma Physics and Controlled Nuclear Fusion Research, Moscow, U.S.S.R., July 30-August 3, 1973.
- F. L. Ribe and M. N. Rosenbluth, Phys. Fluids 13, 2572 (1970).
- H. Weitzner, Phys. Fluids 14, 658 (1971).
- J. P. Freidberg, Plasma Phys. Contr. Nucl. Fusion Res. 3, 215 (1971).
- M. N. Rosenbluth et. al., Phys. Fluids 12, 726 (1969).
- H. Grad and H. Weitzner, Phys. Fluids 12, 1725 (1969).
- J. P. Freidberg and B. M. Marder, Phys. Fluids 14, 174 (1971).
- H. Weitzner, Plasma Phys. Contr. Nucl. Fusion Res., (IAEA, Vienna, 1971) Vol. III, p. 223.
- J. P. Freidberg, Phys. Fluids 14, 2454 (1971).
- F. L. Ribe, ed., Los Alamos Scientific Laboratory Report LA-5026-P (Rev)(1973).
- F. L. Ribe, Los Alamos Scientific Laboratory Report LA-4098-MS (1969).
- A. M. Gondhalekar and B. Kronast, Phys. Review A, 8, 441 (1973).
- Los Alamos Scientific Laboratory report LA-4888-PR, p. 36 (1971).
- R. F. Gribble, S. C. Burnett and C. R. Harder, "Feedback Stabilization on an $\ell = 1$ Theta-Pinch Plasma Column," Proc. 2nd Topical Conf. Pulsed High-Beta Plasmas, Max-Planck-Institut für Plasmaphysik report IPP 1/127, July 1972.
- K. S. Thomas, C. R. Harder, W. E. Quinn and R. E. Siemon, Phys. Fluids 15, 1658 (1972).
- W. E. Quinn, "Considerations Concerning the Scyllac Major Radius of Curvature," Los Alamos Scientific Laboratory report LA-DC-72-1535 (Dec. 1972).
- K. Höthker et al., Sixth European Conference on Controlled Fusion and Plasma Physics (Moscow 1973), p. 299.
- M. Keilhacker et al., Sixth European Conference on Controlled Fusion and Plasma Physics (Moscow 1973), p. 307.
- W. F. Dove, Phys. Fluids 14, 2359 (1971).
- D. W. Forslund, R. L. Morse and J. Fu, Phys. Fluids 15, 1303 (1972).
- R. Gribble, Q-7 Quarterly Report, April 1 - June 30, 1973.
- D.E. Evans and J. Katzenstein, Rep. Prog. Phys. 32, 207 (1969).
- A. W. De Silva and G. C. Goldenbaum, in Methods of Experimental Physics, Vol. 9, Part A, H. R. Griem and R. H. Lovberg, Ed. (Academic Press, New York, 1970), Chap. 3.
- G. M. Malyshev, G. V. Ostrovskaya, G. T. Razdobarin, and L. V. Sokolova, Sov. Phys. - Doklady II, 441 (1966).
- J. Katzenstein, Appl. Opt. 4, 263 (1965).
- P. H. van Cittert, Z. Instrumentenk. 46, 557 (1926).

28. F. R. Lipsett, G. Oblinsky, and S. Johnson, *Appl. Opt.* 12, 818 (1973).
29. B. Kronast, H. Röhr, E. Glock, H. Zwicker and E. Fünfer, *Phys. Rev. Lett.* 16, 1082 (1966).
30. D. E. Evans, M. J. Forrest and J. Katzenstein, *Nature* 212, 21 (1966).
31. S. A. Ramsden, R. Benesch, W. E. R. Davies and P. K. John, *IEEE J. Quant. Elec.* QE2, 267 (1966).
32. M. Daehler and F. L. Ribe, *Phys. Rev.* 161, 117 (1967).
33. See e.g. Sec. II H3 on the three-grating polychrometer.
34. W. R. Ellis, "Fusion Reactor Applications of the High Density Linear Theta Pinch," paper submitted to First Topical Conf. on the Technology of Controlled Nuclear Fusion, San Diego, Calif. (April 16-18, 1974).
35. D. J. Dudziak, Los Alamos Scientific Laboratory, unpublished results.
36. W. R. Ellis and G. A. Sawyer, "Scaling Laws for the Linear Theta Pinch, I: A Comparison of Magnetic and Laser Heating," Los Alamos Scientific Laboratory report LA-5434-MS (Oct. 1973).
37. H. Knoepfel and R. Lupi, *J. Phys. E: Sci. Inst.* 5, 1133 (1972).
38. J. M. Dawson, A. Hertzberg, R. E. Kidder, G. C. Vlases, H. G. Ahlstrom, L. C. Steinhauer, Plasma Physics and Controlled Nuclear Fusion Research, Vol. 1, 673, IAEA, Vienna (1971).
39. W. R. Ellis, "Joule Losses in Linear Theta Pinches: Laser vs Magnetic Heating," *Proc. Fifth Sym. on Eng. Problems of Fusion Research*, Princeton, N.J. (Nov. 6-9, 1973).
40. W. R. Ellis, "Scaling Laws for the Linear Theta Pinch, II: Circulating Power in a High-Field Reactor," Los Alamos Scientific Laboratory report LA-5499-MS (Dec. 1973).
41. J. P. Freidberg, Los Alamos Scientific Laboratory, Unpublished results.
42. R. A. Krakowski, F. L. Ribe, T. A. Coultas, and A. J. Hatch, "An Engineering Design Study of a Reference Theta-Pinch Reactor (RTPR)," Vol. 1, USAEC report ANL-8019/LA-5337-MS (Dec. 1973).
43. W. R. Ellis, W. B. Riesenfeld, and G. A. Sawyer, "Proposal for the Construction of a Scylla IV-P Confinement Studies Theta Pinch," Los Alamos Scientific Laboratory report LA-5474-P (Dec. 1973).
44. D. J. Dudziak and W. R. Ellis, "A Preliminary Appraisal of a Fusion/Fission (Hybrid) Reactor Based on the Linear Theta Pinch," paper submitted to the Ninth Intersociety Energy Conversion Engineering Conference, San Francisco, Calif. (Aug. 26-30, 1974).
45. W. R. Ellis, "A Preliminary Appraisal of a Linear Theta-Pinch FERF," Los Alamos Scientific Laboratory report (to be published).



III. IMPLOSION HEATING EXPERIMENT

(J. E. Hammel, I. Henins, J. Marshall, and A. R. Sherwood)

A. SUMMARY

The Implosion Heating Experiment (IHX) has been in planning and construction for about two years. It is expected to be in preliminary operation by about the end of February 1974. It has two main objectives, one scientific and one technical. The scientific objective is to study the physics of the implosion heating process in theta pinches under conditions of more violent implosion than have been used in the past. The technical objective is to develop the high-voltage pulse technology required to obtain these more violent implosions. Both objectives are required for realistic extrapolation toward future generations of theta pinches, perhaps leading someday to a controlled thermonuclear reactor.

In order to facilitate the physics investigations a large diameter (400-mm) theta-pinch coil has been chosen. This gives space and time in which to study the imploding sheath. An attempt is being made to simplify the implosion process by keeping the field strength of the driving magnetic piston nearly constant during the collapse time. It is desirable to keep the plasma density in the normal range for theta pinches, so all design studies have assumed a deuterium ion density of $10^{21}/\text{m}^3$. With this ion density, and assuming an elastic bounce model for the interaction between the ions and the magnetic piston, a magnetic field strength of 1 T produces an electric field strength at the surface of the plasma in the laboratory system of ~ 200 kV/m and an ion energy of ~ 2.5 keV.

This is about twice the normal electric field in high-performance theta pinches, and the ion energy is high enough to be interesting. A field strength of 1 T was chosen as a design goal, and with a convenient coil length of 1.0 m this requires a current of 800 kA. A current risetime is required which is short compared with the implosion time of the plasma and a pulse length is desirable which is larger than the implosion time. The design goals for these times were taken as ~ 100 ns and ~ 500 ns. In order to provide 200 kV/m around a 400-mm-diameter discharge tube, a voltage of 250 kV must be applied in the presence of the plasma. The plasma however represents an extremely low impedance load. With the chosen parameters it has an effective resistance during the implosion of $\sim 0.3 \Omega$. The high-voltage generator has been designed to have an impedance approximately equal to that of the plasma so that a total emf of 500 kV is required.

By January 1973 it had been decided to drive the IHX theta-pinch coil through four feed slots with 125-kV pulse-forming networks (PFN's) using capacitors similar to those in the Scyllac preionization system. The Scyllac capacitors were known to be capable of handling 125-kV pulsed voltage, although they are used and rated at 70 kV dc. In order to achieve acceptably low inductance, capacitors similar to those used in Scyllac were procured with reduced capacitances, to be connected several in parallel. The Scyllac preionization capacitors are 0.7 μF ; those procured for the IHX are 0.2 and 0.4 μF . It had also been

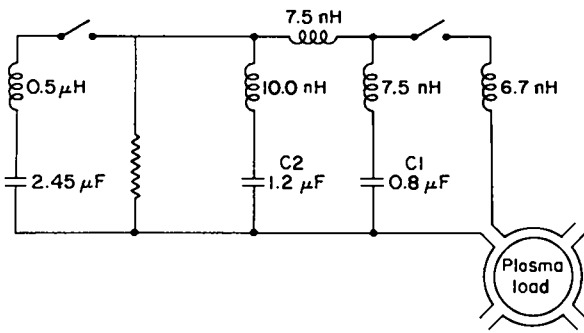


Figure III-1

The pulse-forming network for the IHX. C_1 is four $0.2\text{-}\mu\text{F}$ capacitors in parallel. C_2 is three $0.4\text{-}\mu\text{F}$ capacitors in parallel. The $6.7\text{-}\mu\text{H}$ inductance is that of the switches and coil feed. The network on the left represents two Marx banks in parallel. Identical PFN's are connected to all four coil feed slots.

decided to switch the system with commercially developed field-distortion rail gaps which could be purchased from Physics International, if tests on a prototype gap turned out to be promising. This would save the time and effort required to develop a high-voltage low-inductance switch. It remained to arrive at a final electrical and mechanical design for the PFN's using dimensions and inductances which would result from development.

The final PFN circuit is shown in Figure III-1. It is the result of computer modeling using the NET II code which was modified to take into account in a self-consistent way the electrical effect of the imploding plasma. The calculated current waveform is shown in Figure III-2. The current is calculated assuming a model for the physics of the implosion process, and, of course, that physics is just what the experiment is designed to study. Almost certainly the waveform will differ from the prediction. Information about the implosion process may result from the differences. Another decision made during 1972 was to fast pulse charge the PFN's from Marx banks. A Marx design had been completed by January 1973 and a prototype

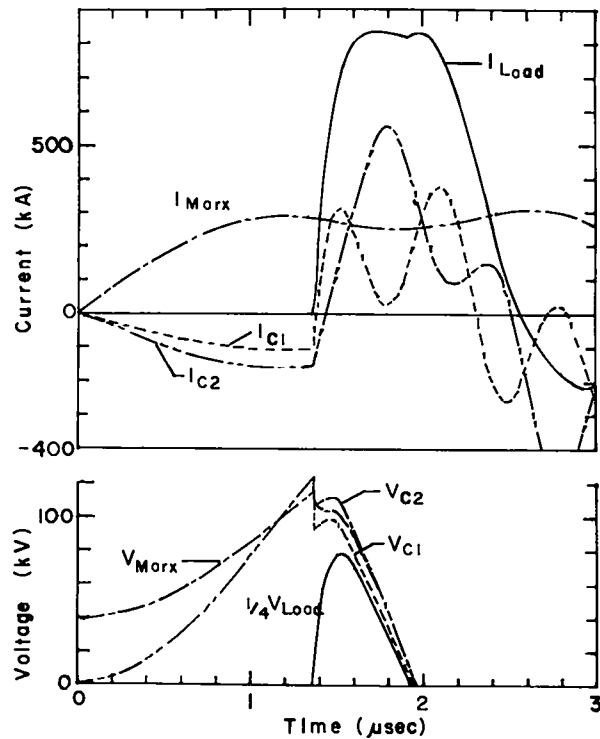


Figure III-2

The calculated waveforms of the circuit of Figure 1. The bounce model for a perfect magnetic piston is assumed, and the initial plasma density is 10^{21} deuterons/ m^3 . The coil is 1 m long with an inner radius of 0.20 m; the inner wall of the discharge tube is 0.18 m.

constructed. As was explained in the last annual report, this design requires two Marx banks per PFN. The fast pulse charging makes the system operate more or less as a peaking capacitor circuit. The load switches are closed while a substantial charging current is still flowing (~ 300 kA). This current is available to the load without having to flow through the capacitors of the PFN with their self-inductance. The result is a considerable upgrading of PFN performance. A problem is introduced, however. If the load switches do not fire at the proper time ($1.35\ \mu\text{s}$ after Marx erection), the PFN capacitor voltage will continue to rise

rapidly and could conceivably reach 190 kV. This would almost certainly destroy capacitors. A means had to be found to deal with this situation.

A number of techniques and components had to be developed to arrive at a practical, sufficiently reliable PFN design. These will be discussed separately below. They include methods of suppression of electrical flashover along insulator surfaces, some depending on novel geometric arrangements of the insulation, some on resistive voltage grading with conducting plastic, and some on shaping of the electric field so as nowhere to exceed the breakdown strength of air. Among the components developed are a voltage gasket insulated header to provide low-inductance high-voltage connection between capacitors and collector plate, and a surface-flashover overvoltage-protection switch.

Enough of the critical development was finished by May 1973 that final design of the system and procurement of parts could be started. The PFN design was essentially complete by August and nearly all parts were on hand by the middle of December. A few capacitors remain to be delivered in January, but these are not seriously holding up the assembly of the machine. By September the first four Marx banks were operational, and at the end of the year the other four Marx banks had been mechanically assembled. Near the end of the year the first PFN had been constructed and satisfactorily tested to 130 kV, that is, to a voltage slightly exceeding the full design value. The successful performance of this first quarter of the total system prompted the decision to start on the second PFN. This unit was under construction at the end of December.

Preionization studies were started during the summer on Scylla I-B in cooperation with Ken McKenna and Richard Kristal of Q-3 and Keith Thomas of Q-7. This was on a 20-cm-diameter tube and so not directly applicable to IHX. Both

theta-pinch and Z-pinch preionization were tried. The theta-pinch method appeared to be satisfactory, leading to perhaps 70% ionization, and it does not introduce certain difficulties found with the Z-pinch. Accordingly plans were made to attempt theta-pinch preionization on the 40-cm tube. The vacuum system with the four feed-slot coil was set up in a separate room, so as not to interfere with work on the PFN's, a preionization system was developed using four of the Scyllac preionization capacitors, pulse charged to ~ 100 kV with a Marx generator, and studies of the degree of ionization are in process.

In summary, several significant objectives have been achieved in producing a fast-rising high-current system. The desirable feature of having the current source operate at 0.5 MV without being under a liquid dielectric will be achieved by the development of the several high-voltage techniques described below.

B. DEVELOPMENT OF THE CURRENT SOURCE

1. Marx Banks

The basic Marx bank design was completed last year and is discussed in the last annual report. The capacitors chosen for the Marx banks dictated that a total of eight banks be constructed to charge the PFN's. The construction and testing of a final prototype bank of this design was done early this year. This bank has seen considerable use throughout the year in our separate high-voltage testing area.

In order to conserve valuable floor space in the experimental area it was decided to arrange the eight Marx banks into four stacks, each stack consisting of two Marx banks arranged vertically with the high voltage appearing at the center of the stack. The upper bank required some minor modifications, to the electrolytic resistors for example, because of the fact that it must be constructed "upside-down." The main design problem in

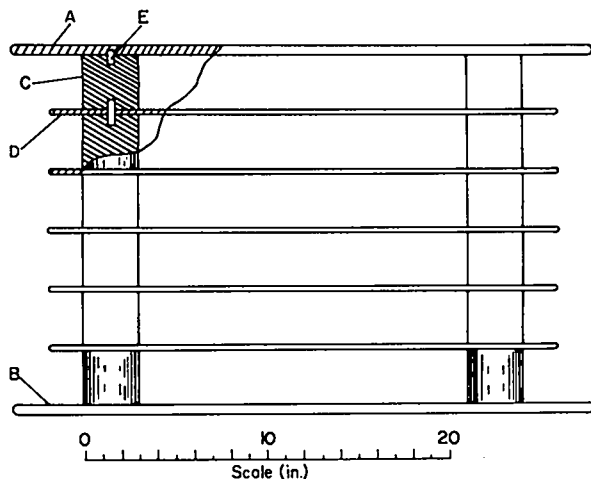


Figure III-3

Insulating support for stacked Marx banks.
 (A) Output plate for top Marx bank,
 (B) Output plate of bottom Marx bank,
 (C) Cylindrical phenolic spacers,
 (D) Aluminum plates, and
 (E) Dowel pins.

the stacking concept, however, involved devising an insulating support structure for setting the upper Marx bank upon the lower one. Our solution to this problem is a capacitive voltage grading system consisting of aluminum plates spaced apart by 76-mm-long phenolic insulators as shown in Figure III-3. If such an insulator is placed in a uniform field region such that the electric field lies parallel to its surface, it is observed that breakdown does not occur along the surface of the insulator when the system is overvolted, but rather occurs through the air. So if the electric field is kept below the breakdown strength of air and parallel to the insulator surface, breakdown will not occur. Each upper Marx bank, then, sits upon a stack of six sets of the phenolic insulators with five intermediate aluminum plates. This arrangement has been tested to 240 kV. A photograph of one of the Marx stacks is shown in Figure III-4.

A master trigger system for firing the eight Marx banks has been developed and installed. Each Marx bank has a trigger cable, which can be charged to -40 kV,

capacitively coupled to the electrolytic trigger resistors. These trigger cables are all of equal length and are connected to a single trigatron shorting switch. The system is simple and provides for the simultaneous triggering of all the Marx banks.

A 600-mA, 50-kV Marx-charging power supply has been installed. It has a constant-current output which can be varied for charging any number of Marx banks. The control system senses the instantaneous charging voltage, V , and also the voltage V' at the midpoint of the series-connected capacitors. If V' deviates by more than 1 kV from $V/2$ the system is dumped. This prevents overcharging half of the capacitors if one capacitor becomes shorted. When the charging voltage reaches a preset level, the control system shuts off the power supply and allows either manual or automatic triggering of the experiment and the diagnostics. A spark-gap pressure-regulating system has been installed which also flushes the gaps after each shot. Several other control system features, such as a flushing system for the rail gaps and a safety interlock system, have also been installed and tested.

2. Low-Inductance Capacitor Connection

The design for the capacitor header insulation reported in the 1972 annual turned out to be unsatisfactory, primarily because it allowed sparks to start along insulator surfaces before they came to the elastomer gasket. It was found that once a high-voltage breakdown is started in air along an insulator, it is very hard to stop at the insulator-elastomer gasket interface. An improved design minimizes this problem by reducing the electric field strength and by eliminating air spaces at the edge of the gasket.

This design is shown in Figure III-5. The usual capacitor insulator barrier is cut down to further reduce the inductance. Then Dow Corning 184 Sylgard silicone compound is poured in place to form

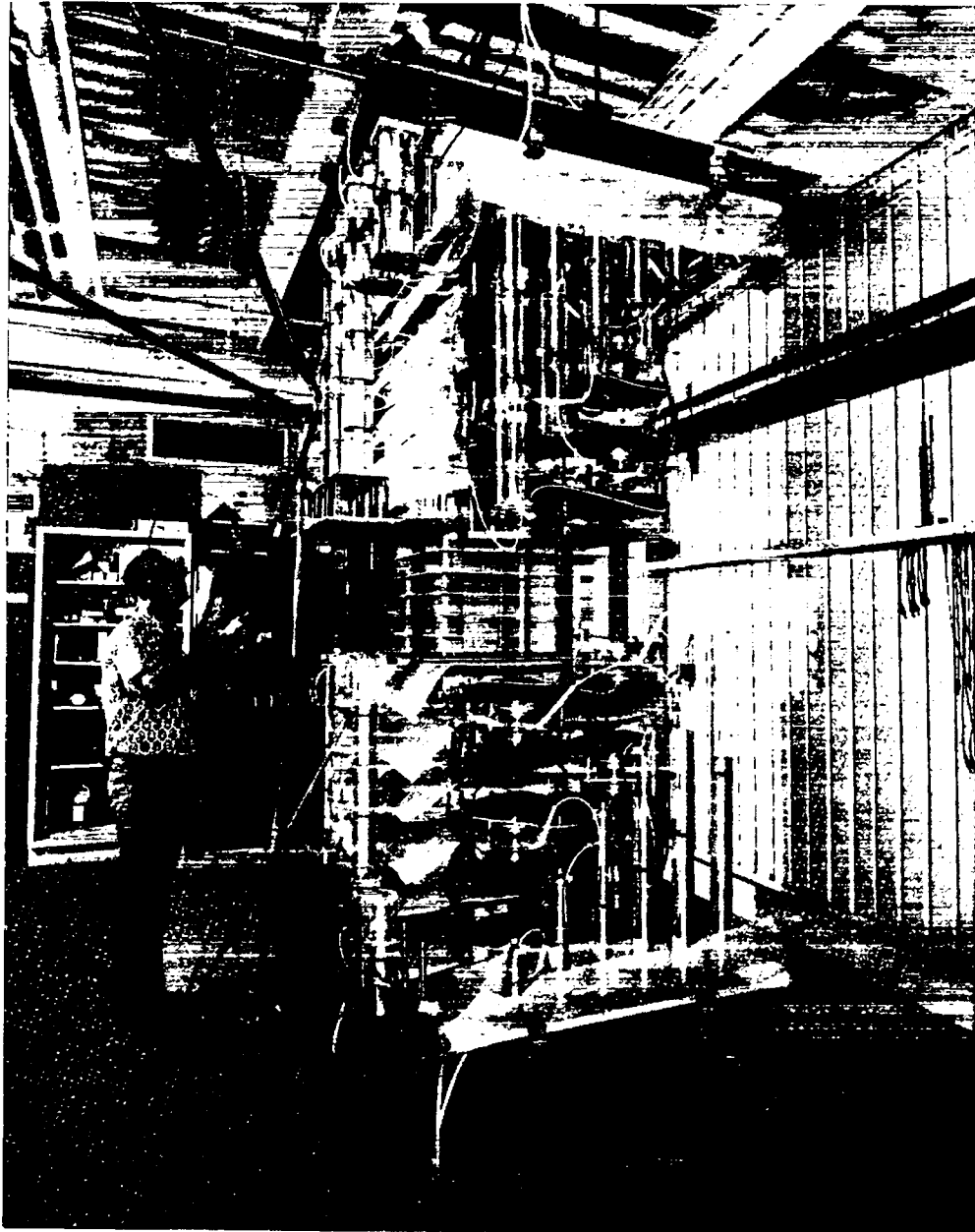


Figure III-4
Stacked Marx banks for the IHX.

the elastomer gasket. A thin layer of silicone grease (Dow Corning High Vacuum Grease) is used between the gasket and each of the four layers of 0.8-mm- (1/32-in.) thick polyethylene sheet insulation. An additional 6.4-mm- (1/4-in.) thick polyethylene spacer is used above the sheet insulation to reduce the electric

field strength at the outside edge of the gasket. Approximately 2.67×10^4 N of force is used to compress the insulation on the gasket. Since the silicone rubber gasket is molded 0.25 mm higher than the surrounding plate, the force is distributed over the gasket surface at about 1.38×10^6 Pa. This insulating

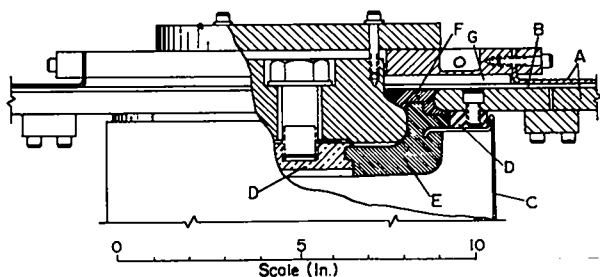


Figure III-5

Scale diagram of low-inductance connection between parallel plate line and the 125-kV capacitor header. (A) Transmission line plates, (B) Transmission line insulation: four sheets of 0.8-mm polyethylene, (C) Capacitor can, (D) Capacitor terminals, (E) Capacitor insulator, (F) Poured-in-place silicone rubber high-voltage gasket, and (G) 6.4-mm-thick polyethylene spacer.

arrangement has repeatedly been successfully tested on several capacitor headers to 200 kV with pulses rising in less than 1 μ s and with a decay time of around 100 μ s.

Raising the voltage on one sample to failure produced a breakdown through the capacitor insulator at 235 kV. Therefore this design appears to be quite adequate for the 125-kV service. Two of the PFN's have now been assembled and tested for over a hundred shots around 120 kV and several shots as high as 130 kV.

A year ago Mylar was to be used for the parallel plate insulation. However, during the capacitor header tests it became apparent that polyethylene was more reliable. While Mylar has higher dielectric strength in a uniform electric field, it is much more susceptible to puncture from an electric breakdown in the grease or air next to it.

3. The Rail-Gap Load Switches

The main load switches are multi-channel field-distortion rail gaps built by Physics International. They are used

in pairs, two of them connecting each PFN to its coil feed slot. The rail gaps are a modification of a design used under water for switching considerably higher voltages. Extensions on the acrylic-plastic spark-gap bodies allow operation in air at 125 kV with voltage grading as described below.

We have encountered three types of problems in the testing and preliminary use of these rail-gap switches. One problem was a voltage insulation problem. As supplied the switches will hold off 125 kV when operated in one Los Alamos atmosphere of freon. When operated in air, however, they will invariably flash over along the insulation from one main electrode of the switch to the other. This flashover spark takes about 2 μ s to become fully developed when the voltage is 125 kV. This problem has been very satisfactorily solved by the technique of voltage grading using conducting plastic. This solution is described in more detail in another section of this report.

A second problem in the use of these rail-gap switches is to develop a trigger system capable of producing multichannel operation. All eight switches will be triggered from a single source, that is, from a master gap. The full system has not yet been triggered or even assembled, but master gaps with eight load cables have been used to trigger one gap successfully. Also the modified Physics International master gap (see below) has successfully triggered two rail gaps during the checkout of the first PFN.

Satisfactory multichannel operation (i.e., 15 to 20 channels) has been obtained for a single switch with the following trigger systems:

a. cable attached to trigger electrode and charged to trigger bias voltage (40 kV), shorted at its back end with a stabbed polyethylene switch;

b. cable separated from the trigger electrode by an isolation gap and charged

to 80 kV, shorted at its back end with a triggered gas gap (not quite as good as the other system);

c. Scyllac master gap system charged to 100 kV and separated from the trigger electrode by an isolation gap;

d. same as c, but without the isolation gap;

e. a field-distortion master gap purchased from Physics International but modified by the addition of a Condenser Products low-inductance (<25 nH), 70-kV, 0.02- μ F capacitor. This modification allows a bias voltage to be applied to the master gap without the use of isolation gaps between each cable and the corresponding trigger electrode.

Of these trigger systems we are presently considering only the last two. The Scyllac master gap system seems to be the more reliable because it can produce higher output pulses, but it is quite bulky and complicated compared to the modified Physics International master gap. This latter gap also gives satisfactory performance except that perhaps a little more work is needed on its own trigger system.

The final problem area concerns the working gas for these switches. Our initial attempts to obtain multichannel operation failed because we were operating in the "fizzle phase" of SF₆. As explained by Phil Champney of Physics International, SF₆ has very poor breakdown characteristics at low pressures (around 1.4×10^5 Pa or less). High purity dry N₂ in the $3.0 \times 10^5 - 5.5 \times 10^5$ Pa range has given operation with 10 to 20 spark channels. Interestingly, air in a similar pressure range gave much poorer performance of the switch. Thus we have been using the high purity dry N₂ for the filling gas. There is evidence, however, that this gas may be subject to a different set of problems. Our prototype switch suffered a substantial loss of breakdown strength and exhibited very erratic behavior after a few months

of operation (i.e. several hundred shots). Almost doubling the pressure of the filling gas did not improve the erratic behavior, which was characterized by large shot-to-shot variation in breakdown strength. According to J. C. Martin of AWRE this behavior, called dropping out, is fairly common for high-voltage switches and is corrected by changing the filling gas. When we disassembled this switch for inspection it was found to have a dry black powderish substance on the insulation surface. Phil Champney reports that they found the same sort of black powder when they used N₂ and that they have since shifted to a different gas mixture. Further tests on our prototype switch with different gas mixtures are planned for the near future.

4. Edge Insulation for Parallel Plate Lines

Flashover prevention provided by a simple extension of sheet insulation beyond the edge of parallel plate high-voltage electrodes diminishes in effectiveness as voltages are raised to 100 kV and higher. Tests have shown that the voltage standoff for a given voltage waveform is a function of both the edge extension of the sheet insulation and its thickness. Figure III-6 shows flashover curves obtained for various thicknesses of polyethylene. The voltage waveform in these tests approximated a single half cycle of a slightly under-damped sine curve rising in 5 μ s to peak. In order to minimize time effects, the voltage amplitude was adjusted so flashover occurred at 4 μ s while the voltage was still rising. We have also observed that the flashover voltages are not significantly different for the same dimensions of Mylar and polyethylene.

Our understanding of the flashover process under pulsed-voltage conditions is that at the high electric fields imposed on the insulation, the air at the electrode edge breaks down and a large

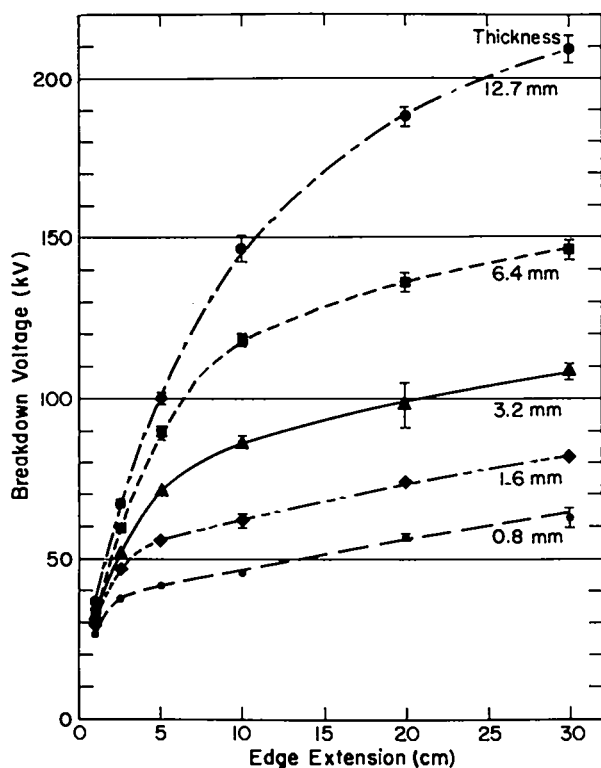


Figure III-6
Flashover voltages for a straight extension of polyethylene insulation of various thicknesses from the edge of a parallel plate transmission line.

number of streamers start from each electrode edge. Some of these streamers may coincide on the opposite surfaces of the insulation, and since the streamers are conductors, they tend to extend the potential of each plate outward along the surface, further ionizing the air at their tips. The streamer propagation is influenced by their intrinsic impedance, the source impedance, and by the field strength at the streamer tips. A similar process has been suggested by J. C. Martin in one of his notes on "Dielectric Breakdown and Tracking" (SSWA/JCM/Hun/5).

Therefore, if the insulator surface can be separated so that the streamers propagating outward find the field strength decreasing at their tips, the flashover voltage may be increased. The common technique of flaring apart

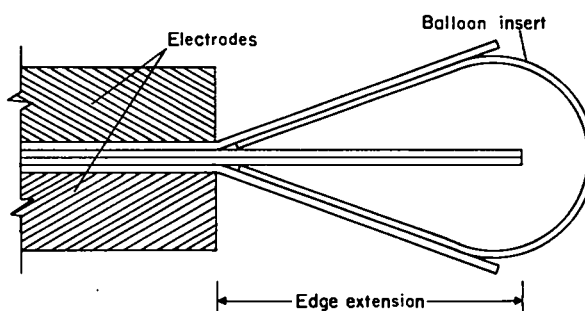


Figure III-7
Flashover prevention by "ballooning" the insulation at the edge of a parallel plate transmission line.

the edges of insulating sheets to increase flashover potential apparently depends more on this reduction of capacity between the two sides of the overhanging insulation than it does on increase of surface path. It is somewhat inconvenient and messy to use in practice, and we have investigated alternative methods of decreasing the capacity between the surfaces along which streamers must propagate to form the arc. Many arrangements were tried, some better than others, not always for obvious reasons. The arrangement which we settled on we call "ballooning." It is easy to apply, holds off more than 200 kV for the test pulse we were using ($\sim 5\text{-}\mu\text{s}$ exposure time), and takes very little space. As shown in Figure III-7 the insulation between the plates, consisting of four sheets of 0.76-mm polyethylene sheets, is allowed to extend 0.1 m beyond the edges of the plates. A ballooning strip of insulation 0.3 m wide, consisting of a sheet of 0.76-mm polyethylene, is inserted with one edge as far in as possible between the top two sheets of main insulation, and the other edge similarly between the bottom two sheets. In order to be effective the separation by the ballooning sheet has to start at the edges of the electrodes. The entire assembly protrudes less than 0.15 m

beyond the edge of the parallel plate line conductors. Occasional pieces of adhesive tape are used to keep the ballooning strip from falling out.

5. Overvoltage Protection

At the time that the PFN has reached 125 kV, the Marx bank is delivering a considerable amount of current (~ 300 kA), which normally adds to the current from the PFN to deliver the peak current of about 800 kA to the load. However, if the load switches should fail to close, this Marx current, because of the circuit inductance, would seriously overcharge the PFN capacitors. Therefore, it is desirable to have some sort of an overvoltage protection switch.

When taking the data shown in Figure III-6 it was observed that, for a given insulation edge extension and thickness, the flashover voltage is very repeatable and that there is little damage to the insulation. This observation led to the development and adoption of an overvoltage protection "switch" which is merely a place along the edge of the main insulation of each PFN which is tailored to allow a flashover if the voltage exceeds 125 kV. It seems inadvisable, of course, to allow the flashover to occur on the main insulation itself. So the "switch" actually consists of a pair of electrodes mounted on a replaceable piece of insulation which is interleaved into the main insulation. The device is placed at the thick (20-mm) section where the two plates of the transmission line are separated to provide the inductance between the two capacitive legs of the PFN; this is a convenient place for the interleaving of the insulation. For the voltage risetime of this experiment, namely about $1.5 \mu\text{s}$, we find that a 55-mm extension of 12.7-mm-thick polyethylene flashes over between 130 kV and 136 kV; these dimensions are the ones used. Incidentally, the whole switch is enclosed in a sound-absorbing box because for our

energies it is quite loud if it is allowed to operate in the open room.

6. Prevention of Flashover by Conducting Plastic

The rail switches developed by Physics International for the IHX were designed to operate in an atmosphere of freon or sulphur hexafluoride to prevent flashover around the switch. This requirement would entail added design difficulties in providing the gas-tight enclosure around the switches. Another approach to the flashover problem is to provide electric field grading rather than brute-force breakdown strength. The use of water around the switch for this grading would again present difficult design problems. A much more convenient solution would be to provide the grading by conducting sheet material. The material selected for a test of the sheet grading was a polyolefin film with a carbon filling. It is obtained from Custom Materials, Inc. under the trade name Velostat. The first test was made with a sheet of 0.15-mm thickness having a resistance of $7500 \Omega/\text{sq}$. In various configurations the voltage hold-off was increased over nongraded hold-off by a large factor for pulses 4 to 6 μs in duration. The breakdown was no longer along the insulator surface, but through the conducting plastic. The hold-off was about 650 kV/m for test specimens from 0.15 to 0.30 m in length. It thus appears that the limit is at a current density of 90 amp/m. The 0.15-mm Velostat was then used on a rail-gap switch prototype with the sheet placed between the switch and the polyethylene transmission-line insulation (completely covering the bottom and sides of the switch) and securely connected to the two main switch electrodes. With this configuration the breakdown voltage was about 195 kV which is safely above the 125-kV operating voltage. The breakdown again appears to be governed by the limiting current density found in the test

specimens. The current connections between the Velostat and the electrodes must be made with the current limitation in mind. Elastomer backing of the sheet is used to ensure a uniform connection, and all corners are well rounded to remove current concentrations.

After the tests with the 0.15-mm Velostat, a 0.20-mm sample was obtained and tested. The resistance of the sample was 13.5 k Ω /sq, (70% higher resistance than the original material). This material had a different breakdown mode than the 0.15-mm sheet. In the test the breakdown is no longer in the Velostat, but is now along the insulator. For this test, two layers of Velostat raise the breakdown voltage. It appears, therefore, that the mode of breakdown is lack of voltage grading along the insulator. For two sheets of 0.20-mm, 13.5 k Ω /sq sheet, the voltage hold-off is now above 680 kV/m.

Velostat grading is also being used at the point where the Marx output cables connect to the PFN. The conducting sheet is a great simplification over the water grading originally planned for these connections. Each cable has a skin-back length of about 0.46 m which is wrapped with a layer of Velostat as is shown in Figure III-8. In addition, a layer of Velostat is placed along the insulating path that separates the two electrodes to which the cable braid and center conductor are attached respectively. The 0.46-m length so graded is found to hold off more than 185 kV. Again, it is important that

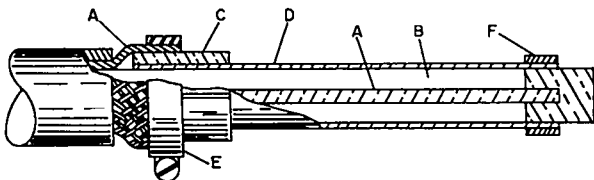


Figure III-8

Schematic diagram of voltage grading of a cable skinback by conductive plastic. (A) Cable conductors, (B) Cable insulation, (C) Split-ring conducting clamp, (D) Conducting plastic wrap, (E) and (F) Hose clamp.

the current connections to the Velostat be carefully designed to avoid current concentrations.

7. Fast Resistive Dividers for High Voltages

Often it is necessary to measure the pulse shapes and amplitudes of fast-rising high-voltage pulses. Capacitive voltage dividers can be made to have the high-frequency response, but they suffer in low-frequency response and in ease of calibration. On the other hand, resistive dividers are easy to calibrate, but they

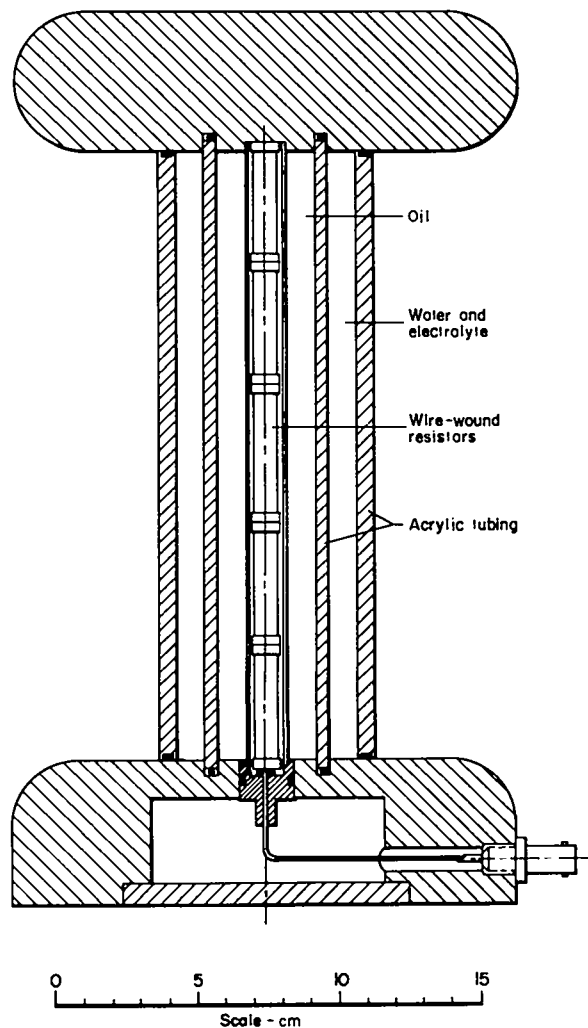


Figure III-9

Scale diagram of shielded resistive high-voltage divider.

commonly do not have the necessary high-frequency response because of distributed capacitive loading along the usually long length of the resistor string. This capacitive loading can be eliminated by placing the resistor string in an enclosure in which the potentials next to the resistor string are graded to be the same as those along the resistor itself. This has been accomplished as shown in Figure III-9 where the 50-k Ω resistor string is placed along the axis of an annular electrolytic resistor of the same length. The voltage divider resistor has to be long enough to withstand the applied voltage and of high enough resistance to not overheat during the measurement; therefore, it is made up of five 10-k Ω noninductive 1%-tolerance wire-wound resistors (Dale Electronics NS-10-27). Each of these resistors has a net reactance of 1.1 pF, will withstand 50 kV immersed in oil, and can absorb 11 J with a 200°C temperature rise in the wire. The annular electrolytic resistor contains 350 cm³ of water and can absorb a maximum of 3 kJ with 2°C temperature rise, thus its resistance can be made much lower than that of the dividing resistor.

The voltage divider described above has an output risetime of <10 ns with an 8-k Ω electrolytic grading shield. Without the shield the risetime is slowed down to over 100 ns.

8. Stabbed-Polyethylene Switch Development

Early in the year we conducted a program to develop the technique of producing reliable stabbed-polyethylene switches. These switches, which are used in various other laboratories in this country and abroad, can be convenient off-the-shelf items to have available; in addition, we were considering their use in the over-voltage protection system for the PFN's.

In this program we verified several of the results found elsewhere. For example:

a. the voltage at which the switch breaks down depends upon the depth of the

stabs as well as the thickness of the remaining insulation;

b. the voltage at which the switch breaks down is not a linear function of the thickness of the remaining insulation;

c. the voltage at which the switch breaks down is about twice as high if the electrode on the stabbed side of the insulation is negative than it is for the case where the polarity is reversed.

For a set of switches all stabbed at the same time the variance in the breakdown voltage is typically ~5%.

If a stabbed dielectric switch were used as the overvoltage protection system this switch would be repeatedly subjected to a voltage of 90-95% of its breakdown voltage. The question then arises whether the switch will suffer degradation, and if so, how rapidly. Tests were made to investigate this matter and we found that indeed our stabbed polyethylene switches have a finite lifetime. One repeatedly subjected to 90% of its rated voltage would last only 10 to 20 shots, one subjected to 86% about 25 to 30 shots, and one subjected to 75% more than 50 shots. It appears that these lifetimes are purely statistical in origin. The evidence is that switches subjected to lower voltage shots equal in number to one-half or three-fourths of the expected lifetime are then found to still break down at full breakdown voltage. One would expect the breakdown voltage to be lowered under these conditions if a degradation mechanism were the dominant effect.

The short lifetime observed for a switch operated under the conditions envisioned for the overvoltage protection application caused us to abandon this approach when a more promising solution appeared.

C. PREIONIZATION

The ideal initial conditions for the IHX are a magnetic-field free plasma with a density of 10^{21}m^{-3} . At the time of the last annual report, no work had been done on the preionization phase of the experiment.

It was thought that a Z-pinch would be the likely preionization method. Since that time two developments have led to a high-voltage theta pinch as the method of preionization to be installed on the experiment. The first of these is a calculation which indicates that proper circuit design will allow a theta-pinch preionization bank to drive the main coils in such a way that the PFN is not degraded and the preionization bank is not overvolted. High currents in the preionization phase, even with the required isolation can be achieved with pulse-charged 125-kV capacitors. One 0.7- μ F, 125-kV capacitor at each feed point will produce 110 kA.

The second development supporting the decision to preionize with a theta pinch is the result from experiments on the 200-mm-diameter Scylla 1-B. These results are reported in some detail in another section of this report. In brief, the Scylla 1-B preionization tests showed that the theta pinch was as effective as the Z-pinch method. The theta pinch gives, in addition to simplicity, the distinct advantage of avoiding problems introduced by the Z-pinch electrodes and electric fields when diagnostic probes are put into the plasma.

The first experiments on the preionization of the 40-mm-diameter IHX have begun with one 0.7- μ F capacitor tied to each of the four gaps with about 1- μ H isolating inductance. The capacitors are switched by a standard Scylla-type gap which was found to hold the pulsed 125 kV without difficulty. The four capacitors and the master trigger are charged by one of the IHX-type Marx banks. The first preionization data were taken at a capacitor voltage of 85 kV producing a peak current of 75 kA with a period of 4.5 μ s. The electron density was measured by the usual coupled cavity method. The fraction of ionization (defined as electron density over twice the deuterium filling density) was very low in these first measurements. At 1.3 Pa the ionization amounted to about 5% at late times when the

PI current has damped out. There is evidence that higher voltage on the PI bank will greatly increase the ionization level. Preparations for operation at voltages up to 125 kV on each capacitor are now being made.

D. COMPUTER MODELING OF THE HEATING IN A FAST PISTON IMPLOSION OF AN UNMAGNETIZED PLASMA

In the design of the current source, the switching and the preionization for the experiment, a bounce model for the plasma was used to predict the performance of the system. In the bounce model,¹ the plasma is assumed to be completely collisionless with the piston reflecting ions at twice the piston velocity. Another model used in calculations for the system is the snowplow model. The snowplow is at the opposite extreme from the bounce in that it simulates a high-collision rate after the piston interaction. In this model the plasma is assumed to be gathered up by the piston after which the center-of-mass of the plasma moves with the piston velocity. In both cases the piston current sheath width is small compared with other dimensions. The calculations using these two models bracket the results to be expected from an impervious imploding piston.

A simple method which achieves the snowplow configuration is for a cold ion to be reflected from the piston elastically with twice the piston velocity, and immediately collide with a stationary ion. The center-of-mass of the pair will be moving with the piston velocity, i.e., a snowplow. After the collision only one-half the original particle energy is in the directed energy of the two particles so the random energy of the two will account for the remaining one-half of the original particle energy. Of course, any number of processes could set up this configuration; however, this one is particularly simple in showing how the energy is distributed in the snowplow. As this process continues

the random energy will cause the annular region of snowplowed particles to expand, forming a growing sheath in front of the piston.

The calculation combines this picture of the imploding piston with the circuit of the current source of the driving theta-pinch field. The relation between the current in the theta-pinch coil and the motion of the piston and sheath is given by

$$\begin{aligned}
 2\pi r I^2 \mu_0/2 &= 2\pi r (1/2 \cdot \rho_0 v) 2v \\
 &+ \rho_0 \pi (r_0^2 - r^2) dv/dt \\
 &+ \rho_0 \pi 1/2 (r_0^2 - r^2) d\bar{v}_r/dt \\
 &+ 1/2 \bar{v}_r (\rho_0 v) 2\pi r \quad (1)
 \end{aligned}$$

ρ_0 = initial ion density
 r_0 = original diameter of plasma
 v = piston velocity
 \bar{v}_r = expansion velocity of sheath
 I = coil current/length .

The first term on the right side gives the piston pressure from the primary impinging ions. The coefficient of one-half arises because a second ion is picked up in an ion-ion collision. The second term is the contribution from the inertia of the snowplowed mass. The third and fourth terms are the contribution to the piston pressure from the expanding snowplowed sheath. In previous snowplow calculations the third and fourth terms have not been included.² With the assumption of complete randomness in the snowplow frame, it is reasonable to use the average ion velocity for \bar{v}_r , thus

$$\begin{aligned}
 \bar{v}_r &\approx 0.6 \left[\frac{\int v^2 dr}{(r_0^2 - r^2)} \right]^{1/2} \\
 &= 0.6 \left[\frac{\int_0^t v^3 r dt}{r_0^2 - r^2} \right]^{1/2}
 \end{aligned}$$

The circuit for the current source and theta-pinch load is shown schematically in Figure III-1. Since the 0.40-m coil is fed at four points this schematic is one-fourth of the total circuit. This circuit has now been built as a source for the fast theta-pinch implosion heating experiment.

For the analysis, the circuit and the plasma load described by Equation 1 are numerically evaluated with time in a self-consistent manner using the NET II code. The calculation continues until the front of the sheath (after passing through center) again hits the piston. The results of the calculations are shown in Figure III-10 for the following conditions

capacitor voltage = kV (500 kV for the whole coil)
 initial ion density = 10^{21}m^{-3}
 coil radius = 0.2 m
 initial plasma radius = 0.18 m .

The bounce model consists of an impervious magnetic piston which elastically collides with the background cold plasma. It is assumed that reflected particles move in a radial direction with twice the piston velocity and suffer no further collisions with the background plasma. The bounce model uses essentially the first term of equation 1 with a factor of two to account for all of the background particles which are involved. The results of the numerical calculations for the identical parameters as given for the snowplow are also shown

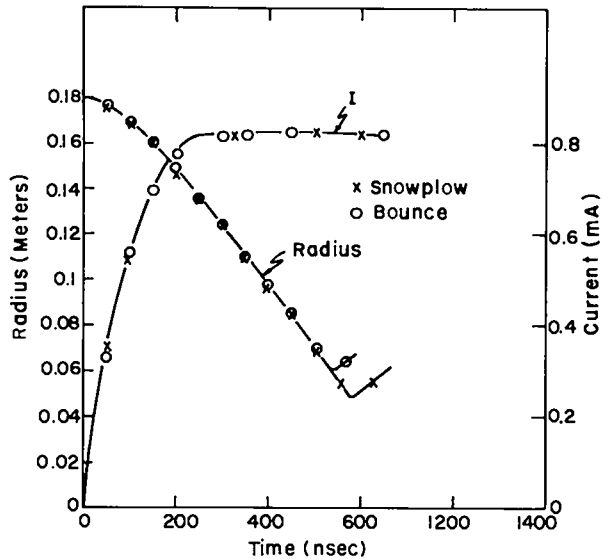


Figure III-10

Piston radius and coil current as a function of time. Both bounce model and snowplow model plasma loads are shown. The driving circuit is that of Figure III-1 except for minor variations in the inductances used. For both bounce and snowplow the average deuteron energy is 2.0 keV when the piston has reached one-third the initial radius.

in Figure III-10. It is seen that the two extreme models give only minor differences in all the results. The piston moves in slightly faster for the snowplow and reaches a slightly smaller radius before turn-around. The total particle energy is not significantly different for the two cases.

When the effects of the random energy and sheath expansion are added these two extreme models give results which differ only in certain details. Such important features as piston velocity and resultant plasma energy are essentially the same. If the experiment shows that a reasonable piston is formed, then from a practical point of view of heating a plasma, these results indicate that details of plasma interactions are unimportant. An important question to be answered by a heating experiment is the transparency of the driving magnetic piston. An impervious fast piston appears to give a plasma temperature which

is largely independent of the details of the process.

REFERENCES

1. Freidberg, J. P.; Morse, R. L.; and Ribe, F. L.; Staged θ Pinches with Implosion Heating, Los Alamos Report LA-DC-72-1400 (1972)
2. Artsimovich, L. A., Controlled Thermonuclear Reactors, (Gordon and Breach Science Publishers), p. 154.

IV. Z-PINCH PROGRAM

A. SUMMARY (J. A. Phillips)

In the Z-pinch program we examine the diffuse toroidal pinch generated by the ZT-1 experiment.¹ The particular type of pinch being investigated has approximately equal poloidal and toroidal magnetic fields. The toroidal current exceeds the Kruskal-Shafranov limit. Stability is achieved by the close proximity of a conducting wall, and the strong shear of the magnetic field, due to reversal of the toroidal magnetic field in the region outside the pinch. The advantages of this reversed field pinch include: 1) toroidal equilibrium, and 2) theoretical predictions of complete MHD stability for all wave numbers and modes. The purpose of the present phase of the experiment is to investigate the requirements necessary to establish a high-temperature, stable, reverse-field pinch.

In the fast mode of operation full programming of the magnetic fields has been reached and the pinch, though not yet completely stable, is closer to having MHD stability.¹ During the past year attention has been directed toward determining plasma parameters. These include the following:

a) Electron temperature measurements indicate a non-Gaussian velocity distribution and a low electron temperature < 100 eV. (Sections B and C)

b) Ion temperatures are found to be considerably higher than those for the electrons. Ion temperatures in excess of 800 eV are found with the experiment run in the fast mode. (Section D)

c) The plasma temperatures ($T_i + T_e$) inferred from plasma pressure profiles are in agreement with the independently measured values for electron and ion temperatures. (Section D)

d) The total particle line density is found to be constant and equal to the initial line density until the onset of pinch instability. Contributions from the discharge tube wall are small. (Section E)

In order to understand the requirements for establishing stable profiles it was considered advisable to reduce the I_z current in the pinch. The growth rates of instabilities would be reduced by this change and make it easier to study the evolution of the magnetic field profiles. The electrical circuit for the Z-current has therefore been modified (Section F). MHD stability analyses of measured magnetic field profiles are described in Section G. There is evidence that unstable modes can be stabilized by reversing the longitudinal field. Stable times of 8-10 μ s have been achieved with stability limited by diffusion.

In addition we have considered the following:

a) Necessary criteria for both energy and pressure balance on Z-pinches with diffusion have been established.²

b) An analytic expression for the growth rate of Suydam instabilities has been obtained for the case where the modes are symmetric about a singular radius. (Section H).

The low electron temperatures found in the ZT-1 experiment are unexpected. The plasma resistivity is then high and the diffusion of the poloidal magnetic field to the axis is rapid. Stable plasma confinement by the pinch for long times is then difficult, with the magnetic fields diffusing quickly toward unstable profiles and ohmic heating raising the plasma pressure above that which the pinch can contain.

Mechanisms responsible for the low electron temperature have not yet been identified.

Engineering support for the ZT-1 experiment includes the following:

- 1) Studies of a transfer capacitor circuit to replace the fuses on the experiment have continued.³
- 2) A fuse package capable of interrupting 500 kA and absorbing 30 kJ of energy has been developed for use in the present ZT-1 experiment.³
- 3) Field distortion spark gaps have been designed to crowbar the Z-current in ZT-1. These spark gaps use a molybdenum shell as the electrode surface (Section I).

B. ELECTRON TEMPERATURE BY THOMSON SCATTERING (L. Burkhardt, J. Di Marco, P. Forman, H. Karr)

Thomson scattering measurements are being made to determine the electron temperature. A plasma volume, 8 mm long and 2 mm in diameter, located 1 cm from the minor axis of the machine, is viewed at an angle of 90° from the incident laser beam. The $\Delta\vec{k}$ vector ($\vec{k}_{in} - \vec{k}_{out}$) has both radial and

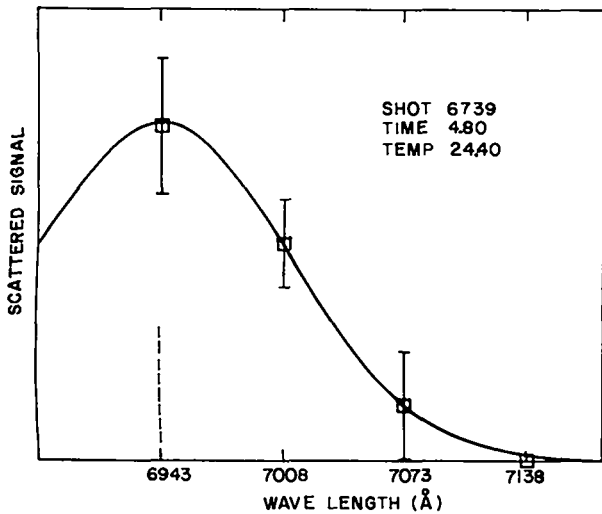


Figure IV-1
Thomson scattering spectrum taken with the slow mode of operation. The temperature is given in eV; the time in μ sec.

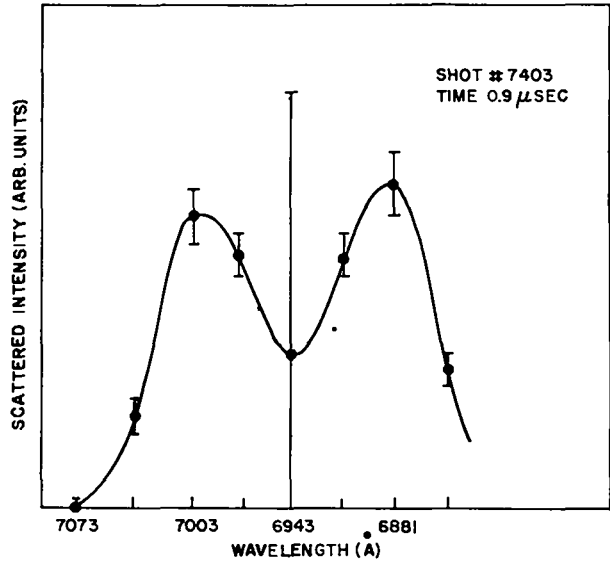


Figure IV-2
Thomson scattered spectrum taken with the fast mode of operation.

poloidal components but no toroidal component.

Striking differences are observed between the scattered spectrum for the slow and fast modes of operation of the ZT-1 experiment. Figure IV-1 shows the data taken in the slow mode. The time indicated is in μ s and is measured from the initiation of the I_z current. The temperature is obtained from a least-squares fit to a Gaussian. The data are typical of many shots taken in the slow mode, and the electron temperature varies from 10 to 50 eV, depending on the time of the measurement. The density, typically $3 \times 10^{15} \text{ cm}^{-3}$, obtained by comparison with Raleigh scattering in nitrogen, is as expected from compression of the filling gas.

Figure IV-2 shows data typical of those obtained in the fast mode. The solid curve is only included as a guide to the eye. The data are seen to be symmetric about the laser line at 6943 Å. The distribution is clearly not Gaussian but is double humped. It should be noted that the parameter $\alpha = 1/\Delta k \lambda_D$, where

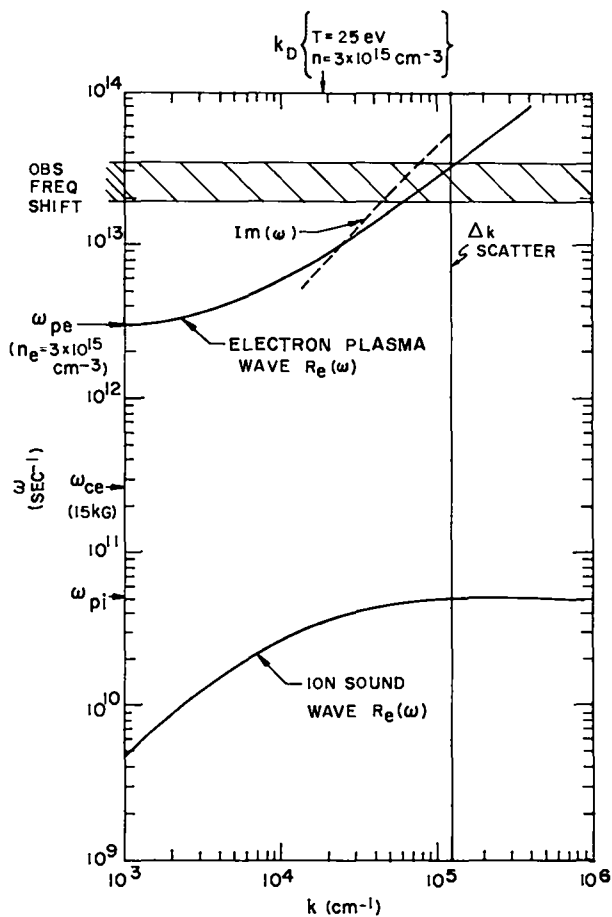


Figure IV-3

Plot of the dispersion relation for hot electron plasma waves.

λ_D is the Debye length, is much smaller than one in this experiment. Unfortunately large systematic errors on the 6943Å channel were present when the data of Figure IV-2 were obtained. These will be eliminated on future runs.

The wave number and frequency of the double humped feature shown in Figure IV-2 coincide with the dispersion relation of Bohm-Gross modes, see Figure IV-3, assuming an electron temperature of 25 eV. A 35° scattering experiment will help to determine if this is an accurate explanation of the data. Whatever the phenomenon is, it appears that it must be associated with electrons. Ion oscillations or waves are orders of magnitude lower in frequency. The

distorted spectrum is observed for times ranging from 0.75 μ s to 5 μ s in the discharge. Since the Landau damping of these waves is large, a strong driving mechanism would have to be present. There is experimental evidence for runaway electrons in the plasma.

C. ELECTRON TEMPERATURES FROM TIME-RESOLVED SPECTROSCOPY (B. Howell, H. Karr)

The time integrated impurity emission spectrum was observed for the ZT-1 plasma in the fuse mode. A plot of the densitometer measurements of the spectrum is shown in Figure IV-4. Carbon is the dominant impurity with some aluminum, oxygen, and silicon also present. Emissions from the ionization states of CI up to CV are observed. In the time-resolved spectra described below, weak CV emission is observed at 2278 Å but this weak emission is not observed in the above spectrum. For comparison, in the Scylla III spectrum for which $n_e = 3 \times 10^{16} \text{cm}^{-3}$ and $T_e \approx 300 \text{ eV}$, the CV line is comparable in intensity to the neighboring CIII 227.8-nm line. This indicates that the electron temperature in ZT-1 is less than in the Scylla III experiment.

Preliminary time-resolved spectral measurements have been made of emission from the successive ionization states^{4,5} of the intrinsic carbon impurity in the pinch. CIII came in early (<0.5 μ s) and never died away. The CV signal came in after 2 or 3 μ s and a peak at roughly 0.5 μ s was sometimes observed. This is seen in Figure IV-5. The large amplitude signal starting at 2 or 3 μ s is thought to come in when the plasma hits the wall. The early peak is not understood. However it may indicate that some of the electrons were briefly hot enough to excite CV emission during formation of the pinch.

The lifetimes of various ionization states were obtained from the solutions to the transient stripping equations.⁵ The fractional abundances of the ionization states versus time are plotted in Figures

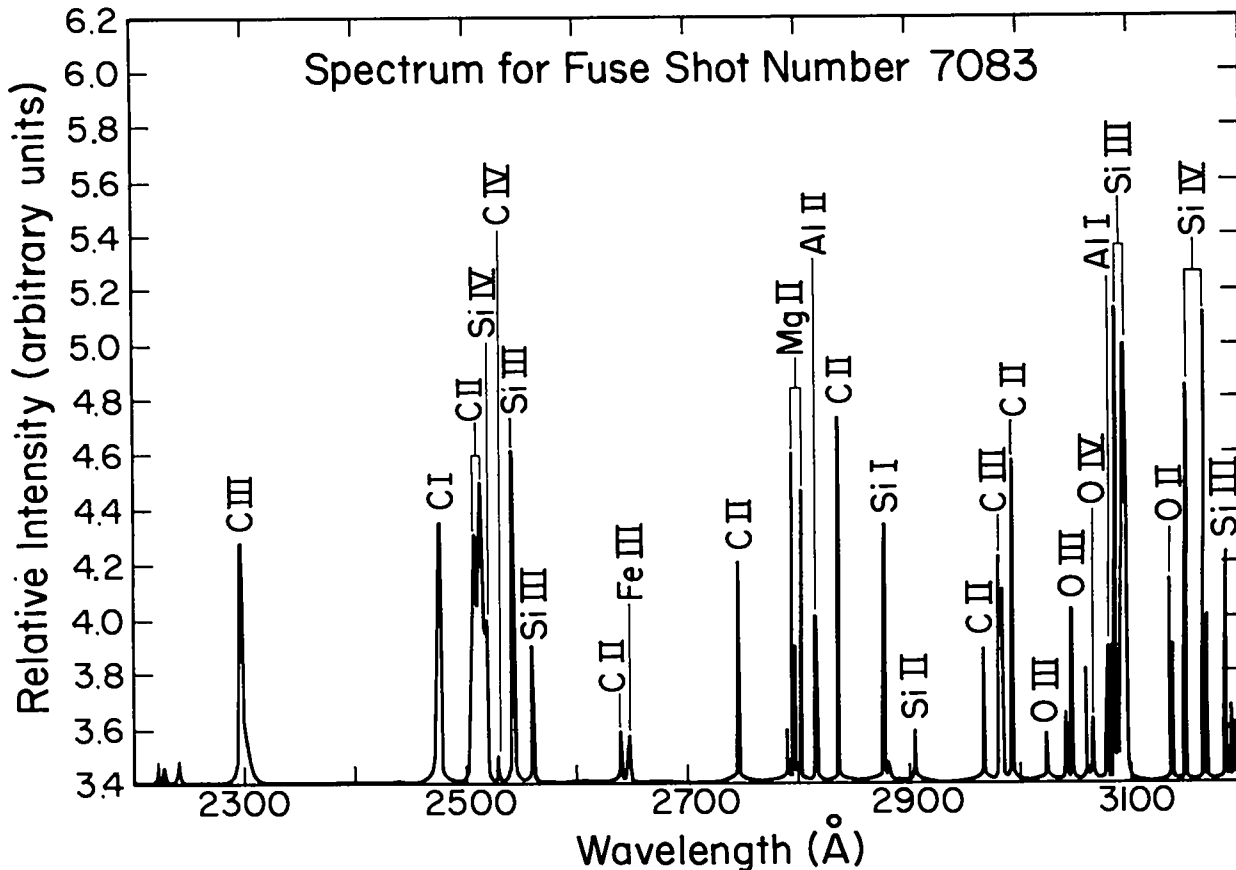


Figure IV-4
Impurity spectrum for pinch in the fast mode.

IV-6 and IV-7 for 25 and 100 eV, respectively. From these curves the electron temperature inferred for ZT-1 is ~ 30 eV.

The energy losses due to carbon line emission have also been considered. Using the formula for the excitation radiation loss rate given by McWhirter,⁴ it is found that for a 1% impurity of carbon, all in the CIV state emitting in the dominant 1548 Å line, the electrons would cool at a rate of 15 eV per μ s.

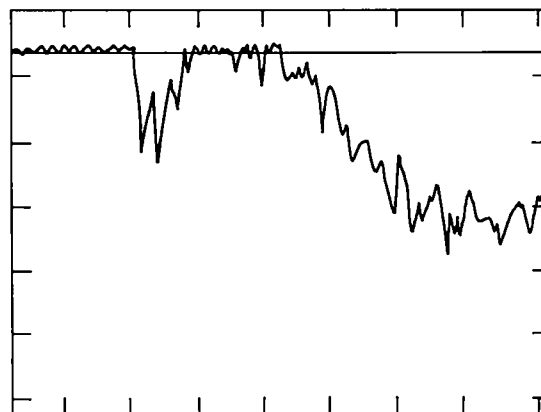


Figure IV-5
Photomultiplier intensity vs time for carbon V (2278 Å) at 0.5 μ s/division. The initial spike comes at 0.3 μ s after the start of I_2 .

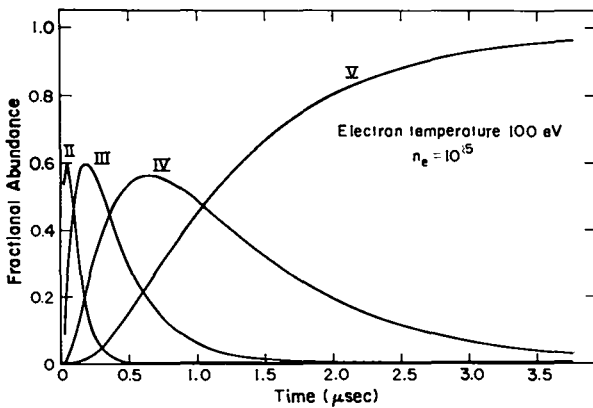


Figure IV-6
Fractional abundances of carbon ionization states vs time in a plasma whose electron temperature is 100 eV and density is 10^{15}cm^{-3} .

D. ION TEMPERATURE FROM DOPPLER BROADENING MEASUREMENTS (B. Howell, H. Karr)

To obtain information on the plasma ion temperature, measurements were made of the Doppler broadening of spectral lines from impurity ions added in known amounts to the plasma. Up until now only the HeII 4686 Å line has been investigated. The ion-ion collision time is short enough in the resistor mode that the ions should relax to a thermal distribution. The time for the cold electrons to cool the hotter ions is about 1.5 μs for a 30-eV plasma at $3 \times 10^{15} \text{cm}^{-3}$ density. However no significant cooling was seen in a time of $\sim 5 \mu\text{s}$.

The Doppler broadening was measured with an eight-channel polychromator modification to the McPherson Model 216 monochromator. The first modification had a 2-mm-diameter cylindrical lens inserted on the output aperture⁶ of the monochromator to diverge the beam to an array of eight light pipes and photomultipliers positioned to obtain wavelength separations of 0.85Å between channel centers. This allowed ion temperature measurements over a range of $\sim 25 \text{ eV}$ to $> 1 \text{ keV}$ and was useful for the fuse mode. In the resistor mode, (Section F), the heating was much less and a second modification was made to the polychromator

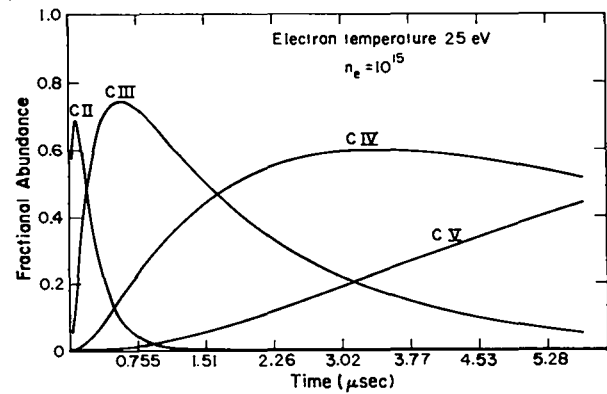


Figure IV-7
Fractional abundances of carbon ionization states vs time in a plasma whose electron temperature is 25 eV and density is 10^{15}cm^{-3} .

to measure the smaller Doppler broadening. This consisted of taking out the 2-mm cylindrical lens and using instead a negative lens before the focus of the monochromator to magnify the image slightly. Then a set of eight fiber optic light guides, each 0.063 mm wide, was used. This gave a separation between channels of 0.67Å and extended the ion temperature range down to about 15 eV.

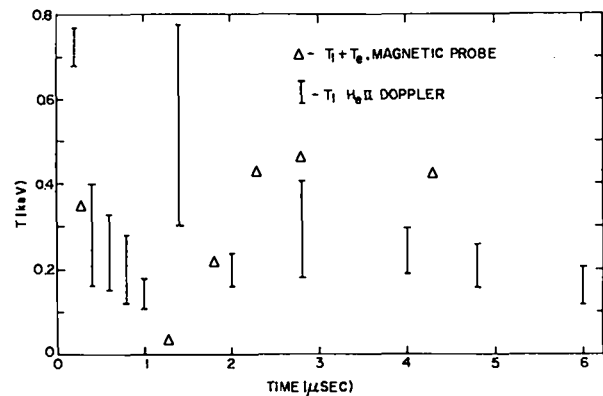


Figure IV-8
Comparison of ion temperature from Doppler broadening to plasma temperature found using probe measurements and pressure balance.

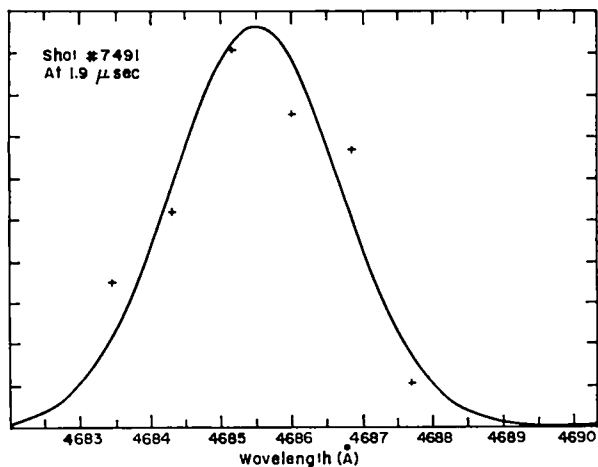


Figure IV-9
Least-squares fit to the Doppler broadened 4686 Å line of He II.

One of the series of measurements for the fuse mode is shown in Figure IV-8 and the results are compared with plasma temperatures obtained from the magnetic probe measurements showing fair agreement between the two methods of temperature measurement. The signal on six of the photomultiplier channels at a given time and the least-squares fit to a Gaussian are shown in Figure IV-9. Finally a plot of ion temperature for the resistor mode is shown in Figure IV-10. The observed widths of the 4686 Å line were appreciably greater than the Zeeman broadening⁷ and Stark Broadening⁸ so that only small corrections would be needed.

E. PLASMA DENSITY MEASUREMENTS WITH LASER INTERFEROMETER (L. Burkhardt, J. Di Marco, P. Forman, H. Karr)

Measurements of the electron line density along a minor diameter through the pinch discharge have been made using the 33900 Å infrared radiation from a He-Ne laser, with the Ashby-Jephcott interferometer technique.⁹ The laser beam passes through a small aperture in the primary and a clear quartz section of the discharge tube located 5.3 cm away from a pump port. The beam is modulated to produce fringes by means of a rotating mirror or, more

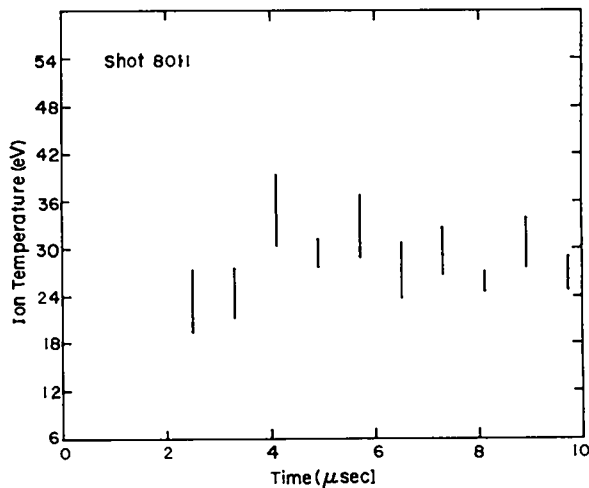


Figure IV-10
Ion temperature from Doppler broadening in the resistor mode.

recently, by a pair of counter rotating CaF plates in the beam to vary the optical path length of the external cavity. Figure IV-11 shows the mean electron density over the path of the beam through the plasma as a function of time measured from the start of the preionization stage, ~20 μs before the main discharge in the resistor mode. At the time of firing the main discharge, the

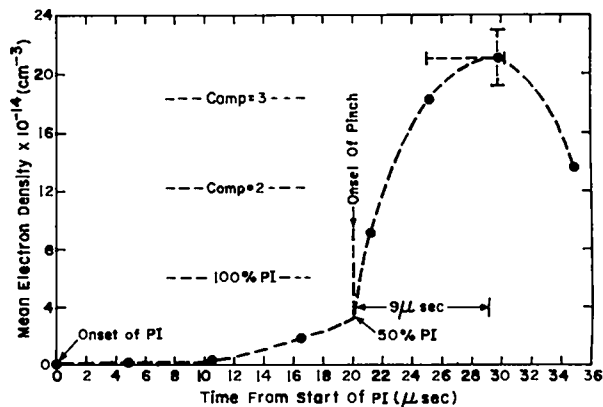


Figure IV-11
Plasma electron density versus time determined with a He-Ne laser (33900 Å infrared line) interferometer using the modulated Ashby-Jephcott method.

preionization reaches a level of $\sim 3 \times 10^{14}$ cm^{-3} , corresponding to 50% ionization at the filling pressure used. During the pinch formation, the line density increases as the pinch compresses. A compression of ~ 3 is reached for the conditions of Figure IV-11. The density reaches a peak in ~ 9 μs and falls off to $\sim 70\%$ peak value at ~ 15 μs . There is no indication of large particle loss or impurity influx in this time period. This is a good agreement with probe measurements and streak observations.

F. DERATING OF THE ZT-1 EXPERIMENT
(L. Burkhardt, J. Di Marco, P. Forman,
R. B. Howell, H. Karr, J. Phillips and A.
Schofield)

The results presented in this report together with results previously documented,^{1,10} show that a high ion temperature of several hundred eV is achieved in the fuse or fast mode of operation with I_z 's of 1.3×10^{12} A/s and I_z 's of 200 kA. The plasma is partially stable for 6 μs (calculated growth times are ~ 60 μs for $t \gtrsim 5$ μs) at which time a sudden disruption occurs, as evidenced by the onset of light seen in the streak and the increased number of unstable modes calculated from magnetic probe data, with growth times of 0.7 μs . Because of this behavior it has been postulated¹⁰ that the sudden disruption might be due to a change of magnetic field, perhaps due to diffusion, leading to an unstable configuration rather than the slow growth of an initial instability. In order to understand the requirements for establishing stable profiles it was considered advisable to reduce the I_z current in the pinch. The growth rate of the instabilities would be reduced by this change making it easier to study the evolution of the magnetic field profiles, as well as to increase the time during which field programming can be performed.

One method of derating I_z is to install resistors (typically 0.4 to 0.6 Ω) in series with the capacitor bank and pinch. The

resistance is greater than the critical value for the circuit ($R_C = 0.05 \Omega$). With this technique the initial I_z is equal to the bank voltage divided by the system inductance. Values of I_z from 4 to 20×10^{10} A/s can be obtained. The risetime of the current from the L/R time constant of the circuit is ~ 0.5 μs . The peak current is ~ 80 kA with 40 kV on the main bank. The current decay, determined by the RC time constant of the circuit, is 60 to 90 μs .

The design of the resistor consists of 0.203-mm stainless steel, 152.4 mm wide and 9.14 m long. It is folded for low inductance, rolled up into a cylinder, and immersed in an oil bath to dissipate heat. The machine is being operated with four resistors, one in each quadrant. At 20 kV and with the maximum magnetic storage inductance of 160 nH, I_z is 40 kA and the \dot{I}_z is 6×10^{10} A/s, as expected.

The data acquisition rate is increased with resistors, compared with fuse operation, in that the time between discharges is greatly reduced. The resistor design also allows the machine to be changed from fuse to resistor operation within ~ 2 hours.

Figure IV-12 shows the pinch current and voltage obtained with the main bank

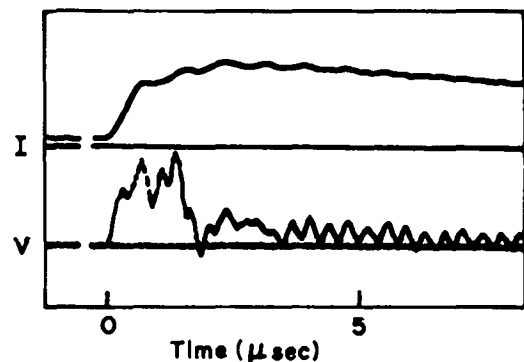


Figure IV-12
Current and voltage obtained when operating in the derated mode. Peak current and voltage are ~ 40 kA and 8 kV, respectively.

charged to 20 kV. Peak current is ~ 40 kA and the voltage is ≤ 8 kV per quadrant of the torus. The following data are obtained with a plasma having 20% helium and 80% deuterium as the initial filling gas. The filling pressure is approximately one Pascal. Doppler width measurements of the He II 468.6-nm line give an ion temperature of ~ 40 eV. The Thomson scattered signal indicates a temperature of ~ 5 eV for the electrons.

Streak photographs of the discharge under several operating conditions are shown in Figures IV-13 and IV-14. The streak is taken looking down from the top of the discharge with the major axis of the torus beyond the top of the page. The data displayed below each streak are: 1) the total \oint_z flux measured across a minor cross section of the discharge tube, i.e., the flux associated with the longitudinal magnetic field; 2) the current I_0 in the winding that produces the B_z longitudinal magnetic field, and is a measure of the B_z magnetic field in the vacuum region outside the plasma column; 3) the B_z sine-cosine coils which measure the first Fourier components of the B_z magnetic field. This latter type of probe responds ideally only to a net helical displacement of the plasma current.¹¹ A signal is then interpreted as due to an instability in the plasma.

The streak photograph in Figure IV-13a shows an instability with the experiment run in the "stabilized" pinch configuration but without reverse B_z . The longitudinal flux is maintained constant by means of an electrical crowbar in the circuit. Correlations of the instability, as displayed by the streak with the small negative step in I_0 and the signal in the B_z sine coil, are considered good. The streak in Figure IV-13b is obtained under the same initial conditions except that a B_z reversing field is applied late in the discharge period at ~ 7 μ s. The time of application of the reversing field is most easily seen in the flux measurement. The general behavior of the pinch reproduces the previous discharge,

going unstable in about 3 μ s. Figure IV-14 displays two sets of data taken under identical conditions as in the previous figure, except for the gradual advancement of the time of application of the reversing field. In Figure IV-14a some radial displacement of the pinch is evident, but the magnitude is reduced. This effect is also seen in the reduced amplitude of B_z sine coil signal. The data in Figure IV-14b show that the radial displacement is very small when the reversing field is applied 0.6 μ s after the start of the pinch implosion. The original instability appears to have been reduced significantly so that no obvious displacement of the pinch is visible in the streak. However, a new instability is generated when the flux is allowed to reverse, violating one of the necessary stability conditions. The B_z sine coil signal shows the new instability occurring at different times, which are correlated to the time at which the flux reverses. To correct this, modified spark gap crowbar switches are being installed to allow the B_z current to be crowbarred at this very slow rate of change of the reversing field.

Figure IV-15 shows the streak of an unstable pinch with the reversing field applied at the time of the implosion. With a faster rate of change of this reversing field the crowbar is effective in preventing the flux from reversing. Obviously, setting up stable pinches is not yet simple. Magnetic field profiles must be analyzed along with all of our additional diagnostics to establish some understanding of the complicated processes of stabilizing the pinch. That an instability can be suppressed by a reversed magnetic field is shown by these data. What type of instabilities is being suppressed, and what is required to set up the correct fields is being investigated.

When the criteria for establishing stable profiles are established, the I_z current will be increased to generate

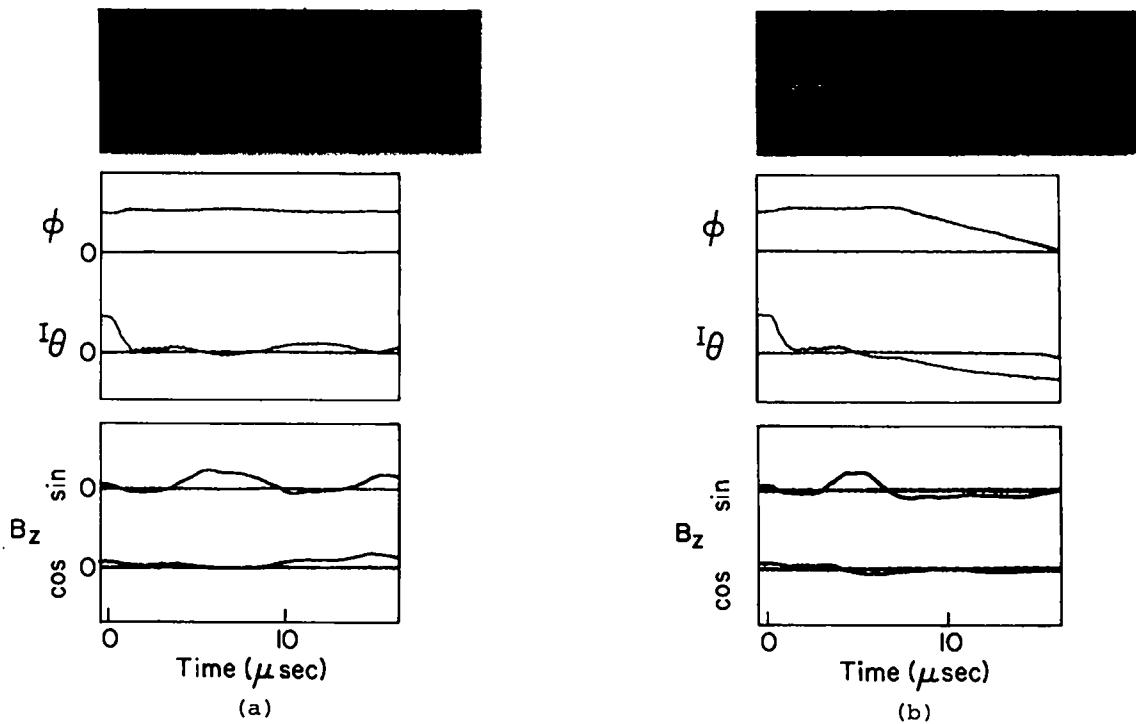


Figure IV-13
 Time correlation of the streak photographs with longitudinal flux, I_θ , and B_z sine-cosine coils, a) no reversing field is applied, b) the reversing field is applied at $\sim 7 \mu s$.

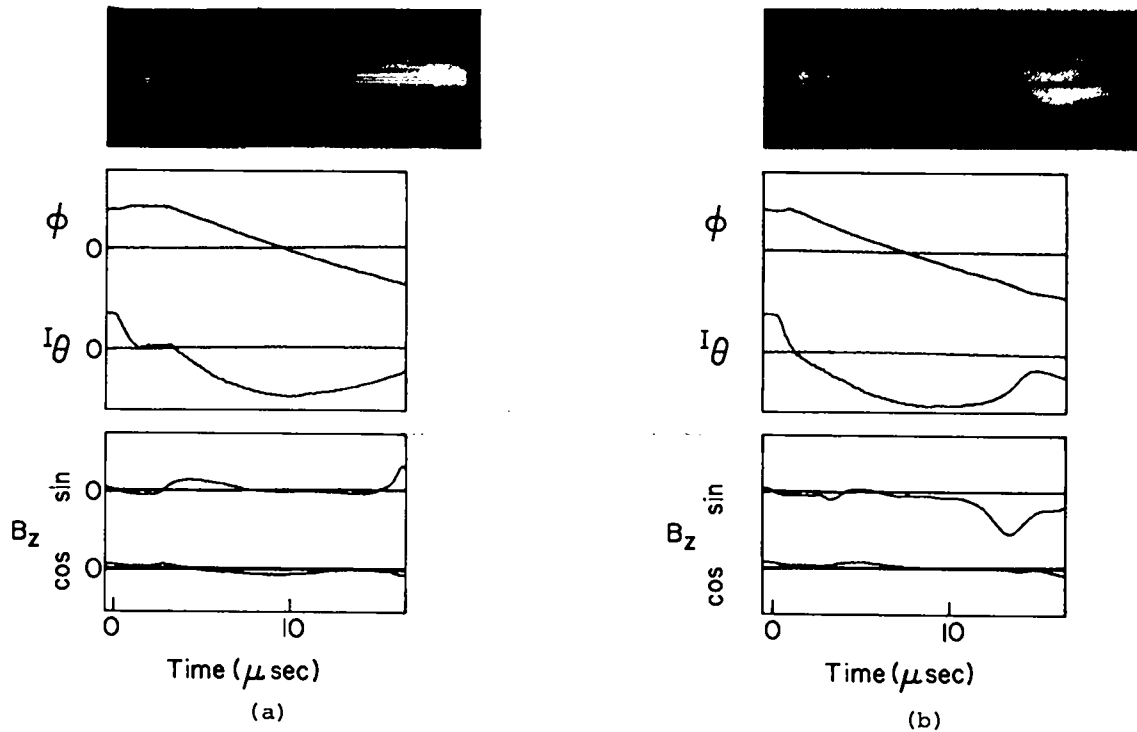


Figure IV-14
 Time correlation of the streak photograph with longitudinal flux, I_θ , and B_z sine-cosine coils, a) reversing field applied at $\sim 3 \mu s$, b) reversing field applied at $0.6 \mu s$.

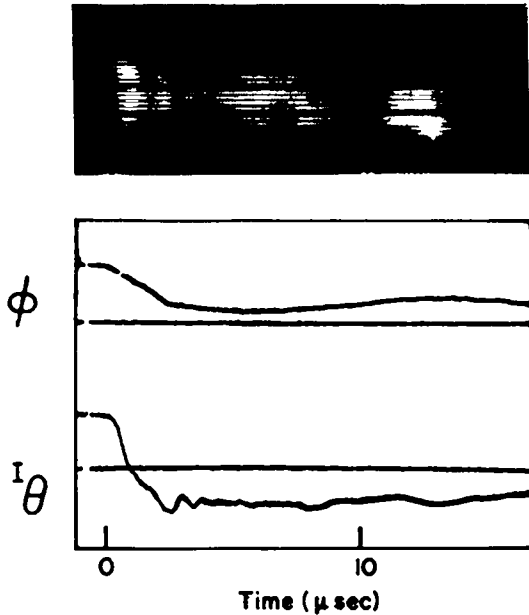


Figure IV-15
Time correlation of the streak photographs with the longitudinal field being changed faster than in Figures IV-13 and IV-14.

higher plasma temperatures and to determine scaling.

G. MHD-STABILITY ANALYSIS (A. Haberstich)

Magnetic field profiles measured under the derated mode of operation of ZT-1 have been analyzed for MHD stability, using the techniques described in our previous annual report.¹ Tentative results are reported in Figure IV-16.

The figure shows the e-folding time of the fastest calculated $m = 1$ mode, as function of time for two discharges, one with an initial axial bias field of 0.071 T (solid line), the other with a bias field of 0.063 T (dashed line). The filling pressure is 2.1 Pa (16 mTorr) of D_2 in both cases.

The behavior of the growth time is quite different from the fuse shot result reported earlier in that the instability sets in gradually, rather than suddenly as

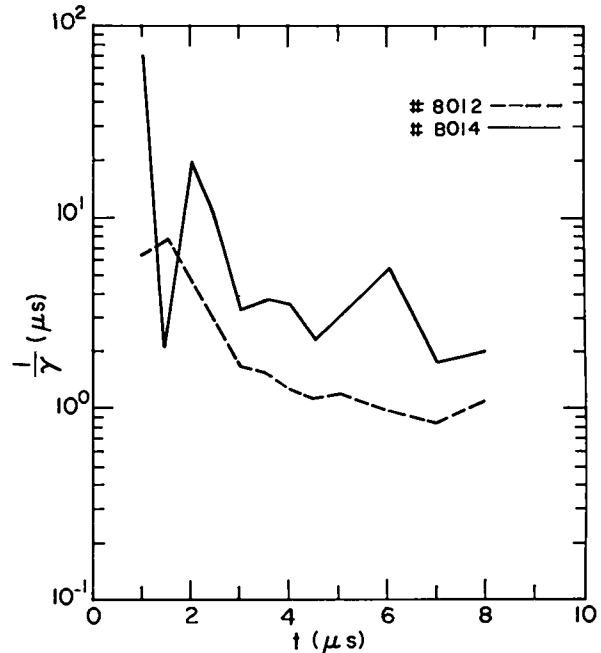


Figure IV-16
MHD Stability Analysis. Calculated growth times of $m = 1$ modes as functions of time for two discharges in ZT-1. Initial bias field 0.071 T (solid line) and 0.063 T (dashed line).

in the fuse mode of operation. The time of penetration of the axial current is of the order of 4.5 μs and it is likely that diffusion plays a significant role in limiting the stable time of the discharge. Increasing the electron temperature, as in the fast mode, should slow down the diffusion.

H. SYMMETRIC SUYDAM MODES (A. Haberstich)

Suydam modes are localized MHD modes occurring at the singular radius r_s where $\underline{k} \cdot \underline{B} = 0$, \underline{k} being the wave number of the perturbation and \underline{B} the total magnetic field. An analytic expression for the growth rate of this instability has been obtained for the case where the Suydam modes are symmetric about r_s .

The growth rate is found to be an increasing function of the Suydam ratio¹²

$$s = 8 \frac{\mu_0 p'}{r B_z^2 (p'/p^2)}$$

where p is the plasma pressure, P the pitch length, B_z the axial magnetic field, r the radius, and the primes denote differentiation with respect to r . Also, the growth rate is a decreasing function of the local beta $\beta \propto p/B^2$. The modes are single humped for high shear and double humped for low shear.

Although the derivation assumes a large value of the azimuthal wave number m , the results have also been applied to low m -number modes. Figure IV-17 shows, as function of the radius r , the growth rates γ obtained with the analytic solution and with the conventional normal mode analysis.¹³ The agreement is good at large radii. The discrepancy at small radii is due to the fact that, in this example, the Suydam modes are asymmetric in that region.

I. CROWBAR SPARK GAPS (A. Schofield)

Field distortion spark gaps have been designed and purchased to crowbar the Z-current in ZT-1. These spark gaps use a molybdenum shell as the electrode surface. The shells are 0.75-mm molybdenum sheets formed to the electrode shape by metal spinning techniques. Both molybdenum and tantalum shells have been tested. With a peak current of ~ 60 kA and a q of ~ 9.5 coulombs per shot the electrodes shells showed less than 0.03-mm erosion after 250 shots (2375 coulombs). The shells do not exhibit a great deal of mechanical strength and require solid backing to prevent being deformed by the magnetic field of the switched current. One advantage of the shell-type electrode is that the surface exposed to the discharge

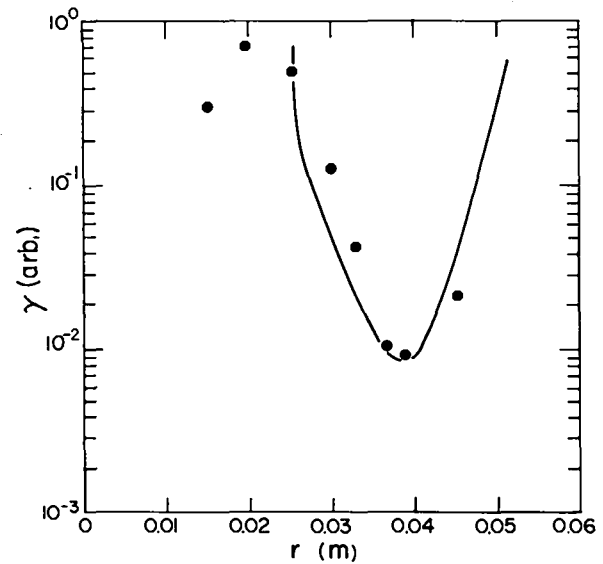


Figure IV-17
Symmetric Suydam Modes. Comparison of growth rates calculated with the analytic solution (solid line) and with the normal mode analysis (dots) as function of radial position.

is refractory metal with no possibility of the arc "seeing" the structural parts of the electrode which are usually aluminum.

REFERENCES

1. Fred L. Ribe, compiler, "LASL Controlled Thermonuclear Research Program for the 12 month period ending December 1972," Los Alamos Scientific Laboratory Report LA-5250 (June 1973).
2. Theoretical Physics Section, this Annual Report.
3. Engineering Section, this Annual Report.
4. R. W. P. McWhirter, "Ionization Times of Impurities in Hydrogen Plasmas", Proc. of Phys. Soc. (London) 75, 520-525 (1960).
5. R. F. Post, "Impurity Radiation Losses from a High Temperature Plasma", Int. Summer Course in Plasma Phys., Riso, Denmark, Report #18, 313-346 (1960).
6. R. F. Scott, E. N. Dacus, R. G. Tuckfield, Jr., "Optical Emission Line Profile Analyzer", Review of Scientific Instruments", Vol. 33, No. 9, 1001-1002 (1961).

7. K. E. Weimer, "Doppler Broadening of the He⁺ 4686 Line in Ion Temperature Measurements", Project Matterhorn, Princeton University Report NYO-7885 (January 1957).
8. H. F. Berg, A. W. Ali, R. Lincke, H. R. Griem, "Measurement of Stark Profiles of Neutral and Ionized Helium and Hydrogen Lines from Shock-Heated Plasmas in Electromagnetic T Tubes", Physical Review, Vol. 125, No. 1, 199-206 (1962).
9. D. A. Baker, J. E. Hammel, F. C. Jahoda, "Extension of Plasma Interferometry Technique With a He-Ne Laser", Review of Sci. Instr. Vol. 36, No. 3, 395-396 (March 1965).
10. J. Di Marco, J. Phillips, "The Present Status and Future Program of the ZT-1 Experiment", Los Alamos Scientific Laboratory internal document (November 1973).
11. "LASL Controlled Thermonuclear Research Program for the 12 month period ending October 31, 1968," Los Alamos Scientific Laboratory report LA-4075 (January 1969)
12. B. R. Suydam, "Stability of a Linear Pinch", Proc. Intern. Conf. Peaceful Uses Atomic Energy, 2nd, Geneva, Vol. 31, 157-159, (1958).
13. J. P. Freidberg, "Magnetohydrodynamic Stability of a Diffuse Screw Pinch", The Physics of Fluids, Vol. 13, No. 7, 1812-1818 (1970).

V. THEORETICAL PHYSICS PROGRAM

A. GENERAL SUMMARY (W. B. Riesenfeld)

During the reporting year the LASL CTR theory group has concentrated its efforts into three broad areas of research which to a large degree reflect the organizational structure of the confinement and research programs. The work is therefore predominantly programmatic in nature, although certain smaller and less programmatic projects in useful and interesting plasma physics have been pursued by individual staff members as permitted by time and warranted by opportunity. Such a combination of activities is thought to provide an atmosphere of intellectual stimulation while fully satisfying the programmatic research requirements. The present report describes progress in the three main research areas, but several of the paragraphs below also give a glimpse into some of the auxiliary work. Since this report also covers progress for the quarter of October 1 through December 31, 1973, the account below emphasizes the activities of that period.

The first major research area provides theoretical support to the Scyllac toroidal theta-pinch confinement program. This effort has seen major advances in the refinement of the MHD models which are used to describe the equilibrium and stability of toroidal theta-pinch configurations. In particular, the so-called "Everest" calculational program is successfully extending the MHD stability analysis to diffuse plasma and magnetic field profiles for $\ell=1$ equilibria, making only minor and experimentally justifiable approximations. This program is expected to have great impact in providing reliable theoretical data references and guidance to the Scyllac program. The

ion Vlasov-fluid model, which gives a more realistic plasma description than the MHD model, has received intensive development in its application to all the major research areas, and in relation to Scyllac theory it is being used to investigate the influence of finite ion gyro radius effects on the stability of $m=1$ as well as $m \geq 2$ modes. The entire toroidal theta-pinch $\ell=0,1$ confinement system has been subjected to a scaling analysis which takes into account the requirements of toroidal equilibrium, wall stabilization of the $m=1$ mode, and ion gyro-stabilization of the $m \geq 2$ modes. The result is a semiquantitative understanding of the optimum values of major radius and other physical parameters which probably must be designed into a scientific feasibility experiment or a physics test reactor based on a stable toroidal theta pinch. The physical significance of the wall stabilization of the $m=1$ mode in $\ell=1$ equilibria has been investigated. Finally, the influence of cross-sectional shape upon the stability of several types of pinches has received preliminary study.

Our second major research area is the program in numerical simulation of Vlasov plasmas and computer applications. This program is of course closely related to all of our other research efforts. Its studies of microinstabilities in high-beta systems, of anomalous transport coefficients in collisionless plasmas, of spatially inhomogeneous structures such as implosion sheaths, and of the nonlinear evolution of instabilities provide physical input for almost all of the theoretical work. During the reporting year this research program has seen significant increases in effort,

funding, and staffing, attesting to its rapidly growing role in the theoretical and computational support of the CTR program. Significant progress has been achieved in two-dimensional implosion simulations and in understanding microinstabilities in theta-pinch sheaths. Other fields of active research include the Darwin model simulation method for electromagnetic modes, numerical Vlasov equilibria, hybrid model implosion simulations, Vlasov-fluid models for linear stability analysis, Vlasov-fluid model studies of the stability of hot pinches, and comparisons of various simulation algorithms. The long-range aim of this research effort is to provide physically realistic descriptions of thermonuclear plasmas in a geometrically realistic three-dimensional framework. It will doubtlessly take many years of hard work to achieve this ambitious goal, but tangible progress is gratifyingly evident. The organization of a centralized computing facility to service all of the major CTR laboratories and university contractors will hopefully furnish us with a powerful new tool of which we intend to make maximum use. Accordingly, the next year will see additional computer applications efforts related to the operation and maintenance of the remote terminal, along with the programming and software activities which the latter will require.

The third research area covers theoretical support for the toroidal dynamic Z-pinch and related studies. In this field much progress has been made in devising MHD models which describe the equilibrium and stability of such pinches. Stable diffuse profiles have been found through the use of a set of elaborate computer programs, and the features of the plasma pressure and magnetic field profiles which assure stability against both pressure driven and current driven modes have been checked against the predictions of analytic theory. Comparison with the results of the experimental program, where stability has generally not been observed so far, has led to what is

perhaps the major advance of the year. It was conjectured, and then analytically demonstrated, that for the experimental ZT-1 parameters the conditions of energy balance, pressure balance, and rapid poloidal magnetic field diffusion lead to a final compressed pinch state which, in the absence of effective energy loss mechanisms, carries a beta value which exceeds the critical value for stability as demanded by theory. If this interpretation turns out to be correct, an important key may have been found for overcoming the difficulties which seem to be blocking experimental progress. The program is not only interested in profile-stabilized systems such as the dynamic Z-pinch, but also in q-stabilized systems such as belt pinches. The toroidal MHD equilibrium codes have been adapted to the study of such systems and have produced interesting results which connect the shape of the elongated plasma cross section to the boundary conditions. The hope for such systems was that the noncircular cross section would provide an extra stability margin, i.e., that the critical beta for current driven kink modes could be increased. Preliminary finite-beta calculations have indicated, however, that the stability condition imposed on the safety factor q becomes more strigent than is the case for circular cross section, and that extreme deformations may defeat their purpose. This issue is not settled, but in both experimental and theoretical aspects of this problem we note a gratifying and fruitful interaction with the high-beta research group at the Max Planck Institute for Plasma Physics at Garching.

B. SCYLLAC SUMMARY (J. P. Freidberg)

During the past year several different problems relating to Scyllac theory have been investigated. The major thrust was in the area of MHD theory, where of course the problem is to understand the stability of the $\ell=1$ Scyllac configuration. Within this area three basic problems were addressed.

Two were ideal MHD calculations, using different expansions, but both examining straight $\ell=1$ systems with diffuse profiles. The third was an investigation of finite Larmor radius effects on the $m=1$ mode as well as on the $m \geq 2$ modes in Scyllac. A second major area of investigation concerned theoretical scaling laws and their implications on theta-pinch feasibility experiments. These calculations are based on somewhat crude theories, but nonetheless represent the best theories available today. The final area investigated dealt with the physical significance of the $m=1$, $\ell=1$ wall stabilization term. This effect is vital to the future of the Scyllac program. Because of this and because of the unusual behavior of wall stabilization in diffuse $\ell=0$ calculations, it was useful to reexamine the $\ell=1$ wall stabilization to insure that it was understood. Given below is a brief summary of the progress made in each of these areas.

1. MHD Theory

a) "Everest" is a calculation of the stability properties of a diffuse $\ell=1$ equilibrium. The only simplification is that of small z -dependence. The slow z -expansion in "Everest" is an excellent approximation to the experimental situation. By carrying out this computation to sufficiently high order (i.e., leading and first order) we will have obtained the most reliable theoretical Scyllac results for some time to come (i.e., until fully three-dimensional computations become feasible). The calculation is largely numerical and, because of the lowest order $\ell=1$ cancellation, it requires extreme accuracy. The equilibrium solution is computed numerically and is used in a δW minimization.

Because of the magnitude and complexity of the problem the first quantitative results (i.e., leading order) will probably not be available for about six months, and the full results not available for perhaps 1-1/2 years.

b) A simpler diffuse MHD calculation for diffuse $\ell=1$ profiles was undertaken

last summer. The basic assumption here is that the helical fields are small compared to the θ -pinch field, but no assumption is made regarding the z -dependence. The motivation for this calculation is that the most important destabilizing term arises from a higher order effect in the slow z -variation, but is not too dependent on the size of the helical fields. Thus, despite the fact that the theoretical ordering disagrees with the experimental situation, it is hoped that the important destabilizing term will be reasonably treated on a time scale much shorter than Everest. This calculation is largely analytic and this portion of the work is completed. There remains some numerical work which will require about two months of concentrated effort to get quantitative results.

c) A fairly extensive effort has been undertaken recently to investigate finite Larmor radius (FLR) effects on the $m=1$ Scyllac mode. It is well known that a pure $m=1$ displacement is not influenced by FLR effects. However, the Scyllac configuration is stable to a pure $m=1$ displacement and only goes unstable if small $m=0$ and 2 components are present in the displacement. This latter component could be influenced by FLR effects. The calculation is entirely analytic at present and is progressing steadily. It is however quite complicated and it is hoped that significant results can be obtained within six months.

2. Scaling of Wall-Stabilized Scyllac Experiments

The Scyllac concept^{1,2} consists of producing toroidal equilibrium in a high- β theta pinch by superimposing a combination of helical ($\ell=1$) and bumpy ($\ell=0$) fields on the basic toroidal θ -pinch field. An investigation of the stability of this system indicates that several opposing requirements must be satisfied simultaneously in order that all of the gross modes be stabilized. Our purpose here was to investigate the scaling laws based upon existing theory and to determine their implication for future

experiments such as a "scientific feasibility" experiment. It should be emphasized that the existing theories have been derived from sharp-boundary models and thus the results will be semiquantitative at best. In addition, certain theoretical constraints are required to be satisfied even though some of the corresponding physical phenomena have not been well verified experimentally. It is our feeling that the criteria which are required to be satisfied represent the most pessimistic predictions of existing theory. However, the basic conclusion of our investigation is that, despite these pessimistic requirements, reasonable values of the physical parameters exist such that the known theoretical conditions can be satisfied.

Consider a next-generation experiment where certain parameters will be assumed fixed by scientific objectives as well as economic considerations. In particular, fix the D-T ion temperature $T_i = 6$ keV, the magnetic field $B = 50$ kG, and plasma $\beta = 0.8$. These values are consistent with the scientific goals of a feasibility experiment. The economic constraints require that the volume of magnetic energy be as small as possible. Not too surprisingly, it turns out that to minimize the total volume requires using as small a value of coil radius, b , as possible. Taking into account the requirements of shock heating, assume the minimum b to be fixed at $b = 10$ cm. Under these conditions it must be determined what existing theory requires of the plasma radius a , the major radius R , the pitch number h of the helical field, the $\ell = 1$ plasma displacement δ_1 , and the $\ell = 0$ plasma displacement δ_0 in order to satisfy the following three conditions:

- (1) sufficient $\ell = 1$ and $\ell = 0$ fields for toroidal equilibrium
- (2) sufficient wall stabilization to stabilize the $m = 1$ mode
- (3) sufficient finite gyro radius effects to stabilize $m \geq 2$ modes. Each of these

requirements will now be discussed separately.

We begin by noting that the application of helical field distorts the shape of the plasma such that the plasma radius is given by

$$r = a[1 + \delta_1 \cos(\theta - hz) + \delta_0 \cos hz]. \quad (1)$$

The conditions that the theoretical constraints given below be valid are that:

- (1) $ha \ll 1$; this corresponds to a helical period long compared to the plasma radius,
- (2) $\delta_0/\delta_1 \ll 1$; this corresponds to making $\ell = 1$ the dominant plasma displacement. In present Scyllac experiments, typical values are $ha \approx 0.15$ and $\delta_0/\delta_1 \approx 0.1$.

The theoretical condition for toroidal equilibrium^{3,4} is given by

$$\delta_0 \delta_1 = \frac{g_1(\beta)}{h^2 a R}, \quad (2)$$

where from sharp-boundary theory

$$g_1(\beta) = \frac{2}{3-2\beta}. \quad (3)$$

Equation (2) is by far the most reliable of the constraints that we shall impose. The scaling implied by this relation has been confirmed experimentally² over a significant range of parameters including two different major radii, $R = 2.4$ m and 4.0 m. In addition, the sharp-boundary coefficient $g_1(\beta)$ turns out to be correct to within 10%.

The theoretical condition for stabilizing the gross $m = 1$, $k \approx 0$ mode^{4,5,6,7} is given by

$$\delta_1^2 \left(\frac{a}{b}\right)^4 \geq g_2(\beta) h^2 a^2 \delta_1^2 + g_3(\beta) \delta_0^2, \quad (4)$$

where

$$g_2(\beta) = \frac{(4-3\beta)(2-\beta)}{8\beta(1-\beta)} \quad (5)$$

$$g_3(\beta) = \frac{(3-2\beta)(1-\beta)}{\beta(2-\beta)}. \quad (6)$$

The first term in Eq. (4) represents a wall stabilization effect arising from the induced helical dipole current flowing in the plasma. Because of the strong fourth-power dependence, relatively large values of a/b (~ 0.4) are required in order to achieve significant wall stabilization. In addition, the next-generation experiment will be heated by a staged⁸ power supply in which the shock (implosion) heating is provided by a fast, high-voltage circuit and the adiabatic compression by a slow, low-voltage circuit. As previously stated, these conditions require the first wall radius, b , to be no smaller than 10 cm. This allows the formation of a well-defined piston front of thickness $c/\omega_{pi} \ll b$ at normal filling densities of approximately 10^{15} cm^{-3} . Another important consideration in choosing the minimum value of b is that too small a value leads to excessively low inductance of the implosion heating coil. This leads to the result that the magnetic energy of the high-voltage source is inefficiently coupled in and is largely lost in irreducible stray inductance.

The second term in Eq. (4) is a destabilizing term arising from bad curvature of the $\ell = 1$ field. An $m = 1$ instability has been observed in straight $\ell = 1$ systems and the experimentally measured⁹ growth rates agree to within a factor of 2 with those given by the theory.^{4,5,6} However, extensive scaling measurements have not been made, in particular with respect to ha and δ_1 . A recent set of experiments on Scylla IV,¹⁰ using two different values of h , gave results that are in approximate agreement with the scaling laws (i.e., the g_2 term of Eq. (4)).

The last term in Eq. (4) is a destabilizing term arising from bad curvature of the $\ell = 0$ field and is the least understood of all the effects considered here. The $\ell = 0$ coefficient, g_3 , given by Eq. (6) is a sharp-boundary result. Sharp-boundary

theory also predicts wall stabilization of this mode by the $\ell = 0$ fields, although in a more sophisticated diffuse model, no such effect exists. To be conservative we have omitted this stabilizing effect. In high-temperature θ -pinch experiments¹⁰ $\ell = 0$ growth rates have been measured which range from slower to much slower than those predicted theoretically. However, we use the theoretical value of growth rate which, from the above evidence, is probably pessimistic.

A final point concerning the design of the next-generation experiment is that we assume the implosion heating coil and first wall to have a helical configuration, rather than a straight cylindrical shape as has been conventional in the past. The purpose of this is to allow reasonably "fat" plasmas ($a/b \sim 0.4$) to have significant helical displacements ($\delta_1 \sim 1$) without the plasma touching the tube as it would in a straight discharge tube.

The theoretical condition for the final constraint, that of finite gyro radius stabilization on $m \geq 2$ modes,¹¹ is given by

$$\left(\frac{r_L}{a}\right)^2 \geq g_4(\beta) h^2 a^2 \delta_1^2, \quad (7)$$

where

$$g_4(\beta) = \frac{8\beta^2(1-\beta)}{2-\beta} \quad (8)$$

and $r_L = [2m_i T_i / e^2 B_0^2]^{1/2}$ is the ion thermal gyro radius. The experimental evidence is far from complete in evaluating the importance of this constraint. On the one hand, ideal MHD predicts very fast gross $m = 2$ modes which are not observed experimentally. However, in all of these experiments to date, Eq. (7) has been satisfied. There is as yet no first-hand experimental knowledge of whether Eq. (7) describes the correct transition or if the scaling is correct. Nevertheless, it is our best theoretical estimate, and hence we shall require it to be satisfied.

In scaling a next-generation experiment, we consider β , b , and the gyro radius r_L as fixed parameters and eliminate δ_0 and h from Eqs. (2), (4), and (7), leaving a relationship between R , δ_1 , and a (or alternatively a/b , since b is assumed constant). This relationship is given by

$$R \geq g_3^{1/2} g_1 g_4 \frac{b^3}{r_L^2} \left[\frac{(a/b)^8}{(a/b)^6 - (g_2/g_4) (r_L/b\delta_1)^2} \right]^{1/2}. \quad (9)$$

The optimum design of an experiment is one in which R , and hence the cost, is minimized. If we examine R as a function of a/b for a given δ_1 we note that Eq. (9) has a reasonably broad minimum at a critical value of a/b given by

$$\frac{a}{b} = 2^{1/3} \left(\frac{g_2}{g_4} \right)^{1/6} \left(\frac{r_L}{b\delta_1} \right)^{1/3}. \quad (10)$$

Since the minimum is broad we introduce a parameter α , defined by

$$\frac{a}{b} = 2^{1/3} \alpha \left(\frac{g_2}{g_4} \right)^{1/6} \left(\frac{r_L}{b\delta_1} \right)^{1/3}, \quad (11)$$

which measures the deviation of a/b from the optimum. Values of $\alpha \neq 1$ may significantly improve the value of certain other physical quantities, while leading to only a small increase in R .

Using Eq. (11) we substitute back and find the following expressions for R , ha , and δ_0/δ_1 :

$$R = \frac{2^{4/3} \alpha^4}{(4\alpha^6 - 1)^{1/2}} g_3^{1/2} g_1 g_4^{5/6} g_2^{1/6} \left(\frac{b^8}{\delta_1 r_L^5} \right)^{1/3} \quad (12)$$

$$ha = \frac{1}{2^{1/3} \alpha g_4^{1/3}} g_2^{1/6} \left(\frac{r_L}{\delta_1 b} \right)^{2/3} \quad (13)$$

$$\delta_0/\delta_1 = \frac{(4\alpha^6 - 1)^{1/2}}{2^{1/3} \alpha} \frac{g_2^{1/3}}{g_3^{1/2} g_4^{1/3}} \left(\frac{r_L}{\delta_1 b} \right)^{2/3}. \quad (14)$$

From Eqs. (11) - (14) it follows that if δ_1 is made as large as possible then: (1) R is minimized (favorable for economics); (2) a/b is minimized (favorable for staged heating); (3) ha and δ_0/δ_1 are minimized (favorable for validity of theory). Here we assume $\delta_1 = 1$, which represents the largest value presently used in the Los Alamos experiments.

The implications of these relations are shown in the two examples, with $\alpha = 1$ and 0.85, of Table V-I. In both cases we set $\beta = 0.8$, $T_i = 6$ keV, $b = 10$ cm, $\delta_1 = 1$, and $B = 50$ kG. For a 50% - 50% mixture of deuterium and tritium, we calculate $r_L = 0.354$ cm.

TABLE V-I

PARAMETERS OF A LARGE SCYLLAC EXPERIMENT FOR TWO VALUES OF THE PARAMETER α WHICH MEASURES THE DEPARTURE FROM THE CONDITION OF MINIMUM MAJOR RADIUS R

	$\alpha = 1$	$\alpha = 0.85$
R	27.5 m	35.0 m
a/b	0.455	0.387
ha	0.084	0.099
δ_0/δ_1	0.331	0.160

For the optimum case $\alpha = 1$, the values of $R = 27.5$ m and $ha = 0.084$ are quite acceptable. The value of $\delta_0/\delta_1 = 0.331$ is somewhat larger than would be desirable, and the value $a/b = 0.455$ is uncomfortably large with respect to the requirements of a staged heating system. By going slightly off optimum to $\alpha = 0.85$ these problems are significantly alleviated. The major radius is increased to 35.0 m -- still a reasonable value. Both $ha = 0.099$ and $\delta_0/\delta_1 = 0.160$ are comfortably in the range where

the theory is valid and where we have had most of our experimental experience. The value $a/b = 0.387$ is a substantial improvement over the $\delta = 1$ case, although it still is probably slightly higher than would be desirable.

If we had simply taken the constraints of equilibrium, Eq. (2), and wall stabilization of the $\ell = 1$ driven instability, the first two terms of Eq. (4), we would have

$$R \geq g_1 g_2 a \frac{(b/a)^4}{\delta_1 \delta_0} . \quad (15)$$

The parameters of the $\alpha = 0.85$ case then give $R = 23.1$ m, a considerably smaller value than those required by the remaining constraints of stabilization of the $\ell = 0$ -driven instability and finite Larmor radius stabilization.

3. Physical Significance of Wall Stabilization

We give a simple physical picture of the wall stabilization term arising in the $m = 1$ Scyllac dispersion relation. It turns out that this term arises from the interaction of a helically twisted $\ell = 1$ dipole current with induced wall currents. To do the calculation we compute the force on a rigid, helically symmetric dipole current, resulting from moving the dipole a distance ξ_x in the x-direction. This corresponds to an $m = 1$ displacement. We show, perhaps somewhat surprisingly, that the force in the x-direction is independent of the angle between the dipole and the x-direction. The calculation goes as follows. After displacing the dipole by ξ_x , the geometry at a given arbitrary z-plane is shown in Figure V-I. Here b is the radius of the conducting wall. The dipole consists of two currents $I, -I$ separated by a distance d . At the given z , the dipole makes an angle hz with the x-axis. The image current for each of the dipole currents is of opposite sign and is located a distance y from the origin such that $xy = b^2$ where x is the distance from the dipole current to the origin. If we

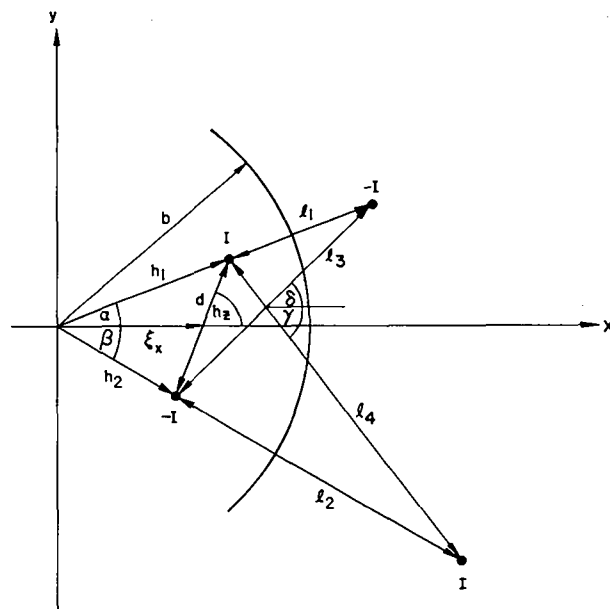


Figure V-I
Geometry at a given arbitrary z plane.

treat the dipole as rigid, then the force/length in the x-direction is given by

$$\frac{F_x}{L} = \frac{\mu_0 I^2}{2} \left[-\frac{\cos \alpha}{l_1} - \frac{\cos \beta}{l_2} + \frac{\cos \delta}{l_3} + \frac{\cos \gamma}{l_4} \right] .$$

The distances and angles can readily be calculated in terms of d, ξ_x , and b . For simplicity we expand in ξ_x and $1/b$ keeping terms up to $1/b^4$ and linear in ξ_x . We find

$$-\frac{\cos \alpha}{l_1} \approx \frac{1}{b^2} \left(\frac{d}{2} \cos hz + \xi_x \right) + \frac{h_1^2}{b^4} \left(\frac{d}{2} \cos hz + \xi_x \right)$$

$$\frac{\cos \beta}{l_2} \approx \frac{-1}{b^2} \left(\frac{d}{2} \cos hz - \xi_x \right) - \frac{h_2^2}{b^4} \left(\frac{d}{2} \cos hz - \xi_x \right)$$

$$\frac{\cos \delta}{l_3} \approx \frac{1}{b^2} \left(\frac{d}{2} \cos hz + \xi_x \right) - \frac{1}{b^4} \left[\frac{d^2}{2} \left(\frac{d}{2} \cos hz + \xi_x \right) - h_1^2 \left(\frac{d}{2} \cos hz - \xi_x \right) \right]$$

$$\frac{\cos \gamma}{l_4} \approx \frac{-1}{b^2} \left(\frac{d}{2} \cos hz - \xi_x \right) + \frac{1}{b^4} \left[\frac{d^2}{2} \left(\frac{d}{2} \cos hz - \xi_x \right) - h_2^2 \left(\frac{d}{2} \cos hz + \xi_x \right) \right]$$

where

$$h_1^2 = \frac{d^2}{4} + \xi_x^2 + d \xi_x \cos hz$$

$$h_2^2 = \frac{d^2}{4} + \xi_x^2 - d \xi_x \cos hz.$$

Combining terms we find

$$\frac{F_x}{L} = \frac{\mu_0 (Id)^2}{\pi b^4} \xi_x.$$

This can be cast in a more familiar form by writing the dipole moment Id in terms of the diamagnetic $l = 1$ field on the plasma surface, $B_d(a)$.

$$Id = \frac{2\pi a^2}{\mu_0} B_d(a).$$

Using standard Scyllac theory $B_d(a)$ can be expressed in terms of δ_1 , the helical distortion, B_0 , the vacuum θ -pinch field, β and ha .

$$B_d(a) = \frac{\beta}{2} ha \delta B_0.$$

If we introduce a frequency

$$\omega^2 = (F_x/L) / \pi \rho_0 a^2 \xi_x$$

we obtain finally

$$\omega^2 = h^2 v_a^2 \beta^2 \delta^2 \left(\frac{a}{b} \right)^4.$$

This is the usual $m = 1$ wall stabilizing term.

4. Diffuse $l = 1$ Scyllac Stability Calculation (B. M. Marder, J. P. Freidberg)

"Everest," a two-dimensional, diffuse, $l = 1$ stability calculation is progressing well and should soon be yielding quantitative information. Two fundamental difficulties seem to have not been overcome in this calculation. They are convergence of the equilibrium algorithm and achievement of very high accuracy in all phases of the calculation.

A previously developed method for examining the stability properties of screw pinches with arbitrary cross section has been applied in the Tokamak low- β regime to study the doublet configuration. Optimistic predictions on the enhancement of the critical β for stability produced by the doublet shape do not seem justified by our analysis. In its regime of operation (β poloidal = 1) only a modest increase in β of about 25% seems possible. Since the β is so low to begin with, this is not of real significance.

5. Optimization of Plasma Column Cross Section (B. M. Marder)

A method by which one could determine the stability properties of a screw pinch of arbitrary cross section has been developed and is described in Los Alamos Report LA-UR-73-1068 (see also Q-6 Quarterly Progress Report for April 1 - June 30, 1973). The material has been submitted

for publication. A problem which suggests itself is the inverse calculation -- to determine which cross section has the best stability behavior. This is a far more difficult problem than the original one in which a cross section is given and critical β 's are sought as a function of q . This problem has, however, been formulated as an exercise in the calculus of variations. As such it consists of nine nonlinear coupled integrodifferential equations for eight functions and an eigenvalue. It appears that a numerical algorithm might be found to enable one to determine optimum cross sections in a toroidal geometry. It was possible to prove one result analytically. From the calculations done at Los Alamos in the last year by Freidberg, Haas, and Marder, as well as others, it seems reasonable to guess that in a straight geometry no cross section has better stability properties than the circle, and, indeed, I have shown this to be the case. This result was not so obvious a year ago when elliptical cross sections were in vogue. Toroidal effects alter this picture, however, and noncircular cross sections are still under active study.

C. HIGHLIGHTS OF THE NUMERICAL SIMULATION AND COMPUTER APPLICATIONS PROGRAM

1. Two-Dimensional Implosion Simulations

(C. W. Nielson)

Over the course of the year a large-scale computer code was developed which includes in two dimensions all six field components and full electromagnetic interaction. Inhomogeneous boundary conditions are incorporated which allow gradient effects to be simulated for the first time in a two-dimensional code. It remains difficult to simulate physically realistic parameter values, so artificial values are chosen and varied in an attempt to discover the parametric dependence. Such a dependence would allow scaling the results to the physical regime.

The principal result of these studies has been to demonstrate the overwhelming importance of gradient instabilities in the initial formation of the sheath. At early times the wavelength of the instability and the size of the sheath are comparable. Analytic studies had previously noted such instabilities but had dismissed them as unimportant. These simulations have revived interest in them as the possible source of the very fast field diffusion during the first several nanoseconds of a theta-pinch implosion.

2. Microinstabilities in the Theta-Pinch Sheath (N. T. Gladd)

There remains uncertainty as to which instabilities are responsible for the anomalous resistivity leading to sheath broadening in a theta pinch; candidates include the modified two-stream instability, the ion acoustic instability, the electron cyclotron drift instability, the lower hybrid drift instability and, as recently suggested by Freidberg, an ion Larmor radius modified flute instability. A comprehensive analysis of the linear theory of these modes which includes the effects of finite β and temperature anisotropies in addition to the traditionally included parameters is being performed. The analysis is being carried out with both homogeneous and inhomogeneous equilibria.

A primary motivation for this analysis is its use in conjunction with two-dimensional inhomogeneous electromagnetic simulations of the implosion phase of the theta pinch. Results from analytic theories of this turbulence are essential also to the success of hybrid simulation codes which introduce the anomalous transport in an ad hoc way.

The complexity of the dispersion relation necessitates numerical analysis and a general code for analyzing complex functions has been developed. This code has facilities for root location, root counting, efficient following of roots through

parameter space, and automatic mapping of marginal stability curves and maximum growth curves. This code will be made interactive as soon as appropriate computational facilities are available, and this step should greatly facilitate the analysis of the dispersion relation.

3. Darwin Model Simulation Method (H. R. Lewis, C. W. Nielson, T. A. Oliphant)

The proper way to neglect radiative effects in Maxwell's equations was first deduced by C. G. Darwin in connection with atomic physics calculations. He expanded the full set of Maxwell-Lorentz equations in Lagrangian form in terms of v/c of the source particles, keeping terms up to $(v/c)^2$. The resultant set of equations gives an "action-at-a-distance" set of equations which contains Faraday's law of induction and part of the displacement current due to time-varying charge distributions but no retardation and no electromagnetic waves.

These equations, or subsets of them, have been used in innumerable plasma physics calculations where radiation is not important. Simulation codes based on them are also numerous, but have heretofore been successful only in restricted special cases, namely when only one-dimensional variations are allowed or when electrostatic effects are completely ignored. Attempts to implement the full set in two dimensions have until now been faced with violent numerical instabilities.

The source of the numerical instabilities is the "transverse" part of the electric field, the part which comes from the time derivative of the vector potential. It can be shown that any numerical method which actually takes that time derivative in the context of the Darwin model will be numerically unstable since it contradicts the instantaneous action-at-a-distance property of the model. We have derived an implicit equation for the transverse electric field which displays explicitly that this field depends only on the instantaneous

values of source positions and velocities. The elliptic partial differential equation which must be solved is of a new form and much of the work we have done has been in testing various means of solution for this equation. A combination of direct Poisson inversion and global iteration has been found to be a satisfactory method of solution and results are being obtained for theta-pinch implosion simulations which can be compared with previous simulations made with a fully electromagnetic code which includes radiation. The great advantage is that the Darwin or inductive model can be applied economically in the nonrelativistic regime when the fully electromagnetic code would be prohibitively costly because it must follow the uninteresting light wave propagation effects on a very fast time scale.

4. Numerical Vlasov Equilibria (N. T. Gladd, C. W. Nielson)

In an attempt to study the relatively slow microinstabilities that allow field penetration during the slow compression and confinement phases of a theta pinch, it is desirable to initialize an electromagnetic particle simulation code with a Vlasov-Maxwell equilibrium. Since analytic forms for such equilibria exist only in a very few nonphysical cases, a numerical technique to generate such an equilibrium at will is required. Mathematically, the problem is that of solving two coupled nonlinear differential equations for the vector and scalar potentials. Without the assumption of charge neutrality these equations are extremely sensitive to numerical integration and a number of standard techniques were inadequate. However, it has been found that the equations can be directly integrated by using an iterative scheme based on a Taylor expansion of the charge and current densities in conjunction with artificially contrived boundary conditions. The solutions examined to date are based on a particular form of the distribution function based on exponential

dependences of a particular sort. The resulting equilibria differ from the desired form because of large deviations from charge neutrality. Generalizations of the distribution function are being considered in order to generate profiles similar to those of collisionless shocks.

5. Hybrid Model Implosion Simulation (C. W. Nielson, T. A. Oliphant)

To make macroscopic simulation feasible on present computers, some method must be devised to avoid the very fast electron time scale, and to average the fast effects somehow into slow time scale parametric effects. On the other hand, the reflected ions known to be of great importance in a theta pinch cannot be described correctly at all if the ions are considered to be a fluid. The hybrid model being investigated treats the ions as particles and the electrons as a fluid with anomalous transport properties whose detailed character is determined either by theoretical analysis or by empirical fit.

As an initial step, the hybrid simulation code previously developed by Oliphant using classical resistivity has been modified to have a resistivity corresponding to a collision frequency of half the ion plasma frequency when the cross-field drift velocity exceeds the ion-acoustic velocity, and classical when it is less. This fairly crude algorithm was suggested by work of Chodura and collaborators at Garching where it is reported to describe their low-density shock-heating experiments with some accuracy. In the high-density regime, where we compare it to the results in Scylla 1-B, agreement is fair in that the magnetic field profile and excluded flux measurements agree to within about 50% with the hybrid simulation. It is expected as the code is refined, particularly with respect to thermal conductivity effects, and when the anomalous resistivity is made to follow in some detail the best analytic estimates corresponding to local conditions of

temperature and drift velocity, the agreement will be better.

6. Vlasov-Fluid Model for Linear Stability Analysis of High- β Plasmas (H. R. Lewis, B. L. Buzbee (C-3))

In the Vlasov-fluid model¹¹⁻¹⁴ the charged ions are treated as collisionless, the electrons are treated as a massless fluid, charge neutrality is assumed, and the displacement current in Maxwell's equations is neglected. Also, at present, the equilibrium ion distribution function is required to be a function only of the total energy. This model is being applied to study the linear stability of infinitely long, axially symmetric, inhomogeneous equilibria with arbitrary ion gyro radii. To date, two problems have been considered, both with a sharp-boundary equilibrium density profile: 1) theta pinch with a small azimuthal field, and 2) stabilized Z-pinch.

The formulation of the model is in terms of two functions, $s(\underline{r}, \underline{v}, t)$ and $\underline{\xi}(\underline{r}, t)$. The function $s(\underline{r}, \underline{v}, t)$ is related to the perturbed ion distribution function and particle orbits, and it is expanded in a series of eigenfunctions of the unperturbed Liouville operator. The function $\underline{\xi}(\underline{r}, t)$ is related to the perturbed vector potential and is analogous to the MHD plasma displacement; it is expanded in a series of eigenfunctions of the incompressible ideal MHD operator. For numerical studies, the expansions are truncated, in which case the number of eigenfrequencies equals the number of expansion functions. The eigenfrequencies are then usually determined by means of a global Newton's method which finds all of the eigenfrequencies simultaneously. Because the number of eigenfrequencies can be quite large (e.g., several hundred), means were sought for speeding up the computer code that carries out the global Newton's method. Whereas the number of iterations per root required previously increased approximately linearly with the number of

eigenfunctions of the unperturbed Liouville operator that were used, the required number of iterations per root is now nearly independent of the number of Liouville eigenfunctions. This has led to a large increase in speed, especially for the large problems in which the total number of eigenfrequencies is a few hundreds. For example, a problem that previously could not be completed in one hour on the 7600 now finishes in about two minutes. The source of the improvement lies in having experimentally understood the nature of the eigenfrequency spectra and having used that knowledge to greatly refine the initial estimates of the roots that are supplied for the Newton's method. A method related to Nyquist's theorem was tried for extracting information about maximum growth rates without having to find all of the eigenfrequencies. However, that method was found to be more costly than the refined global Newton's method.

Experience with the two problems that have been tried with this method, especially the stabilized Z-pinch, has demonstrated the desirability of obtaining further analytic understanding of the model. As a result, the limit of the model for small ion gyro radius is now being investigated in collaboration with R. A. Gerwin. It is expected that the method will be applied to problems with diffuse equilibrium density profiles during the coming year.

7. Stability of BGK Equilibria (H. R. Lewis)

An important feature of the Vlasov-fluid model is that it appears to be possible to treat the stability of inhomogeneous equilibria by severely truncating an expansion related to the inhomogeneity when the equilibrium distribution function is a function only of the total energy. In order to determine whether a similar formulation is possible and useful in other problems, the techniques used in the derivation of the Vlasov-fluid model were applied to one-dimensional electrostatic

equilibria, and an analogous set of equations were derived, again under the assumption that the equilibrium is a function only of the total energy. It appears likely that stability can also be studied in this case by severely truncating the expansion related to the inhomogeneity.

8. Nonlinear Evolution of Vlasov Plasmas (H. R. Lewis, D. C. Barnes (C-6 and Purdue University))

The nonlinear evolution and long-time behavior of a one-dimensional two-stream unstable plasma has been studied using a standard discrete-particle PIC code, as well as two continuum models. The objectives of the studies were a) to determine whether the asymptotic behavior admits of a useful description in terms of relatively few time-dependent parameters, and b) to find a simulation technique for the continuum Vlasov equations that is significantly more effective than the standard methods. It was found that the continuum models, in which the dependence of particle trajectories on initial conditions was approximated, exhibit serious violations of Liouville's theorem; that is, the mapping of the phase plane at the initial time to the phase plane at later times becomes significantly nonmeasure-preserving in the course of time. Study is under way of the feasibility of using the constraint of measure preservation to simplify the exact equations or to derive more effective approximation schemes.

9. Vlasov-Fluid Model and Stability of Hot Pinches (R. A. Gerwin)

The ion Vlasov-fluid model was studied relevant to its predictions for the stability of hot pinches. During the course of this work, it was necessary to verify that a new formulation of δW (the MHD potential energy of a pinch perturbation) due to J. Freidberg contained the well-known result of $l = 1$ Scyllac stability to the (predominantly) $m = 1$ mode in the limit $h/a \ll 1$ (a = plasma radius, h = helical wave number). This was indeed verified after a

great deal of algebra. It was further found that the MHD displacement corresponding to this instability (the eigenfunction of the minimization problem) was essentially a rigid sideways motion in the limit $h\alpha \ll 1$.

In addition, the numerical formulation of the Lewis-Freidberg Vlasov-fluid stability code was extended to include the effects of ion-ion collisions.

Finally, it was found that a previously neglected term in the Vlasov-fluid trial-function dispersion relation approach of Freidberg¹¹ (the ω^3 term) cannot generally be neglected, even for small ω . The implications of keeping this term in the trial function dispersion relation are now being examined.

10. Comparisons of Some Plasma Simulation Models (H. R. Lewis, C. W. Nielson, D. I. Brown (University of Pennsylvania), and S. J. Gitomer (University of Pennsylvania))

Plasma simulation models in one and two dimensions have been compared with regard to the electrostatic two-stream instability. The primary reason for making these comparisons was to determine the extent to which physical results depend on numerical method for a problem in which collective effects dominate. Previously,¹⁵ comparisons were made of four one-dimensional simulation models using a stable double-streaming situation as a test problem. In that case the comparisons were with regard to collisional effects, energy conservation, and momentum conservation; however, because a stable test problem was used, only tentative conclusions could be drawn as to the comparison among the models when they are applied to a problem in which collective effects dominate. We have applied the same four one-dimensional models to compute the evolution of a two-stream instability, and compared the time dependence of the electric energy as determined by each of the models.¹⁶ The models are characterized by the representation of the electric potential, and by how the electric

field is computed from the potential. The potential is represented either as the exact negative gradient of the potential or it is smoothed by interpolation with a spline function of the same order as the spline function used for the potential. The result of our comparisons is that the evolution of the electric energy of a two-stream unstable plasma does not depend strongly on the choice of model. There is a much stronger dependence on the random numbers that are chosen to represent the initial distribution function in phase space.

Three models were used for the two-dimensional comparisons.¹⁷ In each model the potential was represented as a bilinear spline function. In one model the difference approximation to the Laplacian in Poisson's equation was the nine-point operator prescribed by a variational principle,¹⁸ and the electric field was computed as the exact negative gradient of the potential. In another model the more usual five-point Laplacian was used, and the field was smoothed by interpolation with a bilinear spline function. In the third model the nine-point Laplacian was used with the smoothed field. The test problem was an unstable double-streaming plasma that was initially cold in one direction. As in the one-dimensional case, the two-dimensional evolution of the electric energy did not depend strongly on the choice of model, and there was a much stronger dependence on the random numbers that were chosen to represent the initial distribution function in phase space.

We conclude that the choice among these computer models for practical plasma physics computations should be made on the basis of considerations such as computational speed and storage requirements. Future development of significantly better computer models may emphasize approaches that do not rely exclusively on the use of discrete particles to represent the plasma.

11. Study of Plasma Turbulence Using Measurements on the Solar Wind (H. R. Lewis, W. C. Feldman (P-4))

Work is continuing toward the goal of obtaining a phenomenological description of plasma turbulence from satellite measurements of proton and electron velocity distributions in the solar wind. A preliminary study of the degree of symmetry of the electron velocity distribution has been made,¹⁹ and the mechanism of heat conduction in the solar wind is also under investigation.²⁰

12. Energy Loss of a Relativistic Electron Beam (R. A. Gerwin)

The energy loss of a relativistic electron beam in a slightly resistive, field-free, homogeneous plasma was numerically evaluated, with particular attention paid to the finite beam length (usually assumed infinite) and finite ratio of beam radius to c/ω_p (usually assumed infinite).

D. HIGHLIGHTS OF TOROIDAL Z-PINCH THEORY

1. Z-Pinch Stability Studies (D. A. Baker, L. W. Mann)

We have developed a model for a diffuse cylindrical Z-pinch having as few parameters as seems necessary to obtain good stability properties. The model incorporates hollow pressure profiles and reversed axial field, thus giving stability against diffusion, and eliminates equilibrium wall currents. The model is described in terms of parameters for B_θ and pressure, with B_z being deduced by pressure balance. The pressure is described by the peak value, its value on axis, the radius of the peak pressure, and the radius beyond which $p = 0$. The B_θ field is specified by its maximum value, the radius of the maximum value, and the radius where $d(rB_\theta)/dr = 0$. The radii can be scaled by the wall radius, and the fields and pressures by $B_{\theta \max}$. This still leaves six independent variables to investigate. In particular we have been investigating how these parameters can be exploited to maximize the stable β_θ .

The gross $m = 0$ and $m = 1$ modes are checked for stability by testing the δW integral numerically. The localized Suydam criterion is calculated separately. Profiles have been obtained which are stable for $m \geq 0$ for $\beta_\theta \sim 58\%$. A sequence of plots showing what happens to the minimum wall position for stability as the pressure is scaled up, keeping the same profile shape and B_θ distribution, is shown in Figure V-2. The wall position for stability against gross modes is shown by the arrow. Robinson²¹ quotes a limit of 50% for $m = 0$ but his derivation assumes $p \sim 0$ at the point of B_z reversal. An upper limit using his trial function without that assumption is

$$\beta_\theta \leq 0.5 + \beta_0$$

where $\beta_0 = \frac{2\mu p}{B^2}$ is the local β at the radius where B_z vanishes. For the problems currently being studied, the field reversal is well inside the plasma edge resulting in β_0 's of ~ 0.25 . Equilibria which have B_z reversal well inside the plasma are advantageous if stable operation at high β_θ values is desired.

It has been found that the position of the wall for stability is insensitive to the depth of the pressure depression on axis. Hollow pressure profiles therefore give somewhat smaller critical average β_θ since they have smaller average pressure. Profiles which are initially hollow should remain stable longer as field diffusion proceeds.

The high β_θ configurations are being used to formulate problems to be tested for stability in full toroidal geometry. The stable toroidal configurations reported earlier had a rather low β_θ ($\approx 10\%$).

2. Pressure Balance and Diffusion Heating (D. A. Baker, J. A. Phillips (Q-2))

The experiments in the LASL toroidal Z-pinch (ZT-1) show that the poloidal field diffuses rapidly and that most of the

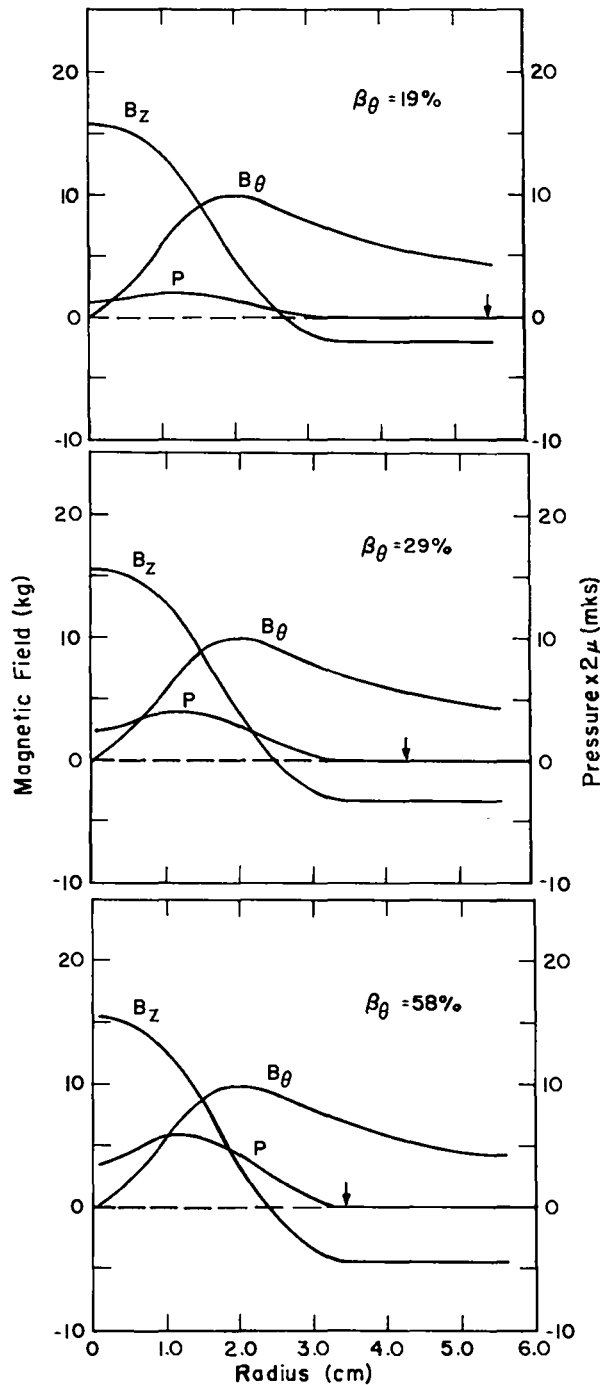


Figure V-2
Equilibrium pressure and field profile showing the effect of increasing pressure on the location of a conducting wall for stability.

profiles now being considered therefore have longitudinal currents nearly uniform inside the pinched plasma column. In many experiments the plasma β_0 's are high. The production of stable configurations would be greatly simplified by operating at lower values, which by MHD theory would have a greater margin of stability. Attempts, however, to lower the plasma energy density have not been completely successful.

These considerations suggest that there are limitations on β_0 due to the processes involved in setting up the plasma and field profiles. In particular, the plasma is ohmically heated during the diffusion of the poloidal field.

Applying energy balance (making use of Poynting's theorem) and pressure balance to a cylindrically symmetric configuration of plasma and fields $\vec{E}(r,t)$, $\vec{B}(r,t)$ one can deduce the following necessary relationship* for a plasma final state with radius r_p having a scalar pressure p and a uniform longitudinal current density.

$$\begin{aligned}
 W_p(0) + 2[2(f-1)\xi+1] W_0 \ln K + 2(f-1)\xi W_0 \\
 - W_{\Theta p} + W_{z \text{ in}} + \frac{3}{2} (W_z - W_R) - [W_z - W_f(0)] \\
 - W_L = 0 .
 \end{aligned} \tag{1}$$

The quantities $W_p(0)$ and $W_f(0)$ are the initial plasma and field energies present at the time of onset of the longitudinal current I .

The remaining quantities are to be evaluated at a time T when equilibrium is reached and are defined as follows:

$$W_0 = \mu I^2 / 8\pi \quad (\text{MKSA units})$$

$$K = R/r_p = \text{compression ratio}$$

*A paper with the derivation of this equation is scheduled to appear in Phys. Rev. Letters, Feb. 1974.

ξ is a mean-value theorem parameter $0 < \xi < 1$ for a rising current and is given by $\int_0^T E_z(0,t) I(t) dt / [I(T) \int_0^T E_z(0,t) dt]$.

$$W_{\theta p} = \int_0^T \phi_{\theta} \dot{I} dt$$

$$W_{zin} = \mu^{-1} \int_0^T \phi_z \dot{B}_z(R,t) dt$$

where ϕ_{θ} and ϕ_z are the B_{θ} and B_z fluxes inside the wall radius R .

f = flux annihilation factor

$$= \int_0^T E_z(R,t) dt / \phi_{\theta}(T)$$

W_z = longitudinal field energy

$$W_R = \pi R^2 [p(R) + B_z(R)/2\mu]$$

W_L = energy lost between $t = 0$ and $t = T$

We apply Eq. (1) to a stabilized Z-pinch energized with a step function $I(t)$ which reaches an equilibrium state with compressed B_z and the diffuse B_{θ} field discussed above. At the time of onset of the longitudinal current ($t = 0$) we assume that the only field present is an initial uniform B_z supplied by a crowbarred conductor so that $\phi_z = 0$ for $t > 0$. Under these conditions $W_f(0) = W_z(0)$ and W_{zin} is zero. For a step function $I(t)$ the term $W_{\theta p}$ is zero. Since $W_p(0)$, $\ln K$, ξ , and $f-1$ are all positive, the first three terms in Eq. (1) cannot be negative. For the compressed field case, if $p(R)$ is negligible, we have $W_z \geq W_z(0) \geq W_R$ so that the grouping of terms $\frac{3}{2} (W_z - W_R)$ is positive and dominates the negative grouping $- [W_z - W_z(0)]$. Thus the loss term must be nonzero in order to satisfy Eq. (1). The condition is only marginally met with no losses for the nontypical special case:

(1) there is no initial plasma energy at the time of current onset [$W_p(0) = 0$], (2) the B_{θ} flux is conserved ($f = 1$), and (3) there is no plasma or B_z field compression [$K=1$, $W_z = W_z(0) = W_R$].

Thus if a cylindrically symmetric stabilized pinch is driven with a current which rises to its final value very rapidly compared to the compression and flux diffusion times it cannot achieve static equilibrium after the B_{θ} field diffuses to a uniform current distribution unless losses or plasma pressure at the wall is present. It follows from continuity that this conclusion will be true also if a small amount of reversed longitudinal field outside the compressed plasma column is added for stability. It may be possible, however, to achieve magnetic containment without the loss requirement by increasing W_R using substantial amounts of reversed longitudinal field outside the pinch applied before the poloidal field diffusion is complete. If this is done by external field programming, any additional energy input (W_{zin}) must be included and, if positive, the latter acts in the opposite fashion to W_R so that care must be taken not to defeat the purpose. This reduction of the loss required to achieve magnetic containment amounts to arranging the configuration so that the longitudinal field supports a portion of the excess pressure arising from poloidal field diffusion in addition to its usual role of supplying stability. To achieve confinement the whole operation must be done in a fashion that a stable configuration results.

For a slow current rise one expects less heating for the final diffused state since the $W_{p\theta}$ term in Eq. (1) will give a negative contribution rather than zero as for the step function case. A measure of the closeness of a given finite current rise to the step function is given by the smallness of the ratio $D = W_{\theta p}(T) / [\phi_{\theta}(T) I(T)]$.

We inquire as to whether the ratio D for Z-pinches is high enough that

equilibrium can be obtained with negligible losses and plasma pressure at the wall. We solve Eq. (1) for D , and since $W_p(0)$ is positive it can be omitted, giving a lower limit on D for the diffuse B_θ profile. We obtain the following necessary condition for energy and pressure balance without losses:

$$D \geq \frac{\frac{1}{2} [2(f-1)\xi+1] \ln k + \frac{1}{2}(f-1)\xi + \frac{1}{8}(1-\beta_\theta) + (W_{zin} + W_z(0) - W_R)/4W_0}{\ln K + \frac{1}{2}}, \quad (2)$$

where

$$\beta_\theta = \int_0^R p \, 2\pi r \, dr / W_0.$$

For common current waveforms ξ is greater than $1/2$ since $E_z(0,t)$ is low at the beginning of the current rise and becomes larger with time as the field diffusion progresses, thus weighting the larger current values. (For the risetime of a sinusoidal current and $E_z(0,t) \propto t^n$, ξ ranges from $2/\pi$ for $n = 0$ to unity for $n \rightarrow \infty$.) For stabilized Z-pinch operation with compression ratios of about two, with small amounts of external reversed field and $p(R) = 0$, the above condition is typically $D \gtrsim 0.5$. If this condition on D is not satisfied in fast compression experiments, radiation and ionization losses are likely to be insufficient and equilibrium can be obtained only after wall contact. The conditions required to establish stable equilibria are difficult to predict since the experimental flux penetration rates are anomalous.

It is of interest to apply condition (2) to a Tokamak. Approximating this case with $K = 1$, $\beta_\theta = 1$, $W_{zin} = 0$, and $W_z(0) = W_R$ we obtain $D \geq \xi(f-1)$. An upper limit on D for the incompressible case can be obtained assuming that the B_θ field diffuses instantaneously to a uniform current distribution during the current rise. The

direct evaluation of $W_{\theta p}$ then gives $W_{\theta p} = W_0$ and $I = 2W_0$, so that the upper limit on D for the incompressible case is $1/2$. Since $\xi > 1/2$ the condition on D will be violated if $f > 2$. Since (1) Tokamaks typically operate with f factors larger than two for the initial setup phase, (2) the flux does not penetrate instantaneously,

and (3) ξ will most likely be considerably greater than $1/2$, the above argument predicts that an energy loss is also needed for a Tokamak to achieve a final state of uniform current for confinement by the poloidal field, i.e., $\beta_\theta = 1$. This suggests that the poorly understood early phase of the Tokamak discharge before it falls into a steady regime is related to the excess heating caused by the poloidal field diffusion. The discharge can lose any such excess energy (above that needed for ionization) by instability, recycling, or other means before it settles down to its equilibrium phase.

The sometimes suggested method of reducing β_θ by reducing the plasma density is far from being a simple conclusion. The plasma density nowhere enters explicitly in the above considerations. Its effect appears indirectly in determining the flux penetration rates which determine the energy input integrals. The density can become important however, by affecting the compression rate and also diffusion rate if it is anomalous.

The arguments given are based on the general assumptions of energy and pressure balance, cylindrical symmetry, and plasma thermalization. The results apply (toroidal corrections aside) to a wide class of containment devices.

3. Belt Pinch Equilibria (D. A. Baker, L. W. Mann)

The motivation behind the belt pinch was twofold: (1) to produce a hot plasma by compression heating, and (2) to achieve stability at high beta as a result of the increased q value associated with the non-circular elongated plasma cross section. The latter motivation was based upon the speculation that large q (i.e., operation well below the Kruskal-Shafranov limit) implies MHD stability.

Our previous work (LA-5250-PR) showed that for a given rectangular boundary shape two types of equilibria were found from the numerical solution of the MHD equilibrium equation -- the desired solutions with highly elongated cross section and those which are short and contracted. The pressure profiles used in these calculations were flat-topped. Numerical convergence to a solution whose plasma cross-section length was about half the corresponding boundary length of the device (as observed experimentally in the early experiments at Garching) was not obtained. More recent calculations with more peaked pressure profiles have demonstrated the existence of a continuum of solutions ranging from the short nearly circular cross section to the elongated ones. Three equilibria having different eccentricity are shown in Figures V-3, V-4, and V-5. The three solutions are obtained by solving the MHD equilibrium equation for varying values of the parameter which controls the width of the plasma pressure profile. A striking result of these calculations which is apparent by comparing Figures V-3 and V-4 is that a very small reduction in the width (relative to the boundary) of the plasma profile as measured at the midplane is accompanied by a large reduction in the length (largest dimension) of the plasma profile. This effect is also shown in Figure V-6, where the length of the plasma pressure profile is plotted vs its corresponding width. Both dimensions are measured from the calculated

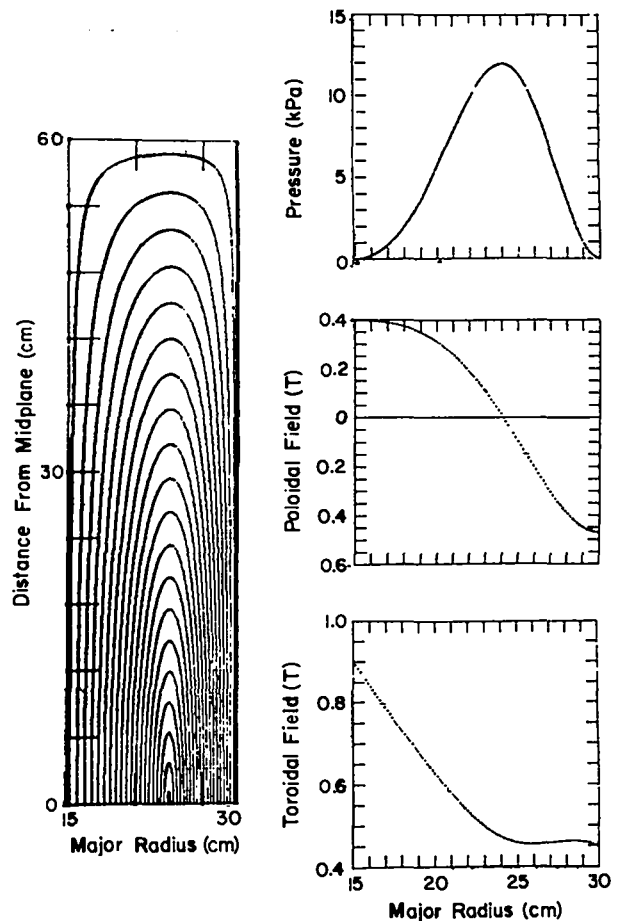


Figure V-3
Poloidal flux lines, plasma pressure, and field profiles at the midplane for a long solution for a ratio of plasma width to boundary width equal to 1.

position of the plasma edges where the pressure is zero. The curves are given for two values of the ratio of the dimensions (length/width) of the rectangular cross-section conducting boundaries. These curves show that small amounts of compression in the radial direction drastically reduce the elongation of the plasma, which in turn reduces the "safety factor"

$$q = \frac{1}{2\pi} \oint \frac{B_{TOR}}{rB_{POL}} dl.$$

The variation of the q factor on the various flux surfaces (for the solution given in Figure V-6) is shown in Figure V-7. Flux surfaces are measured on the abscissa by their minimum distance to the innermost

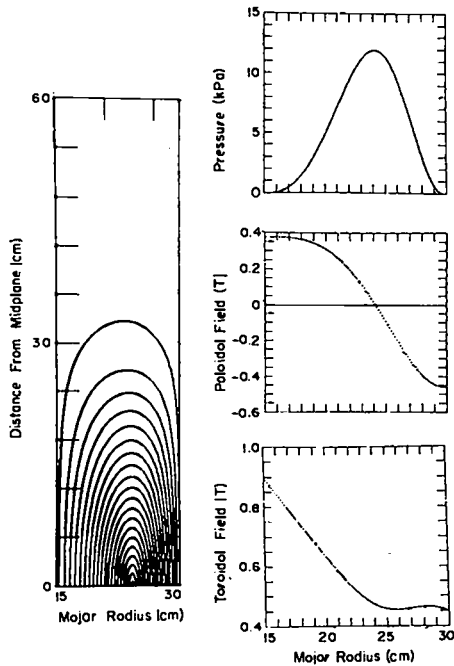


Figure V-4
Intermediate solution -- ratio of plasma width to boundary width equals 0.935.

boundary normalized to the total boundary width. The q value reaches a minimum on the innermost flux surfaces. This minimum q value has been calculated and plotted vs the plasma length in Figure V-8. All of these results are given for a toroidal aspect ratio (mean major radius/boundary width) of 1.5 and a toroidal β value of 0.3. Other aspect ratios show qualitatively similar results. Analogous calculations have been made with the open geometry with a separatrix as in the Garching experiments (see LA-5250-PR). All calculations, whether with open or closed conducting boundaries, have shown that equilibria representing large radial compressions are incompatible with the desired highly elongated, high q solutions. The equilibria can have high toroidal β ($\sim 85\%$) with q everywhere greater than unity. The latter condition is not sufficient for stability and the stability properties are presently under study.

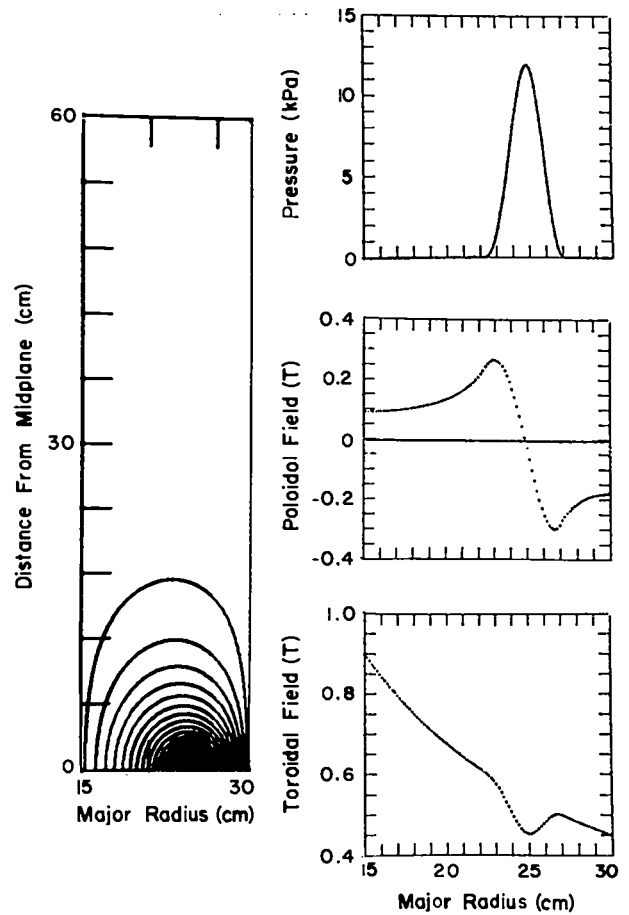


Figure V-5
Short solution -- ratio of boundary width to plasma width equals 0.313.

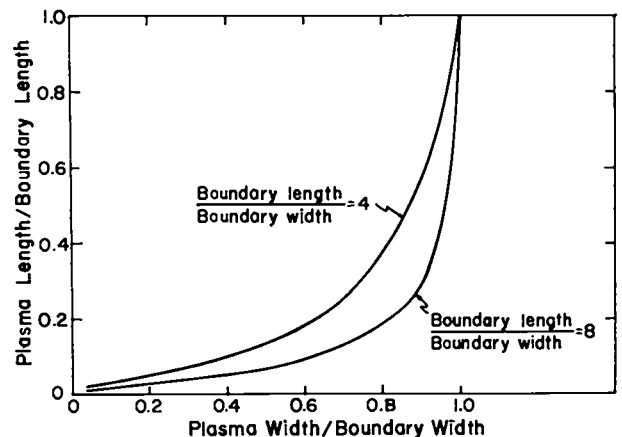


Figure V-6
Effect of width of plasma distribution on plasma height for boundary height to width ratios of 4 and 8.

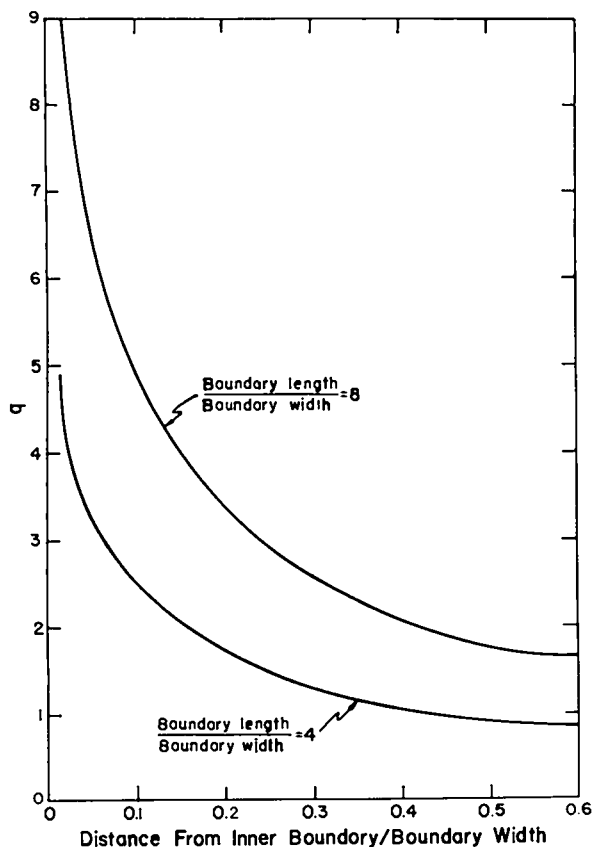


Figure V-7
Variation in q as one moves from the inner wall toward the magnetic axis (left to right) (plasma distribution width/boundary width = 1, beta toroidal = 0.3).

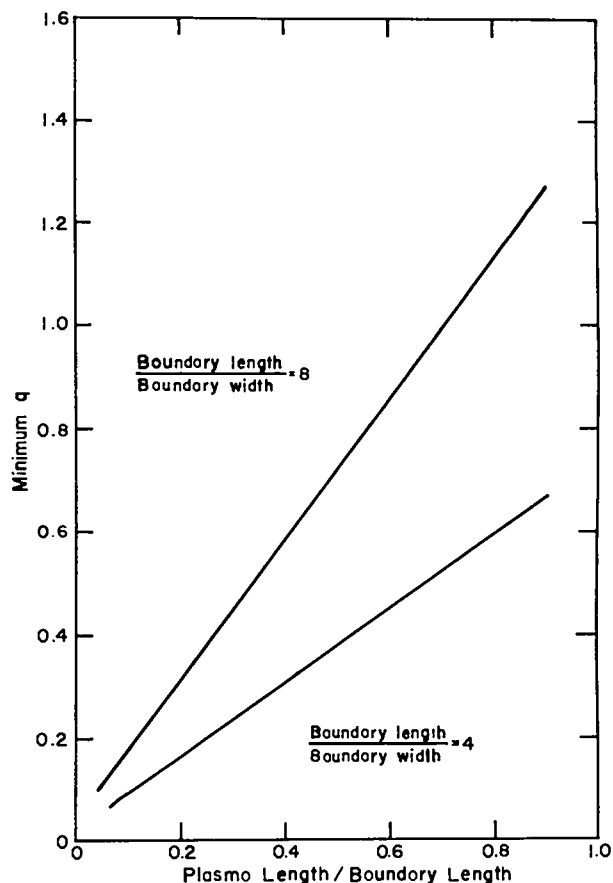


Figure V-8
Relation of q to height of the plasma.

REFERENCES

1. S.C. Burnett et al., Plasma Physics and Controlled Nuclear Fusion Research 1971 (IAEA, Vienna, 1971), Vol. III, p. 201.
2. W. E. Quinn et al., Proc. Sixth European Conference on Plasma Physics and Controlled Nuclear Fusion Research, Moscow, July 30 - August 3, 1973. Also Los Alamos Scientific Laboratory Report LA-UR-73-1053 (unpublished).
3. F. L. Ribe and M. N. Rosenbluth, Phys. Fluids **13**, 2572 (1970).
4. H. Grad and H. Weitzner, Phys. Fluids **12**, 1725 (1969).
5. M. N. Rosenbluth, J. L. Johnson, J. W. Greene, and K. E. Weimer, Phys. Fluids **12**, 726 (1969).
6. J. P. Freidberg, Phys. Fluids **14**, 2454 (1971).
7. H. Weitzner, Plasma Physics and Controlled Nuclear Fusion Research 1971 (IAEA, Vienna, 1971), Vol. III, p. 223.
8. J. P. Freidberg, R. L. Morse, and F. L. Ribe, Proc. Texas Symposium on Technology of Controlled Thermonuclear Fusion Experiments and the Engineering Aspects of Fusion Reactors, 1972. Session V, Paper No. 11.
9. K. S. Thomas et al., Phys. Fluids **15**, 1658 (1972).
10. C. R. Harder et al., Bull. Am. Phys. Soc. (to be published).
11. J. P. Freidberg, Phys. Fluids **15**, 1102 (1972).
12. H. R. Lewis and J. P. Freidberg, Bull. Am. Phys. Soc. **17**, 846 (1972).

13. H. R. Lewis and J. P. Freidberg, paper 41 in Proceedings of the Fifth European Conference on Controlled Fusion and Plasma Physics (Grenoble, France, August 21-25, 1972).
14. Progress Report, LASL Controlled Thermonuclear Research Program for a 12-month period ending December 1972, Los Alamos Scientific Laboratory Report LA-5250-PR (June 1973), p. 98.
15. H. Ralph Lewis, A. Sykes, and J. A. Wesson, J. Computational Physics 10, 85 (1972).
16. D. I. Brown, S. J. Gitomer, and H. R. Lewis, to be published in J. Computational Physics.
17. H. R. Lewis and C. W. Nielson, submitted for publication in J. Computational Physics.
18. H. Ralph Lewis, "Methods in Computational Physics," Vol. 9, pp 328-331, Academic Press, New York, 1970.
19. W. C. Feldman, J. R. Asbridge, S. J. Bame, and H. R. Lewis, Trans. Amer. Geophys. Union 54, 1191 (1973).
20. W. C. Feldman, J. R. Asbridge, S. J. Bame, and H. R. Lewis, to be published.
21. D. C. Robison, Plasma Physics 13, 439 (1971).



VI. EXPERIMENTAL PLASMA PHYSICS RESEARCH PROGRAM

A. SUMMARY (H. Dreicer)

During the past year the LASL Plasma Physics Research (PPR) program continued to be devoted to the study of the plasma AC electrical resistivity and plasma heating produced by the application of high-frequency electromagnetic radiation to fully ionized plasmas. This research centers on the dependence of the classical and anomalous resistivity on the value of the applied electric field.¹ The work includes measurement of the electron velocity distribution as modified by high-frequency heating, and, where feasible, determines the spectrum and intensity of plasma waves excited by the heating process. The resistivity is measured in two different regimes, a classical stable and an anomalous turbulent regime. The transition between these two regimes depends upon the value of the electric field and has been found to be the threshold for AC parametric instabilities² (Section B1). In the classical regime, measurements made for $0.1 \lesssim (\omega_p/\omega)^2 \lesssim 1$ yield the weak electric field (Ohm's Law) resistivity (Section C). At the lower plasma densities ($\omega_p^2/\omega^2 < 0.7$) where it is possible to apply significantly larger fields without exceeding this threshold, a significant deviation from this Ohm's law limit has been observed in the classical regime (Section D). This deviation, believed to be the classical limit of those electric field nonlinearities frequently described in quantum language by the title multi-photon inverse bremsstrahlung absorption, may have important application to the laser heating of θ -pinches. Our observation in this interesting multiphoton regime was made possible by the considerable effort

the group expended in the past to carefully identify the threshold electric field dependence upon plasma density and to accurately measure the classical weak field resistivity.

Above threshold, in the anomalous or turbulent regime, observations yield a larger resistivity than can be explained by two-body Coulomb encounters (Section B3). The evidence indicates that this anomalous resistivity arises from the interaction of the current carrying particles with plasma waves excited by AC parametric instability to saturated nonlinear levels (Section B4). Simultaneous measurements of the electron energy distribution, analyzed during the past year,² indicate that under certain conditions the energy is mainly absorbed by a small number of energetic electrons, while under other conditions a more uniform heating of all electrons occurs (Section B4). The study and understanding of the collective heating mechanisms at work in this regime will continue to be a major task for the PPR group.

Because absorption and heating measurements are intimately connected with heat flow, the group has also devoted some effort to measuring the thermal conductivity $K_{||}$ and to computing the influence of heat flow upon the phenomena we observe. A provisional measurement of $K_{||}$, made in the classical regime, is in reasonable agreement with results predicted by kinetic theory. This measurement will be refined in the future and if possible will be extended into the anomalous or turbulent plasma regime where little understanding about heat flow exists.

The primary motivation of the PPR group's research program is the fact that the electrical resistivity is not yet a well-understood transport parameter although most present devices considered for heating DT plasmas to fusion temperatures and achieving a plasma equilibrium rely strongly upon mechanisms that involve the resistivity. These devices depend, for example, upon ohmic heating (Tokamaks, Stellarators, laser heated θ -pinches), upon the degree of anomalous skin effect (Tokamaks and Z-pinches), upon the maintenance of sharp magnetic piston-plasma interfaces for implosion heating (theta pinches), and upon very efficient energy dissipation by turbulent heating (laser and relativistic beam fusion devices). More specifically, in each of these phenomena there appear to be some conditions under which parametric decay of excited plasma waves, as studied by us, becomes an important nonlinear saturation mechanism for the plasma waves and fluctuations which provide anomalous resistivity. Even the study of collisional processes may provide important information about plasma behavior in CTR devices. For example, our observation that multiphoton processes affect collision rates and resistivity can be extrapolated to the effect that plasma oscillation fields may have upon the electron-ion energy relaxation rate.

It appears reasonably prudent to conjecture that a detailed understanding of resistivity and heat flow will strongly influence the efficient utilization of energy injected into all CTR devices currently under consideration.

Much of our research has also served as a means of testing the validity of the increasingly sophisticated predictions produced by the CTR program's computational activity. Such scientific exchange has occurred between members of the PPR group and personnel at university and CTR laboratories.

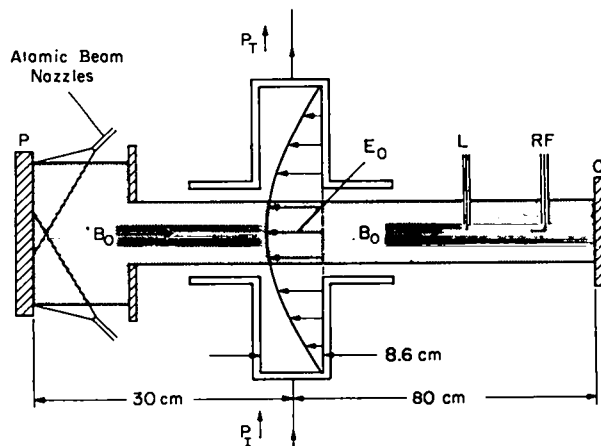


Figure VI-1
Experimental Setup.

Mr. F. Wittman has been responsible for the engineering work associated with our experiments. He and Messrs. N. Gardner and A. Mondragon have provided expert technical assistance in all phases of the group's experimental activities.

B. ABSORPTION OF ELECTROMAGNETIC WAVES NEAR THE ELECTRON PLASMA FREQUENCY (H. Dreicer, R. F. Ellis, J. C. Ingraham)

By using a fully ionized Q-machine plasma column, a high-quality 2-GHz microwave resonator, and a set of plasma probes (Figure VI-1), we have studied the electrical resistivity near the electron plasma frequency, ω_p , and also the effect of microwave absorption upon the electron energy distribution $F(E)$. Scientific progress has occurred in the following areas:

1. Parametric Instability Threshold

During the past year we have measured the threshold for anomalous microwave absorption over a wider range in density (i.e., ω_p^2/ω^2) than reported earlier. We have also shown that the results are essentially independent of confining magnetic field (i.e., ω_c/ω_p). Figure VI-2 shows our experimental observations of the threshold in (v_E/v_T) for a wide range of confining magnetic fields B_0 (or ω_c/ω_p) and density. Here

$$\frac{v_E}{v_T} = \frac{eE_0 / (\pi\omega)}{(2kT_e/m)^{1/2}}$$

E_0 = microwave electric field amplitude

T_e = electron temperature.

At threshold, $E_0 = E_{0c}$ and $v_E/v_T = (v_E/v_T)_c$.

The solid line curves on Figure VI-2 show the theoretical threshold for the parametric decay and oscillating two stream instabilities computed for an infinite uniform plasma with $B_0 = 0$ and $T_e = T_i$. The poor agreement with theory in the over-dense regime, $(\omega_p/\omega)^2 > 1$, occurs because this theory ignores the possibility of parametric excitation of plasma waves propagating obliquely to B_0 , and also ignores finite plasma column effects. Such oblique waves, propagating in an infinite plasma, obey the dispersion relation

$$\omega \cong \omega_p \cos \theta (1 + \frac{3}{2} k^2 \lambda_D^2),$$

provided B_0 is infinite. θ is the angle between B_0 and the wave vector k of the plasma wave. It is important to note that the dispersion relation for electron plasma waves propagating on a similarly magnetized uniform plasma of finite radius (Trivelpiece-Gould modes) is exactly the

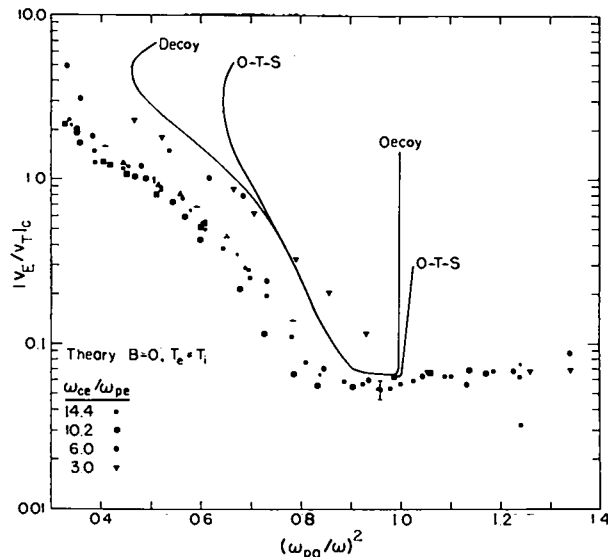


Figure VI-2
Electric field threshold vs density.

same provided that the plasma is bounded by a good conductor. Thus we expected the inclusion of oblique waves in the infinite plasma theory to go a long way toward explaining the finite plasma results. This was a reasonable expectation especially since the infinite plasma threshold theory for oblique waves predicts perpendicular wave numbers that are consistent with our radial boundary conditions. Computations made during the past year have borne out this expectation. We modified the Freidberg-Marder³ theory to include the effect of infinite magnetic field on the electron motions, retained zero magnetic field for the ion motions, and ignored the effect of magnetic field upon the electron-ion collision rate (see Section C). This limit approximates well the ω_c/ω_p ratios for electrons and ions in our experiment. The results, indicated in Figure VI-3, show that the threshold curves for various obliquely propagating waves are very similar to each other, but are shifted along the $(\omega_p/\omega)^2$ axis by the factor $1/\cos^2\theta$. The measured threshold field at any value of $(\omega_{p0}/\omega)^2$ is then associated with that angle of propagation which has the smallest threshold field. For $(\omega_{p0}/\omega)^2 \leq 0.99$ this

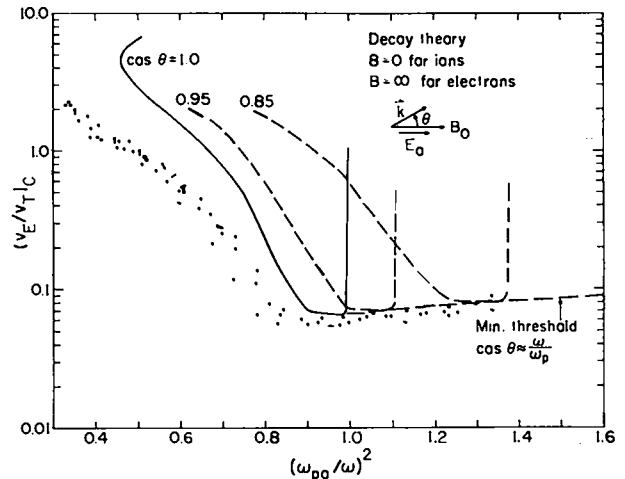


Figure VI-3
Electric field threshold vs density.

minimum threshold is associated with waves propagating parallel to B_0 (i.e., $\theta = 0$) and this case agrees with the $B_0 = 0$ theory shown in Figure VI-2. The modified theory predicts that for $(\omega_{p0}/\omega)^2 \geq 0.99$ the observed threshold field should remain essentially constant at its minimum value (as it does), because the minimum threshold for parametric excitation of oblique waves propagating with increasingly larger propagating angles is being observed. In this range the theory predicts the relationship

$$\cos \theta \approx \frac{\omega}{\omega_p}$$

between ω_p/ω and the propagation angle θ of the wave responsible for minimum threshold. The observed thresholds shown in Figures VI-2 and VI-3 have not been adjusted by any arbitrary parameters to improve the agreement with the theory. In the theoretical treatment the unperturbed electron and ion velocity distribution are assumed to be oscillating Maxwellian distributions at the hot plate temperature of our Q-machine, i.e., $T = 2250^\circ\text{K}$. Figure VI-4 shows the sensitivity of the threshold to the choice of electron temperature. Apparently the main effect occurs for $0.9 \leq (\omega_{p0}/\omega)^2 \leq 1.0$, where the threshold electric field has a minimum and is determined by collisional damping rather than by Landau damping. Our measurement of the collisional damping below threshold in the weak electric field limit (See Section C) is in good agreement with the value implied by the measured minimum in the threshold. At the lower densities, $(\omega_{p0}/\omega)^2 \ll 0.9$, Landau damping is responsible for the sharp increase in threshold field. For the three electron temperatures investigated theoretically the Landau damping of the ion waves remains especially strong. The observation of a somewhat lower threshold in the Landau damped region than theory predicts for an oscillating Maxwellian suggests that the actual distribution may be non-Maxwellian,

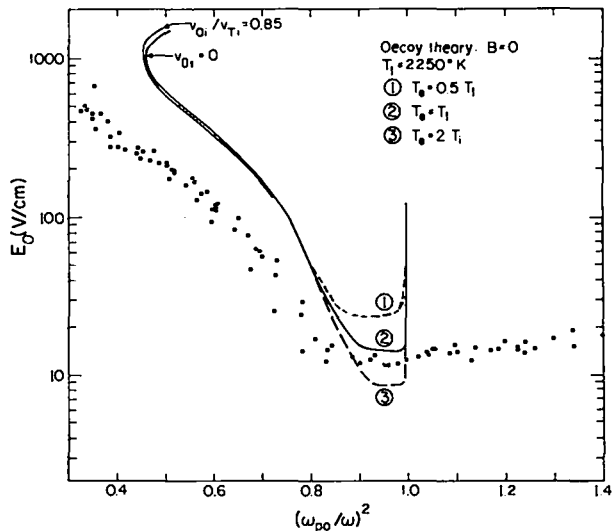


Figure VI-4
Electric field threshold vs density.

perhaps slightly distorted by the absorption which accompanies the threshold measurement. The generally good agreement between these observations and the theoretical predictions is one of the really important accomplishments in this field.

2. Indirect Observation of Landau Damping

According to the theory of AC parametric instabilities the sharp break in the threshold field versus density curve at $(\omega_{p0}/\omega)^2 \approx 0.9$ corresponds to the transition between Landau and collisional damping. For smaller densities (i.e., $(\omega_{p0}/\omega)^2 < 0.9$) the sharp rise in the theoretical threshold field reflects the sharp increase in Landau damping as the wavelength of the excited plasma oscillations decreases with decreasing $(\omega_{p0}/\omega)^2$. The observation of this sharp rise in threshold has interesting implications apart from the measurement of threshold. Our plasma column is characterized by a Debye length, λ_D , of 2×10^{-3} cm, a plasma radius, R , of 1 cm, and according to theory the wavelength of the most unstable parametric waves is about 0.05 cm. Thus agreement between threshold theory and measurement amounts to an indirect experimental verification

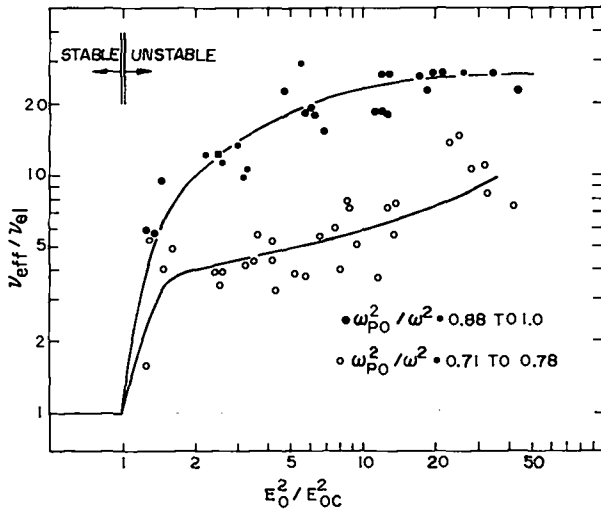


Figure VI-5
Effective collision frequency vs ratio of pump power to pump power at threshold.

of Landau damping under conditions for which $\lambda_D/R = 2 \times 10^{-3}$. This ratio is much smaller than the value of 10^{-1} achieved in the classical Malmberg, Wharton, and Drummond⁴ experiment, and our experiment therefore comes closer to satisfying the infinite plasma conditions of the Landau damping theory. The impact of our threshold results on the physics of Landau damping would become more important if the wavelength of the unstable waves could be measured near threshold.

3. Anomalous Electrical Resistivity

A pulse technique has been used for measuring microwave absorption (Figure VI-5) above the threshold. The data indicate dependences upon density and pump power which must be studied in greater detail before a proper understanding can be developed. The magnitude of ν_{eff} is complicated by the need to know the detailed radial distribution of anomalous absorption while the microwave technique only yields the total absorption over the plasma. In the analysis leading to Figure VI-5 we have used our measurement of the radial distribution of very hot electrons for this purpose (see Figure VI-6). This ignores

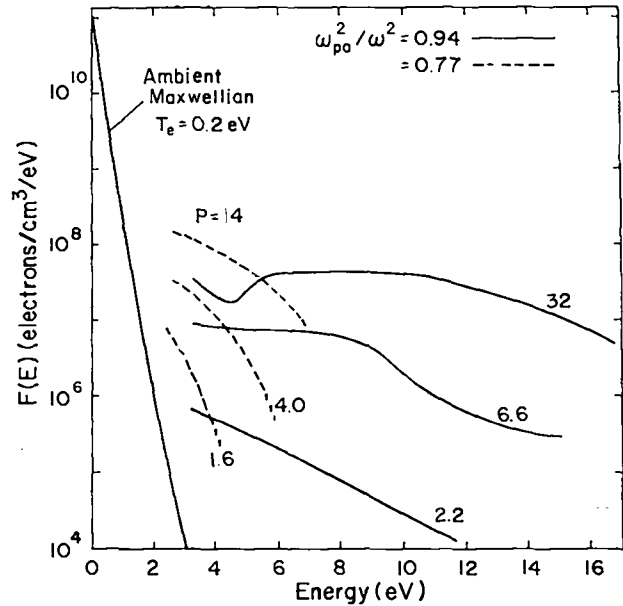


Figure VI-6
Electron energy distributions.

the radial distribution of anomalous heating in the body of the electron energy distribution because too little is known about this. Figure VI-5 also ignores changes in ν_{ei} and in E_{0c} , the threshold electric field, as a result of the heating which accompanies the absorption measurement. These corrections are not expected to alter the magnitude of ν_{eff} significantly, and their detailed study is not expected to become worthwhile until the anomalous absorption mechanism itself becomes more amenable to experimental observation.

4. Anomously Heated Electron Energy Distribution

Retarding potential probe measurements of $F(E)$ have yielded the first quantitative data (Figure VI-6) which show that long tails of hot electrons are produced when the parametric instabilities are driven into their nonlinear regimes. The result indicates that the number and distribution of hot electrons is a very sensitive function of ω_p^2/ω^2 and pump power, and may involve the production of a second bump on the tail. Some heating of the main body of the electron distribution has also been

observed. The sensitive dependence of hot electron properties upon plasma density may be summarized as follows: Two regions of plasma density are found, corresponding to strikingly different properties of the hot electrons: $0.70 \leq \omega_{p0}^2/\omega^2 \leq 0.85$, where Landau damping dominates the threshold; and $0.9 \leq \omega_{p0}^2/\omega^2 \leq 1.0$, where collisional damping dominates the threshold. Figure VI-6 displays $F(E)$ curves for a density in each of these regions, with $P = E_0^2/E_{0c}^2$ as a parameter. The common features for the two cases in Figure VI-6 are the following: (1) n_{HOT}/n_0 , the ratio of hot to ambient electron density, increases strongly with increasing P , but is always less than 1% (see Table VI-1); (2) at the lowest P values $F(E)$ is Maxwellian, but at a much higher temperature than ambient; and (3) the average energy U_{av} of the hot electrons increases linearly with \sqrt{P} (Figure VI-7). The features not in common are these: (1) U_{av} of the hot electrons for the collision-damped region is considerably higher than for the Landau-damped region; (2) the slope of U_{av} versus \sqrt{P} is different for the two regions; and (3) a bump develops in $F(E)$ at higher P values only for densities in the collision-damped region. The sudden change of U_{av} between these two density regions correlates with the expected behavior for electrons moving at the

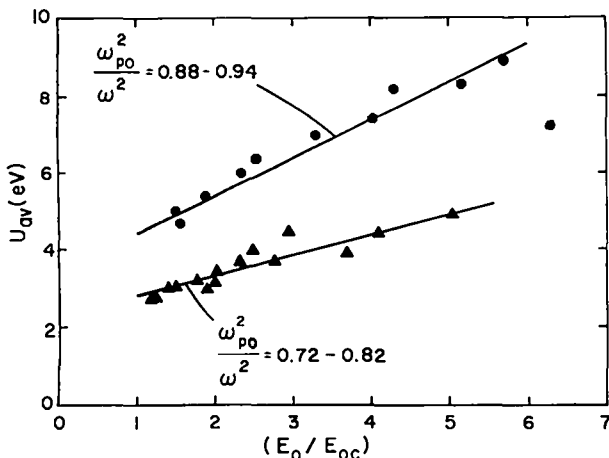


Figure VI-7
Average hot-electron energy versus E_0/E_{0c} .

theoretically predicted³ phase velocity of the most unstable electron wave, suggesting that wave-particle interactions play a role. For example, at $\omega_{p0}^2/\omega^2 = 0.77$ this energy is 1.6 eV, at $\omega_{p0}^2/\omega^2 = 0.94$ it is 5.0 eV, and at $\omega_{p0}^2/\omega^2 = 0.96$ it is 7.7 eV. Note that the position of the bump in $F(E)$ at $\omega_{p0}^2/\omega^2 = 0.94$ is also consistent with these energies, and that such bumps could also exist at $\omega_{p0}^2/\omega^2 = 0.77$ but be at energies too low to be measured by our detector. Another distinction between the two density regions is in the fraction of the measured anomalously absorbed microwave power P_{ANOM} carried by the hot electrons. The absolute power in hot electrons P_{HOT} is computed from $F(E)$. P_{HOT}/P_{ANOM} and n_{HOT}/n_0 are given in Table VI-1 for

TABLE VI-I
HOT-ELECTRON PROPERTIES

ω_{p0}^2/ω^2	P	$10^2 n_{HOT}/n_0$	P_{HOT}/P_{ANOM}
0.77	1.6	0.015	0.021
	4.0	0.10	0.10
	14.	0.75	0.13
0.94	2.2	0.0038	0.12
	6.6	0.096	0.80
	32.	0.77	1.10

the cases shown in Figure VI-6. Only in the collision-damped region, and for higher P values, is a very large fraction of P_{ANOM} given to a very small fraction n_{HOT}/n_0 of the electrons. The estimated uncertainty of P_{HOT}/P_{ANOM} is $\pm 50\%$. Preliminary measurements of the temperature increase of the body of the electron distribution show that a significant fraction of the unaccounted-for P_{ANOM} goes into moderate body heating rather than hot-tail production.

C. WEAK FIELD ELECTRICAL RESISTIVITY
(J. H. Brownell, H. Dreicer, R. Ellis, and
J. C. Ingraham)

Below the threshold for anomalous absorption (Section B1) the electrical resistivity is primarily due to electron-ion encounters. In the weak field limit, where $v_E/v_T \ll 1$, the current obeys Ohm's law and the resistivity is independent of electric field strength. Our measurement of this quantity is based on its relationship to the quality factor (Q) of the microwave resonator used in the experiment (Figure VI-1). The incremental change in $1/Q$ due to microwave dissipation in the plasma is given by

$$\Delta(1/Q) = (\omega_p/\omega)^2 (v_{ei}/\omega) \eta \propto \omega_p^4$$

provided $v_{ei} \ll \omega$. The factor η depends only upon the geometry. A theoretical value of $\Delta(1/Q)$ based upon the Dawson-Oberman electrical resistivity⁵ has been computed for $T = 2250^\circ\text{K}$ (solid line) and is compared with the observations (black dots) in Figure VI-8 for $0.1 \leq (\omega_p/\omega)^2 \leq 1.0$. These data were reported earlier by us,⁶ but are included because other work in this report depends upon it. The excellent agreement between theory and experiment

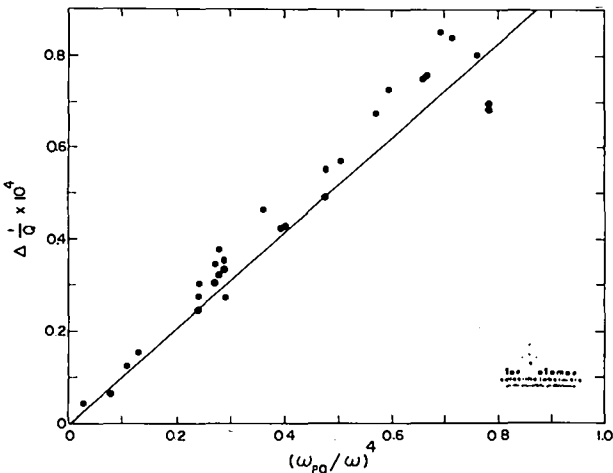


Figure VI-8
 $\Delta(1/Q)$ vs $(\omega_{p0}/\omega)^4$.

in this case has made it possible to utilize the proportionality $v_{ei} \sim T_e^{-3/2}$ for the measurement of electron temperature. An important point which remains to be settled, however, concerns the effect of a static magnetic field upon the weak field electrical resistivity. The Dawson-Oberman computation ignores magnetic field effects while our experiments are carried out on a magnetized plasma column with E_0 parallel to B_0 and with ω_c/ω_p in the range $3.0 < \omega_c/\omega_p < 14.4$, for which Debye length $>$ electron gyration radius. In such a strong magnetic field the usual hyperbolic electron-ion scattering orbit is strongly modified for impact parameters p larger than

$$p_C = \sqrt{h \ell}$$

where

$$h = \frac{e^2}{mv^2} = \text{nearest distance of approach}$$

$$\ell = \frac{v_{\perp}}{\omega_c} = \text{electron gyration radius}$$

v_{\perp} = component of electron velocity perpendicular to B_0 .

The quantity p_C is the impact parameter for which the Coulomb force just equals the magnetic force. If at any p the gyration radius is large enough for the electron to gyrate from $p > p_C$ to $p < p_C$ then it is not possible to use p_C to make a clear separation of Coulomb-dominated and magnetic-field-dominated collision orbits. This is unfortunately the usual situation encountered, and it means that simple collision computations are difficult to make.

During the past year the Dawson-Oberman theory for the AC resistivity, R , was modified by us to include the confining magnetic field⁵ and also arbitrarily large electric fields. The computation can be carried through, but the resulting resistivity formula is complicated. We have so far evaluated this resistivity in the limit of $B_0 \rightarrow \infty$ and $E_0 \rightarrow 0$

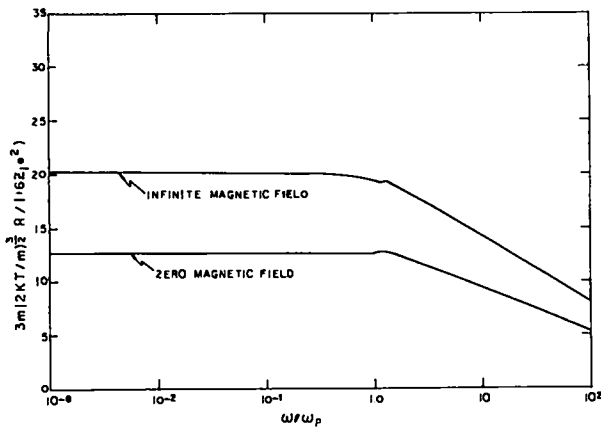


Figure VI-9
Normalized resistivity R vs ω/ω_p .

only. Figure VI-9 shows a comparison between this result and the $B_0 = 0$ result. Inasmuch as the $B_0 = \infty$ limit corresponds strictly to $p_c = 0$ this result may bear little relation to the situation encountered in the laboratory, because finite B_0 always implies a range of impact parameters $p < p_c$ for which the Coulomb force predominates over the magnetic force. This range is completely absent in the $B_0 = \infty$ limit. Evaluation of R for finite B_0 is required to resolve this issue, and this task will be carried forward during the coming year. In view of the fact that our observed resistivity is in good agreement with the zero magnetic field Dawson-Oberman resistivity it appears likely that much larger magnetic fields than are available to us are necessary to produce a noticeable deviation from the zero magnetic field result.

D. EXPERIMENTAL EVIDENCE FOR NONLINEAR INVERSE BREMSSTRAHLUNG ABSORPTION (J. H. Brownell, H. Dreicer, R. F. Ellis, J. C. Ingraham)

During the past year we obtained the first experimental evidence that the classical electrical resistivity (or inverse bremsstrahlung absorption) deviates from Ohm's law, and is a function of applied

electric field strength when the radiation intensity is strong enough for v_e/v_T to approach unity. In our experiment this phenomenon can be separated from the anomalous absorption, because the threshold for anomalous absorption rises rapidly with decreasing density (Figure VI-2). By choosing $(\omega_p/\omega)^2 < 0.7$ it is possible to apply electric fields strong enough to observe deviations from Ohm's law, but too weak to excite the AC parametric instabilities.

We have measured the classical resistivity as a function of v_E/v_T in such a regime with the same microwave technique used to measure the weak field resistivity (Section C). The new problem that arises in this case is the need to separate the effect of Ohmic heating on the electron-ion collision rate, v_{ei} , from the more fundamental influence of a strong electric field upon this collision rate. To explain the distinction we first recall that in weak fields ($v_E/v_T \rightarrow 0$) we have $v_{ei} \propto T^{-3/2}$. Temperature changes can therefore affect v_{ei} . Ohmic heating raises the electron temperature at the rate

$$v_h = \frac{1}{T} \frac{dT}{dt} = \frac{2}{3} (v_E/v_T)^2 v_{ei}$$

when $v_{ei} \ll \omega$ and heat flow can be ignored. The use of microwave measuring pulses whose duration exceeds v_h^{-1} can therefore lead to sizeable changes in v_{ei} . Secondly we note that the applied electric field competes with the Coulomb force and modifies the hyperbolic orbit ordinarily traversed by an electron when it collides with an ion. A measure of this modification is the amplitude δ of the oscillatory excursion in space executed by a free electron. δ is given by

$$\delta = v_E/\omega = \lambda_D (v_E/v_T) (\omega_p/\omega),$$

and equals the Debye length λ_D when v_E/v_T and ω_p/ω are unity. A study of these v_E/v_T

orbit modification effects is simplified by use of measuring pulse lengths τ_p shorter than v_h^{-1} . Otherwise some means of correcting for temperature changes is required.

Our experimental runs were carried out at densities corresponding to $0.55 \leq (\omega_p/\omega)^2 \leq 0.65$. Microwave pulses with pulse durations in the range $0.2 \mu\text{sec} \lesssim \tau_p \lesssim 30 \mu\text{sec}$ were used to measure $\Delta(1/Q)$. Their electric field strengths were restricted to values below threshold which ranged from $(v_E/v_T)_C = 0.5$ to $(v_E/v_T)_C = 0.7$ over the densities studied. For $(\omega_p/\omega)^2 = 0.6$ our earlier weak field resistivity measurements (Section C) yielded $v_{ei} = 6 \times 10^6 \text{ sec}^{-1}$ at $T_e = 2250^\circ\text{K} = T_0$. This means that for applied fields whose magnitude is about one-half the threshold value, we expected significant Ohmic heating only from pulse durations τ_p which were larger than 1 to 2 μsec .

This conclusion was tested by first ignoring the existence of the orbit modifications and using the conventional interpretation of $\Delta(1/Q)$ to deduce the temperature increase due to heating from the measured $\Delta(1/Q)$ values. This procedure is based upon the relation between the conventional v_{ei} and the temperature

$$v_{ei} = 6 \times 10^6 (T_0/T)^{3/2} \text{ (for } T_0 = 2250^\circ\text{K)},$$

as well as on the relation between v_{ei} and $\Delta(1/Q)$:

$$\Delta(1/Q) = \eta(\omega_p/\omega)^2 (v_{ei}/\omega). \text{ (See Section C.)}$$

The resulting values of T/T_0 deduced are shown in Figure VI-10 (black dots), for $v_E/v_T = 0.37$, together with two theoretical curves (solid lines) that give the expected heating as a function of pulse length.

Both theoretical curves are based on the actual pulsed electric field distribution in time and space, but the heating calculation utilizes the measured weak field

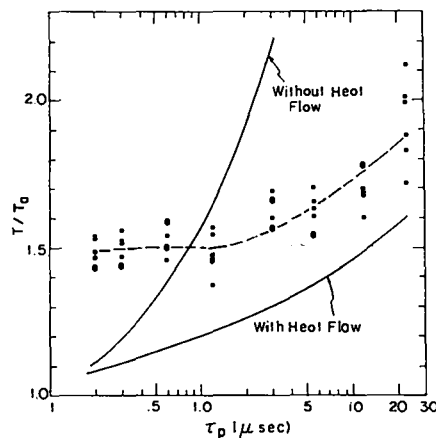


Figure VI-10
 T/T_0 vs τ_p for $v_E/v_T = 0.37$ and $(\omega_p/\omega)^2 \approx 0.6$.

resistivity (Section C). To test the effect of heat flow along the plasma column on the temperatures achieved it was included in one of the two theoretical solutions as indicated. These theoretical curves are numerical solutions to

$$\frac{3}{2} nk \frac{\partial T}{\partial t} - \frac{\partial}{\partial x} K \frac{\partial T}{\partial x} = S(x,t) \quad (1)$$

where

$$K = K_0 (T/T_0)^{5/2} = \text{Spitzer's thermal conductivity}$$

$$S(x,t) = \frac{1}{2} \frac{\omega_p^2}{\omega^2 + v_{ei}^2(T)} v_{ei}(T) E_0^2(x,t).$$

The striking feature of the result shown in Figure VI-10 is the large apparent temperature jump ($T/T_0 \approx 1.5$) deduced from the $\Delta(1/Q)$ measurements for the shortest τ_p used. Moreover this apparent temperature jump is nearly independent of τ_p until τ_p equals $\sim v_h^{-1}$. Provisional temperature measurements carried out with Langmuir probes indicate no such increase for small τ_p in agreement with the theoretical calculations which also predict much less early time heating irrespective of heat flow. By monitoring the electron density

we have also ruled out the possibility that the large apparent temperature deduced for small τ_p might actually be due to a sudden density reduction produced by the microwave pulse itself.

The observation of this large early-time apparent temperature jump leads us to conclude that the value of v_{ei} is altered when v_E/v_T approaches unity. We conclude that the temperature jump deduced for early times is false, but indicates instead that v_{ei} itself has become a function of applied field. Such modification in v_{ei} would manifest itself in a modification of $\Delta(1/Q)$ that follows the detailed time dependence of the applied field without delay.

The data shown in Figure VI-10 correspond to $v_E/v_T = 0.37$ or the single electric field value $E_0 = 74.3$ volts/cm. The effect of varying electric field is shown in Figure VI-11 where the ratio $v_{eff}/v_{ei}(T_0)$ defined in terms of the experimental quantities $\Delta(1/Q(E_0))$ and $\Delta(1/Q(0))$ by

$$\frac{v_{eff}}{v_{ei}(T_0)} = \frac{\Delta(1/Q(E_0))}{\Delta(1/Q(0))}$$

is plotted for $\tau_p = 0.2$ to 0.4 μ sec as a function of E_0 . For the short pulses involved, there is no Ohmic heating in weak fields. Therefore the weak field $\Delta(1/Q)$ values, denoted by $\Delta(1/Q(0))$, yield the classical electron-ion collision rate at the initial temperature T_0 . If the strong field orbit modification were absent and v_{eff} had the weak field dependence

$$v_{eff} = v_{ei}(T) \propto T^{-3/2}$$

then the sole result of applying a microwave pulse would be Ohmic heating, and $v_{eff}/v_{ei}(T_0)$ would be simply given by $(T_0/T)^{3/2}$. Equation 1 has been solved for all of the microwave pulses used in the experiments to determine T/T_0 . The result, (solid black line) in Figure VI-11, gives a measure of the difference between the

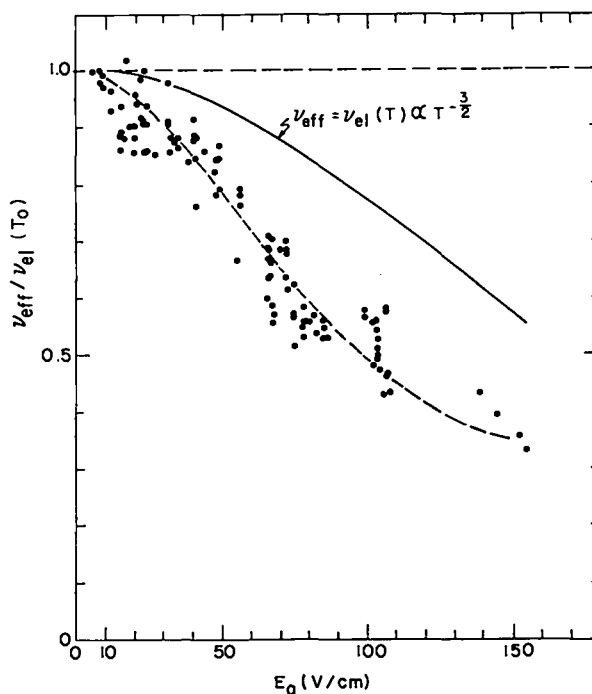


Figure VI-11
 $v_{eff}/v_{ei}(T_0)$ vs E_0 for $(\omega_p/\omega)^2 \approx 0.6$.

expected and the observed effect. It indicates the real nature of the discrepancy involved and shows the convergence of the observations and theory in the weak field limit, as expected. The reader is cautioned not to deduce the actual temperature rise from this theoretical curve, because the source term $S(x,t)$ in Eq. VI-1 is based upon the weak field value of v_{ei} and thus overestimates heating. This is also true of the theoretical curves in Figure VI-10.

The orbit modification effects discussed earlier are presumably included in the theoretical treatment of the resistivity published by Salat and Kaw.⁷ A detailed comparison of our observations with this theory is not yet complete, but it does indeed show that our measured deviation of v_{eff} from $v_{ei}(T)$ due to high fields is of the order of five times greater than their theoretical prediction. This work will continue during the coming year.

REFERENCES

1. H. Dreicer, D. B. Henderson, and J. C. Ingraham, Phys. Rev. Lett. 26, 1616 (1971).
2. Harry Dreicer, Richard F. Ellis, and John C. Ingraham, Phys. Rev. Lett 31, 426 (1973).
3. J. P. Freidberg and B. M. Marder, Phys. Rev. A 4, 1549 (1971).
4. J. H. Malmberg, C. B. Wharton, and W. E. Drummond, Proceedings of the IAEA Conference on Plasma Physics and Controlled Nuclear Fusion Research, Culham, 1, 485 (1965).
5. For the unmagnetized plasma resistivity see J. M. Dawson and C. R. Oberman, Phys. Fluids 5, 517 (1962); For the magnetized plasma resistivity see C. Oberman and F. Shure, Phys. Fluids 6, 834 (1963).
6. LA-5250-PR Progress Report LASL Controlled Thermonuclear Research Program for a 12-Month Period Ending December 1972, Issued June 1972. p. 66
7. A. Salat and P. K. Kaw, Phys. Fluids 12, 342 (1969).



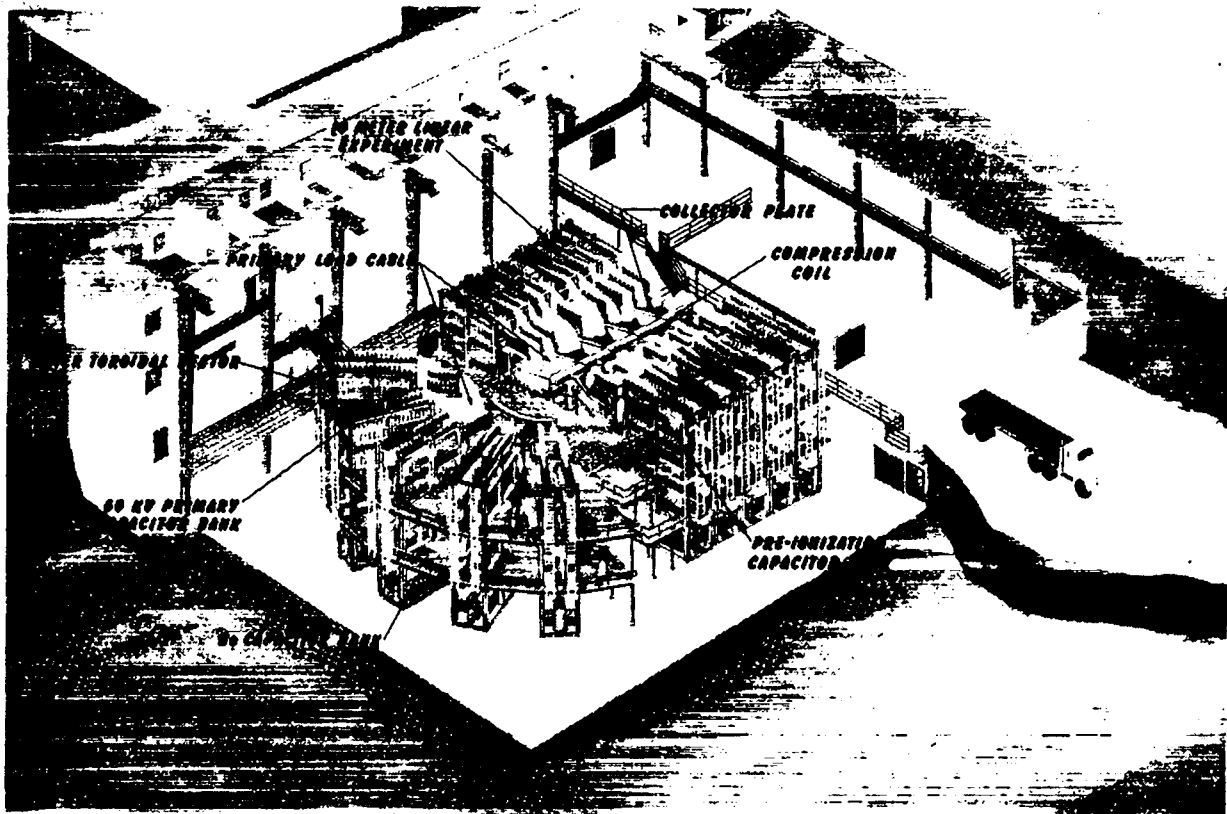
VII. CTR ENGINEERING

A. SCYLLAC ENGINEERING

1. Toroidal Conversion (W. H. Borkenhagen, K. W. Hanks, H. W. Harris, E. L. Kemp, C. F. Hammer, and J. H. Banta)

The first phase of Scyllac shown pictorially in Figure VII-1 was divided into two experiments: a 5-m toroidal sector and a linear experiment that actually consisted of a 5-m linear coil with strong mirrors on each end. A blast wall was installed between the two experiments to isolate them from each other.

The conversion of these two experiments into a single toroidal experiment was phased to maximize the physics experimental program during the construction period. In general, three phases were involved: the continued operation of the linear experiment while the five toroidal sector racks were relocated; operation of the five toroidal sector racks with the new toroidal radius (4 m vs 2.5-m Phase I radius); and finally, integrating all racks into a complete system. The conversion proceeded



SCYLLAC PHASE I

Figure VII-1
Scyllac Phase 1.

as planned, and in the 52 weeks in 1973, the linear experiment operated 7 weeks and the enlarged toroidal sector operated 23 weeks.

The conversion proceeded in the following manner. Referring to Figure VII-1, the blast wall remained in place and the linear experiment continued to operate while the five toroidal sector racks were disconnected and moved back radially approximately one meter using air pallets.¹ The collector plates were modified, reinstalled, and connected to a new coil. In March, the blast wall was removed and the two linear racks adjacent to the toroidal sector were moved into their proper toroidal location. A new blast wall was

installed through these two racks so physics could be conducted on the new toroidal sector while conversion proceeded in the other racks. One linear rack was removed from the building to allow maneuvering room for the remaining seven racks. When they were in position the last rack was installed. Finally, the blast wall was removed and physics experiments have ceased until the toroidal experiment will begin operation. Figure VII-2 shows the collector plate system in the toroidal configuration.

Two types of personnel were involved in this conversion, union crafts and skilled technicians.² The crafts performed the construction work for a total cost of

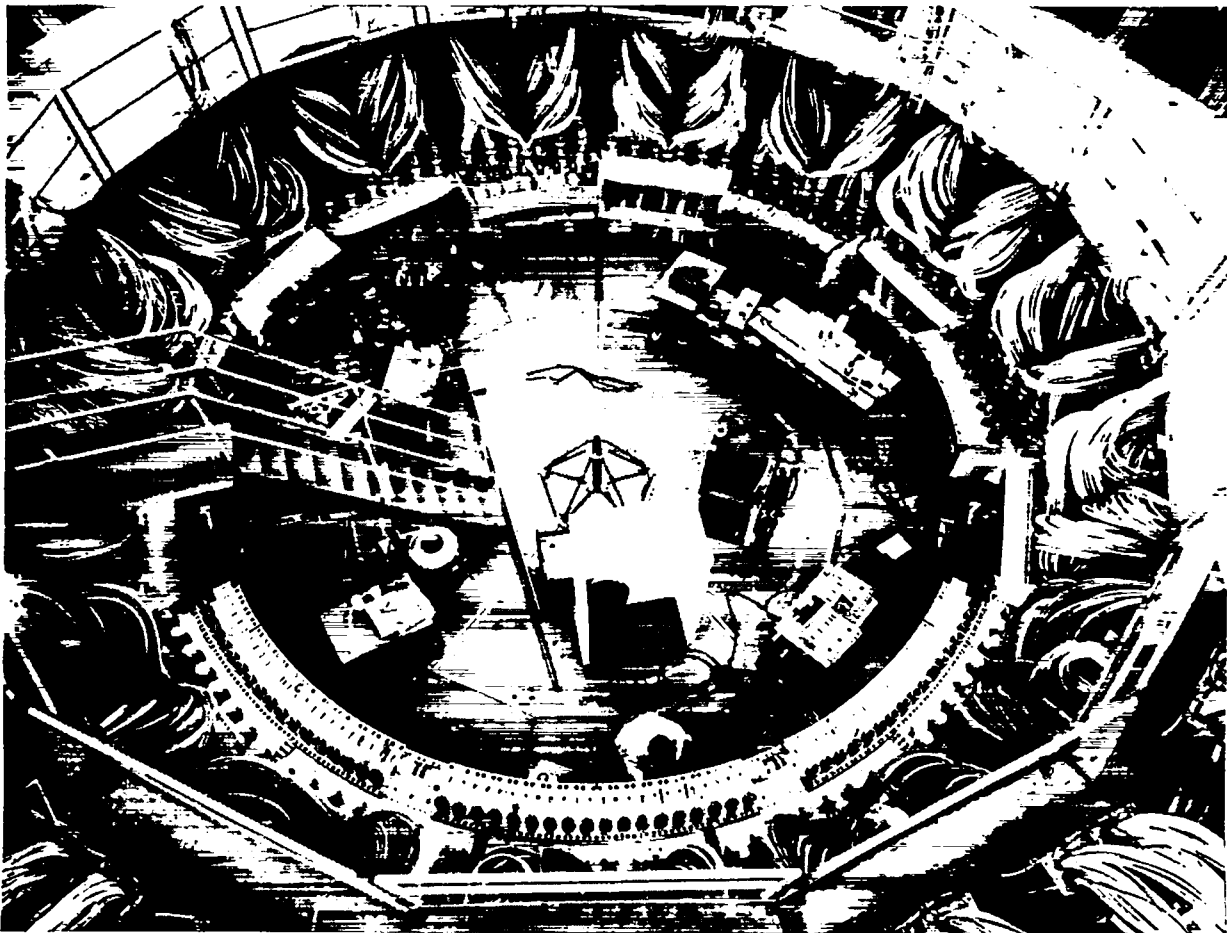


Figure VII-2
Scyllac collector plate system in toroidal configuration.

\$550,000 while the technicians completed the unconventional work. Approximately 20 craftsmen and 15 technicians were involved in this program for a full year. The construction work was completed at the end of December and toroidal physics experiments are expected to begin in May 1974.

2. Toroidal Feedback System (K. J. Kutac, W. H. Borkenhagen, E. G. Sherwood, G. A. Barnes, and L. S. Schrank)

The toroidal Scyllac system requires a feedback stabilization system to control an instability that is generated by the fields required to obtain equilibrium in a curved theta-pinch geometry. The feedback system, described in LA-4888-PR, consists of a position detector, a signal processor, a power amplifier, and $l = 0$ field coils. Only a few (three to six) position detectors and signal processors are required for the system while 60 power amplifier modules are required as well as 240 $l = 0$ coil assemblies. Each power amplifier module includes two ML-8618 power amplifier triodes as well as amplifier and driver circuits.

Two teams were organized to fabricate, install, and check out this system. The fabrication team modified all the modules from the Scylla IV experiment and then began fabrication of the remaining 50 modules. The operations team installed and operated 32 modules on the 4-m radius toroidal sector experiment. This feedback system performed relatively well and showed some evidence of controlling the plasma although the experiment was terminated before the feedback was optimized. Fabrication and installation of the remaining 28 modules is under way.

B. COMPONENT DEVELOPMENT

1. Components for SFX Capacitor Bank

(R. A. Haarman, E. L. Kemp)

The theta-pinch Scientific Feasibility Experiment (SFX) will require over 200 MJ of magnetic energy in the compression coil which will ultimately be supplied by a Magnetic Energy and Transfer System (METS).

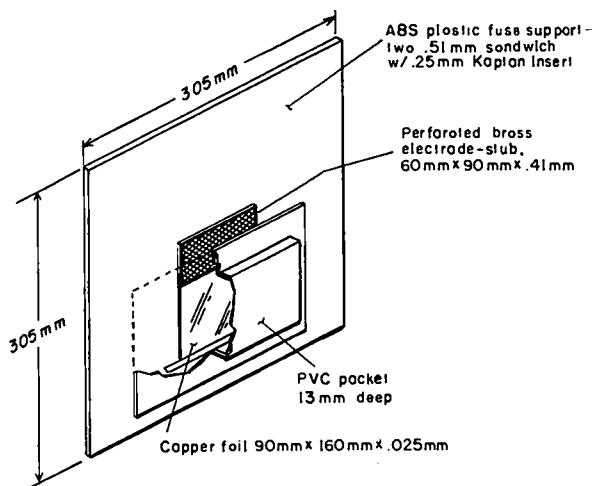


Figure VII-3
High-energy fuse package.

The METS system requires a large transfer capacitor bank to improve its transfer efficiency. This capacitor bank may actually be first used to energize the compression coil for the initial SFX experiment.³ The principal components for this capacitor bank are a low cost capacitor, a crowbar ignitron, and a series switch.

The development of a low cost capacitor and a crowbar ignitron has begun. The presently available 170- μ F, 10-kV, 8500-joule capacitor sells for about three cents per joule. This capacitor is being fully evaluated in a crowbarred circuit to determine its life and failure mechanism. Higher stressed, lower cost units are being ordered for evaluation.

The most difficult component in this circuit is the crowbar switch. A size D ignitron is being evaluated for this application. Six type NL 5553B/T2600 ignitrons were evaluated in a test circuit carrying a peak current of 100 kA with an L/R time constant of 4 ms which required the tubes to conduct a total charge of 400 coulombs. Two of the tubes went beyond 15,000 shots at which time they were opened to determine their internal condition. These two tubes did not prefire during these tests and showed very little evidence of arc transfer

to the wall when they were opened. The other four tubes failed for a variety of mechanical problems that can be corrected. A new bank is being built to evaluate tubes at 1000 coulombs which is the goal for this component.

2. High-Energy Fuse Development (R. S. Dike and R. A. Haarman)

A fuse package⁴ capable of interrupting 500 kA, developing an 80-kV pulse, and absorbing 30 kJ of energy has been developed for use in the present ZT-1 experiment. The same fuse can also be used in the proposed ZT-S experiment with two fuses per quadrant, one mounted above the other and connected in parallel.

After a series of tests of various arc-inhibiting materials described in LA-5250-PR, it became clear that sand was the superior arc-inhibiting medium. Figure VII-3 shows a sketch of the fuse package. The PVC sand container is flexible enough to absorb the blast wave without rupture. The Eastman 910 adhesive, which is used to bond the PVC pocket to the cyclac fuse support, is strong enough to prevent the PVC from tearing away from the support. Kapton sheets are inserted between the fuse supports in a sandwich design to provide increased dielectric strength.

The advantages of the fuse package include the capability of inverted mounting, no sand or debris being expelled when the fuse is fired, and the relative ease of replacing fuses after each shot and thereby increasing the amount of experimental data that can be obtained per day.

3. Transfer Capacitor Prototype Circuit (R. S. Dike, R. A. Haarman, and R. Holm)

A prototype transfer capacitor test header has been built to determine the characteristics of the transfer capacitor circuit described by J. N. DiMarco in LA-5250-PR. This header, shown in Figure VII-4, is proposed to replace the fuse switched inductive storage circuit on future Z-pinch experiments. The prototype is being used to evaluate the components

required for this system, in particular a 0.08- μ F, 100-kV capacitor, a transfer switch, and a damping resistor, as well as to evaluate the high-voltage characteristics of the header design.

The header has been fired about 1000 shots during which the header design was modified to make it operate reliably at 100 kV, the design goal. This testing occurred with one-fifth of the design energy in order to minimize the fault energy. The header is now relatively reliable at 100 kV.

The transfer switch characteristics have been investigated in the self-breakdown mode and the triggered mode; however, the switch inductance is relatively high and approximately 70% of the total voltage appears across the transfer switch. At the one-fifth energy level, an \dot{I} of 1.5×10^{12} amps/sec has been achieved at 100 kV on the transfer capacitors. The current transfer characteristics appear to follow the theoretically predicted values.

Effort continues in decreasing the transfer switch inductance, transferring higher currents by increasing energy levels, and placing the header in an automatic firing mode for component life testing.

C. ENGINEERING ANALYSIS

1. Prediction of Failures in CTR Systems (G. P. Boicourt)

The problem of predicting failure rates⁵ is becoming more important in CTR engineering because of the large systems under consideration. A large theta-pinch system will contain thousands of identical components, many of which are barely beyond the development stage and whose failure rate may be fairly high. If such a system is assembled without due regard for these failure rates, there is a real danger that it will not operate satisfactorily.

The usual "mean time between failures" calculation is not applicable here because it assumes all the components in the system are on the flat part of their failure-rate curve. This means the early failure components have been eliminated before the

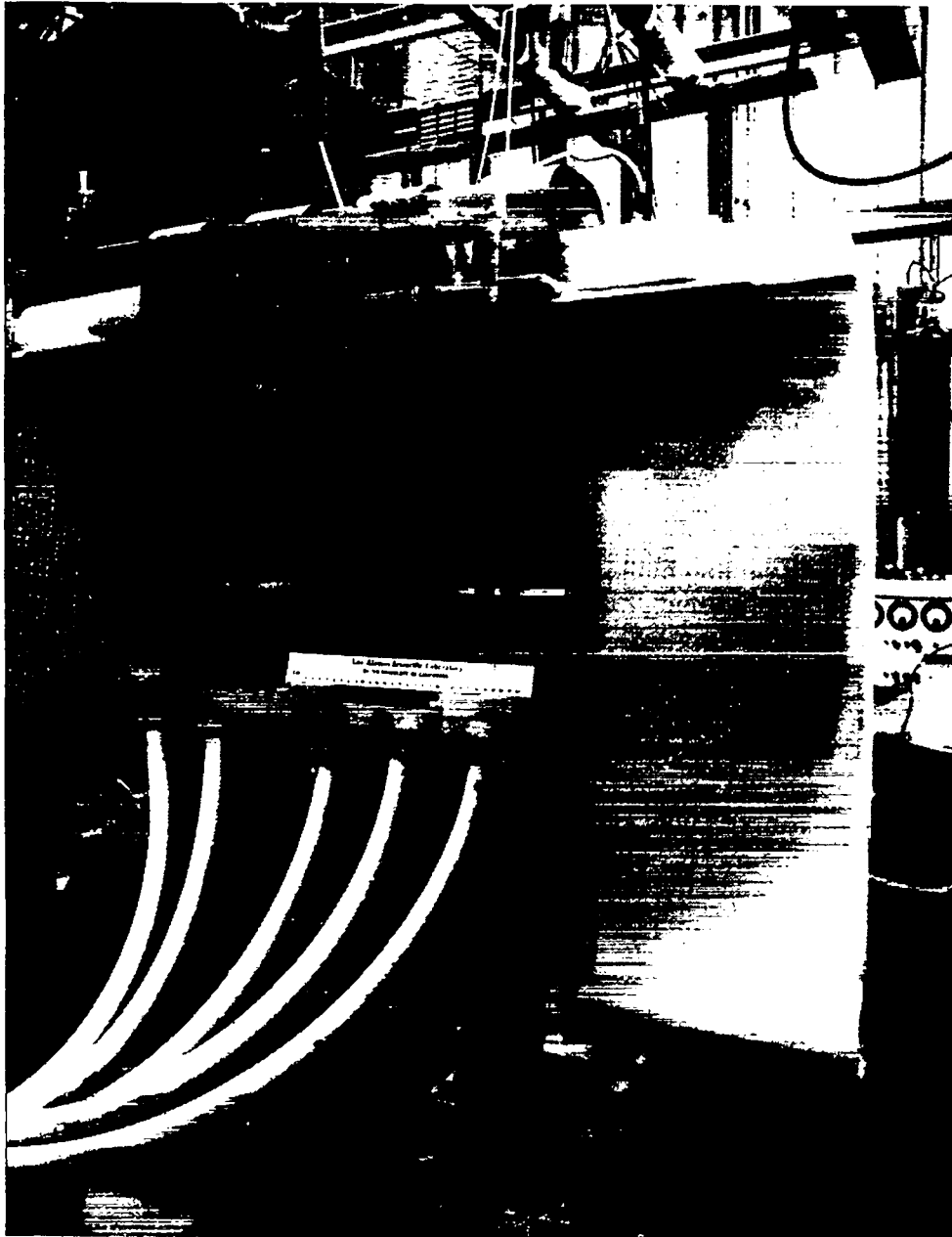


Figure VII-4
Prototype transfer capacitor test header.

components are installed in the system. Unfortunately, some of the critical components in a large CTR system may not be tested sufficiently to reach the flat part of the failure-rate curve because of the time and expense involved. Usually only a few types of components determine the failure rate in CTR systems and this makes

possible the Monte Carlo calculation of an analogous quantity, the "expected time to next failure," provided the failure distributions of the critical component types are known.

The "expected time to next failure" is defined to be the reciprocal of the failure rate of the composite systems and

is thus time dependent. For the case where failures are independent, the failure rate of the system is given by the expression

$$r(t) = - \frac{1}{R_s} \frac{dR_s}{dt} \quad (1)$$

where R_s is the system reliability function. For systems which are series systems in the probabilistic sense

$$R_s = \prod_{i=1}^N R_i$$

where R_i is the reliability of the i^{th} component,

$$R_i = \int_t^{\infty} f_i(t) dt = 1 - F_i(t)$$

Therefore, since

$$f_i(t) = \frac{-dR_i}{dt}$$

and

$$\frac{dR_s}{dt} = \sum_{i=1}^N \left(\prod_{\substack{j=1 \\ j \neq i}}^N R_j \right) \frac{dR_i}{dt} = \left(\prod_{j=1}^N R_j \right) \left(\sum_{i=1}^N \frac{1}{R_i} \right) \frac{dR_i}{dt}$$

we have

$$r(t) = \sum_{i=1}^N \frac{f_i(t)}{1 - F_i(t)} \quad (2)$$

This can be simplified a little by noting that if we have M_j components that obey identical statistics and J such groups then

$$r(t) = \sum_{j=1}^J \frac{M_j f_j(t)}{1 - F_j(t)} \quad (3)$$

provided each component in each group has

been operating the same length of time. If some components have been replaced, then the M_j can be reduced accordingly and terms for each replacement component added to the sum of equation (3) as required.

A computer program has been written to predict the "expected time to next failure" for a system having up to ten types of failure distributions. The number of failure distributions will be expanded in the future. The use of ten component types is sufficient since the more usual parts of the system, i.e. power supplies, control circuits, etc., have low failure rates and will be well tested before installation. Thus they can be lumped together into a single composite type following exponential statistics as is done in the usual "mean time to failure" calculation.

The logic of the program is as follows. For a given shot the probability of failure is computed using known component failure distributions and Monte Carlo methods are used to determine if a failure occurred. If so, the Monte Carlo method is again used to find the failed component which is then replaced before the computation proceeds to the next shot. At any time the failure rate and "expected time to next failure" can be computed using the known failure distributions and the previous history of the system. Example calculations and applications can be found in the reference.⁵

2. Fitting Test Data to Weibull Statistics (G. P. Boicourt)

A prime objective of component testing is to determine whether a given component is of sufficient quality to perform satisfactorily in a large system. In order to use the failure data obtained from the tests of samples of a component type, it is advantageous to describe the failures by a probability distribution. A distribution which has great generality and describes many mechanical and electrical components is the Weibull distribution.

The Weibull distribution in complete generality is a function of three parameters. Its density function is given by

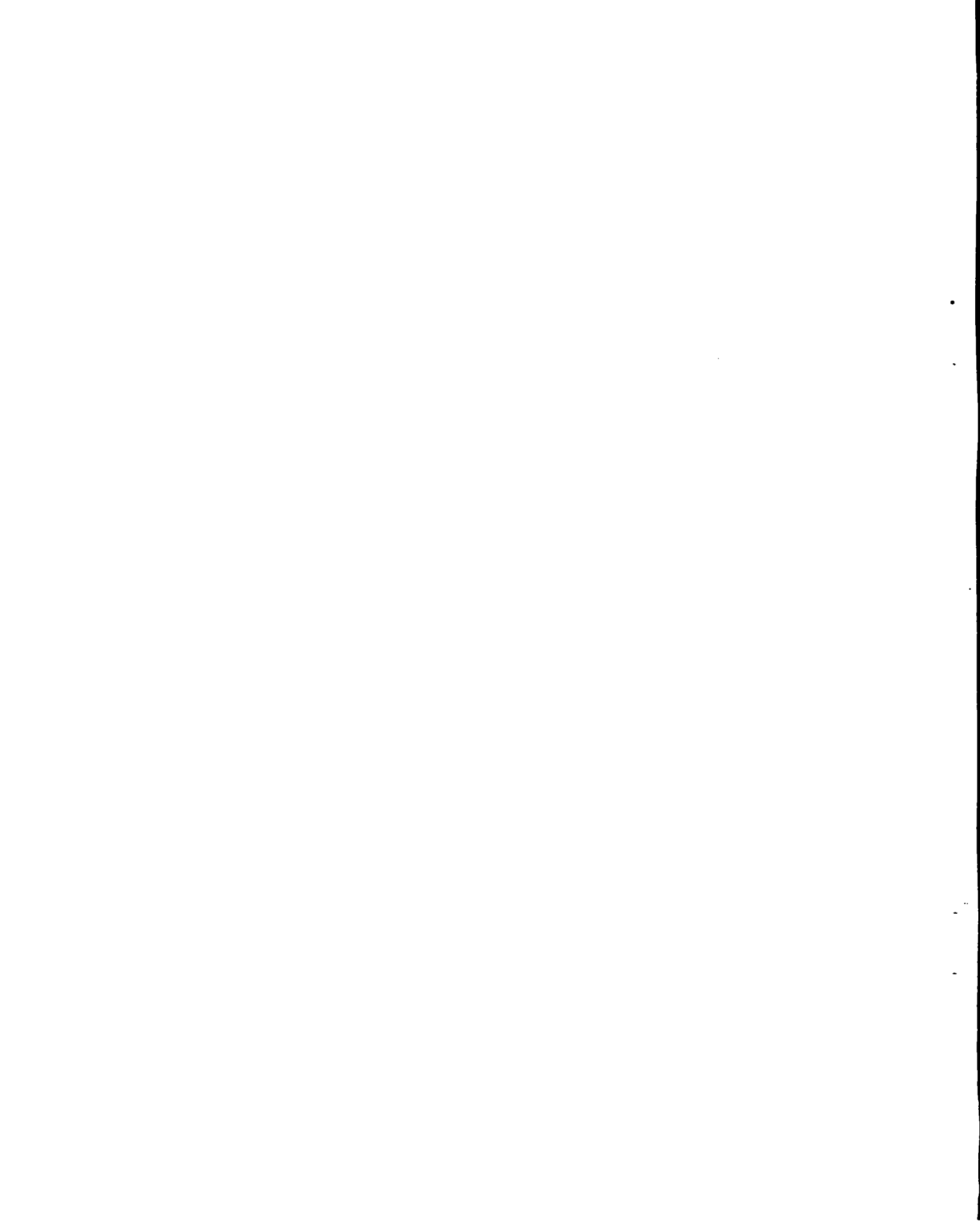
$$f(t) = \frac{\beta}{\alpha} t^{(\beta-1)} e^{-\frac{(t-\gamma)^\beta}{\alpha}}$$

The literature tends to treat only the two-parameter distributions and assumes that the location parameter, γ , is zero. Unfortunately, at least two common CTR components, cables, and capacitors obey Weibull statistics with nonzero γ . Thus, if full value is to be obtained from the testing of these components, some way of fitting the test data to the three-parameter distribution is required.

A FORTRAN IV program has been developed to fit data to a three-parameter Weibull distribution. The fit is accomplished by assuming that γ is nonzero, performing weighted least-squares fits, and using the data from the last fit to improve the next fit iteratively. Two weights are used: a weight of one to emphasize the early failures and aid in picking up possible multiple distributions, and a weight chosen proportional to the reciprocal of the variance. The latter weight is the theoretically correct weight when only one distribution is present. Specialized Weibull plotting routines were developed and are included in the program. These provide optional standardized Weibull plots of the raw data and fitted data. The program is able to handle data which includes suspended items, that is, units which have been removed from test prior to failure. This feature allows periodic examinations of operations data on components in situ since a component may still be operating and be weighted in the analysis.

REFERENCES

1. James J. Banta and Charles F. Hammer, "Moving Energy Storage Capacitor Racks with Air Bearings," IEEE report 73CH0843-3NPS (April 1974).
2. H. W. Harris, E. L. Kemp, W. E. Quinn, and F. L. Ribe, "Project Management of Scyllac Construction," IEEE report 73CH0843-3NPS (April 1974).
3. E. L. Kemp, "The Study of Capacitive Energy Storage for A Theta-Pinch PTR Compression Coil," IEEE report 73CH0843-3NPS (April 1974).
4. R. A. Haarman, R. S. Dike, and M. J. Hollen, "Exploding Foil Development for Inductive Energy Circuit," IEEE report 73CH0843-3NPS (April 1974).
5. G. P. Boicourt, "The Prediction of Failures in CTR Systems," IEEE report 73CH0843-3NPS (April 1974).



VIII. FUSION TECHNOLOGY

A. INTRODUCTION (R. A. Krakowski)

Activity in the reactor technology area commenced in CY 1972, and has accelerated considerably during the past year. The first major iteration on an engineering design of a Reference Theta-Pinch Reactor (RTPR) has been completed jointly by ANL and LASL.¹ An environmental assessment based on this engineering design is near completion. Computational efforts in neutronics, CTR blanket physics, heat transfer/fluid flow, and materials evaluation have generated a realistic calculational base upon which future, more detailed design efforts and reactor assessments can proceed. Numerical simulation of the thermonuclear burn and gas cooling dynamics has been advanced. Experimental research in both insulator and metal technology has moved ahead. Given below is a synopsis of the results of the activities during 1973.

B. REACTOR DESIGN STUDIES (R. A. Krakowski, Q-DOT)

The Argonne National Laboratory and the Los Alamos Scientific Laboratory have initiated and completed an engineering design of a fusion reactor which uses the theta-pinch principle of plasma confinement.¹⁻³ The RTPR operates in a pulsed mode, and during the 10.0-sec duty cycle the following sequence of events occurs: (a) implosion heating of the preionized DT plasma to ~ 1 keV (0.000-0.010 sec), (b) adiabatic compression of the plasma to ignition at ~ 6 keV (0.010-0.030 sec), (c) thermonuclear burn of the high-beta plasma at constant magnetic field (0.030-0.110 sec), (d) quench of the burning (~ 15 keV)

plasma by a programmed relaxation of the magnetic field (0.110-0.130 sec), (e) transfer of the plasma internal energy by conduction through a neutral gas layer⁴ to the blanket (0.130-1.130 sec), and (f) removal of excess blanket enthalpy by flowing lithium metal, ash removal, re-fueling, and preionization for the next power pulse (1.130-10.0 sec).

Figure VIII-1 illustrates schematically the essential elements of the staged theta-pinch concept. A low-energy magnetic field, (~ 1.4 T), implodes a fully ionized, low-temperature plasma. The implosion field is driven by a large azimuthal electric field (~ 0.2 kV/mm) which is derived from a capacitive discharge and

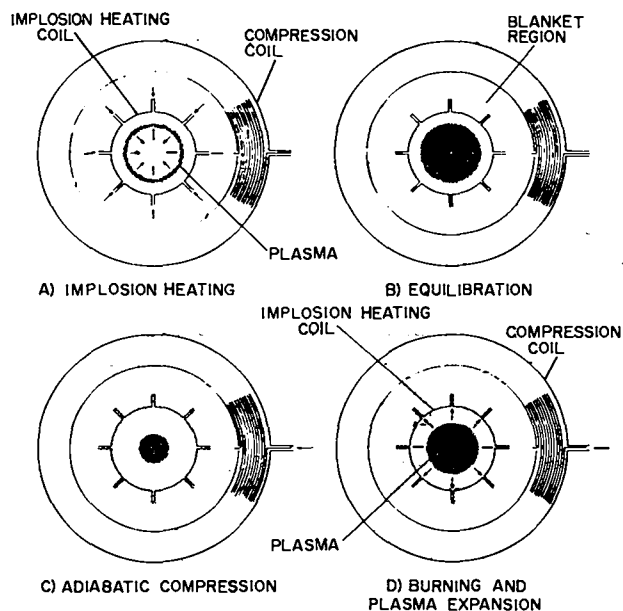


Figure VIII-1
Plasma heating, thermonuclear burn, and direct conversion in a staged theta-pinch reactor.

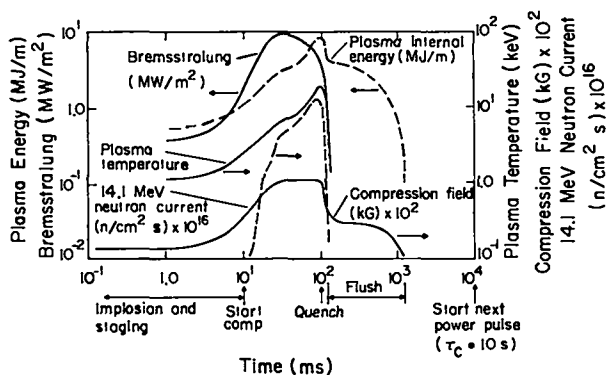


Figure VIII-2
Instantaneous fluxes to which the first wall will be subjected during a 10-sec RTPR power cycle.

must have a risetime of a few tenths of a microsecond to be effective in heating the plasma without significantly decreasing the plasma radius.* The implosion stage is followed by a slowly rising (\sim tens of milliseconds) compression field ($\sim 11.0T$) which is generated by massive, room-temperature coils that are energized by an external, superconducting magnetic energy store. The energy contained by the compression field is appreciable (178 MJ/m) and must be efficiently recovered. The shaded regions of Figure VIII-1 represent a magnetic field perpendicular to the plane of the figure. The arrows indicate the flow of energy into and out of the system. As the plasma is reduced in radius, the density and temperature increase adiabatically. Shortly before the maximum compression field is attained, the plasma ignites and the thermonuclear burning accelerates at a constant compression field. The energetic alpha particles (a DT cycle is being considered) thermalize in the dense plasma and the internal energy of the plasma increases proportionately. The plasma, therefore, expands against the constant magnetic field, doing

*Large values of the ratio of plasma radius to first-wall radius are desirable for effective wall stabilization of the plasma.

useful (direct-conversion) work in the process. After the burn the compression field is reduced to $\sim 3.2T$, the density and temperature decrease, and the thermonuclear burn is quenched. The plasma internal energy, which is still significant following the quench (~ 4.1 MJ/m), is conducted through a neutral gas layer to the first wall of the reactor; the neutral DT gas layer is introduced during or immediately after the adiabatic compression. Once the plasma internal energy has been slowly transferred to the lithium primary coolant, the burn ash is removed, new fuel is injected and ionized, and the system is readied for the next power cycle. The total duty time is governed by the desire to derive a maximum of useful energy per cycle; the need to restrict the radiation, thermal, and stress levels to which the first vacuum wall will be exposed; and the need to evacuate and refuel the plasma chamber. The unoptimized choice of 10 sec for the RTPR duty cycle is based on the latter considerations. Figure VIII-2 summarizes the radiation fluxes to which the RTPR first wall will be subjected; evaluation of the first-wall materials response has been summarized elsewhere.^{5,6}

Table VIII-1 summarizes important design parameters for the RTPR power plant, which is depicted in Figure VIII-3. The fusion reactor/power plant is shown diagrammatically in Figure VIII-4 and consists of 10 major systems as follows: implosion heating, plasma compression/confinement, magnetic energy transfer and storage, first wall, blanket, biological shielding, fuel supply/removal, fuel/ash removal and reprocessing, lithium processing, and energy conversion. A total of 36 GJ (101 MJ/m) of recoverable neutron, gamma, and bremsstrahlung energy is deposited into the RTPR blanket every 10.0 sec. Liquid lithium is used as the primary coolant. Other materials used include alumina (provisionally chosen as the first-wall insulator), niobium for the first-wall and blanket

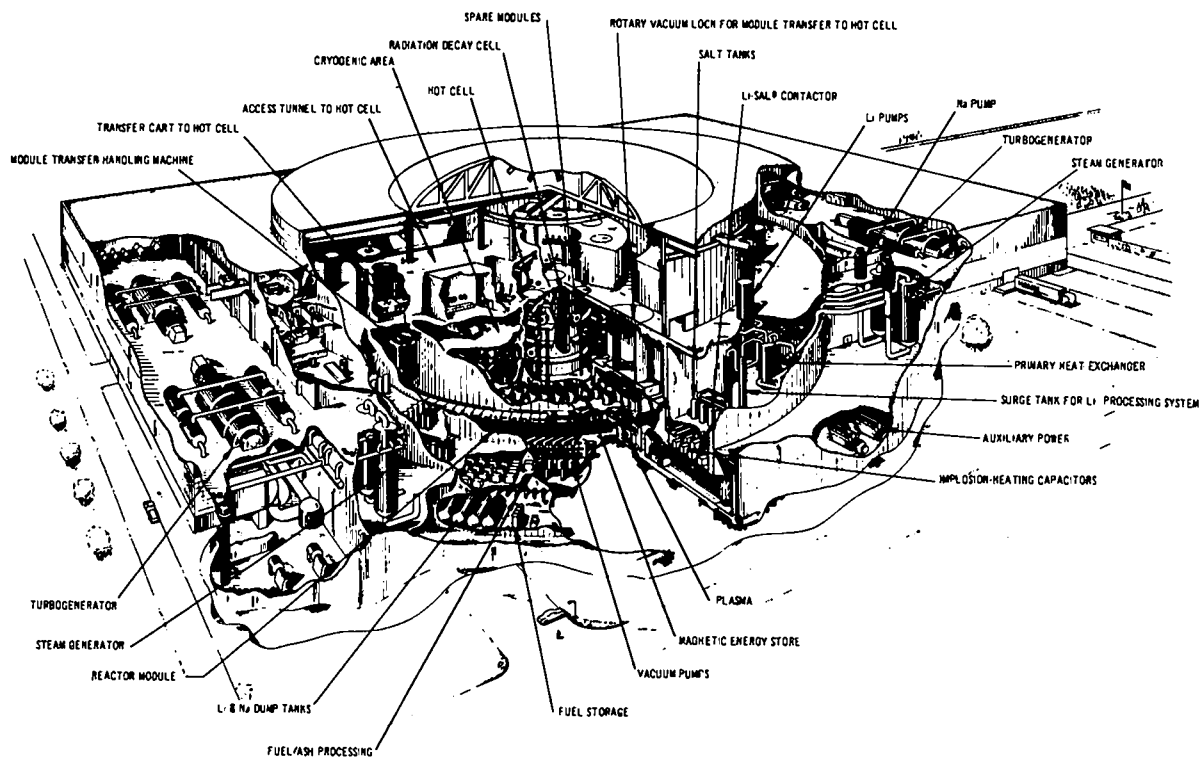


Figure VIII-3
Cutaway view of RTPR power plant.

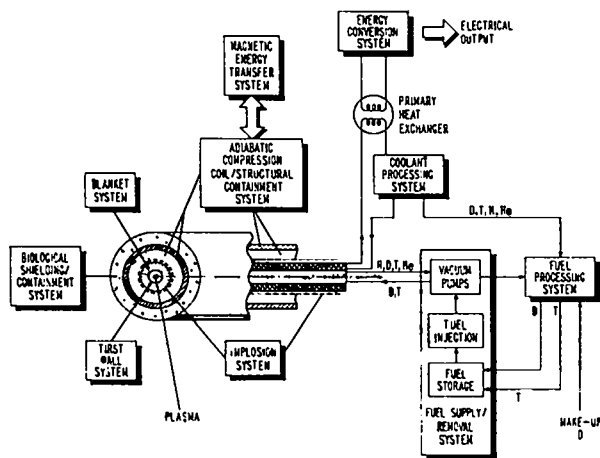


Figure VIII-4
Diagram of ten major subsystems in RTPR power plant.

structural material, beryllium neutron breeder and graphite as a moderator. Two energy conversion schemes are considered: a) a conventional, low-temperature system which uses a Na/steam cycle, and b) an advanced high-temperature steam system which uses a potassium topping cycle. Special attention is given to the plasma burn dynamics, overall energy balance, blanket neutronics and thermal response, radiation shielding, radiation effects, corrosion of construction materials, thermal and irradiation response of the Al_2O_3/Nb first wall, and tritium recovery and containment. Unique features of the design include a superconducting magnetic energy

transfer and storage system and modular blanket structure (shown in Figure VIII-5), which permits easy access for maintenance.

The first-wall loading corresponds to 2.0 MW/m^2 based on the 14.1-MeV neutron current or 2.9 MW/m^2 based on total thermal power generation by neutrons (3.3 MW/m^2 based on a total thermal power generation). The ratio of instantaneous-to-average neutron flux is ~ 100 , and continuous, full-power operation is assumed. Table VIII-2 summarizes the calculated thermal excursions, thermal stresses, dpa and transmutation rates, and H/He production rates expected of the RTPR first wall. In certain instances the conditions (neutron fluence, instantaneous neutron flux, gas generation rate, transmutation rate, etc.) under which the first-wall materials are expected to function have never before been experienced. Extrapolation of existing fission-reactor and accelerator irradiation data, however, forecasts potential troubles. A major goal of the RTPR design exercise is to define major problem areas and where possible to identify quantitatively the kinds of design changes which will alleviate these problems. The engineering design is detailed enough to provide the basis for a subsequent environmental (Sec. G) impact study and an assessment of future research/development needs.

TABLE VIII-1

SUMMARY OF RTPR POWER PLANT CHARACTERISTICS^a

Minor diameter (first wall)	1.0	m
Major diameter	112.	m
Number of 2-m-long modules	176.	
Blanket thickness	0.4	m
Blanket construction material	Al ₂ O ₃ , Nb-1%Zr, Be, C	
Duty cycle ^b	10.0	sec
Burn time	~0.080	sec
Uncollided (14.1-MeV) neutron current averaged over the power cycle	8.92 x 10 ¹³	n/cm ² -sec
Total instantaneous neutron flux averaged over the ~ 0.08-sec burn period	1.11 x 10 ¹⁷	n/cm ² -sec
Total neutron flux averaged over the power cycle	9.04 x 10 ¹⁴	n/cm ² -sec
Annual fluence of uncollided 14.1-MeV neutrons (2.0 MW/m ²)	2.81 x 10 ²¹	n/cm ² -yr
Annual fluence of 14.1-MeV neutrons	5.52 x 10 ²¹	n/cm ² -yr
Annual fluence of neutrons with E > 10 MeV	6.43 x 10 ²¹	n/cm ² -yr
Annual fluence of all neutrons	2.85 x 10 ²²	n/cm ² -yr
Bremsstrahlung energy flux at the first wall	71.62	J/cm ² -pulse
Total power density in Al ₂ O ₃ ^c	1652.2	J/cm ³ -pulse
Total power density in Nb ^d	493.4	J/cm ³ -pulse
Burnup/pulse	4.8	%
Breeding ratio	1.11	
Ratio thermal power to recirculating power	15.6 (13.6) ^e	
Gross thermal output	3,600.	MWt
Thermal conversion efficiency	40. (56.4)	%
Recirculating power fraction	0.16 (0.13)	
Gross electrical output	1,440. (2030.)	MWe
Net electrical output	1,210. (1770.)	MWe

^aBased on a sodium/steam power conversion system. Plant characteristics for a power conversion system which uses a potassium topping cycle are summarized in Ref. 1. Flux, fluence, and energy values are evaluated at the first wall.

^bThe duty cycle is limited to a lower value of 3.0 sec by first-wall heat transfer and fuel/ash pumpout time constants.

^c86.6% bremsstrahlung, 3.9% gamma, 9.5% neutron.

^d58.0% bremsstrahlung, 37.2% gamma, 4.8% neutron.

^eNumerical values in parentheses refer to a power conversion system which uses a high-temperature potassium topping cycle.

TABLE VIII-2

SUMMARY OF FIRST-WALL RESPONSES TO RTPR POWER CYCLE

(Burn Time ~ 0.080 sec, Plasma Cooling Time ~ 1.0 sec, Duty Cycle ~ 10.0 sec)

				<u>Stresses induced in</u>	
Fusion neutron (14.1-MeV) current	8.91×10^{14}	n/cm ² /pulse		<u>Insulator</u> (Al ₂ O ₃)	
Total neutron flux	9.03×10^{15}	n/cm ² /pulse		isothermal (300-800 K)	-2.57×10^{8a} Pa
Bremsstrahlung flux (0.5-1.0 Å)	71.62	J/cm ² /pulse		during burn	-2.00×10^8 Pa
				during plasma cooling	-1.20×10^8 Pa
<u>Average energy density in</u>					
<u>Insulator</u>			<u>Metal</u> (Nb)		
neutron	156.3	J/cm ³ /pulse		isothermal (300-800 K)	0.80×10^{8a} Pa
gamma	63.5	J/cm ³ /pulse		during burn	0.80×10^8 Pa
bremsstrahlung	1432.4	J/cm ³ /pulse		during plasma cooling	0.60×10^8 Pa
total	1652.2	J/cm ³ /pulse		pumping differential	0.20×10^8 Pa
<u>Metal</u>			<u>Rate of</u>		
neutron	23.6	J/cm ³ /pulse		Average atom displacement	
gamma	183.4	J/cm ³ /pulse		Al ₂ O ₃	$\sim 30^b$ dpa/yr
bremsstrahlung	286.4	J/cm ³ /pulse		Nb	36 dpa/yr
total	493.4	J/cm ³ /pulse		Average helium production	
<u>Temperature transients in</u>				Al ₂ O ₃	1685 ppm/yr
<u>Insulator</u>		<u>Inside</u>	<u>Outside</u>	Nb (maximum)	59 ppm/yr
during burn		310	250	Hydrogen production	
during plasma cooling		75	60	Al ₂ O ₃	975 ppm/yr
total		385	310	Nb	204 ppm/yr
average		350		Neutron transmutation	
<u>Metal</u>				Al ₂ O ₃	1413 0 ppm/yr
during burn		250	220		862 Al ppm/yr
during plasma cooling		40	30	Nb	2900 ppm/yr
total		290	250		
average		270			

TABLE VIII-2 (CONTINUED)

SUMMARY OF FIRST-WALL RESPONSES TO RTPR POWER CYCLE

<u>Product</u>	<u>Production (ppm/yr)</u>	
H	975	<u>Summary of Impurity Generation Rate in Al₂O₃</u>
He	1,685	
C	1,340	0[(n,γ), (n,p), (n,d), (n,α), (n,n'p), (n,n'α)]
N	66	product → 4,967 ppm/yr
Na	9	Al[(n,γ), (n,p), (n,d), (n,t), (n,α), (n,n'p), (n,n'α)]
Mg	830	product → 4,883 ppm/yr
Si	23	

^aThese stresses arise because of the analytic assumption that the composite structure is stress-free at room temperature. In view of current techniques used to apply ceramic layers to metal backings, the stress-free (or reference) state will be closer to RTPR operating temperatures, and the stresses listed above for the 300-800 K transition are expected to be near zero.

^bEstimated by extrapolation of neutron spectral results calculated for other materials.

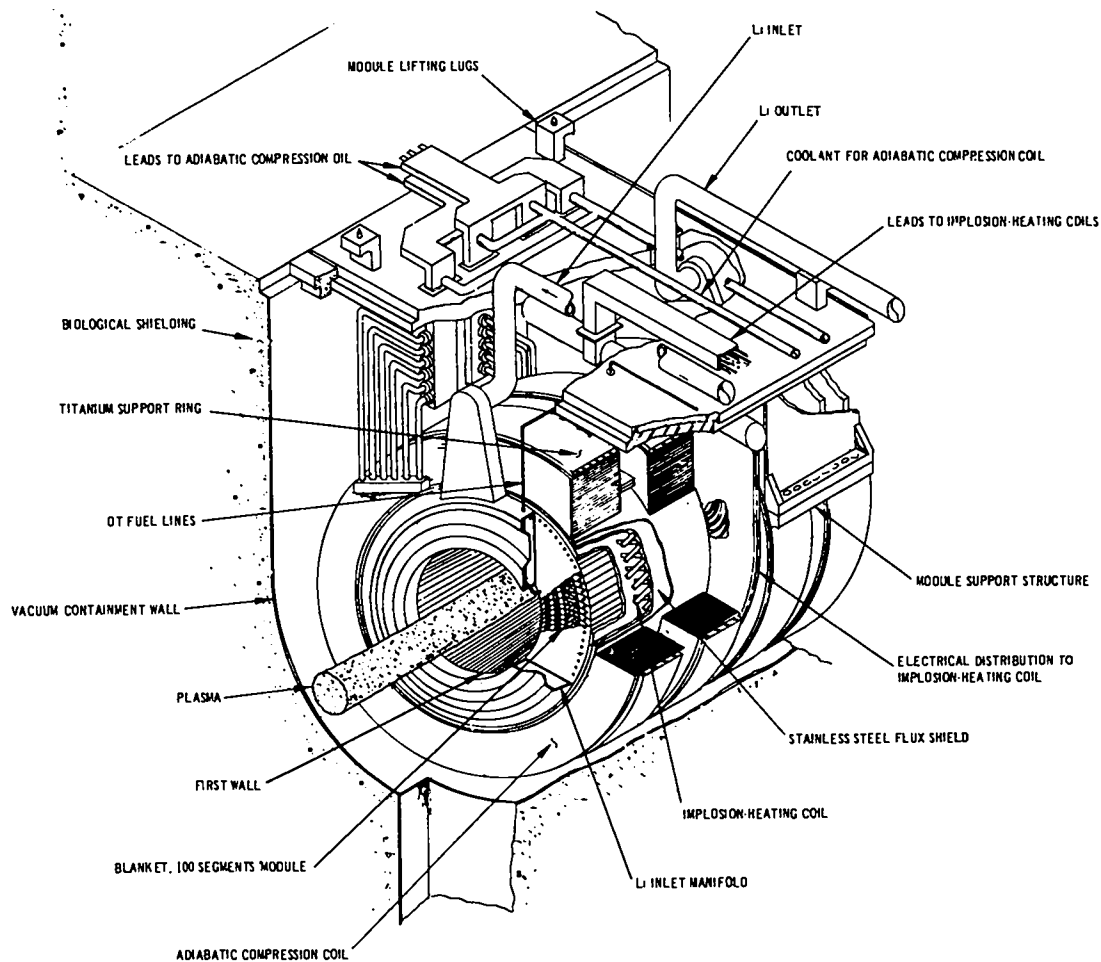


Figure VIII-5
Cutaway view of RTPR module. 176 such modules form the 112-m-diameter torus. First-wall diameter is 1.0-m.

C. THETA-PINCH REACTOR NEUTRONIC STUDIES
(D. J. Dudziak, T-1)

Several modifications of the original Reference Theta-Pinch Reactor^{7,8} (RTPR) design were studied from a neutronics viewpoint. Included were substitution of molybdenum for niobium (RTPR,MOD6)* and variations in the thickness of the Li-Be and and graphite regions (MOD7 and MOD8).

* "MOD" numbers refer to specific details of the neutronic model used for the RTPR neutronic analysis and generally refer to small variations of materials distribution in space and kind.

Results show that simple substitution of molybdenum for niobium throughout the reactor will decrease the tritium breeding (~5%) principally because of increased parasitic capture by structure in the graphite region. It can be inferred from the calculations, however, that substituting molybdenum in only the first wall would increase breeding approximately 3%. The latter effect is due to increased (n,2n) and decreased parasitic absorption reaction rates in molybdenum versus niobium for the hard neutron spectrum at the first wall. Table VIII-3 summarizes some of the reaction rates in the two cases. All

breeding ratios given do not account for resonance self-shielding, which will result in increases by ~5%.

Tritium breeding is also sensitive to the amount of beryllium which is located in the hard neutron spectrum just outward of the first wall. A roughly linear increase in breeding occurs as the Li-Be region is extended outward at the expense of the graphite region, at least up to 40 mm. Table VIII-4 shows that within a wide range the breeding ratio is easily adjustable without altering the total blanket thickness. However, a slight penalty is paid for increased breeding because the neutron leakage to the compression coil also increases, aggravating the radiation damage and nuclear heating problems. Such damage and heating could, if necessary, be alleviated by extending the blanket radius.

Energy deposition in various RTPR blanket modifications was evaluated in detail. Of particular interest is the recoverable, high-grade energy per neutron. Table VIII-5 summarizes the component and total energy depositions at a 3.5 MW/m² wall loading of 14.06-MeV neutrons. Gamma transport calculations were performed only for MOD4 and MOD8.*

A major difference in computed neutron energy deposition occurs, depending upon the kerma factors chosen. Most neutronics studies to date have used the ORNL set of kermas,⁹ so for comparison purposes among CTR reactor concepts those values in Table VIII-5 are most appropriate. However, recent calculations by Abdou and Maynard,¹⁰ using ENDF-III data, have provided generally much lower kerma values. Because all transport and photon production calculations (with minor exceptions) performed at LASL used the ENDF-III data, the Ref. 10 values in Table VIII-5 should be most

*MOD4 is the same as the RTPR MOD1 of Ref. 7, except with 10 v/o lithium in the graphite region. MOD7 and MOD8 are the same as MOD4, except for the region thickness variations noted above.

consistent. The reference set of neutron kermas used in these calculations was composed mostly of the ORNL values⁹ supplemented by Abdou's values¹⁰ for materials not included in the ORNL compilation (viz., O, Al, and Ti). From Table VIII-4 it is apparent that increasing the Li-Be region thickness not only enhances the recoverable energy but the breeding as well.

Since all neutron transport calculations for this RTPR design were normalized to 3.5 MW/m², it is interesting to compare the rates of displaced atoms, between niobium and molybdenum first walls. The respective values in the first wall for niobium and molybdenum are virtually the same: 59.0 dpa/y and 61.2 dpa/y, respectively.

1. Reference Theta-Pinch Reactor (RTPR) Engineering Design Nucleonic Studies

A comprehensive nucleonic analysis has also been performed for the more recent RTPR engineering design study.¹ For convenience this engineering design study is designated RTPR MARK II to differentiate the neutronic model from the original RTPR. Characteristics analyzed included neutron and gamma-ray flux distributions, tritium breeding ratio, nuclear energy deposition, displacements per atom, transmutation, activation, and other reaction rates. These studies employed a new calculational model including 36 discrete regions from the plasma to the titanium support, thus giving more detailed reaction rate distributions and more accurate integral parameters. Otherwise the calculational procedure was the same as that discussed previously, (one-dimensional discrete-ordinates calculations using the DTF-IV code in an S₄-P₃ mode, and 100-group cross sections).

Tritium breeding ratio for the reference engineering design¹ was computed to be 1.11 after accounting for resonance self-shielding; this breeding ratio corresponds to a tritium inventory doubling time of 36 days. Variations on the reference design were made to explore the

TABLE VIII-3
RTPR MOD6 vs MOD4
(Mo vs Nb structure)

<u>Reaction</u>	<u>MOD6 Mo</u>	<u>MOD4 Nb</u>	<u>MOD6- MOD4 Mo-Nb</u>	<u>MOD6/ MOD4 Mo/Nb</u>
1. (n,2n) in first wall (Region 4)	0.0638043	0.0481011	0.01570	1.326
2. Parasitic absorption in first wall (Region 4)	0.0463598	0.0587085	-0.01235	0.7897
3. Net absorption (2-1) in first wall	-0.017445	0.010674	-0.028119	
4. (n,2n) total in Mo(Nb)	0.119057	0.0884778	0.030579	1.346
5. Parasitic absorption total in Mo(Nb)	0.323921	0.242936	0.080985	1.333
6. Net absorption (5-4)	0.204864	0.154458	0.050406	1.326
7. Parasitic absorption in Mo(Nb) in graphite (Region 6)	0.167115	0.084766	0.082349	1.971
8. Parasitic absorption in Mo(Nb) in Li-Be (Region 7)	0.105658	0.093518	0.01214	1.130
9. Parasitic absorption in enriched Li (Region 8)	0.0045031	0.0055446	-0.001042	0.812
<u>MOD6 net breeding ratio:*</u>			<u>1.0196</u>	
<u>MOD4 net breeding ratio:*</u>			<u>1.0714</u>	

*Not accounting for resonance self-shielding.

TABLE VIII-4
EFFECT OF INCREASED THICKNESS OF Li-Be REGION

	<u>MOD4</u>	<u>MOD7</u>	<u>MOD8</u>
Li-Be region thickness (mm)	96	116	136
Graphite region thickness* (mm)	220	200	180
Tritium breeding ratio†	1.071	1.125	1.172
Neutron flux with energies >1 MeV, at compression coil (n/cm ² -sec)	1.80 x 10 ¹³	1.94 x 10 ¹³	2.08 x 10 ¹³
Neutron energy deposition in compression coil (MW m ⁻¹)	0.121	0.129	0.138

*Graphite outer radius constant--620 mm.
†Not accounting for resonance self-shielding.

TABLE VIII-5

RTPR ENERGY DEPOSITION (3.5 MW/m²)

Regions	Neutron									
	MOD1				MOD4				Gamma - MOD4	
	ORNL Kerma		Abdou Kerma		ORNL Kerma		Abdou Kerma		Gamma - MOD4	
	(MW/m)	(%)	(MW/m)	(%)	(MW/m)	(%)	(MW/m)	(%)	(MW/m)	(%)
Electric insulation → ⁶ Li (recoverable)	6.946	98.2	5.952	97.8	7.025	98.0	5.835	97.4	2.079	71.3
Thermal insulation → mop-up (waste)	0.130	1.8	0.135	2.2	0.147	2.0	0.154	2.6	0.837	28.7
Total	7.076		6.087		7.172		5.989		2.916	

RECOVERABLE ENERGY DEPOSITED PER NEUTRON FROM PLASMA

	MOD1		MOD4		MOD6	MOD7	MOD8
	ORNL	Abdou	ORNL	Abdou	ORNL Eclectic	ORNL Eclectic	ORNL Eclectic
	(MeV/n)	(MeV/n)	(MeV/n)	(MeV/n)	(MeV/n)	(MeV/n)	(MeV/n)
Neutron	14.80	12.68	14.97	12.43	14.80	15.67	16.26
Gamma	4.43*	4.43*	4.43	4.43	4.43*	4.43*	4.56
Total	19.23	17.11	19.40	16.86	19.23	20.10	20.82

* MOD4 gamma values in this case.

sensitivity of breeding ratio to thickness of the beryllium multiplier. Other changes in region thickness included the thinning of the second graphite region and corresponding thickening of the enriched ^6Li region. Within the constraints of constant blanket thickness and unchanged blanket materials, the breeding ratio was easily adjusted between values of 1.08 and 1.19. As summarized in Table VIII-6, the beryllium thickness is the principal determinant of breeding ratio. In a test calculation to ascertain if large margins for breeding were available without modifying total blanket thickness (and hence magnetic volume), the first graphite region was replaced with beryllium. The resulting 1.37 breeding ratio indicates that possible future increases in neutron leakage or structural parasitic absorption can be compensated by increased beryllium multiplier. Doubling times given in Table VIII-6 are for a blanket tritium inventory of 95.9 g, external tritium inventory of 5.86 kg, and tritium consumption of 1.5 kg per day.

Detailed results for the new calculational model were reported in the joint ANL-LASL engineering design study¹ of an RTPR. No major changes in energy deposition, displaced atom rates, or transmutation were observed, as compared to the old 0.50-m radius homogenized model discussed previously. In addition niobium activation rates were provided to ANL for estimation of coolant activities. Activation rates for 63 impurities in niobium and lithium have also been computed, but the results remain to be analyzed.

A bulk biological shield design for the RTPR MARK II was performed in cooperation with ANL. Using the blanket neutron fluxes as boundary "sources," ANL computed neutron transmission through 2 meters of ordinary concrete. The blanket gamma-ray sources were used for a similar gamma-ray transmission calculation; gamma-ray doses represent ~99% of the total dose outside

the shield. Details of the calculation were presented in a joint ANL-LASL paper.¹¹

Details of radiation damage rates, transmutation, and nuclear heating can be found in the joint ANL/LASL design report.¹ These reaction rates were calculated for a reference neutron wall loading of 2.0 MW/m^2 corresponding to a 10-second cycle time. Figure VIII-6 shows a composite neutron and gamma-ray energy deposition distribution for the RTPR blanket and magnetic coils at the reference 2.0 MW/m^2 . Neutron flux spatial distributions over the same regions are shown in Figure VIII-7 for three neutron energy ranges. These flux distributions were subsequently used to calculate afterheat and radioactive inventories, which are discussed as a subsequent section (Sec. V-G) on the environmental aspects of the RTPR.

2. RTPR Blanket Sensitivity Studies

A set of blanket calculations was performed to determine the sensitivity of important reaction rates to the multigroup

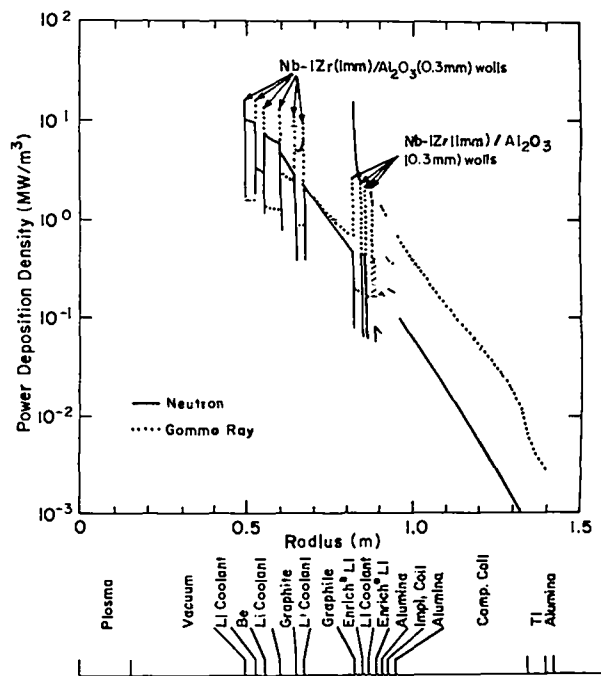


Figure VIII-6
Gamma-ray and neutron power distribution in RTPR blanket.

TABLE VIII-6

RTPR MARK II BREEDING STUDY

Region (No.)	Thickness (mm)				
	MOD0	MOD1	MOD2	MOD3	MOD4
Lithium Coolant (5)	30	25	25	30	30
Be (7)	25	30	35	20	20
Lithium Coolant (9)	45	45	40	50	50
Second Graphite (21)	150	140	135	135	150
Enriched ^6Li (25)	24	34	39	39	24
Lithium Coolant (27)	10	03	03	03	10
Enriched ^6Li (29)	24	31	31	31	24

MOD	Breeding Ratio*	Doubling Time† (Days)
4	1.08	49
3	1.09	44
0	1.11	36
1	1.15	26
2	1.19	21

* Including 0.07 for resonance self-shielding.

† After including resonance self-shielding.

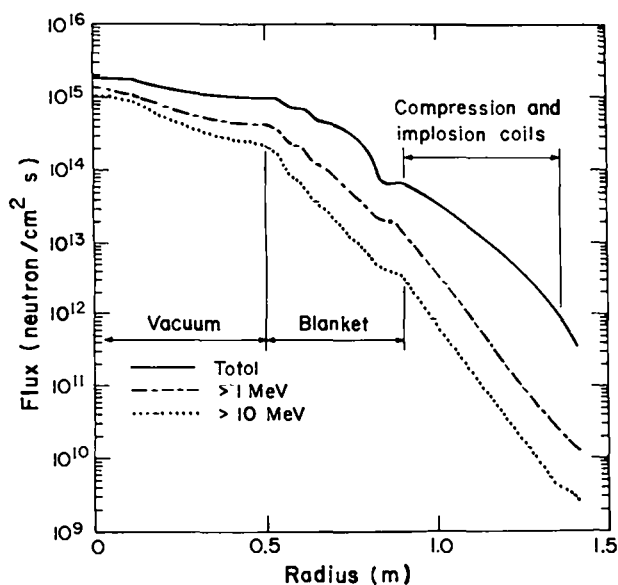


Figure VIII-7
Spatial variation of neutron flux in RTPR blanket.

treatment of the $\text{Be}(n,2n)$ secondary distributions. The secondary energy-angle distributions are approximated differently by various cross-section multigroup codes. A corrected treatment of the P_0 - P_3 scattering matrices using a newly developed LASL processor code yields a 6% decrease in tritium breeding and an 11% decrease in total recoverable energy, both of which are significant. Further study is being done to verify these preliminary results.

3. Linear Theta-Pinch Neutronics

Neutron transport and energy deposition calculations were completed for a linear theta-pinch conceptual reactor design. The reactor was assumed to have a 0.1-m radius bore and a 0.11-m-thick compression coil (Cu-0.5 w/o Be). Cooling of the coil, which operates at 800 K, was provided by 10 v/o ^7Li , and 20 v/o of the coil is assumed to be Al_2O_3 insulator.

The coil was surrounded by a 0.79-m-thick region of ${}^7\text{Li}$ at 1100 K, which proved inadequate for tritium breeding because of high-neutron leakage rates. A more realistic blanket would incorporate a moderator and/or greater thickness so adequate breeding may be achievable. Because the coil is inward of the breeding region of the blanket, joule losses should be insensitive to the blanket region thickness. An average plasma radius of 0.02 m was used, assuming an isotropic source per pulse of 6.81×10^{18} neutrons per meter of length in the plasma. This corresponds to ~ 24.4 MJ/m² wall loading of 14.06-MeV neutrons. Assuming 18.9-MeV energy release per plasma neutron one calculates MJ/m² or 20.6 MJ/m, at least half of which is estimated to be deposited in the magnetic coil. Although the copper parasitically absorbs $\sim 24\%$ of the plasma neutrons, the compression coil is a net positive contributor to neutron balance, because $\sim 26\%$ of the plasma neutrons undergo (n,2n) reactions in copper. However, tritium breeding is adversely affected because

the (n,2n) neutrons from copper are generally below the ${}^7\text{Li}(n,n'\alpha)\text{T}$ threshold. Rapid transmutation of the copper into Ni, Zn, and Co will occur from radiative capture, (n,2n), and (n,x) reactions, and is shown in Table VIII-7; a cycle time of 10 seconds was assumed for Table VIII-7. Neutron heating rate spatial distributions have been computed for the linear reactor; gamma-ray transport and heating calculations remain to be done. Radiation damage rates of ~ 50 dpa/y would be expected in the coil if pulsed once every 10 seconds.

4. CTR Irradiation Facility at LAMPF¹²

Monte Carlo calculations for a temporary graphite beam stop experiment are being performed in cooperation with LASL groups CMB-8 and P-11. The resulting neutron flux spectrum will then be compared to one unfolded from foil activation by group CNC-11. High-energy neutron production and transport are being computed with an intranuclear cascade code,¹³ followed by low-energy ($E \leq 20$ MeV) neutron transport using the MCN Monte Carlo¹⁴ code.

TABLE VIII-7

LINEAR θ -PINCH
Cu* TRANSMUTATION FOR A 10-SECOND CYCLE
 INNER SURFACE OF COPPER COIL (0.1025m)

<u>Reaction</u>	<u>ppm/y Ni(+Co)</u>	<u>ppm/y Zn</u>
${}^{63}\text{Cu}(n,\alpha)$	2.37 + 2 (${}^{60}\text{Co}, 5.272\text{y}$)	
${}^{63}\text{Cu}(n,2n)$	3.01 + 3	
${}^{63}\text{Cu}(n,p)$	7.57 + 2	
${}^{63}\text{Cu}(n,\gamma)$	6.25 + 2	6.25 + 2
${}^{65}\text{Cu}(n,\alpha)$	2.37 + 2	
${}^{65}\text{Cu}(n,2n)$	2.94 + 3	2.94 + 3
${}^{65}\text{Cu}(n',p)$	(β^- decays back to ${}^{65}\text{Cu}$ in 2.52 h)	
${}^{65}\text{Cu}(n,\gamma)$		5.65 + 2

 * Isotopic Abundances: ${}^{63}\text{Cu}$ - 0.691
 ${}^{65}\text{Cu}$ - 0.309

A cooperative dosimetry program was discussed in detail with CTR Dosimetry Center (ANL) personnel who are participating in the foil activation analyses. The purpose of the comparison exercise is to verify the Monte Carlo calculations. Calculations will then be performed for the regular copper beam stop to predict flux intensities and spectra at the Irradiation Facility. Additional, one-dimensional S_n calculations are in process to assess the effectiveness of a nickel reflector in enhancing the flux intensity. If found to be effective, a nickel lining will be placed on the irradiation cavity walls in proximity to the irradiation experiments.

Dosimetry planning for LAMPF has continued on a minimal, intermittent basis. Discussions were held with participants at a recent LAMPF applications conference regarding two subject areas: (a) measurement of high-energy neutron fluxes by double scattering and time-of-flight; (b) theoretical modeling and computation of recoil ion transport and interactions in materials. A multigroup Monte Carlo transport code has been activated and modified for LAMPF beam stop neutron flux calculations. The code has been tested on a benchmark calculation and was found to be inadequate for P_3 calculations.

5. Development of Monte Carlo Capability

The CTR blanket benchmark is being used to debug a multigroup Monte Carlo neutronics code. Calculations were being performed with uncorrected P_0 cross sections and will be repeated with transport-corrected P_0 and P_0 - P_3 cross sections for comparison. The benchmark is being used to gain confidence in the code and its suitability for LAMPF beam stop neutron transport calculations, as well as future RTPR studies. Capability will then exist to perform neutron streaming calculations in the RTPR coolant pipe channels and shield ducts. Identical cross-section sets are being used in the Monte Carlo and discrete-ordinates calculations.

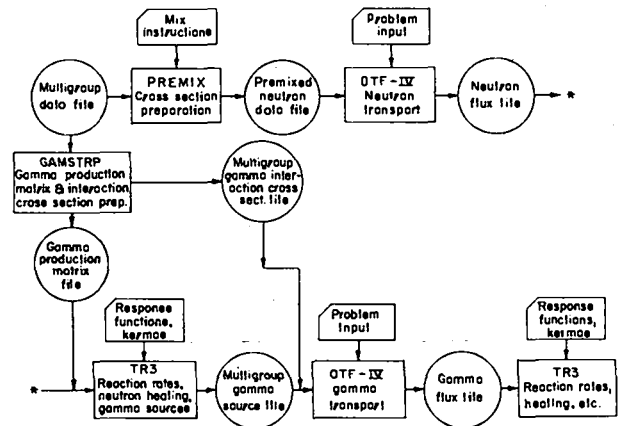


Figure VIII-8
CTR nuclear analysis computational system.

6. CTR Nuclear Analysis Code System (D. J. Dudziak, F. Brinkley, and P. Rood)

Progress has been made toward development of a systematic calculational scheme applied to CTR nuclear analysis. The current system is shown schematically in Figure VIII-8. PREMIX is a code written to premix region materials for DTF-IV, thereby conserving storage during its execution. GAMSTRP is a minor service code to strip selected records from a master data file containing multigroup neutron interaction, photon production, and photon interaction data sets. Another minor code not shown in Figure VIII-8 is TODTF, which prepares response functions and kerma factors in DTF input format. The principal development has been the TR3 code. This code is essentially a DTF-editing post-processor that computes quantities of interest for CTR neutronic analyses. Such quantities are renormalized fluxes, fluxes summed over selected groups, integral fluxes, differential fluxes in energy, radiation damage (displacements per atom and helium production), activation of blanket materials, spatial distribution of nuclear heating, integral heating by region, and gamma source spatial-spectral distribution. Most of these quantities are also plotted on film and the gamma sources are prepared on an input file for DTF-IV.

In the process of performing radioactivity and afterheat calculations, two new versions of TR3 were developed, denoted TR3A(Nb) and TR3A(V). Continuing minor improvements are also being made to the code. Currently TR3 is linked to DTF-IV, but modifications are planned to create multigroup Monte Carlo flux output in a compatible format. Improvements in TR3 have been mainly providing optional plot capabilities (e.g., grid lines or tick marks), improved plot scales, and minor output format changes to increase clarity. Also, a spin-off code (TR3G) has been provided specifically for postprocessing of gamma-ray fluxes. All system codes are now in the LASL file manager called UPDATE. Future plans for TR3 include incorporation of a sensitivity module, which will be an adaptation of an existing LASL code.

7. 14-MeV Intense Neutron Source Design Support (D. J. Dudziak)

Assistance was provided on the proposal for an intense 14-MeV neutron source. In particular, a section of the proposal on "Scientific Justification of Need" was written to describe the facility's usefulness in blanket neutronic studies; i.e., benchmarks and (at a later stage) engineering mockups. Also, one-dimensional transport calculations (DTF-IV) were performed for a spherical mockup of the RTPR to estimate the reflected flux enhancement to be expected at such a facility. Normalized to a unit source, the values $\phi(E = 14 \text{ MeV})$, $\phi(E > 1 \text{ MeV})$, and $\phi(E > 0)$ relative to the 14-MeV current at a 149-mm-radius alumina first wall were: 1.14, 2.04, and 3.79, respectively. By comparison, the corresponding relative and absolute values for the cylindrical-geometry original RTPR at 3.5 MW/m² (14-MeV current of 1.56×10^{14} n/cm²/s) are, respectively: 1.97, 4.22, and 9.10.

D. NUCLEAR DATA PROGRAM (D. W. Muir, L. Stewart, R. J. LaBauve, G. M. Hale, and D. R. Harris, T-2)

The effort to provide reliable nuclear data for the LASL fusion program concentrated during 1973 on the expansion of the LASL/CTR multigroup library and the improvement of the national ENDF/B evaluated files for CTR applications.

1. The LASL/CTR Multigroup Library

Neutron and photon interaction data must be processed into the group-averaged form required by the discrete ordinates code used in the design of fusion reactors. The LASL/CTR library of processed data has been expanded this year to include new data for fluorine and molybdenum and modified data for beryllium. A new section of multigroup neutron effects cross sections was added for the evaluation of material damage, radiological hazards, and decay afterheat; 75 different reaction cross sections are now found in this section.

The LASL/CTR library now contains nearly half a million data entries and this number is expected to double during the next calendar year. To validate its contents, a national fusion blanket benchmark was analyzed in considerable detail.¹⁵ Comparison with other results led to the revision of the Nb(n, γ) cross sections in the LASL library. To provide rapid visual checks of the data, a short computer code was written which displays various sections of the library in histogram form.

In averaging neutron cross sections over broad energy groups, it is important to use the proper weighting function, namely the energy spectrum of neutrons which fall in that group. This is especially true for threshold reactions in the vicinity of the 14-MeV fusion peak. For this reason, the detailed shape of the fusion peak was reviewed¹⁶ and numerical examples constructed to examine the sensitivity of certain cross sections to the thermal broadening of the 14-MeV peak.

2. Neutron Cross-Section Evaluated Files

Reevaluation and review of nuclear data for CTR applications continue to be important activities due to known deficiencies in the available evaluated files such as ENDF/B (the national evaluated data file). The newly organized CTR Subcommittee of the U. S. Nuclear Data Committee has become a forum for identifying these deficiencies and, in an effort to correct them, this Subcommittee has recommended that critical reviews be prepared by the evaluators for certain CTR materials available on ENDF/B. The LASL materials are: hydrogen, lithium (both stable isotopes), nitrogen, oxygen, and aluminum. These reviews are intended to serve as a guide to the Subcommittee for recommendations of future efforts in the measurements and evaluation programs of interest to CTR. Major deficiencies are already identified in the ${}^7\text{Li}$ evaluation, so a reevaluation of this material is planned at LASL in fiscal 1975.

In addition to deficiencies in the basic evaluated data, the ENDF/B formats are not completely adequate for all CTR applications. For example, the problems of adequately describing prompt and delayed neutron heating (kerma), transmutation, and activation processes are yet to be solved. The process of prompt neutron heating was discussed at a Seminar at the Radiation Shielding Information Center.¹⁷ It was pointed out that the use of energy-balance techniques can reduce considerably the amount of new evaluated data required for multigroup prompt heating calculations. To implement this approach, however, new formats for energy-dependent nuclear Q-values and minor modifications in the multigroup processing codes would be required.

3. Other Activities

Intensity-limited 14-MeV neutron cross-section measurements were reviewed and specific experiments suggested for the proposed Los Alamos Intense Neutron Source

(INS). Although primarily a radiation damage facility, this project will provide a unique capability for the production of long-lived (10^2 - 10^6 years) activities and the measurement of (n, α) cross sections as small as 1 mb.

In connection with laser fusion concepts and other engineering applications, the ${}^{11}\text{B}(p,\alpha){}^8\text{Be}$ cross section has been evaluated using R-matrix theory.* These results show that, for plasma energies above ~ 150 keV, the reaction rate $\langle\sigma v\rangle$ is similar in magnitude to the D-T and D- ${}^3\text{He}$ fusion reaction rates and actually exceeds the D-D rate.

E. ELECTRICAL INSULATOR RESEARCH (J. M. Bunch, F. W. Clinard, Jr., CMB-5)

During 1973 a number of experimental studies were carried out or initiated on electrical insulators for the Reference Theta-Pinch Reactor (RTPR). Additional efforts were initiated at midyear to evaluate insulators and bonded insulator/metal composites for possible use at the first wall of the Fusion Test Reactor (FTR).

1. DC and Pulsed-Voltage Dielectric Strength of Insulators

The insulating liner of the RTPR first wall should have the highest bulk dielectric strength possible, so that a thin layer can be used and heat transfer problems minimized. This insulator will be subjected to high-temperature (~ 1100 K), pulsed-voltage application. Both theoretical and experimental reasons¹⁸ exist to expect higher dielectric strength in the pulsed mode than in the DC mode for most materials at elevated temperatures. The primary goal of this study is to evaluate, understand, and exploit dielectric strength enhancement under pulsed-voltage conditions for RTPR applications.

*This work supported by other agencies.

The plasma chamber of the FTR will probably be made of insulator-coated metal segments arranged so that their inner edges form the first wall. This insulator must withstand a pulsed voltage similar to that anticipated for the RTPR at room temperature or at a suitable degassing temperature (~ 400 K). An additional goal of this study is to identify insulators which exhibit an adequate dielectric strength and that can be satisfactorily bonded to the metal substrate which serves as the FTR first wall.

The electrical behavior of high-density, high-purity, polycrystalline Al_2O_3 has been investigated over a range of temperatures. A number of other materials for FTR applications have also been tested: sintered AlN , Si_3N_4 , Si_2ON_2 , and Y_2O_3 ; plasma-sprayed Y_2O_3 and Al_2O_3 and bonded Si_3N_4 . The latter material appeared to be a conductor and will not be discussed further.

The apparatus used to determine voltage breakdown characteristics consists of a furnace and sample holder inside a pressure vessel containing N_2 at pressures up to 3 MPa. The N_2 serves as an electrical insulating medium for the suppression of corona and surface flash-over. The sample (a disk 25 mm in diameter and 0.25 to 0.5 mm thick) rests on a cylindrical Ni pedestal ~ 10 mm in diameter. The sample is contacted at the center of its upper side by a roughly spherical Ni contact of radius ~ 5 mm, to which the test voltage is applied. In most cases contact has been made directly to the bare samples, but in a few instances, metallic surface coatings have been evaporated onto the samples over small areas under the Ni contacts, thus providing a more intimate and well-controlled contact and giving some control over field uniformity within the sample.

DC measurements are made by gradually increasing a DC voltage applied to samples in the apparatus just described, until breakdown occurs. In pulsed studies the

test voltage is supplied by a 0.25- μF capacitor charged to a selected voltage, in series with a 5000-ohm resistor (to limit breakdown current), a triggered switch tube, and the sample electrodes. When the tube is triggered, the sample voltage rises to the preset value in $\sim 10^{-6}$ sec, then decays with a time constant of ~ 1 sec. An oscilloscope connected across the sample is triggered shortly before the switch tube, and is used to measure the time to breakdown by observation of the sharp drop in sample voltage when breakdown occurs. Test pulses are applied repeatedly to a given sample starting at a low voltage and increasing the voltage by steps until breakdown occurs.

Theory¹⁹ predicts that for "impulse thermal" breakdown, which occurs when the voltage pulse duration is short compared to the characteristic sample thermal diffusion time, the time to breakdown τ should vary in proportion to $(T_1^2 \rho_0)/(bE^2)$, where E is the constant applied field, T_1 the initial sample temperature, and the sample resistivity is assumed to vary with temperature according to the relation $\rho = \rho_0 e^{-b/T}$. The field is approximately constant in these experiments for times much shorter than 1-sec, and therefore the latter expression is valid. Under these conditions a unique breakdown strength can be defined only when a pulse length is specified. The technique used here is designed to measure this relation in terms of time-to-breakdown vs applied field. For longer times the breakdown field approaches a (generally lower) "dc" value. For shorter times the breakdown field should approach an "intrinsic" value, which depends on the details of the electronic collision processes in the crystal lattice, and which in general would be expected to increase with sample temperature, (in contrast to the "thermal" breakdown field). For times short compared to the electron collision mean-free-time, the breakdown

enters another regime where the breakdown voltage may be further enhanced over the "intrinsic" value.

Enhancement of high-temperature breakdown strength for short times was observed for high-purity, high-density polycrystalline Al_2O_3 samples, but the time to breakdown varied more rapidly with voltage than expected. As a result, a more-or-less unique "pulse" breakdown value can be specified, nearly independent of time, and this value compared to the dc value at the same temperature. These data are shown in Figure VIII-9 along with room-temperature values obtained from the manufacturer's literature. Higher dielectric strengths and an apparent increase in breakdown strength with temperature are observed for the thinner samples.

Field nonuniformity resulting from the nature of the contact geometry may be partly responsible for the scatter and the departure from predicted delay-time dependence. However, the latter also may be explained by a different delay mechanism, such as ionic polarization, which appears to satisfactorily fit data for NaCl.¹⁸ Also, some scatter in pulsed voltage dielectric strength is predicted theoretically.¹⁹

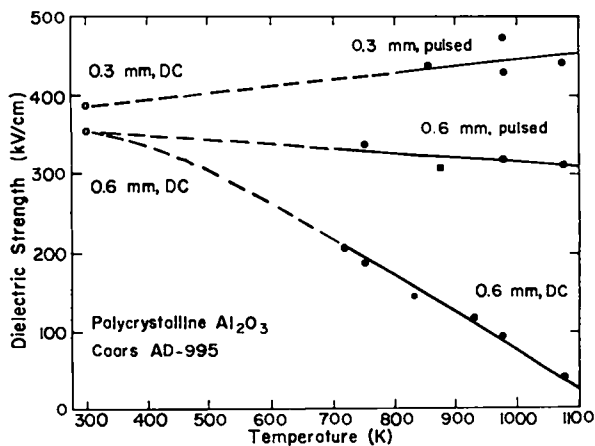


Figure VIII-9
DC and pulsed dielectric strength of alumina.

The effects of improving field uniformity by using evaporated chromium contacts with diffuse edges on high-purity, high-density Al_2O_3 samples are being investigated. For the samples investigated to date, an increase in breakdown strength of as much as 50% over the data presented in Figure VIII-9 has been observed. However, more work needs to be done in developing evaporated contacts which are chemically stable at the higher test temperatures.

The LASL Materials Technology Group has fabricated a number of sintered ceramics and plasma-sprayed ceramic/metal samples for evaluation as possible FTR first-wall materials. Dielectric strength data for these materials and other samples obtained from outside sources, all of which are suspected to contain considerable porosity, are presented in Table VIII-8. Although the results obtained thus far are preliminary, two facts appear obvious. Firstly, little difference is usually observed between pulsed and D.C. dielectric strengths for a given material at a given temperature. This behavior could be explained if breakdown initiated within pores in the samples by processes which occurred quickly compared to the bulk mechanism. Secondly, the breakdown strength of all the materials, including plasma-sprayed Al_2O_3 , is low compared to that for the high-density Al_2O_3 . This behavior is also explicable in terms of sample porosity; it has been shown theoretically and experimentally²⁰ that breakdown strength decreases dramatically with even modest sample porosity. Tests are currently under way to evaluate porosity in the samples tested to date.

Although a dielectric strength requirement has not yet been specified for FTR, a reasonable value is 10 kV/mm. Results obtained to date suggest that conventional plasma-sprayed insulators may be able to meet such a requirement at room temperature with a reasonable factor of

TABLE VIII-8

DIELECTRIC STRENGTHS OF INSULATOR/METAL AND INSULATOR SAMPLES

Materials*	Temperature, K	Dielectric Strength, kV/cm		Remarks
		dc	Pulsed	
Plasma-Sprayed Insulator/Metal Samples				
Al ₂ O ₃ /Inconel	293	303	---	LASL - fabricated
	873	130	---	LASL - fabricated
	873	---	~ 200	Plasmadyne - fabricated, 0.5-mm-thick Al ₂ O ₃ , purported to be of fairly high density
Al ₂ O ₃ /SS	873	91	91	LASL - fabricated
Y ₂ O ₃ /SS	293	252	---	LASL - fabricated
Insulator Samples				
AlN	873	118	---	MRC - fabricated, hot pressed
Si ₃ N ₄	873	118	157	MRC - fabricated, hot pressed
Si ₂ ON ₂	873	20	98	Norton - fabricated, hot pressed
Y ₂ O ₃ - 10% ThO ₂	293	224	---	LASL - fabricated, hot pressed
Y ₂ O ₃	293	244	---	LASL - fabricated,
	873	---	98	slip-cast and sintered

*Metal substrate thicknesses ~ 1 mm; insulator thicknesses ~ 0.3 mm, unless otherwise specified.

safety. It is also possible that considerable enhancement of dielectric strength can be expected if plasma-spraying techniques which minimize porosity are employed. However, results described here may not be directly related to a fusion reactor first-wall application for the following reasons: (a) breakdown in a reactor would presumably be influenced by the plasma; (b) the time dependence of the applied pulse will undoubtedly differ from that used for these studies, and (c) the much larger area of the first wall compared to our samples could lead to a large degradation in effective (statistical) breakdown strength. The last uncertainty can be resolved by proof-testing of large components, while the first two can be addressed by

testing first wall segments in an FTR environment.

2. 14-MeV Neutron Damage in Single Crystal Al₂O₃

The nature of 14-MeV neutron radiation damage to insulators has received little study because interest in this area is quite recent and because no intense sources of 14-MeV neutrons as yet exist. Experiments have been initiated in this area for two reasons: (a) to evaluate 14-MeV neutron damage in potential RTPR insulators, and (b) to compare 14-MeV neutron damage with that observed from fission neutrons and protons. The goal of the comparative study is to develop fusion neutron damage simulation techniques which will allow use of the intense fluxes of

other irradiating particles which are now available. In work done to date single-crystal Al_2O_3 (sapphire) has been irradiated with 14-MeV neutrons and the resulting damage has been compared with that obtained from fission neutron irradiation of the same material.²¹

The change in optical absorption which accompanies irradiation is being used as a measure for radiation damage. The measurement of coloration in insulators provides a damage index that is generally more sensitive to low damage levels than other indices (such as direct measurements of electrical properties) and is specifically sensitive to isolated point defects.

Point defects in insulators, such as those caused by irradiation, can trap electrons or holes and become "color centers," which produce unique optical absorption spectra. The area under the spectrum or the height of a spectral peak for a given color center is proportional to the concentration of the corresponding defect, assuming that the fraction of defects populated by electrons is constant. The latter condition was approximately fulfilled in these experiments by x-raying each sample to color saturation before performing the optical measurements. In practice a superposition of spectra corresponding to several kinds of defects is usually observed. Although models for the optically active defects have been deduced for some materials, this has not been the case for all the defects observed in Al_2O_3 . In analogy with other materials the assumption is made that the coloration comes from defects that comprise a significant fraction of the total damage.

The source of 14-MeV neutrons used in this study was the Lawrence Livermore Laboratory ICT rotating target Intense Neutron Source.²² Single crystal Al_2O_3 * samples

*uv grade sapphire window material, approximately 99.999% pure, c axis perpendicular to bombarded surface, obtained from Crystal Products Division of Union Carbide, San Diego, CA.

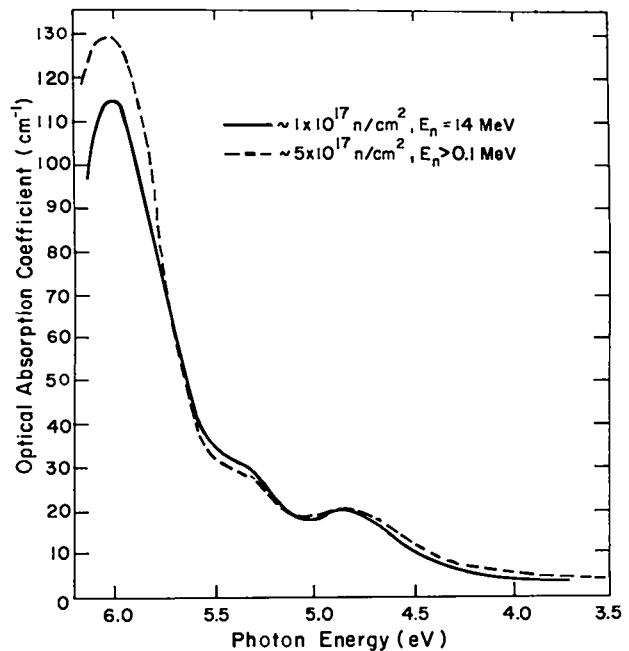


Figure VIII-10
RT optical absorption spectra for single crystal Al_2O_3 after near-RT irradiation by, respectively 14-MeV neutrons (present work) and fission neutrons (Levy).²¹

were irradiated at room temperature at a flux of $\sim 10^{10}$ n/mm² sec to a fluence of $\sim 10^{15}$ n/mm². Figure VIII-10 compares a typical absorption spectrum with that obtained by Levy,²¹ who exposed similar samples at 338 K to a total fluence of $\sim 5 \times 10^{15}$ fission n/mm² from the Brookhaven National Laboratory graphite moderated reactor.

The two spectra appear similar. Levy has resolved his spectrum into sets of Gaussian curves; it appears the spectrum from 14-MeV neutron irradiated Al_2O_3 has the three principal peaks at or near the same wavelengths as Levy's, and the ratio of peak heights is about the same. Although the prominent peaks of the spectra are qualitatively similar, the amount of damage per neutron can be seen to be about 4 times greater for the 14-MeV neutrons, if it is assumed that the coloration in the three peaks accurately reflects the total damage. This result is in rough agreement with an estimate based on interpolation of

calculations by Robinson,²³ which compared damage effectiveness of 14-MeV and 1-MeV neutrons for various elements; uncertainties in this correlation between theory and experiment stem partly from uncertainties in the knowledge of the fission spectrum in Levy's study.

Thermal annealing of the coloration is another source of information concerning similarity in the damage in the two experiments. At these dose levels the defects produced are probably mostly isolated Frenkel pairs; other neutron irradiation experiments²⁴ have indicated that only about 10% of the defects produced in Al_2O_3 at room temperature survive immediate spontaneous recombination. Defects that survive do so either because one member of the pair has been trapped, or is so widely removed from a complementary defect that recombination does not occur at the given temperature because of low mobility. The temperature at which annealing of a given absorption peak begins to progress rapidly is related to the energy at which the responsible defect or its complement becomes mobile. Since the bulk of the neutron damage energy goes into collisions whose energies do not depend in detail on the initial neutron energy, one should expect the environment seen by the defects produced by 14-MeV and fission neutrons to be similar, and thus the annealing behavior should also be similar. This postulate is borne out by Figure VIII-11, which compares isochronal step annealing in air of the optically active defects as seen by reduction of the heights of the three main peaks. Small differences between the annealing results and those of Levy may reflect the somewhat different annealing techniques used.

Annealing begins at temperatures corresponding to typical interstitial migration temperatures ($< 0.5 T_m$), and extends to temperatures typical of self-diffusion ($\sim 0.5 T_m$). It is thus apparent that annealing of defects which are stable near

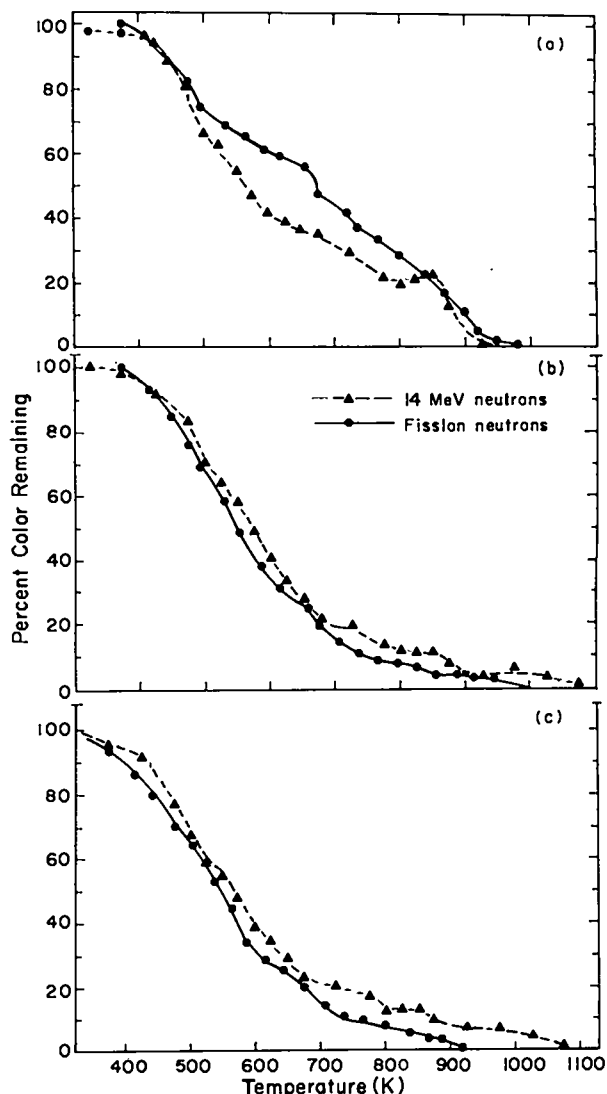


Figure VIII-11
Isochronal annealing (in air) of the three prominent optical absorption peaks in single crystal Al_2O_3 after irradiation with, respectively, 14-MeV neutrons (present work) and fission neutrons (Levy).²¹ (a) height of 6.02-eV band; (b) height of 5.34-eV band; (c) height of 4.85-eV band.

room temperature does not occur by simple recombination but rather by complex defect interactions, as is usually observed in such studies. It may be concluded that for the damage observed optically in Al_2O_3 , 14-MeV and fission neutron damage are qualitatively similar, although 14-MeV neutrons are about 4 times as effective per neutron in causing damage.

3. Evaluation of Postirradiation Electrical Resistivity at Elevated Temperatures

The first-wall insulator of the RTPR is not required to behave as a dielectric during the intense bremsstrahlung and neutron irradiation. The function of the insulator is to support the high voltages imposed on the first wall for ~ 0.1 μ sec at the beginning of the thermonuclear burn cycle. The irradiation is severe only after this heating or preburn stage. Subsequently, the insulator will have several seconds at 1100-1500 K to recover electrically before the dielectric requirement is imposed by the next implosion stage. Therefore it is important to determine the rate of recovery of dielectric properties at these temperatures and to understand the mechanisms of dielectric degradation and recovery in a radiation field.

An apparatus has been constructed for measurement of postirradiation resistivity at elevated temperatures. This device utilizes protons from the LASL Van de Graaf Accelerator to create ionization electrons and atomic displacements in insulators of interest. Samples are thin enough to allow passage of the protons, and guarded electrodes enable bulk resistivity to be monitored. Samples are held at elevated temperature, and the pulsed nature of RTPR radiation simulated by a beam shutter. Postirradiation resistivity is measured with a high-speed recorder monitoring the analog output from an automatic-ranging picoammeter. To test the apparatus, resistivity measurements have been made on SCB glass* in the unirradiated condition from room temperature to 1100 K.

4. Fission Neutron Irradiation of Bonded Insulator/Metal Composites at Elevated Temperatures

It is desirable that radiation-induced swelling of first-wall insulator and metal

*SCB is a name for a glass which is composed of $BaO/Al_2O_3/SiO_2$.

be as small as possible to minimize stress effects. A limited amount of information is available on insulator swelling, primarily from fission reactor exposures. Behavior of common insulators often differs widely; for example, it has been found²⁵ that polycrystalline Al_2O_3 suffers $\sim 3\%$ volumetric swelling after exposure to fission neutron fluences of 5×10^{19} n/mm² ($E_n > 0.1$ MeV) at ~ 1000 K, whereas Y_2O_3 does not appear to swell under these conditions.

An EBR-II fission reactor exposure of Al_2O_3 and Y_2O_3 samples bonded to Nb-1% Zr, which was initiated in December 1972 under another LASL project, has been taken over by the CTR Electrical Insulator Program. The irradiation capsule, which was held at ~ 1000 K during irradiation, was recently removed from the reactor and shipped to Los Alamos. Although detailed dosimetry analysis has not yet been made, it is estimated that the maximum fluence attained was $\sim 8 \times 10^{19}$ n/mm² ($E_n > 0.1$ MeV).

5. Development of SCB Glasses for Fusion Reactor Applications

Consideration is being given to the use of glassy insulators in fusion reactor applications. Advantages can include: good radiation damage resistance, good applicability to metal substrates, and good tolerance of transmutation-induced impurities. The principal disadvantage of glasses is their poor thermal conductivity, which may render them unsuitable for use as a first wall insulator. However, they may still be useful for other fusion reactor applications.

During FY 1973, Atomics International (AI) Division of Rockwell International carried out a study of a family of glasses for possible fusion reactor applications, under subcontract to LASL. These materials, which are of the $BaO-Al_2O_3-SiO_2$ type and referred to as SCB glasses, were known to resist structural damage in exposures to moderate fission neutron fluences at

elevated temperatures. However, nothing was known about their electrical properties.

The following tasks were performed by AI: evaluation of electrical properties, determination of coatability on Nb-1% Zr and TZM (molybdenum alloy), execution of preliminary proton irradiation studies, and optimization of frit compositions. Results of the development study are described in the final report issued by AI;²⁶ the findings are summarized below.

a. The original glass composition suffered severe loss of electrical integrity after exposure to hydrogen at elevated temperatures. Several of the modified frits showed little or no degradation after such exposures.

b. Preliminary findings indicated that good coatings could be obtained on Nb-1% Zr, but not on TZM.

c. Elevated temperature proton irradiation resulted in bubbling of samples when the bombarding particles stopped in the glass. There was some indication that when protons passed through (a more realistic case), damage was minimal.

d. DC dielectric strength of some modified frits at 1073 K was fairly good, and improved with pulsed voltage application. However, dielectric strength decreased rather rapidly with increasing glass thickness. DC electrical resistivity at 1073 K was quite high.

F. ALLOY RESEARCH (W. V. Green, R. A. Yeske, CMB-8)

The radiation, thermal, and stress environment to which the RTPR first-wall alloy will be subjected has been estimated and summarized in Table VIII-2 (Sec. VIII-B). The long-term objective of the experimental work described herein is to quantify the materials limitations and to provide improvements on these limitations when possible. The intense neutron irradiation of the blanket structure will displace atoms, produce interstitial gases (He and H), and generate impurities via transmutation

reactions. Vacancy agglomeration leading to void formation will induce embrittlement of structural alloys.

These processes will occur in the presence of cyclic thermal and hydraulic stresses as well as corrosive, flowing Li coolant. Facilities with which to expose candidate structural metals (refractory metals, vanadium, stainless steel, SAP) to conditions which remotely simulate the anticipated RTPR conditions, unfortunately, do not exist. The effort, therefore, in the metals research area have concentrated on (a) out-of-pile testing of candidate metals to determine creep/fatigue properties and (b) the planning of irradiation testing facilities which have potential for providing an environment which closely resembles that of the future CTR (i.e., the beam-dump irradiation facility at LAMPF). Additionally, a program has been planned which will subject mock-up RTPR blanket specimens (i.e., insulator-coated metal segments) to simulated stress and irradiation environments.

1. Response of Refractory Metals to Cyclic Stresses

The thermal stress anticipated for a Nb first wall in the RTPR has been summarized in Table VIII-2. Stress levels on the order of 60 to 80 MPa are expected to occur once every 10 s; this corresponds to 2.7 MHz each year (85% load factor). The failure of the structural alloy via fatigue crack growth, accumulation of pulses of thermal creep deformation, or by irradiation creep represent real potentialities. Unfortunately, published data on the high-temperature mechanical response of refractory metals and their alloys to cyclic stress are almost nonexistent. Although the study of creep under 14.1-MeV neutron irradiation must await the development and construction of an appropriate facility, some insight into this problem can be obtained from out-of-pile investigations.

Extremely good vacuum is required to investigate the high-temperature, fatigue

properties of niobium or its alloy (Nb-1%Zr). The available vacuum fatigue tester was not suitable in this respect, but proved adequate for molybdenum. Since the properties of Mo are "representative" of Nb (or V), initial tests of the mechanical properties were made on the former metal.

A programmable tester (MTS) was fitted with a cold-trapped, diffusion-pumped vacuum system. The force-displacement relationship was determined at all times at temperatures of 1150 K, and rapid quenching by cold He was possible with the test specimen under stress. Typically a 2-sec stress cycle was used (1 sec to maximum and 1 sec to minimum stress).

Table VIII-9 summarizes experimental results obtained at 1150 K. The samples exhibited both reversible and irreversible strain during each stress cycle. The non-recoverable strain is summarized vs number of cycles in Figure VIII-12. As expected for high-temperature creep, these data display an initial period of rapid strain rate, which decreases to a constant rate and eventually terminates in failure.

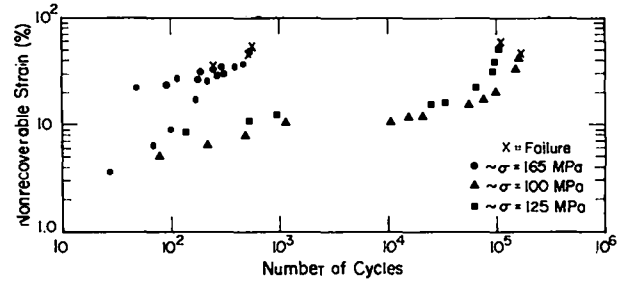


Figure VIII-12
Percent of strain which was irrecoverable vs number of cycles for molybdenum tested at 1150 K for various stresses.

Microscopy indicated that failure occurred via a large number of intercrystalline cracks. Fatigue failure ensues by the propagation of a single crack across the grains until the crack eventually spans the entire sample cross section, whereas failure via creep involves the opening and linking of many intercrystalline cracks. Hence, the failure of Mo at 1150 K under tension is by creep rather than fatigue mechanisms.

The number of cycles required for failure depends strongly on the stress

TABLE VIII-9

RESPONSE OF MOLYBDENUM TO CYCLIC STRESS AT 1150 K

Sample(a) No.	Area (m ² x 10 ⁻⁵)	Minimum Stress (MPa)(b)	Maximum Stress (MPa)(b)	Cycle Stress (MPa)(b)	Full Cycles to Failure	Strain to Failure Pct
3	3.60	5	130	125	1.07 x 10 ⁵	67.
4	3.60	5	170	165	5.5 x 10 ²	37.
5	3.64	5	170	165	6.2 x 10 ²	42.
6	3.72	Tensile test with $\dot{\epsilon} = 5 \times 10^{-3} \text{ sec}^{-1}$ = Y.S. = 102 MPa, VTS = 191.3 MPa				57.
7	3.67	5	105	100	1.6 x 10 ⁵	57.
8(c)	3.10	5	80	75	>2.5 x 10 ⁶	0
9	3.06	5	170	165	1.33 x 10 ²	35.

(a) Samples 1 and 2 were used in preliminary tests.
(b) 1 MPa = 141 psi.
(c) This sample showed no strain and no failure.

amplitude, and in a similar way the time to failure and the creep rate depends strongly on the stress level. The steady-state creep rate depends on the stress raised to the fourth power for temperatures in excess of one-half the melting point (1140 K equals $0.4 T_m$ for Mo). For fatigue dominated mechanisms the number of cycles to failure increases with decreasing stress until a limit is reached below which failure increases with decreasing stress until a limit is reached below which failure does not occur. The cyclic stress amplitude for sample 8 (75 MPa, Table VIII-9) appears to be below this limit, which lies above 2.5 MHz. On the basis of these preliminary results, it does not appear possible to fail Mo by fatigue at 1150 K, since failure by creep occurs first at high stresses and the stress is below the fatigue limit at low stresses. This situation is shown schematically on Figure VIII-13.

Since the temperature considered herein represents a larger fraction of the Nb melting point than for Mo, the life determinant for Nb probably will also be creep rather than fatigue. Whether this conclusion holds for dilute alloys like TZM or Nb-1%Zr remains to be elucidated by further experimentation. Furthermore, the stress cycle used in these tests is different than that expected for the RTPR,

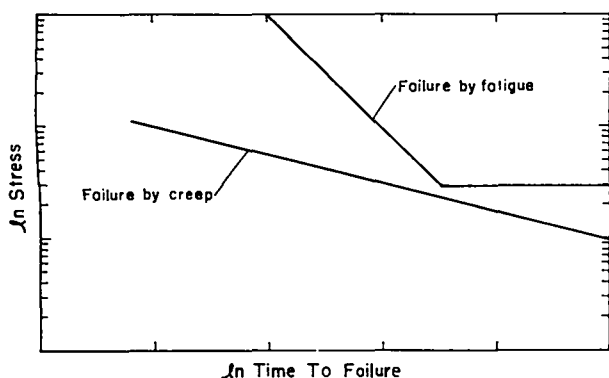


Figure VIII-13
Schematic diagram illustrating the dependence of creep life and fatigue life on stress for Mo at 1150 K.

and this difference also limits the extension of these results to forecast the RTPR first-wall response. In spite of these uncertainties, the conclusion that alloy failure via creep rather than fatigue represents a potential reality for RTPR materials, and future experimentation will be directed at a clearer elucidation of this potential. The influence of radiation embrittlement on the failure mechanism will also be investigated.

2. LAMPF Irradiation Facility

The development of the LAMPF beam step as a neutron irradiation facility is well in progress. This effort is equally supported by DCTR and DPR. The fatigue tester/vacuum system will be capable of good vacuum and, therefore, the testing of Nb alloys will be possible. The design of the irradiation facility, experiment stringers, furnaces, temperature/stress controllers, and neutron dosimeters is nearly completed and components are being fabricated. The irradiation cavity is assembled, although this cavity will be lined with 0.1 m of Ni to enhance the neutron flux (see Section VIII-C). A low-level proton beam has been delivered to the beam dump, and a 10- μ A beam is expected by May 1974. Present expectations suggest the first materials irradiations will be started in the winter of 1974.

G. ENVIRONMENTAL STUDIES (R. Krakowski, Q-DOT, and Donald J. Dudziak, T-1)

The engineering design of the Reference Theta-Pinch Reactor (RTPR) has been subjected to an environmental impact study by the Los Alamos Scientific Laboratory and the Argonne National Laboratory.²⁷ To facilitate a realistic assessment of the environmental effects anticipated for the RTPR, two specific sites were chosen where nuclear (fission) power plants now exist or are under consideration: one site supports a high population adjacent to a large lake (Bailly, near Chicago) and the other site is located on a river in a low

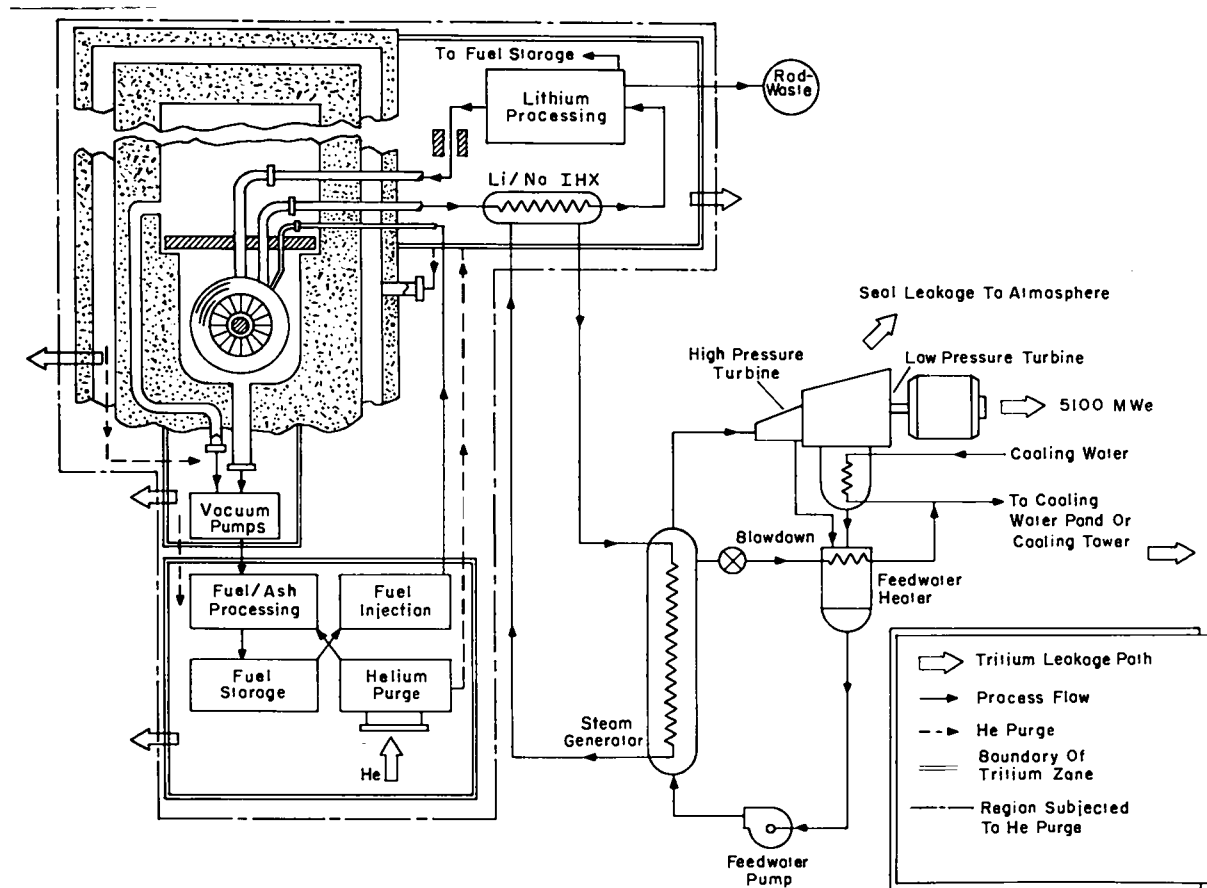


Figure VIII-14
RTPR power plant schematic indicating potential tritium leakage paths.

population zone (Oconee, in South Carolina). Environmental effects under conditions of normal operation (tritium release, structural and impurity activation, thermal effects, radwaste accumulation and transport, resource commitment, and land despoilment) and accidents (maximum credible accident, magnet malfunction, failure of cryogenic systems, fuel injection accident, liquid-metal fires, loss of coolant, and very unusual occurrences) were examined.

A major portion of this study was devoted to understanding quantitatively the rate of routine tritium release to the environment. Figure VIII-14 illustrates the RTPR power plant from the viewpoint of tritium release paths. Tritium migration through the coolant system and into the steam generator represented the major

leakage rate: <6 Ci/day with a 2.5-mm-thick copper diffusion barrier (99% effective) at the Li/Na heat exchanger, compared to ~0.1 Ci/day from all other potential sources. The leakage rate without the copper diffusion barrier was found to be >30 Ci/day. The leakage of 6 Ci/day corresponds to 2.8×10^{-5} % per day of the total tritium contained by the power plant. Table VIII-10 summarizes the dose rates anticipated for the two sites considered, and were determined using two methods of airborne dose rate calculation and three potential power plant cooling schemes. For all cases and for both methods of calculating doses the annual doses are far below the ICRP²⁸ limit (500 mrem/yr), the average background (~125

TABLE VIII-10

MAXIMUM ANNUAL AVERAGE INDIVIDUAL DOSES
FROM THE RELEASE OF 6 Ci/day OF TRITIUM (mrem/yr)

Case	Site 1 (Bailly)		Site 2 (Oconee)	
	ICRP ²⁸	MK ²⁹	ICRP ²⁸	MK ²⁹
Once-through Cooling	0.064 (water)	---	0.064 (water)	---
Wet Cooling Tower	0.0059 (air)	0.12 (air)	0.027 (air)	0.18 (air)
	0.80 (water)	---	0.80 (water)	---
	0.81 (total)	0.92 (total)	0.83 (total)	0.98 (total)
Dry Cooling Tower	0.18 (air)	0.77 (air)	0.17 (air)	0.14 (air)

mrem/yr), and the limits allowed by 10 CFR 20³⁰ (5 mrem/yr).

In addition to tritium, neutron activation of the RTPR blanket structure potentially represents a significant radiation hazard and radwaste problem. Considerable effort was devoted to analyses of induced radioactivity and afterheat. Short- and long-term activities were computed for niobium-1 w/o zirconium (Nb-1%Zr), vanadium-20 w/o titanium (V-20%Ti), and copper-33 w/o alumina materials. Altogether, activities of 28 radioactive isotopes were calculated, several of which were produced by multiple reactions. Table VIII-11 gives a summary of the radioactivity in units of Curies per thermal watt of operating power; afterheat as a percentage of operating power is also given. Values in Table VIII-11 are for the reference design parameters currently being used, viz., a neutron wall loading of 2.0 MW/m², a blanket lifetime of 5 years, and a magnetic coil lifetime of 20 years. Parametric studies were also performed to determine the variation of induced activity with wall loading and operating lifetime. Wall loading had the most pronounced effect, especially in Nb-1%Zr where the relatively short-lived ^{95,95m}Nb activity increased by over a factor of ten for loadings of 0.2 to 6.7 MW/m². Long-lived Nb activities, however, decreased with increased wall loading for shutdown times

beyond 5 x 10⁹ seconds (~150 years) due to a burnout effect. The same burnout effect can be seen for the longer blanket lifetimes. Afterheat calculations are also strongly dependent upon wall loading because of the second-order ⁹⁴Nb(n,γ) ^{95,95m}Nb reaction; values at shutdown varied from 0.312 to 1.52% of operating power as wall loadings increased from 0.2 to 6.7 MW/m². Much of this variation may be illusory, however, because of large uncertainties in the ⁹⁴Nb(n,γ) cross section. Conservative assumptions were made which err on the side of overpredicting ^{95,95m}Nb activities. Calculations of total V-20%Ti radioactivity and afterheat showed only slight (~1%) effects of wall loading and blanket lifetime for two reasons: (a) all isotopes have relatively short half-lives (1 year), and (b) small contributions from second-order reactions, which build up activity proportional to the square of the neutron flux.

Radioactivity expressed in units of Curie per thermal watt of operating power (Ci/Wt) is not useful for assessing biological hazard potential (BHP), because no account is taken of the maximum permissible concentrations (MPC) of the individual isotopes. Thus, a unit of BHP was computed by dividing Ci-Wt by MPC (units of Ci/km³) to estimate relative biological hazards. Figure VIII-15 gives the biological hazard potential (km³/Wt) as a function of

TABLE VIII-11

RTFR RADIOACTIVITY & AFTERHEAT FOR Nb-1Zr & V-20Ti STRUCTURES

$$I_w = 2.0 \text{ MW/m}^2$$

Blanket Life = 5 years

Coil Life = 20 years

	<u>Isotope</u>	<u>Half-life</u>	<u>Absorbable Energy</u> (MeV)	<u>Radio-activity</u> (Ci/Wt)	<u>Afterheat</u> (at shutdown) (%)
	⁸⁹ Sr	50.5d	---	1.04x10 ⁻⁴	
	⁹⁰ Sr	29y	---	4.67x10 ⁻⁷	
	⁹² Nb	2x10 ⁷ y	~1.0	7.36x10 ⁻⁸	
	^{92m} Nb	10.13d	0.9345	0.287	
	^{93m} Nb	12y	0.0304	0.0606	
	⁹⁴ Nb	2.0x10 ⁴ y	1.75	4.45x10 ⁻⁴	
	^{94m} Nb	6.26min	0.0433	1.75	
	⁹⁵ Nb	35.1d	0.821	1.55	
	^{95m} Nb	3.61d	0.235	0.311	
Total Nb-1Zr				3.959	0.991
	⁴⁵ Ca	163d	0.095	4.55x10 ⁻³	
	⁴⁷ Ca	4.54d	1.45	6.56x10 ⁻⁵	
	⁴⁶ Sc	83.8d	2.15	5.10x10 ⁻³	
	⁴⁷ Sc	3.41d	0.26	3.83x10 ⁻³	
	⁴⁸ Sc	43.7h	3.54	0.0226	
	⁴⁹ Sc	57.3min	0.80	4.44x10 ⁻⁴	
	⁵⁰ Sc	1.71min	4.81	1.64x10 ⁻⁴	
	⁴⁵ Ti	3.078h	1.37	2.08x10 ⁻⁴	
	⁵¹ Ti	5.76min	0.98	0.0467	
	⁴⁹ V	331d	0.005	4.58x10 ⁻³	
	⁵² V	3.755min	2.18	0.369	
	⁵¹ Cr	27.71d	0.03	3.62x10 ⁻⁴	
Total V-20Ti				0.426	0.553
	⁶⁰ Co	5.272y	2.62	3.38x10 ⁻³	
	⁶² Co	13.9min	3.89	1.63x10 ⁻³	
	⁶³ Ni	100y	0.022	2.84x10 ⁻³	
	⁶⁵ Ni	2.520h	3.85	9.54x10 ⁻⁴	
	⁶² Cu	9.78min	2.26	0.0262	
	⁶⁴ Cu	12.74h	0.326	0.648	
	⁶⁶ Cu	5.10min	1.23	0.108	
Total Cu coils				0.790	0.247

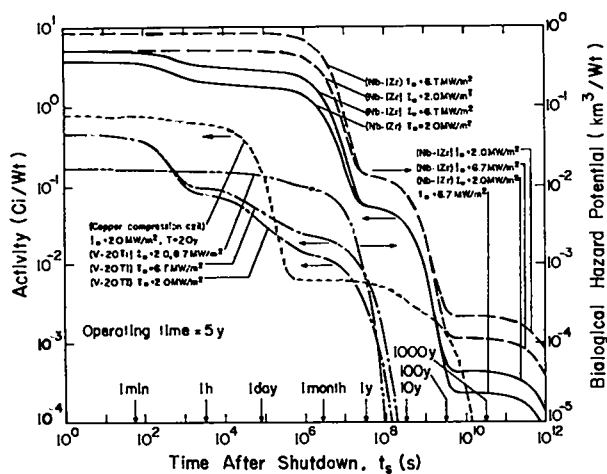


Figure VIII-15
Radioactivity (Ci/Wt) and biological hazard potential (km^3Wt)* for $I_w = 2.0$ and 6.7 MW/m^2 and $T = 5$ y.

shutdown, t_s , for both Nb-1%Zr and V-20%Ti blanket alloys for two wall-loadings (2.0 MW/m^2 for a 10-sec duty cycle and 6.7 MW/m^2 for a 3-sec duty cycle); the activation of the copper compression coil is also illustrated, as is the total radioactivity (Ci/Wt). These data pertain only to a 5-year operating period (100% load factor), although the dependence of activity on wall loading and operating time is treated in detail.³¹ For a corrosion rate of 10.0 $\mu\text{m/yr}$, the lithium clean-up system (assumed 100% effective) will yield approximately 1.7 Ci/kWt-y of radwaste which must be stored or reclaimed.

The nuclear afterheat generated by the radioactivity depicted in Figure VIII-15 is of the same order as that for fission power plants when expressed as a fraction of operating power ($P/P_n \approx 1.0$ and 1.5% for $I_w = 2.0$ and 6.7 MW/m^2 after 5 years of operation). The afterheat power density, however, is a quantity which determines the potential for meltdown in event of a loss-of-coolant accident and is of the order of

*The biological hazard potential (BHP) is defined as the ratio of radioactivity (Ci/Wt) to the maximum permissible concentration in air (Ci/km^3) for a given radioactive isotope.⁵

30-50 times below that for a fission power plant of equivalent power rating.

Although this environmental study is based on an engineering design which is in part speculative and preliminary, no significant environmental impact is anticipated for the RTPR above those expected for any large, power producing facility (i.e., resource depletion, land allotment, etc.). The radiological impact is expected to be far below the already acceptable impact associated with fission power plants of the same power rating. Future design iterations based on better data will permit a more detailed, thorough environmental assessment to be made.

H. NUMERICAL STUDIES OF RTPR BURN AND PLASMA COOLING PROCESSES (T. A. Oliphant, Q-7)

The thermonuclear burn code (BURN-1) has been replaced by a new code (BURN-2) in which the physical model is the same, but the numerical differencing scheme has been replaced by a more recent, superior one.³² The computer running time for a given accuracy has been reduced by almost an order of magnitude. This speed of running has allowed a free use of this code as a subroutine in a code EBAL-1 written to perform an overall RTPR energy balance for a given set of plasma/burn parameters.

Another improvement in the BURN-2 code has been the introduction of a search procedure for determining precisely the amount of compression field required to obtain thermonuclear ignition. It has been observed that if a compression field is used which is exactly enough for ignition, the reaction does not produce enough energy to overcome bremsstrahlung and thereby to increase substantially the reaction rate to obtain a significant burn. To attain a significant burn rate, it has been found that a value of compression field somewhere between 5% and 10% larger than the threshold field must be used.

Also learned from running EBAL-1 is that if enough energy is introduced to yield a favorable energy balance, the quenching by expansion close to the first-wall radius will not entirely stop the burn; it appears likely that additional energy extraction by the cooling layer will be necessary to fully stop the burn. More close coupling between the burn code and the gas blanket code will be required to examine this quench phenomenon in detail.

The classical formula for the thermal conductivity of a neutral gas, $\chi = \chi_0 \sqrt{T}$, has been used by many authors³³⁻³⁶ in discussing the neutral gas layer surrounding a thermonuclear plasma. This relationship, however, is suspect in that it is based on the short mean free path limit. Moreover it can be seen by inspection that the temperature profiles predicted by the model³⁷ change somewhat over a mean free path, particularly in the vicinity of the central plasma. To investigate the finite mean free path effects, a Monte Carlo approach has been used³⁸ in which the collision processes are performed explicitly for simulation particles. The purely neutral region of the cooling layer between 47 cm and 50 cm was considered and a heat flow equilibrium was allowed to take place across this region by running the Monte Carlo code for a sufficient length of time. The cell temperatures in this equilibrium state are plotted (individual points) along with the smooth function obtained from classical theory in Figure VIII-16. The results from the Monte Carlo code are subject to fluctuations and a smooth, monotonic curve should be visualized as passing through the region occupied by these points. The overall flow rate is severely limited by the long mean free path of the particles entering from the plasma-neutral boundary on the left and a rather pessimistic value of heat flow rate is given; namely the heat flux is a few orders of magnitude below that predicted from classical theory. This change is not

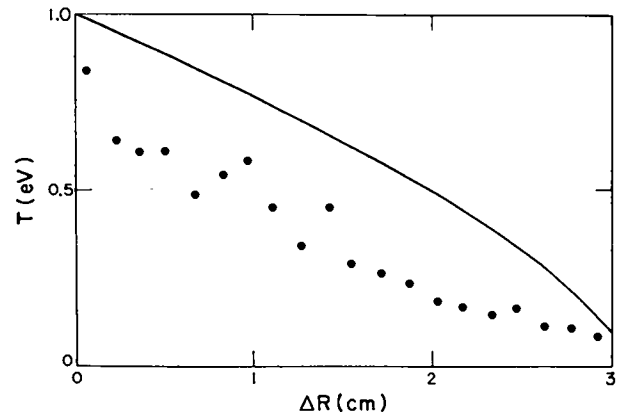


Figure VIII-16
The classical temperature profile (smooth curve) has been plotted along with isolated cell temperatures from the Monte Carlo calculation.

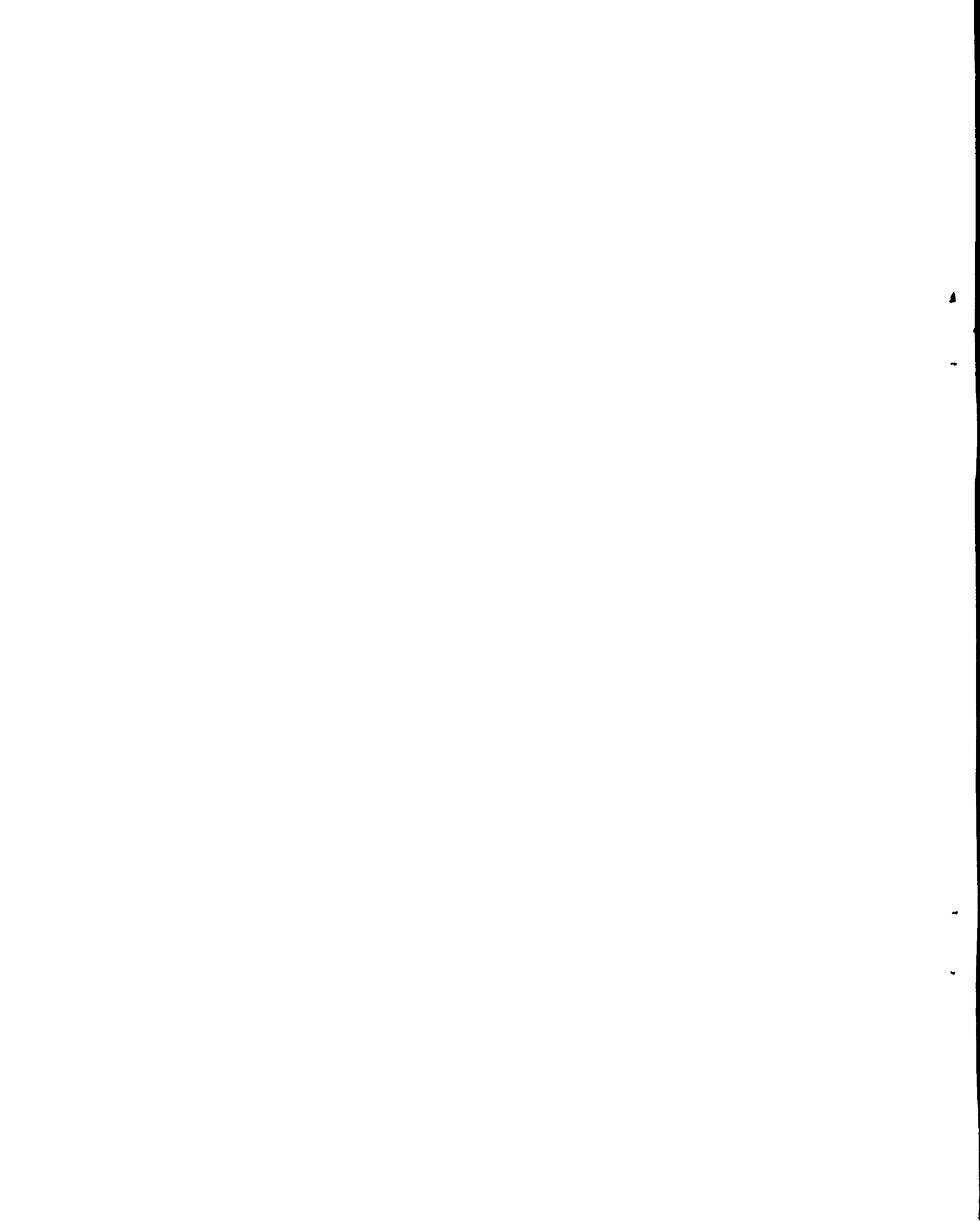
a precise indicator of how much denser the neutral gas will have to be, since the region where classical theory is limited occurs near the ionized region where diffusion effects will alter the situation anyway. New work has been done in reference to the FTR experiment (reported in Sec. X-F). A new version of the neutral gas-central plasma code now being written will remove the difficulties associated with finite mean free path and diffusion across field effects simultaneously and will give more real insight into the details than the previous calculation.

REFERENCES

1. R. A. Krakowski, F. L. Ribe, T. A. Coultas, A. J. Hatch, "An Engineering Design Study of a Reference Theta-Pinch Reactor (RTPR)," Vol. I, USAEC Report ANL-8019/La-5339, to be published (Feb. 1974).
2. T. A. Coultas, R. A. Krakowski, P. Dausvardis, "An Engineering Design Study of a Reference Theta-Pinch Reactor (RTPR)," Trans. Am. Nucl. Soc. 17, 46, (1973).
3. T. A. Coultas, R. A. Krakowski, P. Dausvardis, "Conceptual Design of a Theta-Pinch Power Plant," Proc. 5th Symp. on Eng. Problems of Fusion Research, Princeton, N.J., Nov. 5-9, 1973 (to be published).

4. T. Oliphant, "Flushing and Refueling of a Pulsed Thermonuclear Reactor by Means of a Neutral Gas Layer," Nucl. Fusion 13, 521 (1973).
5. J. M. Bunch, F. W. Clinard, D. J. Dudziak, W. V. Green, R. A. Krakowski, "An Evaluation of Major Material Problems Anticipated for the Reference Theta-Pinch Reactor (RTPR)," Proc. 5th Symp. on Eng. Problems of Fusion Research, Princeton, N.J., Nov. 5-9, 1973 (to be published).
6. R. A. Krakowski, F. W. Clinard, Jr., F. L. Ribe, T. A. Coultas, "Surface Effects at the First-Wall of the Reference Theta-Pinch Reactor," USAEC Report LA-UR-74-42-Rev., Conf. on Surf. Effects in Controlled Thermonuclear Devices, ANL, Jan. 10-12, 1974, to be published in J. Nucl. Mater. (1974).
7. S. C. Burnett, W. R. Ellis, T. A. Oliphant, and F. L. Ribe, "A Reference Theta-Pinch Reactor (RTPR): A Study of a Pulsed High-Beta Fusion Reactor Based on the Theta Pinch," Los Alamos Scientific Laboratory report LA-5121-MS (1972).
8. Donald J. Dudziak, "Discrete-Ordinates Neutronic Analysis of a Reference Theta-Pinch Reactor (RTPR)," Texas Symp. Tech. of Controlled Thermonuclear Fusion Experiment and the Engineering Aspects of Fusion Reactors, Nov. 1972, Proc. to be published.
9. J. J. Ritts, M. Solomito, and D. Steiner, "Kerma Factors and Secondary Gamma-Ray Sources for Some Elements of Interest in Thermonuclear Blanket Assemblies," Oak Ridge National Laboratory report ORNL-TM-2564 (1970).
10. M. A. Abdou and C. W. Maynard, "MACK: A Program to Calculate Neutron Energy Release Parameters and Multigroup Neutron Reaction Cross Sections from ENDF/B," trans. Am. Nucl. Soc., 16, 129 (1973).
11. S. A. W. Gerstl, P. J. Persiani, and Donald J. Dudziak, "Bulk Shielding Studies for a Reference Theta-Pinch Reactor," Trans. Am. Nucl. Soc., 17, 37 (1973).
12. D. J. Dudziak, W. V. Green, T. R. Regenie, and E. G. Zukas, "A Newly Developed Irradiation Facility at LAMPF," Proc. of Am. Nucl. Soc. Topical Meeting Irrad. Experimentation in Fast Reactors, p. 186 (1973).
13. P. A. Seeger, Los Alamos Scientific Laboratory, Personal Communication (1972).
14. E. D. Cashwell, J. R. Neergaard, W. M. Taylor and G. D. Turner, "MCN: A Neutron Monte Carlo Code," Los Alamos Scientific Laboratory report LA-4751 (1972).
15. D. Steiner, "Analysis of a Benchmark Calculation of Tritium Breeding in a Fusion Reactor Blanket," Oak Ridge National Laboratory report ORNL-TM-4177 (1973).
16. D. W. Muir, "Sensitivity of Fusion Reactor Average Cross Section to Thermal Broadening of the 14-MeV Neutron Peak," Los Alamos Scientific Laboratory report LA-5411-MS (1973).
17. D. W. Muir, "Gamma Rays, Q-Values, and Kerma Factors," Los Alamos Scientific Laboratory report LA-UR-73-743 (1973).
18. D. Watson and W. Heyes, "Time Lags in Breakdown of NaCl at High Temperatures," J. Phys. Chem. Solids 31, (1970).
19. R. Cooper, "The Electric Breakdown of Alkali Halide Crystals," Prog. in Dielectrics 5, 97 (1963).
20. R. Gerson and T. C. Marshall, "Dielectric Breakdown of Porous Ceramics," J. Appl. Phys. 30, 1650 (1959).
21. P. W. Levy, "Color Centers and Radiation Induced Defects in Al₂O₃," Phys. Rev. 123, 1226 (1961).
22. R. Booth and H. H. Barshall, "Tritium Target for Intense Neutron Source," Nucl. Instr. and Meth. 99, 1 (1972).
23. M. T. Robinson, in Proceedings of the B.N.E.S. Conference on Nuclear Fusion Reactors held at the UKAEA Culham Laboratory, 17-19 Sept. 1969 (UKAEA, Culham Laboratory, 1969).
24. J. J. Antal and A. N. Goland, "Study of Reactor-Irradiated Al₂O₃," Phys. Rev. 112, 103 (1958).
25. W. A. Ranken, "SEPO Quarterly Progress Report for Period Ending Oct. 31, 1972," LASL Report LA-5113-PR (1972).
26. "Development of Glass Electrical Insulator for Fusion Reactors," Atomic International Report No. AI-73-45 (Oct. 1973).
27. T. A. Coultas, J. E. Draley, V. A. Maroni, R. A. Krakowski, "An Engineering Design of a Reference Theta-Pinch Power Plant; Vol. II, An Environmental Impact Study," USAEC Report ANL-8019/LA-5336 (Apr. 1974). (Also to be presented at the ANS topical meeting on Fusion Power, San Diego, Apr. 1974).
28. ICRP Publication No. 2, "Recommendations of the International Commission on Radiological Protection," Pergamon Press, Oxford (1959).
29. F. Morley, J. W. Kennedy, Fusion Reactors and Environmental Safety: BNES Nuclear Fusion Reactor Conference, Culham Laboratory, p 54, Sept. (1969).
30. 10 CFR 20, Federal Register, 36, 111, June, 1971.

31. Donald J. Dudziak, R. A. Krakowski, "A Comparative Analysis of DT Fusion Reactor Radioactivity and Afterheat," to be presented at ANS topical meeting on Fusion Power, San Diego, Apr., 1974.
32. J. S. Chang and G. Cooper, "A Practical Difference Scheme for Fokker-Planck Equations," J. of Comp. Phys 6, 1 (1970).
33. B. Lehnert, "Screening of a High-Density Plasma from Neutral Gas Penetration," Nucl, Fusion 8, 173 (1968).
34. S. G. Alikhanov, I. K. Konkashbaev, P. Z. Chebotaev, "The Energy Balance in a Dense Fusion Plasma Contained by Walls," Nucl. Fusion 10, 13 (1970).
35. G. K. Verboom, J. Rem, "The Temperature Profile in a Thermonuclear Reactor," Nucl. Fusion 13, 69 (1973).
36. T. A. Oliphant, "Plasma Cooling of a Pulsed Thermonuclear Reactor by a Means of a Neutral Gas Layer," Nucl. Fusion 13, 521 (1973).
37. Los Alamos Scientific Laboratory Report LA-5250-PR, (Figure VIII-2, p. 109, 1972).
38. T. A. Oliphant, "Monte Carlo Treatment of Heat Flow Through a Neutral Gas Layer," Conference on Surface Effects in Controlled Thermonuclear Fusion Devices and Reactors, Session II, Paper No. 6, Argonne National Laboratory, Jan. 10-12, 1974.



IX. MAGNETIC ENERGY TRANSFER AND STORAGE (METS)

A. SUMMARY OF METS EFFORT (Laquer)

The aim of the superconducting magnetic energy storage and transfer project is to provide energy in the 300-MJ range for plasma compression in the next generations of θ -pinch experiments and reactors and to develop the low-loss superconducting energy storage technology needed for efficient θ -pinch reactors.

Highlights of this year's activities have included the following:

- (1) Placing into operation a new expanded facility for all METS work in a remodeled 31 x 18.5 m building.
- (2) Construction and preliminary tests of a 200-kJ energy storage coil.
- (3) Construction of a 3- Ω , 10-kA superconducting switch.
- (4) Operation of 20-kJ, 5- Ω , 1-kA switches at 90% of short sample critical currents.
- (5) Operation of a superconducting 1-kA link or "transmission line" between a storage coil and a switch in separate dewars.
- (6) Modification of energy transfer circuit concept from parallel to series arrangement of coil and switch and experimental demonstration of the operational advantages of this arrangement.
- (7) Systems parametric analysis which suggests greater economy for direct coupled systems with transfer capacitors than is attainable in transformer coupled systems and in systems which do not use transfer capacitors.
- (8) Contractual involvement of three industrial groups in the design and construction of additional 300-kJ energy storage coils to assure the needed long-range

technological base.

(9) Development of design concepts for low-loss superconductors, methods of loss measurement, and initiation of industrial production with adequate quality control of such conductors.

B. NEW METS FACILITY (Blevins, Laquer, Lindsay, Miranda, Rogers, Swannack, Weldon)

The move to the remodeled building SM-218 was completed during the Spring and the 31 x 18.5 m facility is now a fully operational high-voltage cryogenic laboratory with separate facilities for 2-, 30- and 300-kJ energy transfer experiments, switch testing, critical current measurements from 1 A to 25 kA in fields up to 6.5 T, residual resistivity determinations, and energy loss measurements. Oscilloscope instrumentation is shared in a centrally located screen room.

C. 300-kJ ENERGY TRANSFER EXPERIMENT

1. Storage Coil (Blevins, Haarman, Laquer, Miranda, Rogers, Stewart)

Table IX-1 lists the physical parameters for the first storage coil built for the 300-kJ series of energy storage and transfer experiments. The coil, shown in Figure IX-1, consists of 120 turns of fiberglass-wrapped, rectangular cross-section superconductor, edge-wound at Everson Electric Co. on a fiberglass epoxy cylindrical form and potted in a filled epoxy. The conductor with a 6:1 copper matrix to niobium-titanium superconductor ratio is a substitute for the mixed matrix 3 CuNi-3 Cu-1 NbTi used in the original design,¹ but which, unfortunately, was not delivered by the manufacturer. The coil

TABLE IX-1

PHYSICAL PARAMETERS FOR ENERGY STORAGE
COIL, ST 300-1

Construction	Edgewound
Length of Winding (m)	0.730
ID of Winding (m)	0.563
Number of Turns	122.
Length of Conductor (m)	219.5
Conductor Dimensions (mm)	10.16 x 5.08
Copper Matrix to NbTi Ratio	6.
Number of NbTi Filaments	2700.
Inductance (mH)	4.83
Coil Constant (T/kA)	0.1653

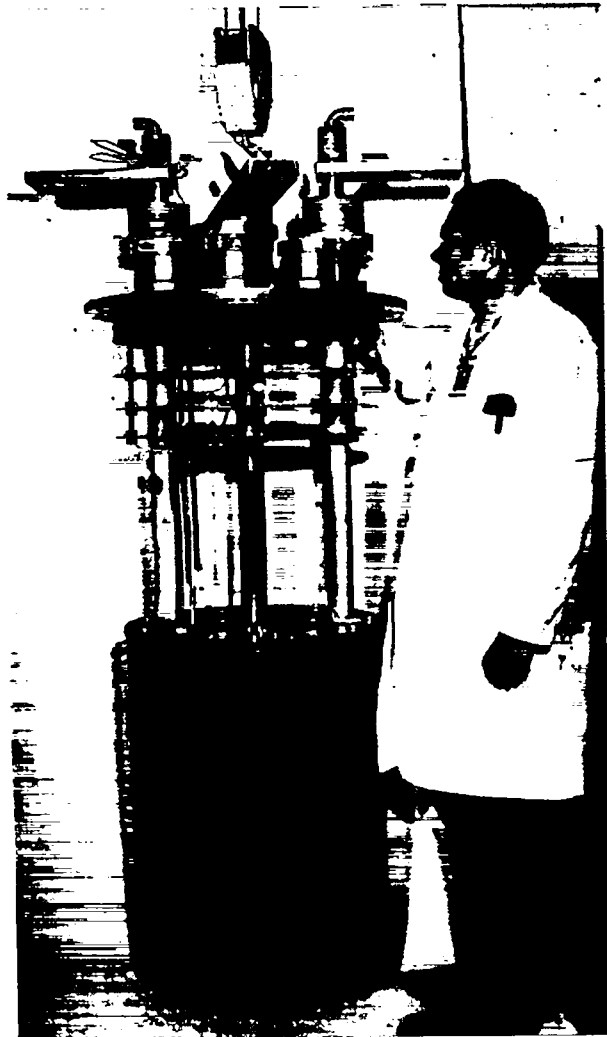


Figure IX-1
Photograph of storage coil ST 300-1.

has been tested to 30 kV at room temperature and has been temperature cycled to liquid nitrogen without any adverse effects. The load line for maximum magnetic field at the conductor intersects the measured critical current curve of the conductor at 9800 A and 1.77 T for a maximum stored energy 228 kJ, Figure IX-2. The coil has been operated at 12.4 kA or 365 kJ stored.

2. Switch (Blevins, Lindsay)

The center-tapped normal-going superconducting switch, shown in Figure IX-3, consists of two parallel Ayrton-Perry wound braids on a phenolic tube. Table IX-2 lists the parameters. The braid is made from 29 3-wire cables of 2.8/1 Cu 70-Ni 30 matrix to NbTi superconductor, is soldered at all crossovers, and is held to the form and itself by a thin layer of cryogenic epoxy adhesive.

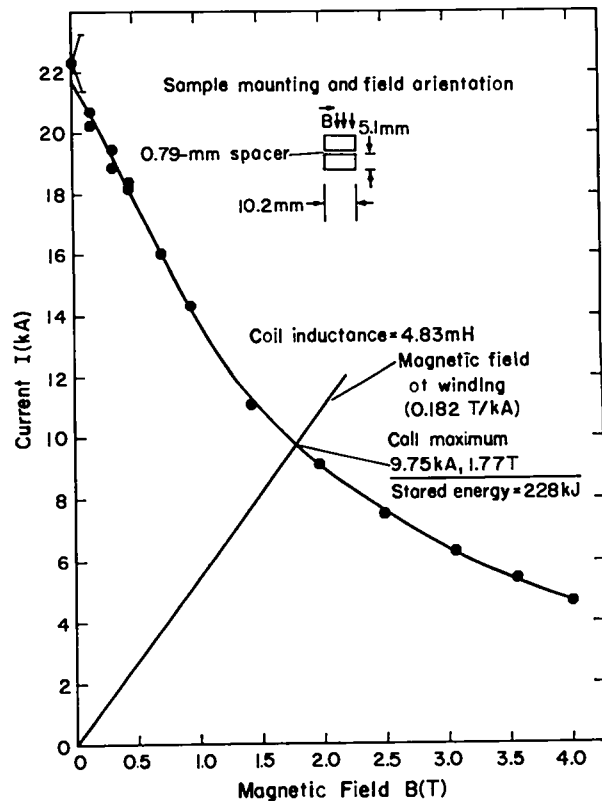


Figure IX-2
Plot of critical current vs field for the conductor used in ST 300-1 and load line for the storage coil.

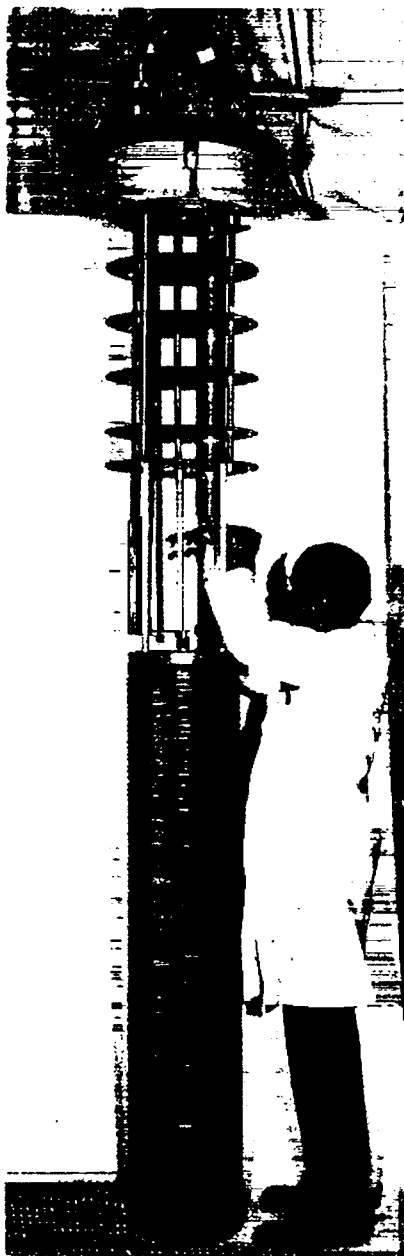


Figure IX-3
Photograph of 3- Ω normal-going superconducting switch SW 300-1.

3. Instrumentation and Controls (Bailey, Haarman, Swannack)

A double 20-kV, 15- μ f capacitor bank and associated spark gap have been assembled for triggering the superconducting switch. Sequence timers, firing controls, and safety interlocks have also been installed. The

TABLE IX-2

SUPERCONDUCTING SWITCH, SW 300-1	
Construction	Ayrton-Perry
Length of Winding (m)	1.45
ID of Winding (m)	0.306
Number of Turns (each half)	45.5
Length of Conductor (each half) (m)	43.8
Conductor Construction	29-element braid of 3-wire cables
Conductor Dimensions (mm)	9.5 x 0.76
Wire Diameter (mm)	0.203
CuNi (70-30) Matrix to NbTi Ratio	2.8
Number of Filaments	61.
Resistance at 300 K (Ω)	3.42
Resistance at 20 K (Ω)	3.00 est

operating characteristics of the power source, a 6-V, 12-kA homopolar generator, have been determined.

D. LOW ENERGY TESTS AND TRANSFER EXPERIMENTS (Laquer, Lindsay, Miranda)

The 30-kJ, 1-kA energy transfer facility has been reassembled with the storage coil and the switch located in separate dewars and connected by a 3-m-long superconducting current link or "transmission line." The facility has been extremely useful as a test bed to evaluate switch designs, switch stabilization, instrumentation improvements, and advanced energy transfer concepts.¹ In particular, it was shown that the arrangement where the coil and switch are in series with respect to the power supply is much more reliable, safer, and easier to operate than where the coil and switch are in parallel. The conventional "persistent mode" method of long-term energy storage, which uses the parallel circuit, is not really required for θ -pinch CTR applications. To date the 30-kJ system has been fired approximately 900 times. Half of these shots were made during 1973, with the series circuit and using center tapped switches triggered from double capacitor

banks, as described in the 1972 report.² It was now proven that the two halves of the switch go normal simultaneously to within 1 μ s in spite of the fact that switching and stored currents add in one-half and subtract in the other and thus are made to exceed I_c with opposite current flow.

E. SWITCH DEVELOPMENT (Blevins, Laquer, Lindsay, Weldon, Weeks).

As of this writing, a normal-going superconducting switch represents the only available high-current circuit breaker allowing microsecond timing. However, it is an expensive device both in terms of materials and refrigeration requirements. The latter have been analyzed in detail³ as a function of the energy deposited in the switch, its mass, the permitted temperature excursion, and the presence of a parallel resistor at room temperature.

On the experimental side, 12 switches have been built for the 30-kJ system to evaluate various materials, configurations, and assembly and potting methods. So far, the noninductive, counterspiralling Ayrton-Perry arrangement of two electrically parallel braided conductors, usually soldered at the crossover points, has been most successful. The prevention of wire motion is the single most important factor in producing switches capable of operating near the sum of the self-field (~ 0.5 T) short sample critical currents of the individual wires in the braid. This immobilization of the wires relative to each other and relative to any magnetic field lines has to be accomplished without loss of thermal contact between the wires and the liquid helium bath by using a specially formulated slightly flexible cryogenic epoxy adhesive known as Aerojet #2.⁴

As the Ayrton-Perry configuration inherently does not fill space very efficiently, some attempts have been made to build more compact pancake switches which, however, create additional insulation and

cooling problems. However, the operation of a number of concentric Ayrton-Perry switch modules in parallel would be expected to alleviate the packing problem and allow easier testing and individual replacement of the 2000- to 5000-A modules that would make up the required 10- to 25-kA switch units. The only problem is that of matching residual inductances with controlled or augmented contact resistances to assure proper current equalization between the modules. A test of this concept was successful in that two nominally 1000-A switches quenched at 2200 A when connected in parallel. Low-resistance, high-current pressure contacts (0.6 n Ω at 10 kA) have been developed that allow reproducible component assembly without the often awkward in-place soldering of superconducting wires. All soldering can be done at the bench.

F. ALTERNATIVES TO CRYOGENIC SWITCHES (Swannack, Thomassen)

The primary technological problem in inductive energy storage involves the interrupting switch. Current and voltage limitations on these switches limit the amount of energy one can store for a given transfer time τ . In the capacitive transfer circuit the limit is $VI\tau/\pi$, or about 0.5 MJ for a 30-kA, 50-kV interrupter and a 1-msec transfer time. The 300-MJ SFX/FTR device would then consist of 600 modules.

The cryogenic switches under development here suffer two major disadvantages. First, when switched the resistance is fairly low, which leads to an unacceptable dissipation. This energy must be removed from a 4° K circuit, hence there is a severe penalty associated with the Carnot efficiency. Estimates of the cost of various subsystems in SFX/FTR indicate that the cryogenic switch costs are \$34 million of the total \$90 million cost. The second disadvantage is the current limitation of a braided and/or cabled multifilamentary

wire. At present, 10-kA switches are being built, but higher currents may be very difficult to achieve, which breaks the energy store into even smaller sized modules.

There are alternatives to superconducting switches which we are exploring. The vacuum interrupters used on a-c power lines for fault protection can be used for d-c interruption if a current zero is forced in the switch with a commutation circuit. The circuit consists of a capacitor bank which is discharged through the switch to reverse the current, and a saturable inductor to slow the rate at which the current goes through zero. The limiting values of dI/dt depend on the type of interrupter. The current must be lower than some value for the deionization time, which is different for each type of switch. Vacuum interrupters with metal arcs have deionization time of some tens of microseconds, whereas the liquid metal arc (mercury vapor) switch under development at Hughes Research Laboratories may have a 5-10 μ sec deionization time.

The rate of recovery of voltage, dv/dt , after interruption must also be limited or the arc will restrike. The value of dI/dt to extinguish the arc is related to dv/dt after interruption, and this relationship has not been extensively explored. Our program on interrupters will attempt to determine this relationship and to devise minimum cost commutation circuits. The costs refer both to capital costs of switches and circuit elements and to the cost in energy necessary to interrupt the current.

The capacitive transfer system to be used on SFX/FTR for inductive energy transfers alleviates some of the problems associated with current interruption. First, the capacitor bank is very large, and by charging it to a fraction of the energy it handles during the transfer cycle it can affect the commutation. Also, the capacitance limits the voltage rise to values much lower than those encountered

in the usual a-c interrupting application.

At present, we are building a test facility for experimentation on the commercial vacuum interrupters in a capacitor transfer circuit. The limitations of these devices will be explored and the technological problems with the entire inductive transfer system will be addressed. The first vacuum interrupters will be available soon for this program.

G. PARAMETRIC ANALYSIS OF ENERGY TRANSFER SYSTEMS (Rogers, Weldon)

An extensive computer parametric analysis has been undertaken⁵ of the SFX and PTR systems requirements and costs. The most important results of this study relate to the alternatives of direct or transformer coupling between the energy storage and the compression coils, and to the use of transfer capacitors to increase the energy transfer efficiency and thus reduce the size of the inductive storage coils.

The studies indicate that the most economical system meeting the 300-MJ SFX plasma compression energy requirements is one where the energy is transferred from ~ 300 modules with direct coupling at a current of 25 kA, a voltage of 60 kV, and with transfer capacitors capable of storing 50% of the transferred energy.

H. INDUSTRIAL COIL DEVELOPMENT (Blevins, Rogers, Thomassen)

Development contracts have been let with Magnetic Corporation of America (MCA), Intermagnetics General (IGC), and Westinghouse (W) to design and build three different 10-kA, 300-kJ energy storage coils. As shown in Table IX-3, there will be different approaches on the choice of superconducting wire, methods of conductor stabilization, and heat transfer to the coil. Thus MCA will use a flat braid of 45 cables of 36 insulated fine single core wires with only copper in the matrix, whereas IGC and Westinghouse propose to

TABLE IX-3

INDUSTRIAL 300-kJ COILS

Wire Element:	<u>MCA</u>	<u>IGC</u>	<u>W</u>
Number of Filaments	1	156	397
CuNi/Cu/SC Ratio	0/1.6/1	1.5/2/1	3/3/1
Wire Diameter (mm)	0.114	0.381	0.508
Number of parallel superconducting wires for 10 kA	1620	400 ± 50	144
Subelement	6 x 6 cable	3 x 4 cable	12-wire cable
Cable Core	Fiberglass	None	nonsuperconducting wire
Assembly Method	Flat Braid	Compacted cable	Roebel transposition
Layers in Coil	1	1	4
Mechanical Stabilization	Epoxy adhesive	Culham epoxy process	Framework

use coarser multifilament mixed-matrix wires in a compacted cable or the Roebel transposition respectively. The latter consists of a steeply pitched spiral winding of 12 parallel cables around a flexible strip of stainless steel. Similarly, the MCA and IGC coils will definitely be potted, albeit by different processes, whereas the Westinghouse coil with a higher copper to superconductor wire may not require potting. The total cost of these contracts is about \$450,000 and the first coils should become available for testing at LASL at the beginning of the 1975 fiscal year.

I. HIGH CRITICAL CURRENT TEST FACILITY (Miranda)

A high-current critical-current test facility has been assembled following an Argonne National Laboratory design.⁶ Currents of up to 25 kA can be induced by a single cycle flux-pump in samples located within a superconducting 4.5 T dipole magnet. The sample can be rotated so as to study critical current anisotropies. The apparatus was used extensively in the development of the 10-kA conductor for the 300-kJ coil, and the critical current curve shown in Figure IX-2 is typical of these measurements. The final stage in manufacturing the rectangular section conductor

apparently flattens the filaments so that critical currents with the applied field perpendicular to the wider face of the conductor are about 25% lower than when the applied field is parallel to the wider face. The apparatus was also used to evaluate the low-resistance high-pressure contacts discussed above.

J. LOW-LOSS SUPERCONDUCTOR (Laquer, W. Turner, Weldon)

The full potential of superconductive inductive energy storage can only be realized if the energy losses in the superconductor are so small that they do not impose an appreciable energy load on the system. This load, of course, includes not only the energy, W_1 , deposited in the cryogenic environment, but also the refrigeration costs, W_2 , to remove that energy. Thus W_2 is about 200 W_1 due to the Carnot limitations of all thermal engines and the mechanical inefficiencies of compressors.

A program has been initiated in cooperation with industry to develop low-loss NbTi superconductors for energy storage coils with millisecond discharge or transfer times. There are three distinct loss mechanisms present in multifilamentary superconductors:

1. Hysteresis in the superconductor

proper which varies as the filament diameter (per unit volume of conductor) and is essentially independent of frequency.

2. Eddy currents in the stabilizing copper which vary as the square of the copper diameter and the first power of the frequency (per pulse and per unit volume of copper).

3. Coupling losses between filaments which appear when the rate of field change exceeds a critical value \dot{B}_c .

Unfortunately, decreasing the coupling losses for millisecond discharges requires large filament diameters which, in turn, increase hysteresis and eddy losses over what they would be with finer filaments. Alternatively, one could reduce the diameter of the individual insulated multifilamentary superconducting wires, but this increases their number and hence the problems in assembling them into a single 10- to 25-kA braid or cable. Clearly, any conductor will represent a complex compromise of many factors. In addition, there are a number of uncertainties and quality control problems in the manufacture of NbTi from the composition and metallurgy of the pure NbTi rods, to the extrusion rate and temperature of the composite billet, and finally the heat treatment and annealing during the wire drawing. All of this information, some proprietary, will be furnished to LASL from pilot production runs now under way at MCA and Supercon. The conductors will be built up from hexagonal NbTi rods surrounded by hexagonal copper shells (for stability) and hexagonal 70-30 copper-nickel shells (for decoupling) as shown in Figure IX-4. Between 150 and 400 of these units will be stacked into internally machined 10-cm-diam by 30-cm-long CuNi extrusion shells to yield about 13 000 m of nominally 0.5-mm-diam wire. Actual diameters will be between 50 and 200% of the nominal value. The \dot{B}_c of each wire also varies at $1/t^2$, where t is the 360° twist pitch of the wire. This effect is stronger

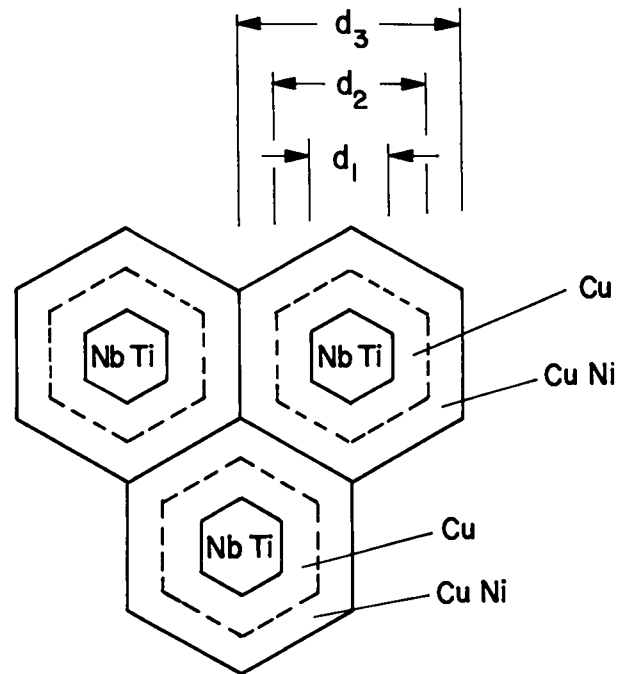


Figure IX-4
Design of low-loss mixed-matrix superconducting wires with stacked hexagonal elements.

than composition and filament diameters. With present technology, it is difficult to reduce to below 6 or 10 wire diameters without breaking filaments and attempts will be made to evaluate this limitation.

The wires will be evaluated by measuring:

1. the residual resistance ratio of the copper in the matrix,
2. the critical current and critical current density as a function of the magnetic field together with the current sharing behavior, i.e., the details of the resistivity variation at the transition from the superconducting to the normal state,
3. the cyclic frequency dependent and independent energy losses discussed above.

It is possible to calculate the expected cyclic losses from existing theories,⁷ but there is little experimental verification on the mixed-matrix low-loss

conductors that we are developing. In addition, the measurement of rate dependent losses in millisecond pulse times and at \dot{B} values of 3×10^3 T/sec (3×10^7 G/sec) represents a difficult experiment which has not been performed anywhere. For this reason, we have assembled a miniature METS system with a normal-going superconducting switch to produce the required field change rates in a small 4-mH, 1000-A, 2-kJ coil.

REFERENCES

1. H. L. Laquer, J. D. G. Lindsay, E. M. Little, J. D. Rogers, and D. M. Weldon, "Design Options and Trade-Offs in Superconducting Magnetic Energy Storage with Irreversible Switching," Los Alamos Report LA-5314-MS, June 1973.
2. F. L. Ribe, progress report LASL Controlled Thermonuclear Research Program, for a 12-month period ending December, 1972, LA-5250-PR, June 1973, p. 124.
3. D. M. Weldon, J. D. G. Lindsay and H. L. Laquer, "Optimization of the Superconducting Switch Design in a Superconducting Magnetic Energy Storage System," Los Alamos Report LA-5218-MS, March 1973.
4. Louis M. Soffer and Ralph Molho, "Final Report: Cryogenic Resins for Glass-Filament-Wound Composites," Report N67-25076 (NASA CR-72114, Aerojet 3343, January 1967.
5. J.D. Rogers, B. L. Baker, and D. M. Weldon, "Parameter Study of Theta-Pinch Plasma Physics Reactor Experiment," Los Alamos Report LAUR-73-1593, paper presented at the Princeton Fusion Technology Symposium, November 1973.
6. J. R. Purcell and H. Desportes, "Short Sample Testing of Very High Current Superconductors," Rev. Sci Inst. 44, 295 (1973).
7. D. M. Weldon, "Energy Loss in Superconducting Magnetic Energy Storage Coils," Los Alamos Report LA-5292-MS, May 1973.

X. DEVELOPMENT AND ENGINEERING OF THE SFX/FTR

The Scientific Feasibility Experiment/Fusion Test Reactor (SFX/FTR) represents the immediate goal of all major, on-going efforts in theta-pinch research at LASL. Therefore, much of the progress reported in other parts of this document is directly or indirectly applicable to the SFX/FTR. In this section we describe the various subsystems in the SFX/FTR design and the development programs which are required before the device can be built. Progress which has not been heretofore discussed is also reported.

A. GENERAL DESCRIPTION OF THE SFX/FTR

The essential elements of the SFX/FTR are presented diagrammatically in Figure X-1. Detailed accounts of work which is specific to a given portion of the SFX/FTR have been covered elsewhere in the document; the development of the "load" component (i.e., first wall, vacuum systems, coils, etc.) has not been previously described and will be addressed in Section F. A decision has not been made to drive the SFX/FTR with a magnetic energy transfer and storage (METS) system or an electrostatic energy transfer system (EETS). This decision must await future developments in METS research and switching technology. A possibility exists of initially operating the SFX/FTR with an EETS (a low-voltage, compact capacitor bank using standard



Figure X-1
Five major systems and systems development required by SFX/FTR.

starter and crowbar switches) with the option of converting later to a METS-driven SFX/FTR if and when the latter technology matures. Figures X-2 and X-3 illustrate conceptually an EETS and METS driven SFX/FTR, and Table X-1 summarizes nominal values of important operating parameters.

The experimental and design activity in each of the major areas identified in Figure X-1 is summarized below. Once the present series of Scyllac experiments demonstrates toroidal equilibrium, the results of the toroidal equilibrium experiments will be used to operate a "staged Scyllac" experiment (25-m major radius), which will require staging of the implosion field; some plasma compression ($\sim 2.T$) is expected. The "staged Scyllac" experiment will lead

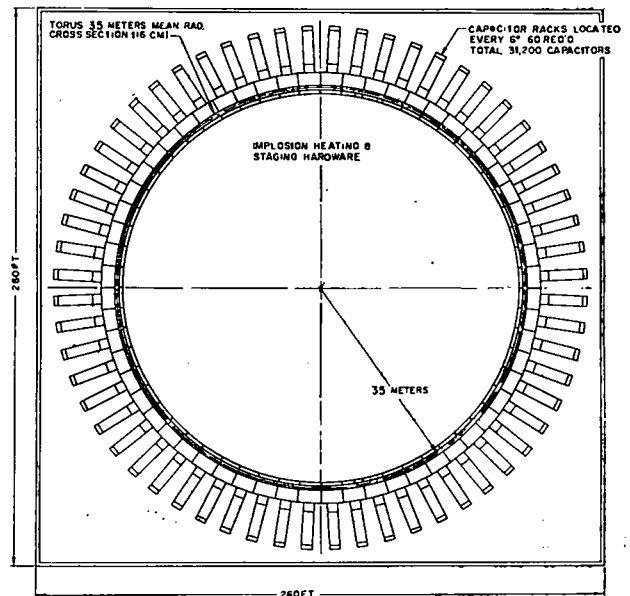


Figure X-2
Conceptual plan view of a staged θ -pinch scientific feasibility experiment powered by low-voltage capacitors (outer racks).

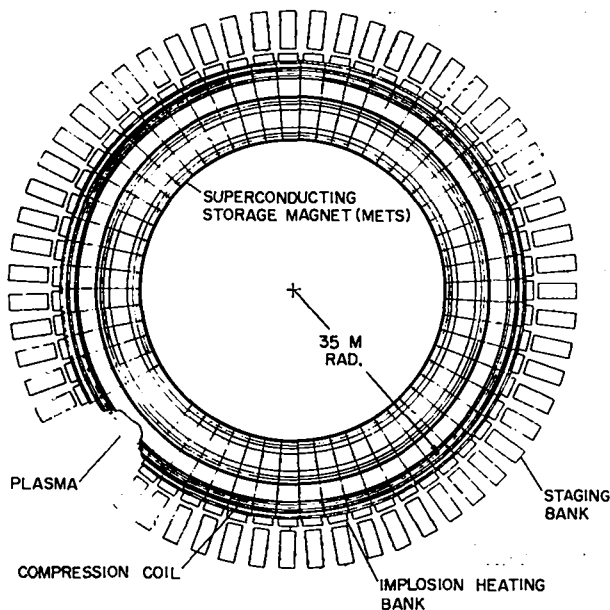


Figure X-3
Conceptual plan view of a staged θ -pinch SFX/FTR powered by a cryogenic magnetic energy supply.

into the SFX/FTR experiment first, by the use of EETS, followed by METS with the EETS converted to a transfer capacitor bank.

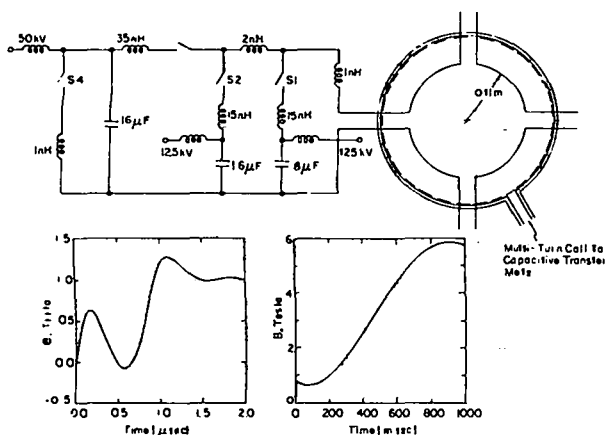


Figure X-4
Circuit diagram and waveforms for the staged θ -pinch SFX/FTR of Figure X-2.

TABLE X-1

SUMMARY OF IMPORTANT SFX/FTR PARAMETERS

β	ratio of plasma pressure to magnetic pressure	~ 0.8
x_f	radius ratio at end of compression	0.30-0.40
δ_0/δ_1	ratio of $l = 0$ to $l = 1$ distortions	0.15
n_f	plasma density in the compressed state	5.0×10^{15} atoms/cm ³
kT_f	plasma temperature in the compressed state	5.4 keV
B_f	final value of compression field	5.-6.T
b	first wall radius	0.1 m
R	major radius of device	30 -35 m
W_B	magnetic energy per unit reactor length	800 kJ/m
E_{θ}^*	implosion heating electric field	2-3 kV/cm
τ_R	risetime of compression field	~ 1.0 msec
τ_D	decay time of compression field	~ 10.0 msec
P_0^*	filling pressure	2-8 mtorr
f_B^*	fractional burnup of DT	~ 0.001

*Specific values of these parameters as determined from thermonuclear burn calculations are summarized in Table X-3.

B. METS AND EETS DEVELOPMENT

The use of capacitors to drive the compression field in SFX/FTR represents a scaling upward in size of an available technology. Roughly 31,000 8-kJ capacitors at 10 kV will be required in conjunction with $\sim 10^4$ starter and crowbar switches. A circuit diagram with voltage and magnetic-field waveforms is shown in Figure X-4. An implosion coil with four feed slots is shown driven by peaking circuits similar to those described in Sec. D. To tie into the compression capacitor bank, the capacitor peaking circuit is crowbarred through a set of switches whose paralleled resistance is on the order of 3 m Ω .

A parameter study of a superconducting magnetic energy transfer and storage driven SFX/FTR has been made;² both direct and transformer coupling between the load and the primary energy storage coil were considered. Without transfer capacitors, only about one-fifth³ of the magnetic energy of the torus is transferred, and the primary energy storage coil must store about 5.8 MJ per meter of compression coil, which corresponds to a total energy of about 1000 MJ. To alleviate this situation a transfer capacitor bank will be used. In many respects this concept also gives a start on the RTPR energy storage problem.⁴

There is an intrinsic lower limit on the risetime of the METS system of about 1 msec, which is set by the superconductor coil current and voltage.³ Therefore an intermediate "staging" capacitor bank of relatively low energy will probably be required as a bridge between the very fast implosion heating circuits and METS. Such a bank is indicated in Figure X-3. Since the risetime of an EETS-driven compression field is considerably smaller than a METS-driven system, the staging requirements for the former will be considerably relaxed.

The design and fabrication of prototype METS coils (300 kJ) has begun at LASL. Additionally, three contracts have been made for similar storage coils with the Westinghouse Corporation, Intermagnetics General Corporation, and Magnetics Corporation of America. Switching within the METS represents a crucial problem, and in addition to superconducting switch development in progress at LASL, plasma switches⁵ and vacuum (mechanical) circuit breakers⁶ are under consideration and study.

C. TRANSFER CAPACITOR DEVELOPMENT (D. Weldon, Q-7)

An important problem encountered in transferring energy from an inductive storage unit directly to an inductive load is the intrinsic inefficiency of the trans-

fer. No more than 25% of the energy originally stored is delivered to the load. However, if a large capacitor bank is placed across the load, the energy transfer can be made as efficient as desired. Under usual conditions of operation this so-called transfer capacitor must store one-half of the energy transferred to the inductive load at one point of the transfer sequence.

A number of circuits involving inductive energy storage and transfer capacitors have been studied to determine some of the relative advantages and disadvantages for use in a scientific feasibility experiment. The circuits studied included the cases in which the load and storage units were transformer coupled and that in which they were mutually connected across the capacitor bank. Results of this analysis along with additional studies on such subjects as high purity aluminum conductors, charging power supplies, current joint resistance, etc. will appear in a forthcoming LAMS report.⁷

A comprehensive parameter study comparing direct capacitive transfer systems; transformer coupled, capacitive transfer systems; and transformer coupled, non-capacitive transfer systems has been initiated. Results of this study should give definitive cost estimates for SFX/FTR experiments based on present day theta-pinch and magnetic energy storage concepts.

D. SFX/FTR STAGING TECHNOLOGY (R. Gribble, Q-7)

A major difficulty anticipated for the SFX/FTR is the requirement for staging or bridging magnetic fields to hold the plasma away from the discharge tube wall from the time of implosion until the compression field is large enough to begin the compression phase. One solution to this staging problem is the use of a bank of 50, 60-kV capacitors that is connected to the implosion coil during the implosion

phase. The staging bank is then crowbarred at peak current to obtain an L/R decay of some 200 μ s for a 1-ms risetime METS system or 50 μ s for an EETS system. The required staging bank energy depends on the resistance of the crowbar circuit, which is assumed to be located mainly in the crowbar gaps. If a 0.1 mohm crowbar gap could be developed, then about 70 kJ/m of staging energy will be needed for METS and about 20 kJ/m would be required for EETS.

E. SFX/FTR IMPLOSION HEATING TECHNOLOGY
(R. Gribble, Q-7)

The implosion heating system involves the free expansion concept discussed in Ref. 1. This process uses a rapidly rising magnetic field, which accelerates ions in a fast implosion until the initially accelerated ions recontact the sheath after passing through the tube center. The field is reduced at this time to a low value, allowing the ions to move outward toward the tube wall with little loss of energy to the field. Just prior to hitting the wall, the ions are stopped or reflected by the rapid application of a more intense magnetic field. Ideally the magnetic field transition times should be much less than an ion transit time across the tube. Practically, however, the production of such a short transition time is very expensive and difficult.

A technically feasible arrangement that does not produce the ideal waveshape appears by simple computer modeling to provide plasma parameters almost as desirable as those produced by ideal waveforms and consists of three sections of capacitors with independent switching of each section. The first section has a quarter-cycle sinewave risetime of about 0.2 μ s and provides the magnetic field for the first implosion of the plasma. Switched into the load coil just after peak current, the slower third section provides the staging field, prolongs the first implosion phase, and prevents the field from going

negative during the second half cycle of the first section. The fast second section is then switched into the load about midway into the second half-cycle of the first to stop and reflect the sheath before the plasma contacts the wall.

A more efficient alternative scheme involves charging the second and third sections to the opposite polarity of the first section and switching again at a point near the beginning of the second half-cycle of the first section. This procedure provides a faster field risetime to stop the expanding plasma, thereby resulting in a lower loss of plasma energy to the field during the expansion. However, the reverse field which is trapped in the plasma by this scheme may result in plasma instability. A schematic diagram of this circuit is depicted in Figure X-5. The switch for the first section is represented by S1; S2 is the second switch, S3 is the third switch, and S4 the staging crowbar switch.

High-voltage coupling between the implosion coil and the compression coil is a problem that always exists in circuits with more than one capacitor bank connected to a load. The total voltage around the implosion coil, whether it be a single or a fractional turn type, is of the order of 300 kV. Clearly any reasonable compression coil design cannot withstand such a large induced potential. By connecting a low inductance capacitor across the compression

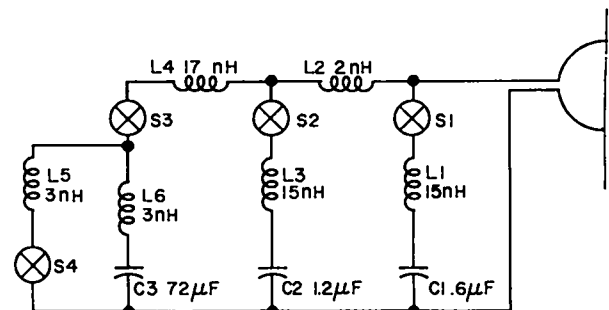


Figure X-5
Circuit diagram of bipolar switch.

coil terminals, a flux is produced in the space between the coils equal to and in the opposite direction of the implosion coil flux, thereby alleviating the problem. However, some voltage will still appear across the capacitor inductance, but this remaining voltage can be further reduced by adding a resistive liner just inside the compression coil.

The penalty exacted for this isolation is the increased implosion system energy storage required to fill the volume between the two coils with magnetic energy. Less implosion system energy is used for larger volumes, but more compression system energy is wasted. The present compromise makes the compression coil volume twice that of the implosion coil. Therefore, almost twice as much energy in the implosion system is required as compared to an arrangement that does not include compression. Utilization of the same coil for both implosion and compression has the same difficulty. A possible solution to this problem is the use of nonlinear elements, such as ferrite material, to fill the void between the coils.

A very simple "ion simulation" calculation was made to estimate the plasma parameters to be expected from an implosion

circuit that used four feed plates. Each feed plate was driven by a 125-kV pulse-forming network described above (PFN) and a 60-kV staging bank. The "ion simulation" calculation used only twenty ions to represent the plasma with a bounce model. No electron effects were included except those implicitly required for charge neutralization. Table X-2 shows the results of this calculation for 10- and 20-mtorr filling pressure and several values of implosion systems stored energy. The value of x_s and kT_s is normalized to 10-kG shock field, B_s , where x_s is the normalized equilibrium plasma radius and kT_s is the ion temperature. In these calculations the implosion magnetic field was not allowed to reverse; the PFN triggering time occurs when section two is switched and likewise for staging time. The difference between kT_s directly calculated from ion energy and that calculated from pressure balance is due to inertial effects still present at the end of the run. The rapidly rising field used to stop the plasma does more than just stop the sheath; this field is sufficient to turn the sheath around and accelerate it, thereby adding more energy to the ions than would be obtained from the pure free expansion procedure (where ions simply stop at the wall).

TABLE X-2

CALCULATION RESULTS OF IMPLOSION HEATING CALCULATIONS

Implosion energy, kJ/meter	62.5	75.	83.3	125.	125.
Staging energy, kJ/meter	109.	109.	156.	156.	156.
Filling pressure, mtorr	10.	10.	10.	10.	20.
PFN trigger time, μ sec	0.70	0.65	0.60	0.46	0.70
Staging time, μ sec	0.35	0.30	0.30	0.46	0.35
Min. plasma radius, mm	56.	47.	43.	32.	39.
Max. plasma radius, mm	100.	103.	102.	99.	99.
x_s	0.64	0.68	0.69	0.61	0.74
kT_s , keV	1.6	1.8	1.7	1.4	1.0
kT_s ,* keV	1.5	1.6	1.7	1.3	1.0
Plasma energy, kJ	6.9	9.2	9.2	7.4	11.7

*Calculated from pressure balance.

F. DESIGN OF SFX/FTR PLASMA CHAMBER (R. Krakowski, Q-DOT, T. Oliphant, K. Thomassen, Q-7)

During the last quarter of CY 1973 an SFX/FTR design group was formed to study specific design and fabrication problems anticipated for the first-wall vacuum requirements, tritium handling, implosion heating/adiabatic compression coils, and general layout. This design team is composed of personnel with expertise in materials science, fabrication, Scyllac theory/experiments, tritium chemistry, and general engineering. The major accomplishments of this newly-formed group are (a) a quantitative identification of the thermal/radiation environment to which the SFX/FTR first wall will be subjected and (b) the initiation of a first-wall design/fabrication/testing program which will lead to a workable SFX/FTR vacuum chamber.

SFX/FTR First-Wall Radiation and Particle Fluxes

A quantitative assessment of the wall problem requires scaling information from wall-stabilized Scyllac experiments to specify the size of the experiment; implosion heating physics to determine the necessary electric field stress on the insulator to achieve ignition after magnetic compression; and a thermonuclear burn calculation specifying the time history of neutron and bremsstrahlung production and plasma internal energy. A concise statement of the scaling laws and their basis in experiment was recently given by Freidberg and Ribe,⁸ and further verification will be forthcoming from the recently completed toroidal Scyllac experiment.

The physics of the implosion process has been explored with both theoretical^{9,10} and computer simulation¹¹ models, and the results of these theoretical analyses will soon come under experimental scrutiny by the implosion heating experiment and the *staging experiment*.¹² The thermonuclear burn code¹³ used in the design of the Reference Theta Pinch Reactor (RTPR)

gives all the required plasma and radiation data except the particle fluxes. The particle flux must be estimated from plasma internal energy and the expansion of the plasma in the decaying magnetic field. Diffusion of the magnetic field into the plasma limits the rapid loss of plasma after the column expands to the wall and the flux between the wall and plasma boundary disappears. The radiation and particle fluxes so computed are factored into a first-wall heat transfer calculation from which the time-dependent temperature and stress loading at the first wall is determined. The results of this wall flux calculation are given below.

The DT plasma is brought to ignition by a combination of implosion heating and adiabatic compression. From the physics of implosion heating as described by a bounce model and free expansion after the contraction of the ions to their minimum radius, the plasma radius after the implosion process is determined. Further, when the initial filling pressure and azimuthal electric field are specified, the magnitude of the plasma temperature and magnetic field after the implosion process are uniquely determined. Specification of the magnetic field to which the plasma is compressed and of the initial electron temperature yields the final electron and ion temperatures, the alpha particle production rate, the final plasma radius, the plasma internal energy, and the neutron and bremsstrahlung wall fluxes. These parameters are the output of a thermonuclear burn code¹³ which follows the evolution of the ion, electron, and alpha particle distribution functions as the alphas are born and deposit their energy in the plasma. The plasma expands adiabatically against the magnetic field, doing direct-conversion work, and the plasma also cools by bremsstrahlung radiation. All these processes are treated self-consistently in following the plasma history.

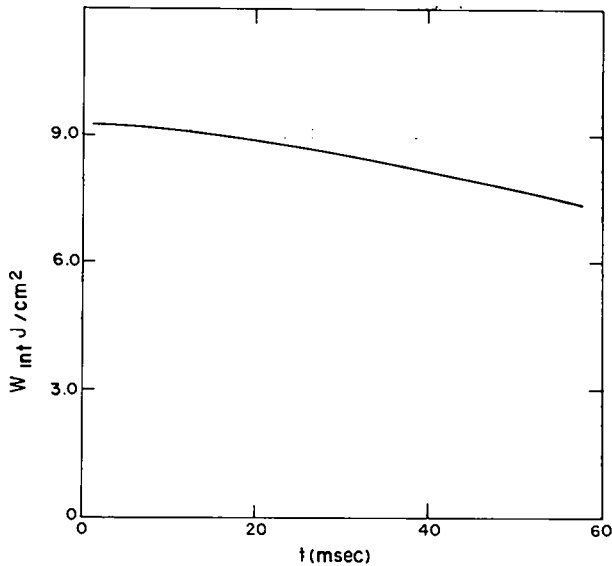


Figure X-6
Internal plasma energy after a 1-msec compression to ignition and 100-msec decay of the 60-kG external field for $p_0 = 5$ mtorr and $E_0 = 3$ kV/cm. The energy is normalized to the wall area which will eventually receive this heat load.

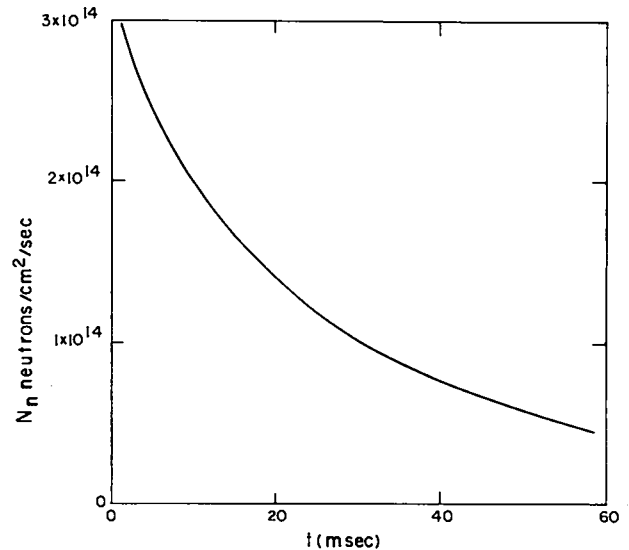


Figure X-8
Neutron current to the wall for the parameters of Figure X-3.

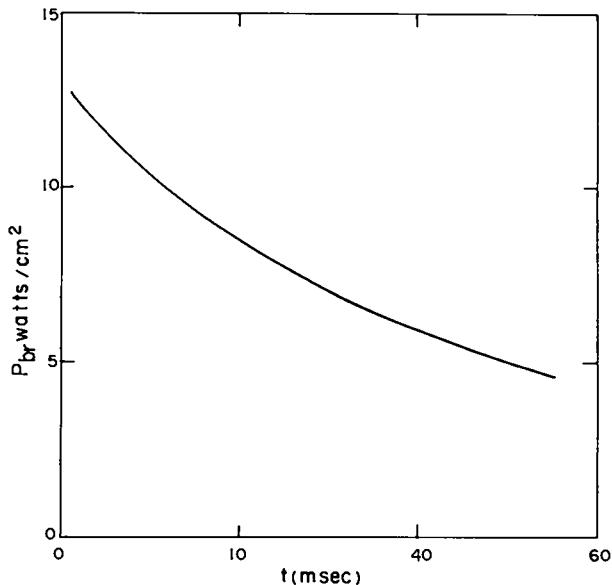


Figure X-7
Wall flux of bremsstrahlung radiation characteristic of a 5-keV plasma for the parameters of Figure X-3.

The results of the application of this code to the FTR plasma are given in Table X-3 for various filling pressures P_0 (mtorr) and electric fields E_0 (kV/cm). In each case the compression field is allowed to reach 6.0 T and then decayed exponential with a time constant τ_D . The computed parameters of interest here are fractional burnup (f_B), neutron and bremsstrahlung wall flux (ϕ and dE_{BR}/dt), and internal plasma energy per unit first-wall area (E_{INT}). The rate at which energy is deposited at the first wall is determined primarily from an MHD diffusion and heat transport calculation, since a portion of the energy is transported by the hot DT. The bremsstrahlung load is not important, and the neutron flux will produce insignificant fluences during the life of the first wall at the anticipated duty cycle (~ 50 pulses/day); the neutron-induced structural activation will not be trivial, however. To indicate the temporal behavior of the fluxes and energies in Table X-3, Figures X-6 through X-8 show the time variation of the plasma internal energy per unit first-wall area, the bremsstrahlung energy flux, and 14-meV neutron

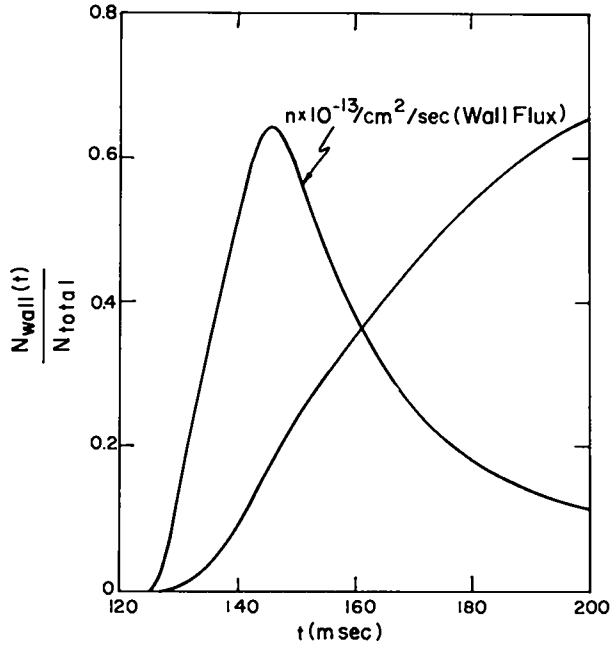


Figure X-9
Number of particles reaching the wall, N_w , normalized to the total number, and the derivative of this function giving the wall flux.

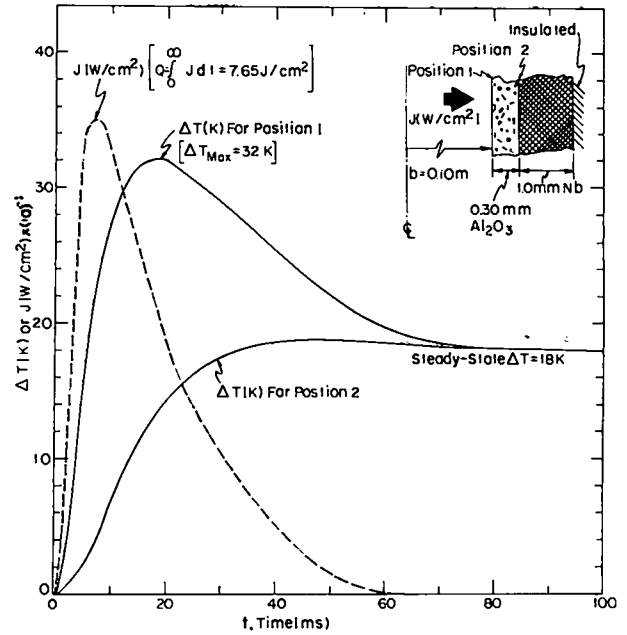


Figure X-11
Temperature transient expected in SFX/FTR first wall..

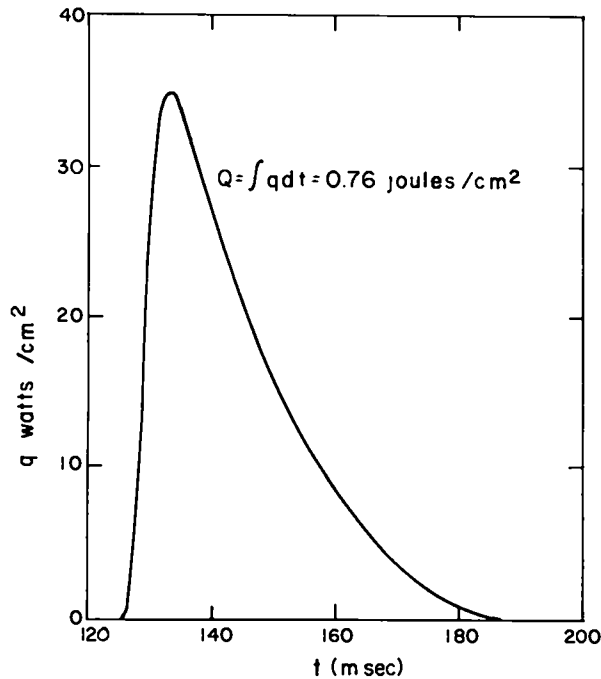


Figure X-10
Heat flux to the first wall and total heat per unit area for the parameters of Figure X-3.

approximation these particles consist of 2-keV ions and electrons and (0.38%) alphas with an average energy of 2 MeV.

The energy flux carried by the ions is shown in Figure X-10, and this energy flow occurs over a period of about 25 msec. The total energy conducted is 0.76 J/cm^2 , or 25% of the internal plasma energy when the plasma first strikes the wall. The remainder may be accounted for by the alpha particles which are 0.38% less numerous, but 1000 times more energetic; hence the alphas account for 3.8 times the 0.76 J/cm^2 or 2.89 J/cm^2 . The temperature transient anticipated for an Al_2O_3 (0.3-mm)/Nb (1.0-mm) first wall under adiabatic conditions is shown in Figure X-11 for the case where Q (J/cm^2) is 10 times that of the expanding DT ions.

G. SFX/FTR FIRST-WALL DESIGN AND FABRICATION

The majority of theta-pinch discharge tubes used to date at LASL have been made of quartz. For the following reasons the SFX/FTR will require the use of ceramic/metal composite construction for the discharge tube (i.e., first wall).

(a) As the first-wall heat load is increased the thermal heat capacity and conductivity must be increased. These increases can be accomplished satisfactorily by the use of thin (~ 0.3 -mm) dielectrics supported on a substantial (~ 1.0 -mm) metallic structure.

(b) Increasing the first-wall diameter (0.2 m for SFX/FTR and 1.0 m for RTPTR) makes impractical the use of a monolithic, ceramic, or glass discharge tube.

(c) The first wall will support the $\ell = 1,0$ (helical, bumpy) distortions required for toroidal equilibrium. Incorporation of these radial perturbations into a monolithic first-wall structure appears impractical.

(d) Since the SFX/FTR will eventually burn DT, a reliable tritium barrier(s) must be provided. The first-wall structure may serve as a tritium barrier and its integrity under stress induced by occasional crowbar failures must be assured.

(e) Internal cooling and tritium purging of the SFX/FTR first wall may be a necessity. The use of a dielectric-coated, metallic structure presents a straightforward method to satisfy these requirements.

The implementation of a ceramic/metal discharge tube represents not only an innovation in fabrication/assembly techniques, but also an extrapolation of present theta-pinch technology (high-voltage technology, coil design, implosion heating) is involved. For this reason a team of experts in the areas of materials engineering, fabrication/assembly technology, high-voltage techniques, and plasma physics has been assembled to attack this problem. Given below is the R/D schedule which has

been adopted for the SFX/FTR first-wall design, fabrication, and testing.

(a) Fabrication of a small (0.5-m-long x 50-mm-i.d.), stainless steel/alumina (or glass) discharge tube which is formed from 36 azimuthal segments (7.5-mm thickness). This discharge tube will be straight and will be tested in an existing Scylla facility for voltage (under crowbar and uncrowbarred conditions) and plasma (DD) implosion characteristics. Considerable pretest (bend strength, dielectric/breakdown characteristics, insulator porosity and bond strength, etc.) and posttest (fracture, surface erosion, changes in mechanical properties) analyses will be made to optimize materials selection and fabrication (assembly techniques).

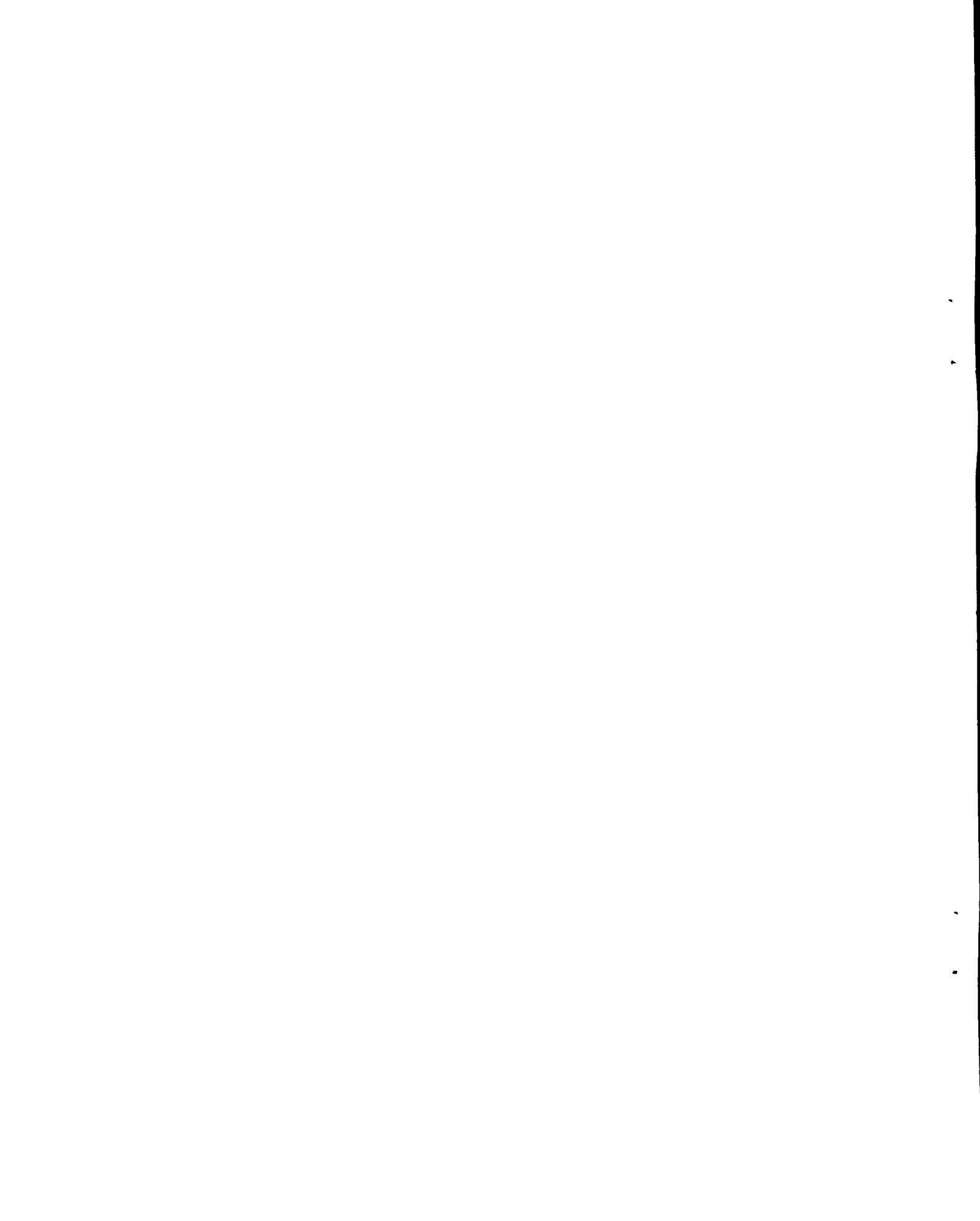
(b) On the basis of the experience gained from (a) above, a larger (~ 100 -mm i.d.) discharge will be tested in conjunction with a specially designed vacuum theta-pinch coil. Similar pretest and posttest analyses will be performed.

(c) A full-sized SFX/FTR discharge tube (200-mm i.d.) will be fabricated and tested in the facility now being used for the heating experiments. Although the first discharge tube may be in the form of a simple cylinder, the $\ell = 1,0$ distortions will be incorporated into this discharge tube.

The major accomplishments of the SFX/FTR design group have been the origination and initiation of R/D plans which will lead to a materials/fabrication technology required of the SFX/FTR by ~ 1976 . Contact with industrial capability will be made during phase (b) and strengthened to the point where fabrication en masse of SFX/FTR discharge tubes (and associated vacuum and coil systems) can smoothly transpire at the end of phase (c).

REFERENCES

1. F. L. Ribe (ed.), "Proposed Experiments on Heating, Staging, and Stabilization of Theta-Pinches," USAEC Rept. LA-5026-P, Feb. 1973.
2. J. D. Rogers, B. L. Baker, D. M. Weldon, "Parameter Study of a Theta-Pinch Plasma Physics Reactor Experiment," 5th Symp. on Engineering Problems of Fusion Research, Nov. 6-9, 1973, Princeton, N.J.
3. F. L. Ribe, "Parameter Study of a Long, Separated-Shock θ Pinch with Superconducting Inductive-Energy Storage," USAEC Rept. LA-4828-MS, Dec. 1971.
4. K. I. Thomassen, "Reversible Magnetic Energy Transfer and Storage Systems," USAEC Rept. LA-5087-MS (1972).
5. G. Hofman, "Inductive Energy Storage and Fast Acting HVDC Interruptors," (IEEE).
6. Ref. to vacuum circuit breakers.
7. D. M. Weldon (LAMS).
8. J. P. Freidberg and F. L. Ribe, "Scaling of Wall-Stabilized Scyllac Experiments," Comments on Plasma Physics and Controlled Fusion, to be published.
9. J. P. Freidberg, R. L. Morse, and F. L. Ribe, "Staged Theta Pinches With Implosion Heating," Texas Symposium on the Technology of Controlled Thermonuclear Fusion Experiments and the Engineering Aspects of Fusion Reactors, Nov. 20-22, 1972.
10. T. A. Oliphant, "A Mixed Snowplow Bounce Model for Shock Heating in a Staged Theta Pinch," Nuclear Fusion, submitted for publication.
11. C. Nielson, private communication.
12. F. L. Ribe, "Proposed Experiments on Heating, Staging, and Stabilization of Theta Pinches," Los Alamos Scientific Laboratory, LA-5026-P, Feb. 1973.
13. T. A. Oliphant, "Fuel Burnup and Direct Conversion of Energy in a D-T Plasma," in Proceedings of the B.N.E.S. Conference on Nuclear Fusion Reactors held at the UKAEA Culham Laboratory 17-19 Sept. 1969 (UKAEA Culham Laboratory, 1969) p. 306.
14. K. I. Thomassen, T. A. Oliphant, "First-Wall Fluxes in a Theta-Pinch Feasibility/DT Experiment," Conf. on Surface effects in Controlled Thermonuclear Devices and Reactors, ANL, Jan. 10-12, 1974, Also USAEC Rept. LA-UR-74-56 (1974).



PUBLICATIONS

PAPERS PUBLISHED OR PRESENTED

D. A. Baker J. A. Phillips	Pressure Balance Limitation in Z Pinches with Diffusion Heating. To be published.	Phys. of Fluids
D. J. Brown S. J. Gitomer H. R. Lewis	The Two Stream Instability Studied with Four One-Dimensional Plasma Simulation Models. To be published.	J. of Comp. Phys.
R. S. Dike J. A. Phillips A. E. Schofield	An All-Metal Discharge Tube for High- Power Z Pinches. To be submitted for publication.	Nucl. Fusion
D. J. Dudziak (contributor)	Fusion Power--An Assessment of Ultimate Potential	WASH 1239
D. J. Dudziak (contributor)	An Engineering Design Study of a Reference Theta-Pinch Reactor (RTPR)	ANL-8019/LA-5336
D. J. Dudziak G. E. Bosler	LAPHAN, A Code to Compute the P0 to P4 Multigroup Photon Production Matrices from ENDF	Nucl. Sci. Eng., 52 No. 2 (1973)
W. R. Ellis	Equations of State and Motion for a Laser- Heated Plasma Column	LA-UR-860
W. R. Ellis	Some Calculated Parameters for a Linear Theta-Pinch SFX	LA-UR-73-1776
W. R. Ellis R. F. Gribble	Some Considerations Regarding a Small Toroidal Shock-Heating Experiment	LA-UR-73-614
W. R. Ellis R. F. Gribble C. R. Harder	Preliminary $l_{1,0}$ Feedback Experiments. Submitted as a technical note.	Phys. Fluids
W. R. Ellis J. P. Freidberg W. E. Quinn	Some Considerations Regarding Wall Stabilization in a Small Experiment	LA-UR-73-615 (Rev.)

W. R. Ellis W. R. Riesenfeld G. A. Sawyer	Proposal for the Construction of a Scylla IV-P Confinement Studies Theta Pinch	LA-5474-P
W. R. Ellis G. A. Sawyer	Scaling Laws for the Linear Theta Pinch I: A Comparison of Magnetic and Laser Heating	LA-5434-MS
W. C. Feldman J. R. Asbridge S. J. Bame H. R. Lewis	Empirical Closure Relation for the Vlasov Moment Equations	Phys. Rev. Lett., 30 No. 7 (1973)
P. R. Forman S. Humphries, Jr. R. W. Peterson	Pulsed Holographic Interferometry at 10.6 μm . To be published.	App. Phys. Letters
J. P. Freidberg	Stability of a Finite Beta, L Equals Two Stellarator	Phys. Fluids, 16 (1973)
J. P. Freidberg F. A. Haas	Kink Instabilities in a High-Beta Tokamak	Phys. Fluids, 16 (1973)
J. P. Freidberg F. A. Haas	Kink Instabilities in a High-Beta Tokamak with Elliptic Cross Section. To be published.	Phys. Fluids
J. P. Freidberg B. M. Marder	Stability of Two-Dimensional Magneto- Hydrodynamic Equilibria	Phys. Fluids 16, (1973)
J. P. Freidberg F. L. Ribe	Scaling of Wall-Stabilized Scyllac Experiments	Comm. Plasma Phys. Controlled Fusion, 1 (1973)
R. A. Gerwin	Energy Loss of a Relativistic Electron Beam in a Plasma	LA-5269-MS
N. T. Gladd W. Horton	Critical Shear and Growth Rates for Drift Waves in a Non-Uniform Current- Carrying Plasma	Phys. Fluids 16, (1973)
N. T. Gladd E. P. Lee	Suppression of the Hose Instability with a Solenoidal Field	UCID-16217
W. V. Green J. Weertman	Dislocation Vibration as a Possible Cure for High Temperature Void Formation in Metals under Fast Neutron Irradiation	Nature 243, No. 5403 (1973)

R. F. Gribble R. Kristal	Multifringe Electro-Optic Phase Modulator	LA-UR-73-1681
G. D. Khoe F. C. Jahoda C. J. Barth H. J. M. Aarts	Design and Feasibility Test of the 90° Thomson-Scattering Experiment for Spica	Rijnhuizen Report 73-77
R. A. Krakowski W. V. Green W. C. Turner	LASL's Experience in Welding Molybdenum	LA-UR-73-505
H. R. Lewis C. W. Nielson	A Comparison of Three Two-Dimensional Electrostatic Plasma Simulation Models. To be published.	J. of Comp. Phys.
H. R. Lewis J. D. Thomas K. J. Melendez	Computation of Fourier Integrals of Truncated Fourier Series	J. of Comp. Phys. 12, No. 4 (1973)
K. F. McKenna T. M. York C. J. Michels	Dynamic Pressure Transducer for Pulsed Plasma Flow Diagnosis	Rev. of Scientific Instruments 44, (1973)
B. M. Marder	Kink Instabilities in Arbitrary Cross- Section Plasmas. To be published.	Phys. Fluids
B. M. Marder	Kink Instabilities in the Belt Pinch. To be published.	Phys. Fluids
B. M. Marder R. E. Siemon	A Long Confinement Experiment (LCE) Proposal	LA-5399-P
J. Marshall	High-Beta Tokamak	LA-5476
R. L. Morse C. W. Nielson	Occurrence of High-Energy Electrons and Surface Expansion in Laser-Heated Target Plasmas	Phys. Fluids 16, (1973)
D. W. Muir	Gamma Rays, Q-Values, and Kerma Factors	LA-UR-73-543
D. W. Muir	Sensitivity of Fusion Reactor Average Cross Sections to Thermal Broadening of the 14-MeV Neutron Peak	LA-5411-MS

T. A. Oliphant F. L. Ribe T. A. Coultas	Direct Conversion by Means of High- β Magnetic Compression and Expansion Cycles	LA-UR-73-404
R. F. Post F. L. Ribe	Fusion Reactors as Future Energy Sources	LA-UR-73-1684
F. L. Ribe	The Los Alamos Program of High-Beta Controlled Fusion Research	LA-UR-73-1213
F. L. Ribe	Proposed Experiments on Heating, Staging, and Stabilization of Theta Pinches	LA-5026-P Rev.
K. S. Thomas H. W. Harris F. C. Jahoda G. A. Sawyer R. E. Siemon	Plasma Experiments on the Linear Scyllac Theta Pinch	LA-UR-73-1460
J. A. Wesson A. Sykes H. R. Lewis	Ion-Sound Instability	Plasma Phys. 15 49 (1973)

*CTR and University of Maryland Meeting
January 1973*

D. A. Baker L. W. Mann	Toroidal Belt Pinch Equilibria (LA-UR-73-104)
J. P. Freidberg F. A. Haas (Culham) W. B. Riesenfeld	Perspective on Various Axisymmetric Toroidal Devices (LA-UR-73-79)

*New Mexico Academy of Science Thirteenth Visiting
Scientist Program
Sponsored by New Mexico Highlands University
January 1973*

H. R. Lewis	Plasma Physics, Fusion Reactors and the Energy Crisis
-------------	---

*University of Colorado, Department of Astro-Geophysics
Boulder, Colorado, February 12, 1973*

H. Dreicer	Anomalous Absorption of Large Amplitude Microwaves Near The Electron Plasma Frequency
------------	--

*Laser Division Colloquium
Livermore, California
February 20, 1973*

H. Dreicer Observation of Parametric Instabilities, Supra-thermal
Electron Production, and Strong Field AC Electrical
Resistivity Near the Critical Plasma Density

Sherwood Theory Meeting, University of Texas, March 1973

D. A. Baker Review of Current Los Alamos Theoretical Work Related to
Toroidal Z-Pinch and Belt-Pinch Equilibria Having Diffuse
Profiles (LA-UR-73-341)

J. P. Freidberg Stability of a Finite β , $\ell = 2$ Stellarator (LA-UR-73-334)

J. P. Freidberg Wall Stabilization in $\ell = 0$ and $\ell = 1$ Systems (LA-UR-73-339)
B. M. Marder
H. Weitzner

J. P. Freidberg Stability of Diffuse Two-Dimensional MHD Equilibria
B. M. Marder (LA-UR-73-333)

J. P. Freidberg Kink Instabilities in a High-Beta Tokamak (LA-UR-73-336)
F. A. Haas (Culham)

J. P. Freidberg Flux-Surfaces for the Scyllac Configuration (LA-UR-73-337)
R. E. Siemon

J. P. Freidberg Linear Stability of High-Beta Plasmas (LA-UR-73-335)
H. R. Lewis

W. P. Gula, T-6 Simulation of a Straight Theta Pinch (LA-UR-73-333)

T. A. Oliphant Flushing and Refueling of a Pulsed Thermonuclear Reactor by
Means of a Neutral Gas Layer (LA-UR-73-344)

T. A. Oliphant Pulsed θ -Pinch Reactor Burn Code (LA-UR-73-343)

B. M. Marder Screw Pinches with Elliptical Cross Sections (LA-UR-73-340)

C. W. Nielson An Implicit, Two-Dimensional, Electromagnetic Plasma
E. L. Lindman, J-10 Simulation Code (LA-UR-73-342)

*Third International Symposium on Toroidal Plasma Confinement
Garching, W. Germany, March 26-30, 1973*

W. R. Ellis Plasma Experiments on $\ell = 1,0$ Helical Equilibria in the
F. C. Jahoda Scyllac Toroidal Sector
W. E. Quinn
G. A. Sawyer
R. E. Siemon

AEC Symposium Series 31, April 1974

J. P. Freidberg Staged Theta Pinches with Implosion Heating, Technology of
Controlled Thermonuclear Fusion Experiments and the
Engineering Aspects of Fusion Reactors, (CONF-721111)

*CTR Electrical Insulator R and D Meeting
Brookhaven National Laboratory, April 5-6, 1973*

W. R. Ellis The Status of the RTPR Engineering Design: An Update
R. A. Krakowski
T. A. Oliphant
F. L. Ribe

*Argonne National Laboratory Meeting
April 29-May 4, 1973*

T. H. Blewitt Radiation Effects in Applications of a Pulsed Spallation
A. N. Goland Neutron Source (ANL-8032)
W. V. Green
J. J. Jackson
V. A. VanLink

*Bell Laboratories, Murray Hill, New Jersey
April 30, 1973*

H. Dreicer Hot Electron Production and Anomalous Microwave Absorption
Near the Plasma Frequency

*Los Alamos Scientific Laboratory Colloquium
May 1973*

W. V. Green Metal and Insulator Research Needs for the Pulsed Fusion
F. L. Clinard Reactor

Joint Committee on Atomic Energy Hearings, July 25, 1973

F. L. Ribe The Los Alamos Scyllac Program of High-Beta Controlled
Fusion Research (LA-UR-73-1055)

*11th Student-Faculty Nuclear Engineering Conference
Argonne National Laboratory, August 1973*

F. L. Ribe Status of Theta-Pinch Experiments (LA-UR-73-1220).
Summary of presentation.

Gordon Conference, Tilton, New Hampshire, August 1973

J. L. Tuck Invited Lecture, Relativistic Beam Fusion

*Los Alamos Scientific Laboratory, August 1973
Summer Study Group on Practical Applications of Accelerators*

W. V. Green High-Temperature Neutron Radiation Damage

*6th European Conference on Plasma Physics and Controlled Fusion Research
Moscow, USSR, August 1973*

D. A. Baker The Toroidal Z-Pinch Program at Los Alamos

L. C. Burkhardt

J. N. DiMarco

P. R. Forman

A. Haberstich

R. B. Howell

H. J. Karr

L. W. Mann

J. A. Phillips

J. P. Freidberg Kink Instabilities in High-Beta Tokamaks and Belt Pinches
F. A. Haas (LA-UR-73-585)

B. M. Marder

W. E. Quinn Review of Scyllac Theta-Pinch Experiments (LA-UR-73-1053)

W. R. Ellis

R. F. Gribble

C. R. Harder

R. Kristal

G. A. Sawyer

F. L. Ribe

R. E. Siemon

K. S. Thomas

*Fifteenth Annual Meeting of the American Physical
Society Division of Plasma Physics
Philadelphia, Pennsylvania, October 31-November 3, 1973*

- D. A. Baker Optimization of Z-Pinch Equilibria (LA-UR-1204)
L. W. Mann
- J. H. Brownell Measurement of Bremsstrahlung Absorption of Microwaves
H. Dreicer and Electron Heating
R. F. Ellis
J. C. Ingraham
- B. L. Buzbee Study of High-Beta Stability with the Vlasov-Fluid Model
H. R. Lewis (LA-UR-73-1202)
J. P. Freidberg
- J. N. DiMarco Electron Temperature Measurements on ZT-1
L. C. Burkhardt
P. R. Forman
R. B. Howell
H. J. Karr
- Dah Yu Cheng Preionization Studies for a High-Voltage, Large-Bore
R. Kristal Theta-Pinch Implosion Experiment
K. F. McKenna
K. S. Thomas
J. E. Hammel
- W. R. Ellis Plasma Equilibrium Studies in the Scyllac Toroidal Sector
R. Kristal
W. E. Quinn
R. E. Siemon
- J. P. Freidberg Kink Instabilities in a High-Beta Tokamak with Elliptic
Cross Section
- R. F. Gribble Numerical Simulations of the Scylla I-B Plasma Implosion
K. F. McKenna
- A. Haberstich High-Beta Symmetric Suydam Modes
- J. E. Hammel Experimental Study of a Fast, High-Density Theta-Pinch
I. Henins Implosion in a 40-cm Coil
J. Marshall
A. R. Sherwood

C. R. Harder	Scylla IV-3, $\ell = 0, 1$ Scaling Results
W. R. Ellis	
R. Kristal	
G. A. Sawyer	
R. B. Howell	Plasma Reflection by an RF-Assisted Magnetic Mirror
P. F. Little	
J. C. Ingraham	Extended Measurements of Threshold for Hot Electron
R. F. Ellis	Production and Anomalous Microwave Absorption Near ω_p
H. Dreicer	
F. C. Jahoda	Plasma Confinement and Energy Losses in the 5-m Linear
G. A. Sawyer	Theta-Pinch Experiment
R. E. Siemon	
K. S. Thomas	
H. J. Karr	Observations on the ZT-1 Toroidal Pinch
L. C. Burkhardt	
J. N. DiMarco	
P. R. Forman	
A. Haberstich	
R. B. Howell	
J. A. Phillips	
R. Kristal	HF Laser Interferometry
H. R. Lewis	Nonlinear Evolution of Vlasov Plasmas (LA-UR-73-1201)
D. C. Barnes	
K. F. McKenna	Implosion Phase Experiments in the Scylla I-B Theta Pinch
K. S. Thomas	
R. E. Siemon	
R. Kristal	
L. W. Mann	Belt Pinch Equilibria Studies
D. A. Baker	
B. M. Marder	Kink Instabilities in Arbitrary Cross-Section Plasmas (LA-UR-73-1200)
C. W. Nielson	Two-Dimensional Simulation of Theta-Pinch Implosion and
N. T. Gladd	Field Diffusion (LA-UR-73-1199)
W. E. Quinn	Plasma Experiments in the Scyllac 5- and 8-Meter θ -Pinch
F. L. Ribe	Toroidal Sectors
W. R. Ellis	
C. F. Hammer	
G. A. Sawyer	

G. A. Sawyer Feedback Stabilization Experiments on the Scyllac
R. F. Gribble Eight-Meter Toroidal Sector
C. R. Harder
K. J. Kutac
R. Kristal
W. E. Quinn
E. Zimmerman

R. E. Siemon Reduction of Stray Light in Thomson Scattering

F. T. Seibel An Automatic Monitoring and Diagnostic Recording System
J. W. Lillberg for the Scyllac Experiment
E. Nelson
G. A. Sawyer

K. S. Thomas The Effect of Strong Magnetic Mirrors on Plasma
H. W. Harris Confinement and Stability in the Linear Scyllac
R. Kristal Experiment

*Lawrence Livermore Laboratory Rotating Target Neutron Source Meeting
Livermore, California, November 1973*

D. J. Dudziak Interim Status Report on LAMPF Radiation Effects Facility

*American Nuclear Society Winter Meeting
San Francisco, November 1973*

D. J. Dudziak Tritium Breeding and Nuclear Heating in a Reference Theta-
Pinch Reactor (RTPR)

S. A. W. Gerstl Bulk Shielding Studies for a Reference Theta-Pinch Reactor
P. J. Persiani (RTPR)
D. J. Dudziak

*5th Symposium on Engineering Problems of Fusion Research
Princeton, New Jersey, November 6-9, 1973*

J. M. Bunch An Evaluation of Major Material Problems Anticipated for the
F. W. Clinard Reference Theta-Pinch Reactor (RTPR) (LA-UR-73-1653)
D. J. Dudziak
W. V. Green
R. A. Krakowski

W. R. Ellis Joule Losses in Linear Theta Pinches, Laser Vs Magnetic Heating (LA-UR-73-1580)

J. E. Hammel The Design of a High-Voltage Generator for the LASL Implosion Heating Experiment (LA-UR-73-1752)

I. Henins
J. Marshall
A. R. Sherwood

J. E. Hammel High-Voltage Technology for the LASL Implosion Heating Experiment (LA-UR-73-1753)

I. Henins
J. Marshall
A. R. Sherwood

*5th Conference on Plasma Physics and Controlled Nuclear Fusion Research
Tokyo, Japan, November 11-15, 1973*

J. H. Brownell Hot Electron Production, Anomalous Absorption and Classical Multiphoton Inverse Bremsstrahlung Absorption Near the Electron Plasma Frequency

H. Dreicer
R. F. Ellis
J. C. Ingraham

*Eastern New Mexico University, Portales, New Mexico
November 30, 1973*

H. R. Lewis The Controlled Fusion Program at the Los Alamos Scientific Laboratory